

國立交通大學

電子物理學系

博士論文

同調波轉換於介觀光學與量子力學之研究

Exploring Coherent Wave Transformations in Mesoscopic

Optics and Quantum Mechanics

研究生：林毓捷

指導教授：陳永富 教授

中華民國一百零二年五月

同調波轉換於介觀光學與量子力學之研究

Exploring Coherent Wave Transformations in Mesoscopic
Optics and Quantum Mechanics

研究生：林毓捷

Student: Yu-Chieh Lin

指導教授：陳永富 教授

Advisor: Prof. Yung-Fu Chen

國立交通大學

電子物理學研究所

博士班論文

A Thesis
Submitted to Institute of Electrophysics
College of Science
National Chiao Tung University
in partial Fulfillment of the Requirements
for the Degree of
PhD
in
Electrophysics

May 2013

Hsinchu, Taiwan, Republic of China

中華民國 一 百 零 二 年 五 月

同調波轉換於介觀光學與量子力學之研究

學生：林毓捷

指導老師：陳永富

國立交通大學電子物理學系博士班

摘要

介觀物理是尺度介於巨觀與微觀的物理科學，使其能涵蓋兩種尺度下的物理特徵；這一尺度下的物理系統也因此孕育了不少有趣的物理現象為許多不同領域的科學家們所深深著迷。直至今日為止，相關的議題還是持續地被關注與研究。本文藉由光在量子(波動光學)與古典(幾何光學)的良好對應性，以光學系統來類比觀察介於量子力學與古典力學之間的介觀現象。再者，由於描述光學系統的波動方程式在近軸近似下與研究量子系統的薛丁格波動方程式有相當良好的數學對應性，在文中我們借助量子力學的理论完備性來探討對應於光波的量子同調態(quantum coherent states)所具有的物理特性。藉由對量子系統的深入分析，我們更容易洞悉波動光學與幾何光學之間的奧妙。也藉此更了解量子態在量子系統中所扮演的重要角色。

文中主要探討同調波在兩種光學系統中的物理面貌，包含光導管(light pipe)與球型雷射共振腔(spherical laser resonator)。看似完全不同的實驗架構，實際上卻以相同的理論架構為基礎。由量子同調態疊加的概念配合嚴謹的理論分析，疊加出來的波函數展現出坐落於古典週期性軌跡(periodic orbit)的物理圖像；透過仔細的實驗觀察，相同的空間圖像也在光學系統中被驗證。藉由同調態在光學與量子力學的相互印證之下，更確立了以量子力學為理論基石的進一步相關研究。

本文另一個重點就是透過雷射共振腔系統外的模態轉換元件(mode

converter)，來連結兩群各具特色的光波同調態。而這兩群光波同調態皆具有獨特的古典週期性粒子軌道形貌，分別是利薩如(Lissajous)曲線和擺線(trochoidal)曲線。此一研究不僅以視覺化的方式呈現數學研究中拓樸學的內涵，也藉由不同耦合機制下的二維簡諧系統，具體的展現了粒子軌道的空間對應轉換關係。由於簡諧系統普遍存在於各個研究領域與問題中，空間轉換同調態的研究與實現想必會是最直接且容易的途徑來刺激或幫助解答更多不同領域中的相關問題。此外，針對實驗結果的理論分析更顯示了這些空間模態擁有很大的角動量，這對於未來的雷射技術提供了一些前瞻性的想法。

而本文另一個探討的議題在介觀物理的研究中一直扮演相當重要的角色，就是波穿透紊亂介質(disordered medium)所展現出來的局域化(localization)現象。本文藉由錐形二次諧波產生(conical second harmonic generation)的方式來觀察紊亂波函數在弱局域化(weak localization)範疇中從遍布態(extended states)到預局域化態(pre-localized states)的連續性變化；透過理論進一步分析實驗量測到的強度分布，我們成功地利用縮版的非線性 σ 模型(reduced version of the nonlinear sigma model)來定量地探討各種形式的強度分布其所對應不同局域化的程度，這是縮版的非線性 σ 模型首次在實驗上的一個應用與對照。再者，為人們所熟知的卡方分布(chi-square distributions)在此一研究中也首次被證實可以有效地使用來定量分析不同局域化的程度，且與縮版的非線性 σ 模型有相當良好的對應關係。由於紊亂系統的實驗並不是很容易觀察，而此一研究提供一個途徑來幫助深入了解紊亂系統所展現出來的物理圖像；另一方面，實驗結果也意味錐形二次諧波產生的方式可以協助研究紊亂晶體中複雜的結構特徵。

Exploring Coherent Wave Transformations in Mesoscopic Optics and Quantum Mechanics

Student: Yu-Chieh Lin

Advisor: Prof. Yung-Fu Chen

Institute and Department of Electrophysics
National Chiao-Tung University

Abstract

Mesoscopic physics, which is in between the microscopic and the macroscopic world, contains physical features of both scales. Distinctive phenomena found in the mesoscopic systems give insights into the quantum-classical correspondence which has attracted lots of attention from researchers. The related issues in mesoscopic regime have been studying and paying close attention. In the thesis we employed optical systems as analog systems to investigate the connection between quantum and classical mechanics. This statement based on the good correspondence between quantum-classical mechanics and wave-ray optics. Moreover, optical wave equation was theoretically elucidated to be in the same mathematical form as the Schrödinger equation. We provided comprehensive studies for the quantum coherent states corresponding to the optical waves. With sophisticated mathematics in quantum mechanics, we are able to understand the wonderland between wave optics and ray optics and the important roles of quantum coherent states in quantum systems.

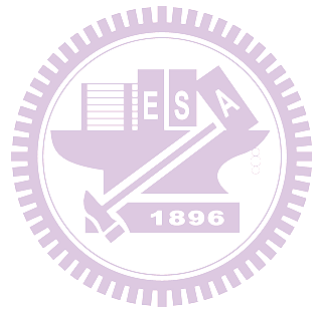
Two kinds of optical systems, light pipes and a laser resonator, were discussed in the thesis. Although it seems that the two setups are totally different, they are

governed by the same theoretical foundation. Within rigorous analyses, the coherent states in corresponding quantum systems revealed intriguing patterns localized on the classical periodic orbits. The same spatial patterns could be found in the optical systems. The validation of the connection between quantum and optical coherent waves enables further studies on related research based on quantum mechanics.

Another topic in the thesis is the linkage of two distinctive optical coherent states localized on the periodic orbits of Lissajous and trochoidal curves. The investigation not only visualized the insight of topology in mathematics but exhibited analog transformational relationship of particle trajectories followed by different coupling mechanisms in a two-dimensional harmonic system. Hence, the realization of the converted spatial coherent states might be an accessible method for the study of fundamental science in various branches. With theoretical analyses, the coherent waves were found to carry large orbital angular momentum and might stimulate further applications.

Besides the two topics mentioned on the above, another topic has been played an important role in the mesoscopic physics—the investigation of localization for disordered wave functions in random media. In this work, we obtain the disordered wave functions from the conical second harmonic generation to explore the continuous transformation of weak localization from extended to pre-localized states. We numerically verify that the experimental density distributions with different extents of weak localization can be excellently analyzed with a reduced version of the nonlinear sigma model. This is the first time that the reduced version of the nonlinear sigma model to be applied to describe the experimental results. Moreover, we perform that the chi-square distributions with fractional degrees of freedom are practically equivalent to the density distributions of the reduced version of the nonlinear sigma model. Since the observation of the disordered wave functions is not accessible, this

work might provide an approach to comprehensively study the intriguing physics behind the disordered systems. On the other hand, the present results suggest the possibility of exploiting conical second harmonic generation as a diagnostic method to understand the complex topological structure of the disordered crystals.



誌謝

Acknowledgement

回憶起剛進交大的時候，剛開始接觸大學的普通物理，一直有個刻板印象，“大學物理只是高中物理的英文翻版”，所以並不會有太大的期待；但上了陳永富老師的普物課，老師帶給學生的啟發和刺激，讓我又重拾對物理的熱忱。課前課後，上課的相關內容總要在腦子裡迴盪個 N 遍，即使花了不少時間只能想通一件事，卻也樂在其中；從大一起就被陳老師的學識與風範所深深吸引，回想之前為了聽老師課堂以外的分享，不是陳老師導生的我，竟也厚著臉皮去參加老師的導生聚。除了在大一普物課深受陳老師的啟發外，在之後的日子裡，也追隨了陳老師，上了老師不少的課程，即使是相同的課程，老師總能傳授給我們新的訊息與知識；而在大二那年暑假，我就正式加入了陳老師的研究團隊，研究的路上，充滿驚奇與挑戰，但我很幸運，能一路跟隨陳老師；老師擁有豐富的實作經驗與深厚的理論功底，總是能適時地引領我、釐清我的盲點；除了研究上的指導，在待人處事與生活上，老師更是我人生路上的嚮導，面對生活上的挑戰，老師給予我的關懷與幫助總能讓我放心於研究的路上而不至於蠟燭兩頭燒。再多的文字也都無法表達我內心對陳老師的感激，但在這裡我還是想要獻上我對陳老師由衷的感謝。在研究的路上，另一個我想要感謝的老師是黃凱風老師，黃老師在研究上對我的啟發也扮演相當重要的角色，黃老師擁有深厚的物理背景，因此對於複雜的物理問題，黃老師總能以清晰簡單的物理圖像，使問題撥雲見日，引領我看到物理之美；黃老師求知若渴的精神和對研究的熱情更是讓我印象深刻，除了關心大家的實驗狀況，黃老師不管聚餐還是走在路上，總是論文、學術資料不離手，隨時跟陳老師熱烈地討論相關的研究議題。兩位老師對研究的熱忱與態度都一點一滴的烙印在我的內心；當然，要成為一個成熟的研究者，對我來說還有許多要努力的地方，但我會以兩位老師作為我的標竿榜樣，持續前行。

在研究的路上，除了兩位老師的幫助與教導，還有許多幫助過我的學長姊

們；亭樺學姊，是我的小師父和能一起哭一起笑的好麻吉，不管是研究還是身邊的五四三總是能話家常，也總是能以大姊大的角度給我適時的提醒與關懷。蘇冠暉蘇老大，老大總是能用寥寥幾句話就解答我問題的癥結點，不得不佩服他敏銳的觀察力和精闢的見解與理解力。依萍學姊，細心體貼的她，不管是生活上和研究上都給予我許多的關心和幫助。興弛學長，在我剛進實驗室時指導我，讓當時是菜鳥的我在研究上能更快地上手。彥廷學長，在研究上常常提供我相關的意見和想法，是個很可以分享與討論的對象。還有已經畢業但也給予我相當多協助的學長姊們，感謝雅婷、家楨、哲彥、仕璋、和漢龍學長。另外也要感謝平時能一起討論和互相鼓勵的好麻吉小江、威哲、郁仁、舜子和建至，讓我在研究的路上能擁有一群貼心的夥伴們而並不會感到孤獨；還有實驗室裡的毅帆、易純、段必、小擘子、咪婷、平平、小佑、奶油、家翰、昱辰、容辰、泰緯、育廷、純甫和文政，在實驗室裡跟大家一起經歷和分享過的美好時光都將成為我最棒的回憶。

最後我要感謝我最愛也最愛我的家人，感謝我的家人一直以來對我無私地付出與鼓勵，我期許自己未來能成為他們最強而有力的肩膀與後盾。

Contents

| | |
|---------------------------|-------------|
| Abstract (Chinese) | i |
| Abstract | iii |
| Acknowledgement | vi |
| Contents | viii |
| List of Figures | xi |

| | |
|--|----------|
| Chapter 1 Introduction to the Thesis | 1 |
| 1.1 Classical Mechanics and Ray Optics : Periodic Orbits..... | 1 |
| 1.2 Schrödinger Wave Equation and Paraxial Wave Equation | 2 |
| 1.3 Optical-Mechanical Analogy | 7 |
| 1.4 Mesoscopic Wave Functions..... | 10 |
| 1.4.1 Periodic Orbits in Mesoscopic Systems..... | 10 |
| 1.4.2 Disordered Wave Functions in Random Media | 11 |
| Reference | 14 |

| | |
|--|-----------|
| Chapter 2 Coherent Wave Transformation in Quantum Harmonic Oscillators and Spherical Laser Resonators | 18 |
| 2.0 Introduction..... | 18 |
| 2.1 Coupled Quantum Harmonic Oscillators..... | 20 |
| 2.1.1 Eigenstates : SU(2) Transformation..... | 21 |
| 2.1.2 Coherent States : Single Periodic Orbits..... | 24 |
| 2.1.3 Coherent States : Multiple Periodic Orbits | 39 |
| 2.2 Analogous Optical Experiments | 56 |
| 2.2.1 Experimental Setup..... | 56 |
| 2.2.2 Eigenmodes : General Huygens' Integral | 57 |
| 2.2.3 Coherent Modes: Single Periodic Orbits | 63 |
| 2.2.4 Coherent Modes : Multiple Periodic Orbits..... | 69 |
| 2.3 Extension Topic : Generation of Optical Vortex Array | 82 |
| 2.3.1 Introduction..... | 82 |

| | |
|--|-----|
| 2.3.2 Transformation of Fundamental Laser Modes..... | 84 |
| 2.3.3 Formation of Optical Vortex Array..... | 86 |
| 2.3.4 Formation of Flower Laguerre-Gaussian Modes..... | 91 |
| 2.3.5 Experimental Setup..... | 92 |
| 2.3.6 Experimental Results and Discussions..... | 94 |
| 2.3.7 Summary..... | 96 |
| Reference..... | 102 |

Chapter 3 Generation of Resonant Geometric Modes in Quantum Circular

| | |
|---|------------|
| Billiards and Light Pipes..... | 107 |
| 3.0 Introduction..... | 107 |
| 3.1.1 Eigenstates..... | 108 |
| 3.1.2 Coherent States..... | 111 |
| 3.1.3 Transient Dynamics of Released Coherent States..... | 115 |
| 3.2 Analogous Optical Experiments..... | 115 |
| 3.2.1 Experimental Setup..... | 115 |
| 3.2.2 Coherent Modes..... | 116 |
| 3.2.3 Propagation of Coherent Modes..... | 117 |
| 3.2.4 Spiral Patterns..... | 121 |
| Reference..... | 128 |

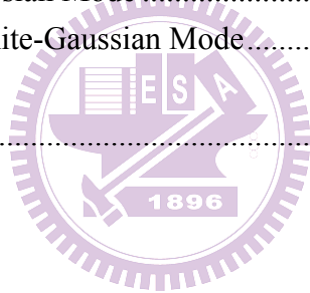
Chapter 4 Formation of Centrally Focused Beam via Intracavity Second

| | |
|---|------------|
| Harmonic Generation..... | 131 |
| 4.0 Introduction..... | 131 |
| 4.1 Theoretical Analyses..... | 133 |
| 4.1.1 Wave Functions of Laguerre-Gaussian Flower Modes..... | 133 |
| 4.1.2 Second-harmonic Laguerre-Gaussian Flower Modes..... | 135 |
| 4.1.3 Propagation of Second-harmonic Waves..... | 138 |
| 4.2 Experimental Observations..... | 141 |
| 4.2.1 Experimental Setup..... | 141 |
| 4.2.2 Generation of Centrally Focused Beams..... | 143 |
| Reference..... | 149 |

Chapter 5 Weak Localization in Disordered Systems with Conical Second

| | |
|---------------------------------|------------|
| Harmonic Generation..... | 151 |
| 5.0 Introduction..... | 151 |

| | |
|---|-----|
| 5.1 Experimental Observations | 153 |
| 5.1.1 Experimental Setup and Results | 153 |
| 5.2 Statistical Analyses | 154 |
| 5.2.1 Porter-Thomas Distribution and 1D Nonlinear Sigma Model | 154 |
| 5.2.2 Reduced Version of the Nonlinear Sigma Model..... | 157 |
| 5.2.3 Fractional Chi-square Distribution | 160 |
| 5.2.4 Relation between Statistical Models | 162 |
| Reference | 164 |
| | |
| Chapter 6 Summary and Future Work | 166 |
| 6.1 Summary | 166 |
| 6.2 Future work..... | 169 |
| | |
| Appendix A | 170 |
| Appendix B | 174 |
| B.1 Input a Hermite-Gaussian Mode | 174 |
| B.2 Input a Rotated Hermite-Gaussian Mode..... | 177 |
| | |
| Curriculum Vitae | 181 |



List of Figures

Chapter 1

Fig. 1.1.1 Confined systems with different boundary conditions.3
 Fig. 1.3.1 Optical-Mechanical analogy. 12

Chapter 2

Fig. 2.1.1 The intensity distribution of the eigenstates $|n_1, n_2\rangle_{\hat{H}}$ with different indices (n_1, n_2) , various values of α values and constant value of $\beta = \pi/2$ 25

Fig. 2.1.2 The intensity distribution of the eigenstates $|n_1, n_2\rangle_{\hat{H}}$ with different indices (n_1, n_2) , various values of β and constant value of $\alpha = \pi/2$: (a)-(e) $(n_1, n_2) = (15, 10)$, (a')-(e') $(n_1, n_2) = (55, 3)$ 26

Fig. 2.1.3 The intensity distribution of the eigenstates $|n_1, n_2\rangle_{\hat{H}}$ with different indices (n_1, n_2) , various values of α and constant value of $\beta = \pi/2$; (Upper) traveling-wave form; (Lower) standing-wave form.27

Fig. 2.1.4 Classical periodic orbits for the case $\omega_1/\omega_2 = 8/1$, $(A_1, A_2) = (35, 100)$, and $(\phi_1, \phi_2) = (-\pi, 0)$ corresponding to Eq. (2.1.13).....29

Fig. 2.1.5 Classical periodic orbits for the case $\omega_1/\omega_2 = -9/1$, $(A_1, A_2) = (60, 150)$, and $(\phi_1, \phi_2) = (-\pi, 0)$ corresponding to Eq. (2.1.13).....30

Fig. 2.1.6 Theoretical results for the intensity distribution of the stationary states $|\Psi_{\bar{n}_1, \bar{n}_2}^{\pm p, q}(\gamma)\rangle_{0,0,0}$ for varying values of β with the parameters of

$$\omega_1/\omega_2 = 5/2, (\bar{n}_1, \bar{n}_2) = (9, 80), \gamma = -\pi/2, \text{ and } \alpha = \pi/2 \dots\dots\dots 36$$

Fig. 2.1.7 Theoretical results for the intensity distribution of the stationary states

$$\left| \Psi_{\bar{n}_1, \bar{n}_2}^{\pm p, q}(\gamma) \right\rangle_{0,0,0} \text{ for different values of } \beta \text{ with the parameters of}$$

$$\omega_1/\omega_2 = -5/2 (\bar{n}_1, \bar{n}_2) = (29, 60), \gamma = \pi/2, \text{ and } \alpha = \pi/2 \dots\dots\dots 37$$

Fig. 2.1.8 Theoretical results for the intensity distribution of the stationary states

$$\left| \Psi_{\bar{n}_1, \bar{n}_2}^{\pm p, q}(\gamma) \right\rangle_{0,0,0} \text{ for different values of } \beta \text{ with the parameters of}$$

$$\omega_1/\omega_2 = -5/2 (\bar{n}_1, \bar{n}_2) = (29, 60), \gamma = \pi/2, \text{ and } \beta = \pi/2 \dots\dots\dots 38$$

Fig. 2.1.9 (a1)-(a4) Numerical simulations of the Wigner d -coefficient with respect to n_1 for various m_1 ; (b1)-(d4) numerical wave patterns for the intensities of eigenstates $|m_1, m_2; 0, 0\rangle_{\bar{H}}$. Detailed description of the parameters; see text.

$$\dots\dots\dots 44$$

Fig. 2.1.10 (a1)-(a8) Numerical simulations of Wigner d -coefficient with respect to n_1 for various β ; (b1)-(b8) corresponding numerical wave patterns for the intensity distribution of eigenstates $|m_1, m_2\rangle_{\bar{H}}$.

$$\dots\dots\dots 45$$

Fig. 2.1.11 Numerical wave patterns for the intensities of eigenstates $|m_1, m_2\rangle_{\bar{H}}$ with respect to varying α' ; (a1)-(a5) $\beta' = 0.4\pi$; (b1)-(b5) $\beta' = 0.74\pi$.

$$\dots\dots\dots 46$$

Fig. 2.1.12 Numerical wave patterns for higher indices m_1 followed by the case in Fig. 2.1.9(b1)-(b4).

$$\dots\dots\dots 48$$

Fig. 2.1.13 (a) Numerical wave patterns for the intensities of eigenstates $|m_1, m_2\rangle_{\bar{H}}$ for $(m_1, m_2) = (1, 59)$ and $(m_1, m_2) = (59, 1)$; probability current $\bar{J}(x, y)$ for (b) $(m_1, m_2) = (1, 59)$, and (c) $(m_1, m_2) = (59, 1)$.

$$\dots\dots\dots 49$$

Fig. 2.1.14 (a1), (b1) Theoretical results in Fig. 2.1.12(a) and 2.1.12(e); (a2), (b2) phase distribution of (a1) and (b1), respectively; (a3), (b3) enlarged figures of the box region in (a2) and (b3), respectively. 51

Fig. 2.1.15 Numerical wave patterns for the intensity distribution of $|m_1, m_2\rangle_{\bar{H}}$ with different indices (p, q) 52

Fig. 2.1.16 (a1)-(a5) Experimental wave patterns. (b1)-(b5) Numerical wave patterns for the intensity distribution of $|m_1, m_2\rangle_{\bar{H}}$ with $(p, q) = (3, 2)$ and varying values of α' 53

Fig. 2.1.17 Numerical results of the intensity distribution for $|m_1, m_2; \lambda_1, \lambda_2; \bar{n}_1, \bar{n}_2\rangle_{\bar{H}}$ with various values of β . Detailed description of the parameters, see text. 55

Fig. 2.2.1 Experimental setup for generating and transforming the laser modes via the cylindrical-lens mode converter. 58

Fig. 2.2.2 Experimental scheme for a rotated HG mode propagating through a cylindrical-lens mode converter. 62

Fig. 2.2.3 Output far-field patterns for the rotated HG modes at various angles passing through the cylindrical-lens mode converter; (a)-(e) transformed far-field patterns for a rotated HG mode of indices $(n, m) = (15, 10)$; (a')-(e') transformed far-field patterns for a rotated HG mode of indices $(n, m) = (55, 3)$ 64

Fig. 2.2.4 Experimental results of the output beam $|U_{\bar{n}_1, \bar{n}_2}^{\pm p, q}(x_2, y_2, z_2; \gamma)|^2$ generated by passing the rotated Lissajous laser mode of positive sign through the

| | |
|--|----|
| cylindrical lenses..... | 70 |
| Fig. 2.2.5 Experimental results of the output beam $\left U_{\bar{n}_1, \bar{n}_2}^{\pm p, q}(x_2, y_2, z_2; \gamma)\right ^2$ generated by passing the rotated Lissajous laser mode of negative sign through the cylindrical lenses..... | 71 |
| Fig. 2.2.6 (a)-(e) Input Lissajous laser modes. (a1)-(e1) corresponding classical Lissajous curves. (a2)-(e2) Output hypotrochoidal laser modes, (a3)-(e2) corresponding classical hypotrochoidal curves. | 72 |
| Fig. 2.2.7 (a)-(e) Input Lissajous laser modes. (a1)-(e1) corresponding classical Lissajous curves. (a2)-(e2) Output epitrochoidal laser modes, (a3)-(e2) corresponding classical epitrochoidal curves..... | 73 |
| Fig. 2.2.8 Experimental far-field patterns corresponded to the numerical results in Fig. 2.1.9(b1)-2.1.9(b4)..... | 77 |
| Fig. 2.2.9 Experimental tomographic transverse patterns observed along the propagation direction from the beam waist; (a1)-(a5) $(\Delta x, \Delta y) = (0.21 \text{ mm}, 0.10 \text{ mm})$; (b1)-(b5) $(\Delta x, \Delta y) = (0.57 \text{ mm}, 0.10 \text{ mm})$ | 78 |
| Fig. 2.2.10 Experimental results corresponded to the theoretical analysis. Detailed description of the parameters; see text..... | 79 |
| Fig. 2.2.11 (a1)-(a5) Experimental tomographic transverse patterns observed along the propagation direction from the beam waist for $(p, q) = (3, 2)$. (b1)-(b5) Corresponding numerical calculations according to Eq. 2.1.31. | 80 |
| Fig. 2.2.12 (a)-(d) Input multiple Lissajous laser modes. (a')-(d') Output multiple trochoidal laser modes. For detailed descriptions for the parameters, see the text..... | 81 |
| Fig. 2.3.1 Theoretical results of $\left \Omega_{0,11}(x, y, z, \alpha)\right ^2$ of various relative phases. | 87 |

| | |
|--|-----|
| Fig. 2.3.2 (a) Theoretical results of $\Omega_{0,11}(x, y, z, \pi/2)$. (b) Phase distribution of (a). (c) Enlarged figure of the box region in (b). (d) probability current \mathbf{p}_\perp for the box region in (b) of $\Omega_{0,11}(x, y, z, \pi/2)$ | 90 |
| Fig. 2.3.3 Theoretical results of superposed state $ \Phi_{0,11}(r, \phi, z, \alpha) ^2$ of various relative phases..... | 93 |
| Fig. 2.3.4 Experimental setup utilized to transform the flower-like LG modes into the crisscrossed HG modes with the cylindrical lenses..... | 98 |
| Fig. 2.3.5 (a) Diagram for the transformational relation of a flower-like LG mode and the crisscrossed HG modes. (b) Operational scheme for the rotation of the mode converter..... | 99 |
| Fig. 2.3.6 Experimental results of an input LG mode with $(p, l) = (0, 11)$ and the corresponding crisscrossed HG modes while rotating the CLMC..... | 100 |
| Fig. 2.3.7 Theoretical analysis: (a) LG modes with non-vanishing radial index p . (b) The resulting modes converted from the LG modes. (c) Phase distribution corresponding to (b)..... | 101 |

Chapter 3

| | |
|--|-----|
| Fig. 3.1.1 Numerical results of Bessel functions with different orders: (a)-(d) are $m=0$, $m=1$, $m=2$, and $m=3$, respectively..... | 110 |
| Fig. 3.1.2 Numerically calculated patterns with Eq. (3.1.2) and using $M=3$ and $\theta_o=0$. The values of the order parameter m_o are 200 and 100 for the results in Figs. 3.1.2(a)-3.1.2(d) and Figs. 3.1.2(e)-3.1.2(h), respectively..... | 112 |
| Fig. 3.2.1 (a) Experimental setup for generating the resonant geometric modes from a | |

cylindrical waveguide; (b) longitudinal section of the cylindrical waveguide, showing the central angle of incidence θ_0 and the effective spreading range $\Delta\theta$ (c) transverse section, showing the off-axis distance R_o of the incident beam and the effective azimuthal spreading $\Delta\phi$ 118

Fig. 3.2.2 Experimental transverse near-field patterns for the observed geometric modes corresponding to the numerical patterns shown in Fig. 3.1.2..... 119

Fig. 3.2.3 Experimental (upper row) and numerical (lower row) patterns for the quasiscattered optical modes for the case of $(p, q) = (2, 5)$ in the free-space propagation. 120

Fig. 3.2.4 Experimental patterns for the optical geometric modes for the case of $(p, q) = (6, 25)$ in the free-space propagation..... 123

Fig. 3.2.5 Experimental patterns for the optical geometric modes for the case of $(p, q) = (21, 62)$ in the free-space propagation..... 124

Fig. 3.2.6 Experimental patterns for the optical geometric modes for the case of $p/q = 0.34$ in the free-space propagation. 125

Fig. 3.2.7 Experimental patterns for the spiral patterns with irregular trajectories in the free-space propagation. 126

Fig. 3.2.8 Experimental patterns for the spiral patterns with irregular trajectories in the free-space propagation. 127

Chapter 4

Fig. 4.1.1 (a)-(h) Theoretical results for the fundamental standing-wave $LG_{0,l}$ modes of different orders corresponding to the intensity distributions

$$\left| \Phi_{0,l}^{(\omega)}(r, \phi, z, \alpha) \right|^2 \dots\dots\dots 136$$

Fig. 4.1.2 (a)-(h) Theoretical simulations for the second-harmonic waves of intensity

| | |
|--|-----|
| distributions $ E_{0,l}^{(2\omega)}(r, \phi, z, \alpha) ^2$ corresponding to Fig. 4.1.1..... | 139 |
| Fig. 4.1.3 (a) The side view of the frequency-doubled beam $ E_{0,12}^{(2\omega)}(r, \phi, z, \alpha) ^2$ as it propagates from the beam waist, (b) corresponding transverse intensity profiles..... | 140 |
| Fig. 4.1.4 (a)-(d) The side views of the frequency-doubled beams with different orders..... | 142 |
| Fig. 4.2.1 Experimental setup of the diode-pumped solid-state laser with intracavity SHG..... | 145 |
| Fig. 4.2.2 Observed far-field patterns of the standing-wave $LG_{0,l}$ modes at the fundamental wavelength..... | 146 |
| Fig. 4.2.3 Frequency-doubled counterparts of the fundamental standing-wave $LG_{0,l}$ modes in Fig. 4.2.2..... | 147 |
| Fig. 4.2.4 Observed transverse intensity profiles along the longitudinal axis..... | 148 |

Chapter 5

| | |
|--|-----|
| Fig. 5.1.1 Experimental setup for the generation of disordered wave functions with the diode-pumped Q-switched Nd:YAG laser of intracavity SHG in the GdCOB crystal..... | 155 |
| Fig. 5.1.2 (a)-(f) Experimental observation of near-field wave patterns measured at different transverse positions of the GdCOB crystal..... | 156 |
| Fig. 5.2.1 (a)-(b) The density distribution $P(I)$ according to experimental data in Fig. 5.1.2(a) and 5.1.2(c), respectively..... | 158 |
| Fig. 5.2.2 (a)-(f) Experimental and theoretical density distributions $P(I)$ corresponding | |

to experimental data in Fig. 5.1.2(a)-5.1.2(f), respectively..... 161

Fig. 5.2.3 Blue dots: The relation between v and g according to the experimental data.
Red line: Empirical form for the relationship between v and g 163

List of Table

Chapter 1

Table 1.1.1 Analogy between classical mechanics and ray optics by Hamilton.....5



Chapter 1

Introduction to the Thesis

1.1 Classical Mechanics and Ray Optics : Periodic Orbits

Classical mechanics helps us to realize the the macroscopic physics world. It could be employed to describe the motion of the macroscopic objects and the classical trajectories that the particles move along. By systematically analyzing the trajectories of the objects in classical systems, one can have further insights into the physical properties of the systems. For example, one can acquire useful information such as the interaction between objects in the many-body system, the effect of the confinement on the objects, and the states that can exist in the system [1]. These are the important factors that determine the behavior of the particles in the classical systems.

There is a great deal of research that concerns the issues in the classical trajectories [1], among which the most well-known are the revolution of heavenly spheres, the motion of billiards in confined systems as depicted in Fig. 1.1.1 , and the orbits of an electron in the hydrogen atom. Most of the classical trajectories related to the systems reveal periodicity and closed form. According to their specialty, they are therefore designated as the *periodic orbits*. Research on the periodic orbits not only shows the physical meaning of great significance but discloses the exotic and diverse appearances which have fascinated scientists from a variety of fields. Moreover, the periodic orbits are characterized by their concise and symmetric mathematical interpretation. Besides of the conical sections, including circular, and elliptic orbits, we are familiar with, there are attracting periodic orbits such as the Lissajous and

trochoidal curves.

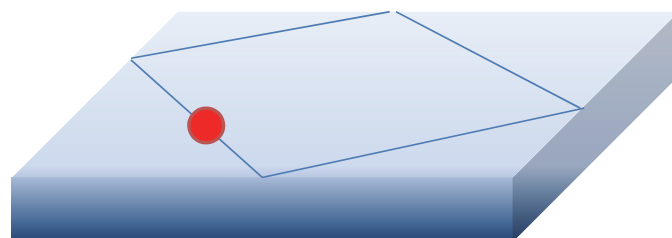
According to the intriguing features and complexity of the periodic orbits in classical systems, scientists wondered whether “light” possess the same characteristics as the classical trajectories. The answer has been provided by Hamilton who proposed his formulation of the optical-mechanical analogy in the early 19th century [2]. The analogy between the classical mechanics and ray optics according to his announcement is given in Table 1.1.1. It is noted that the ray optics shows good analogy to the classical mechanics. Experiments have confirmed that optical rays can reflect in the same manner as the classical objects. The validation suggests that the various classical trajectories could be manifested within light. In a part of this thesis, we focus our attention on the complex classical trajectories by employing the optical experiments to investigate the transformational relationship between different periodic orbits.



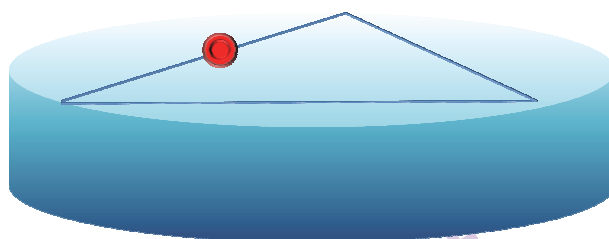
1.2 Schrödinger Wave Equation and Paraxial Wave Equation

In this section, we demonstrate the analogy between the matter waves and the optical waves by validating the tight connection between the Schrödinger wave equation and the Paraxial wave equation for the electromagnetic (EM) waves. On the other hand, the verification also reveals the fact that the wave optics has certain similarity to the quantum mechanics.

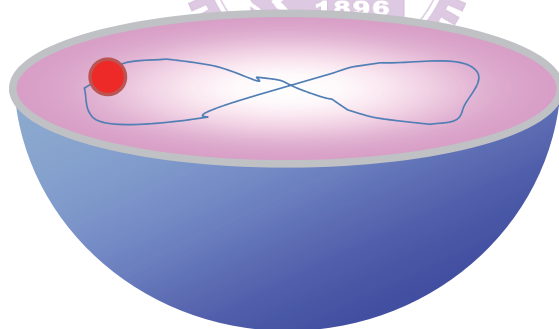
Here we begin with the well-known Maxwell equations that have often been used to describe how electric and magnetic fields are generated and altered by each other and by charges and currents. The four Maxwell equations in the differential



Square billiard



Circular billiard



Harmonic Oscillator

Fig. 1.1.1 Confined systems with different boundary conditions.

form can be given by

$$\bar{\nabla} \cdot \bar{E} = 0, \quad (1.2.1a)$$

$$\bar{\nabla} \times \bar{E} = -\mu \frac{\partial}{\partial t} \bar{H}, \quad (1.2.1b)$$

$$\bar{\nabla} \cdot \bar{H} = 0, \quad (1.2.1c)$$

$$\bar{\nabla} \times \bar{H} = \varepsilon \frac{\partial}{\partial t} \bar{E}, \quad (1.2.1d)$$

where ε is the permittivity, and μ is the permeability of the medium that the EM waves pass through.

Furthermore, taking the curl of the curl equations in Eq. (1.2.1b) and Eq. (1.2.1c) and using the identity $\bar{\nabla} \times \bar{\nabla} \times \bar{A} = \bar{\nabla}(\bar{\nabla} \cdot \bar{A}) - \nabla^2 \bar{A}$, we obtain the wave equations for the EM waves

$$\left(\nabla^2 - \frac{1}{v^2} \frac{\partial^2}{\partial t^2} \right) E(x, y, z; t) = 0, \quad (1.2.2a)$$

$$\left(\nabla^2 - \frac{1}{v^2} \frac{\partial^2}{\partial t^2} \right) H(x, y, z; t) = 0, \quad (1.2.2b)$$

where $v = 1/\sqrt{\mu\varepsilon}$ signifies the speed of the waves in the medium and $v = 1/\sqrt{\mu_0\varepsilon_0} = c$ where c represents the speed of light in free space.

Considering the case of separation in time and space, we can write down the amplitude of the electric field in the form $E(x, y, z; t) = \Phi(x, y, z)e^{i\omega t}$ for a monochromatic wave of angular frequency ω and thus we can rewrite Eq. (1.2.2a) as

$$(\nabla^2 + k^2)\Phi(x, y, z) = 0, \quad (1.2.3)$$

where $k = \omega/v$ is the wave number. It is obvious that the *Helmholtz equation* has been derived in Eq. (1.2.3).

Table 1.1.1 Analogy between classical mechanics and ray optics by Hamilton.

| | Classical Mechanics | Ray Optics |
|-------------------------|---|---|
| Characteristic Function | $S = \int \sqrt{2m(E - V)} ds = 0$ | $t = \int \frac{n}{c} ds = 0$ |
| Integrand | $p = \sqrt{2m(E - V)}$ | $\frac{1}{v_p} = \frac{n}{c}$ |
| Principle | (Least action) $\delta S = 0$ | (Fermat's principle) $\delta t = 0$ |
| Denotations | S : action m : mass $E - V$: Kinetic energy p : particle momentum | t : time of propagation n : refractive index c : light velocity v_p : phase velocity |

Assume that the EM wave propagates along the z direction, the electric field can thus be expressed as

$$\Phi(x, y, z) = u(x, y, z)e^{-ik_z z}, \quad (1.2.4)$$

where $u(x, y, z)$ signifies the transverse amplitude and k_z denotes the z component of the wave vector. Substituting Eq. (1.2.4) into Eq. (1.2.3) leads to

$$\left[\frac{\partial^2}{\partial x^2} + \frac{\partial^2}{\partial y^2} + \frac{\partial^2}{\partial z^2} - 2ik_z \frac{\partial}{\partial z} + (k^2 - k_z^2) \right] u(x, y, z) = 0. \quad (1.2.5)$$

Since, in the paraxial approximation, the term $\partial^2 u(x, y, z) / \partial z^2$ is small enough to be neglected, Eq. (1.2.5) can be simplified as

$$\left[\nabla_{\perp}^2 - 2ik_z \frac{\partial}{\partial z} + k_t^2 \right] u(x, y, z) = 0, \quad (1.2.6)$$

where $\nabla_{\perp}^2 = \partial^2 / \partial x^2 + \partial^2 / \partial y^2$ in the Cartesian coordinate and $k_t^2 = k^2 - k_z^2$. Eq. (1.2.6) is known as the *paraxial wave equation*.

Compare with the time dependent Schrödinger wave equation of two spatial dimensions

$$-\frac{\hbar^2}{2m} \nabla_{\perp}^2 \Psi(x, y, t) + V(x, y) \Psi(x, y, t) = i\hbar \frac{\partial}{\partial t} \Psi(x, y, t), \quad (1.2.7)$$

which can be rewritten as

$$\left[\nabla_{\perp}^2 + \frac{2mi}{\hbar} \frac{\partial}{\partial t} - \frac{2m}{\hbar^2} V(x, y) \right] \Psi(x, y, t) = 0, \quad (1.2.8)$$

we can obtain the relations between Eq. (1.2.6) and Eq. (1.2.8) as follows

$$\begin{aligned} z &\leftrightarrow t \\ k_z &\leftrightarrow -\frac{m}{\hbar} \\ k_t &\leftrightarrow i \frac{\sqrt{2mV}}{\hbar} \end{aligned} \quad (1.2.9)$$

Based on the derivation that the Schrödinger wave equation possesses the same mathematical form as the paraxial wave equation, we are able to interpret the light patterns observed in the optical experiments by the use of the sophisticated quantum theory. On the other hand, it has been confirmed that matter waves can also refract, diffract, interfere, and scatter in the same manner as electromagnetic waves in the quantum systems. Therefore, one can undertake comprehensive studies in the quantum wave functions with the available optical experiments through the tight connection between the quantum mechanics and wave optics.

1.3 Optical-Mechanical Analogy

In the previous sections, we have shown the analogy between the mechanics and optics with systematical analysis. Here we are going to find out the correspondence between waves and rays by considering the EM wave equation and Schrödinger wave equation in the semi-classical limit

Here we start with the EM wave equation in Eq. (1.2.2a). Consider the case of separation in time and space, the amplitude of the electric field of a monochromatic wave of angular frequency ω can be expressed as $E(r;t) = \Phi(r)e^{i\omega t}$ and thus we can rewrite Eq. (1.2.2a) into the Helmholtz equation

$$(\nabla^2 + k^2)\Phi(r) = 0, \quad (1.3.1)$$

where $k = \omega/v = 2\pi/\lambda$, $k_0 = \omega/c$ in vacuum, and $n = c/v = k/k_0 = \lambda_0/\lambda$ is the refractive index of the medium. Let $\Phi(r) = A(r)\exp[ik_0\phi(r)]$, where $A(r)$ represents the amplitude of $\Phi(r)$ and $\phi(r)$ signifies the phase factor for $\Phi(r)$, and then substitute $\Phi(r)$ into Eq. (1.3.1), two equations can be obtained for both the

real and imaginary part are equal to zero as follows

$$-k_0^2 \left\{ [\bar{\nabla} \phi(r)]^2 - \left(\frac{k}{k_0} \right)^2 \right\} + [\bar{\nabla} \ln A(r)]^2 + \nabla^2 \ln A(r) = 0, \quad (1.3.2a)$$

$$k_0 \left\{ \frac{1}{2} \nabla^2 \phi(r) + [\bar{\nabla} \ln A(r)] \cdot [\bar{\nabla} \phi(r)] \right\} = 0. \quad (1.3.2b)$$

In the short wavelength limit for ray optics ($\lambda, \lambda_0 \rightarrow 0 \Rightarrow k, k_0 \rightarrow \infty$), the terms with

k_0^2 dominate in Eq. (1.3.2) and hence we have

$$[\bar{\nabla} \phi(r)]^2 - \left(\frac{k}{k_0} \right)^2 = [\bar{\nabla} \phi(r)]^2 - n^2(r) = 0, \quad (1.3.3a)$$

$$\frac{1}{2} \nabla^2 \phi(r) + [\bar{\nabla} \ln A(r)] \cdot [\bar{\nabla} \phi(r)] = 0. \quad (1.3.3b)$$

Here, we can obtain from Eq. (1.3.3a) that

$$[\bar{\nabla} \phi(r)]^2 = n^2(r), \quad (1.3.4)$$

where $\bar{\nabla} \phi(r)$ suggests the direction of the optical rays. Equation (1.3.4) is the principal equation of ray optics in homogeneous isotropic medium and is the so-called *eikonal equation*. The interpretation successfully verifies the connection between wave and ray optics.

In the following, we consider the case for matter waves and the time-dependent Schrodinger equation can be given by

$$-\frac{\hbar^2}{2m} \nabla^2 \Psi(r;t) + V(r) \Psi(r;t) = i\hbar \frac{\partial}{\partial t} \Psi(r;t). \quad (1.3.5)$$

Similarly, take account of the separation in time and space for the wave function

$\Psi(r;t) = \psi(r) e^{-i\omega t}$, Eq. (1.3.5) can be modified as

$$(\nabla^2 + \kappa^2) \psi(r) = 0, \quad (1.3.6)$$

where $\kappa = \sqrt{2m(E-V)}/\hbar$ and $E = \hbar\omega$. It can be seen that Eq. (1.3.6) has

equivalent form to the Helmholtz equation. Let $\psi(r) = \rho(r)\exp[iS(r)/\hbar]$, where $S(r)$ is the action, and substitute it into Eq. (1.3.6). After the same algebra as the above mentioned with the EM wave, the obtained equation can hold only when both the real and imaginary part are zero. Therefore, a couple of equations can be derived from Eq. (1.3.6) as

$$-\frac{1}{\hbar^2} \left\{ [\bar{\nabla} S(r)]^2 - (\hbar\kappa)^2 \right\} + [\bar{\nabla} \ln \rho(r)]^2 + \nabla^2 \ln \rho(r) = 0, \quad (1.3.7a)$$

$$\frac{1}{\hbar^2} \left\{ \frac{1}{2} \nabla^2 S(r) + [\bar{\nabla} \ln \rho(r)] \cdot [\bar{\nabla} S(r)] \right\} = 0. \quad (1.3.7b)$$

In the classical limit for particles ($\hbar \rightarrow 0$), the terms with $1/\hbar^2$ dominate in Eq. (1.3.7) and thus we obtain

$$[\bar{\nabla} S(r)]^2 - (\hbar\kappa)^2 = [\bar{\nabla} S(r)]^2 - \left(\frac{\hbar}{\lambda}\right)^2 = [\bar{\nabla} S(r)]^2 - p^2(r), \quad (1.3.8a)$$

$$\frac{1}{2} \nabla^2 S(r) + [\bar{\nabla} \ln \rho(r)] \cdot [\bar{\nabla} S(r)] = 0, \quad (1.3.8b)$$

where λ is the wavelength of the matter waves and $p(r) = \sqrt{2m[E - V(r)]}$ signifies the momentum of the classical objects. From Eq. (1.3.8a), we are informed that

$$[\bar{\nabla} S(r)]^2 = p^2(r). \quad (1.3.9)$$

where $\bar{\nabla} S(r)$ indicates the direction of the particle motion. Obviously, Eq. (1.3.9) is closely analogous to Eq. (1.3.4), which implies that the transition from quantum mechanics to classical mechanics is equivalent to the relation between wave optics and geometric optics. The equivalence also confirms the relations we have discussed in previous sections: the trajectory of classical particle is similar to a ray in geometric optics and the matter waves are highly analogous to the optical waves. It is evident that we are able to employ optical experiments to explore the corresponding classical

or quantum phenomena. Figure 1.3.1 displays the complete version of analogy between the optics and mechanics.

1.4 Mesoscopic Wave Functions

In the previous sections, we have presented the tight connection between optics and the mechanics. The purpose of this thesis is to explore the intriguing physical phenomena in the mesoscopic physics which is the intermediate regime between the classical and quantum mechanics. Based on the close correspondence between the optics and mechanics, we use optical experiments to analogously investigate the physical features in the mesoscopic regime. Since optical experiments are characterized by their advantages of reproducibility, stability, and accessibility, the observations are reliable and enable us to have a better understanding of the physical meaning for the mesoscopic wave functions. In this thesis, we focus our attention on two important issues concerning the periodic orbits in the mesoscopic systems and the statistical properties of the disordered wave functions in random medium.

1.4.1 Periodic Orbits in Mesoscopic Systems

In recent decades, there has been great interest in the quantum manifestation of the classical periodic orbits in mesoscopic systems [3-13]. Mesoscopic billiards have been shown to play a crucial role in the exploration of the interplay between the classical orbits and the quantum energy spectrum [1,14-20]. Intriguingly, nonintegrable systems also reveal the localized phenomena that the scarred eigenstates are concentrated on unstable periodic orbits instead of randomly distributed in the systems [21-23]. Moreover, observations of conductance fluctuations related to the quantum transport in nanostructure devices have displayed close correspondence to

the quantum wave functions associated with the classical periodic orbits [24-29]. The phenomena of nonlinear resonances formerly investigated by Fermi with the molecule of CO₂ [30] have been validated to have a great effect on the appearance of the classical trajectories [31]. There is a good deal of research that has been shown to tightly relate to the important phenomena of the nonlinear resonances. For example, the works can be seen in the experimental investigation of tunneling effects, stellar orbits, molecular excitations, and some theoretical studies [31-34].

It can be seen that the localized feature associated with the classical periodic orbits plays a significance role in a variety of mesoscopic systems. As a result, the exploration of the connection between the quantum wave functions and the classical periodic orbits can help to figure out the intriguing physics exhibited in the mesoscopic regime, which is also the central issue of modern physics. In the thesis, we present two kinds of optical systems including the spherical laser resonator and the light pipe to analogously investigate the corresponding wave functions in the quantum harmonic oscillator and the quantum circular billiard. The wave functions and the optical modes that characterized by their fascinating morphologies are shown to be concentrated on the intricate periodic orbits. It can be expected that this work might stimulate more ideas in the quantum-classical connection for the related topics in mesoscopic systems.

1.4.2 Disordered Wave Functions in Random Media

Wave behavior in Random medium is a popular subject that has gone through a remarkable transformation in the past decades. The transformation was initiated by Anderson who suggested the possibility of electron localization inside a semiconductor [35]. The issue is now an important area of research which includes a variety of problems such as wave localization (weak [36-45] or strong [36,46-48]),

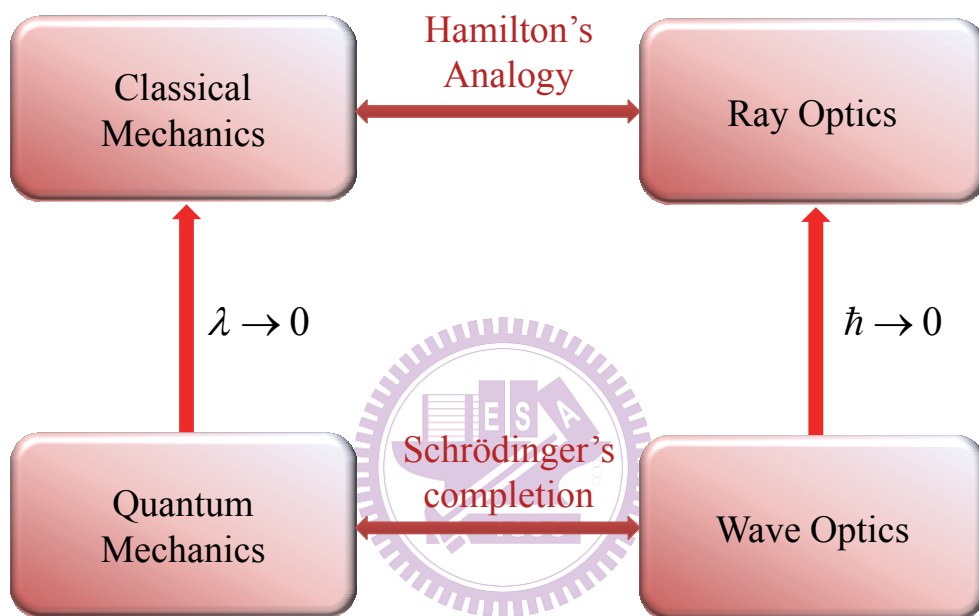


Fig. 1.3.1 Optical-Mechanical analogy.

wave diffusion [49-52], intensity fluctuations [53-57], and correlation [58]. Since disorder phenomena are not restricted to a specific kind of wave, various approaches [36-38,59] have been developed individually in condensed matter physics, optics, acoustics, and atomic physics. It could be found that the localization phenomenon is still an important issue and deserves further investigations.

In this thesis, we experimentally acquire the disordered wave functions from the conical second harmonic generation to explore the variation of weak localization from extended to pre-localized states. We numerically verify that the experimental density distributions with different extents of weak localization can be excellently analyzed with a reduced version of the nonlinear sigma model (RV-NLS model). Moreover, we demonstrate that the chi-square distributions with fractional degrees of freedom are practically equivalent to the density distributions of the RV-NLS model. Our finding indicates that the concept of fractional degrees of freedom can be applied to the statistical properties of disordered wave functions. It is believed that the present work can bring more insight into the localization phenomena of diverse disordered systems.

Reference

- [1] M. Brack, R. K. Bhaduri, *Semiclassical Physics* (Addison-Wesley, 1997).
- [2] T. L. Hankins, *Sir William Rowan Hamilton* (The Johns Hopkins University Press, 1980).
- [3] W. Li, L. E. Reichl, and B. Wu, *Phys. Rev. E* **65**, 056220 (2002).
- [4] R. Narevich, R. E. Prange, and O. Zaitsev, *Phys. Rev. E* **62**, 2046 (2000).
- [5] J. Wiersig, *Phys. Rev. E* **64**, 026212 (2001).
- [6] J. A. de Sales and J. Florencio, *Physica A* **290**, 101 (2001).
- [7] M. Brack and R. K. Bhaduri, *Semiclassical Physics* (Addison-Wesley, Reading, MA, 1997), Sec. 2.7.
- [8] F. von Oppen, *Phys. Rev. B* **50**, 17151 (1994).
- [9] R. W. Robinett, *Am. J. Phys.* **65**, 1167 (1997).
- [10] Y. F. Chen, K. F. Huang, and Y. P. Lan, *Phys. Rev. E* **66**, 046215 (2002).
- [11] Y. F. Chen, K. F. Huang, and Y. P. Lan, *Phys. Rev. E* **66**, 066210 (2002).
- [12] Y. F. Chen and K. F. Huang, *Phys. Rev. E* **68**, 066207 (2003).
- [13] Y. F. Chen and K. F. Huang, *J. Phys. A* **36**, 7751 (2003).
- [14] M. C. Gutzwiller, *Chaos in Classical and Quantum Mechanics* (Springer-Verlag, New York, 1990).
- [15] H. J. Stöckmann, *Quantum Chaos: An Introduction*, (Cambridge University Press, UK, 1999).
- [16] R. Balian and C. Bloch, *Ann. Phys.* **69**, 76 (1972).
- [17] M. V. Berry, *Proc. R. Soc. London* **413**, 183 (1987).
- [18] M. A. Doncheski, S. Heppelmann, R. W. Robinett, and D. C. Tussey, *Am. J. Phys.* **71**, 541 (2003).
- [19] R. W. Robinett and S. Heppelmann, *Phys. Rev. A* **65**, 062103 (2002).

- [20] R. W. Robinett, *Am. J. Phys.* **67**, 67 (1999).
- [21] E. J. Heller, *Phys. Rev. Lett.* **53**, 1515 (1984).
- [22] S. Sridhar and E. J. Heller, *Phys. Rev. A* **46**, R1728 (1992).
- [23] F. Simonotti, E. Vergini, and M. Saraceno, *Phys. Rev. E* **56**, 3859 (1997).
- [24] J. P. Bird, R. Akis, D. K. Ferry, A. P. S. de Moura, Y. C. Lai, and K. M. Indlekofer, *Rep. Prog. Phys.* **66**, 583 (2003).
- [25] I. V. Zozoulenko and K. F. Berggren, *Phys. Rev. B* **56**, 6931 (1997).
- [26] Y. Takagaki and K. H. Ploog, *Phys. Rev. E* **62**, 4804 (2000).
- [27] D. K. Ferry, R. Akis, and J. P. Bird, *J. Phys.: Condens. Matter* **17**, S1017 (2005).
- [28] L. Christensson, H. Linke, P. Ornling, P. E. Lindelof, I. V. Zozoulenko, and K. F. Berggren, *Phys. Rev. B* **57**, 12306 (1998).
- [29] Y. H. Kim, M. Barth, U. Kuhl, H. J. Stöckmann, and J. P. Bird, *Phys. Rev. B* **68**, 045315 (2003).
- [30] E. Fermi, *Z. Phys.* **71**, 250 (1931) [CAS].
- [31] D. W. Noid, M. L. Koszykowski, and R. A. Marcus, *J. Chem. Phys.* **71**, 2864 (1979).
- [32] D. Farrelly and T. Uzer, *J. Chem. Phys.* **84**, 308 (1986).
- [33] G. Contopoulos and B. Barbanis, *Astron. Astrophys.* **153**, 44 (1985).
- [34] A. Elipe, *Phys. Rev. E* **61**, 6477 (2000).
- [35] P. W. Anderson, *Phys. Rev.* **109**, 1492 (1958).
- [36] J. Billy, V. Josse, Z. Zho, A. Bernard, B. Hambrecht, P. Lugan, D. Clément, L. Sanchez-Palencia, P. Bouyer, and A. Aspect, *Nature*, **453**, 891 (2008).
- [37] D. Laurent, O. Legrand, P. Sebbah, C. Vanneste, and F. Mortessagne, *Phys. Rev. Lett.* **99**, 253902 (2007).
- [38] H. Hu, A. Strybulevych, J. H. Page, S. E. Skipetrov, and B. A. Van Tiggelen, *Nature*, **4**, 945 (2008).

- [39] D. S. Wiersma, M. P. van Albada, B. A. van Triggelen, and A. Lagendijk, *Phys. Rev. Lett.* **74**, 4193 (1995).
- [40] P. E. Wolf, and G. Maret, *Phys. Rev. Lett.* **55**, 2696 (1985).
- [41] G. Labeyrie, F. De Tomasi, J. C. Bernard, C. A. Muller, C. Miniatura, and R. Kaiser, *Phys. Rev. Lett.* **83**, 5266 (1999).
- [42] R. Sapienza, S. Mujumdar, C. Cheung, A. G. Yodh, and D. Wiersma, *Phys. Rev. Lett.* **92**, 033903 (2004).
- [43] F. V. Tikhonenko, D. W. Horsell, R. V. Gorbachev, and A. K. Savchenko, *Phys. Rev. Lett.* **100**, 056802 (2008).
- [44] A. Kudrolli, V. Kidambi, and S. Sridhar, *Phys. Rev. Lett.* **75**, 822 (1995).
- [45] M. Gurioli, F. Bogani, L. Cavidli, H. Gibbs, G. Khitrova, and D. S. Wiersma, *Phys. Rev. Lett.* **94**, 183901 (2005).
- [46] S. John, *Phys. Rev. Lett.* **58**, 2486 (1987).
- [47] T. Schwartz, G. Bartal, S. Fishman, and M. Segev, *Nature*, **446**, 52 (2007).
- [48] G. Roati, C. D'Errico, L. Fallani, M. Fattori, C. Fort, M. Zaccanti, G. Modugno, M. Modugno, and M. Inguscio, *Nature*, **453**, 895 (2008).
- [49] E. Abrahams, P. W. Anderson, D. C. Licciardello, and T. V. Ramakrishnan, *Phys. Rev. Lett.* **42**, 673 (1979).
- [50] S. John, *Phys. Rev. Lett.* **53**, 2169 (1984).
- [51] P. W. Anderson, *Philos. Mag. B* **52**, 505 (1985).
- [52] F. Scheffold and G. Maret, *Phys. Rev. Lett.* **81**, 5800 (1998).
- [53] P. A. Lee, *Phys. A* **140**, 169 (1986).
- [54] P. A. Lee, A. D. Stone, and H. Fukuyama, *Phys. Rev. B* **35**, 1039 (1987).
- [55] B. Shapiro, *Phys. Rev. Lett.* **57**, 2168 (1986).
- [56] B. Z. Spivak, and A. Y. Zyuzin, *Solid State Commun.* **65**, 311 (1988).
- [57] M. J. Stephen, and G. Cwilich, *Phys. Rev. Lett.* **59**, 285 (1987).

- [58] S. Feng, C. Kane, P. A. Lee, and A. D. Stone, Phys. Rev. Lett. **61**, 834 (1988).
- [59] M. Kaveh, M. Rosenbluh, I. Edrei, and I. Freund, Phys. Rev. Lett. **57**, 2049 (1986).



Chapter 2

Coherent Wave Transformation in Quantum Harmonic Oscillators and Spherical Laser Resonators

2.0 Introduction

- **Transformation in coupled isotropic harmonic oscillators**

Numerous recent researches on optical spatial modes have come out in modern physics [1-3] ranging from classical simulators of quantum entanglement [4-6] to parallel information [7,8]. The transverse Hermite-Gaussian (HG) modes are emitted by most laser cavities and are formally identical to the eigenstates of two-dimensional (2D) quantum harmonic oscillator (HO) [9]. Consequently, HG modes are often used to represent the spatial quantum photon states within the paraxial regime [10]. Recently, a variety of quantum Lissajous states formed by the coherent superposition of HG eigenstates has been analogously generated from the degenerate laser resonators, which exhibit wave patterns resembling Lissajous figures [11]. Constructing wave states with spatial morphologies well localized on the particle orbits has become one of the most fundamental features in different branches of physics such as solid-state physics, nuclear and atom physics, and laser physics [12,13].

Likewise, the Laguerre-Gaussian (LG) modes correspond to circular eigenstates of the 2D HO and play a prominent role in singular optics [14]. In the early 1990s, it was shown that a high-order HG mode can be converted into a LG mode by using

astigmatic lenses [15,16]. Since this discovery, researchers have made tremendous progress in manipulation [17], detection [18], and application [19,20] of the orbital-angular-momentum states of light. The generation of optical coherent states with intensities localized on intriguing periodic orbits might be an enabling tool to explore further possibilities for creating a new class of quantum light-matter entangled states.

In section 2.1.1 and 2.2.2, we theoretically and experimentally present the continuous transformation between the HG and LG modes. Furthermore, in section 2.1.2 and 2.2.3, we theoretically verify that converting the HG modes into the LG can lead to the spatial morphologies of the two-dimensional (2D) coherent states to be transformed from Lissajous figures to trochoidal curves. With this transformational relationship, we experimentally generate various structured lights by exploiting a cylindrical-lens mode converter to transform the optical Lissajous modes. The present investigation manifests a notable method to generate optical coherent waves with various orbital spatial morphologies.

- **Transformation in coupled commensurate harmonic oscillators**

For the past few decades, models developed from quantum mechanics have been employed progressively to explore the emergent phenomena in numerous different branches of physics because they can be interpreted with the same theoretical forms as quantum formulas [2,21-24]. One of the most profound similarities is that the electromagnetic wave equation in paraxial approximation is isomorphous to the Schrödinger equation [25-28]. Consequently, the electromagnetic radiation modes in the optical resonator or waveguide are analogs of the wave functions of a quantum system [9,11,29]. The tight connection between the paraxial beam propagation and quantum mechanics has been extensively exploited to study wave chaos phenomena

[29-31], disorder induced wave localization [32], semiclassical physics [33,34], and transient dynamics of quantum states [35-37].

The coupled HOs have been employed successfully to explore the hydrogen atom problem [38], charged particles in external field [39,40], states of deformed nucleus in the Nilson model [41], shell effects in nuclei and metallic clusters [42], and orbital magnetism in quantum dots [43]. More recently, the isotropic HOs with SU(2) coupling interactions have been used to investigate the generation and evolution of quantum vortex states [44] and the transformation geometry between Lissajous and trochoidal orbits [45]. It has been shown [46,47] that the commensurate HOs can be mapped into the isotropic HOs via the canonical transformation. Although the isotropic HOs with SU(2) coupling interactions have been verified to be a striking analytical model, the quantum states of canonically mapped commensurate HOs with SU(2) coupling interactions have not been thoroughly explored yet.

In section 2.1.3, we theoretically explore the eigenstates of a commensurate HO with SU(2) coupling interactions under the canonical transformation. The spatial patterns of the high-order eigenstates are found to be markedly localized on Lissajous figures to trochoidal curves from single to multiple periodic orbits. In section 2.1.4, controlling the pumping size in large-Fresnel number degenerate cavities, we have experimentally observed the laser transverse modes that display the wave patterns to be analogous to the derived eigenstates. Moreover, by exploiting the cylindrical-lens mode converter, we have experimentally presented the beam transformation from multiple Lissajous orbits to the multiple trochoidal curves.

2.1 Coupled Quantum Harmonic Oscillators

2.1.1 Eigenstates : SU(2) Transformation

It is well-known that the Hamiltonian for the 2D isotropic HO with the dimensionless spatial variables \tilde{x} and \tilde{y} is given by

$$\hat{H}_0 = \frac{\omega_0}{2} (\tilde{p}_x^2 + \tilde{p}_y^2 + \tilde{x}^2 + \tilde{y}^2), \quad (2.1.1)$$

where ω_0 is the angular frequency of the HO. Furthermore, Eq. (2.1.1) can be rewritten in terms of the ladder operators, and hence it becomes

$$\hat{H}_0 = (\hat{a}_1^\dagger \hat{a}_1 + \hat{a}_2^\dagger \hat{a}_2 + 1) \omega_0, \quad (2.1.2)$$

where $\hat{a}_1 = (\tilde{x} + i\tilde{p}_x)/\sqrt{2}$, $\hat{a}_1^\dagger = (\tilde{x} - i\tilde{p}_x)/\sqrt{2}$, $\hat{a}_2 = (\tilde{y} + i\tilde{p}_y)/\sqrt{2}$, and $\hat{a}_2^\dagger = (\tilde{y} - i\tilde{p}_y)/\sqrt{2}$. Here we chose $\hbar=1$ for the units. The eigenstates of \hat{H}_0 can

be derived to be the two-mode Fock state $|n_1, n_2\rangle_{\hat{H}_0} = [(\hat{a}_1^\dagger)^{n_1} (\hat{a}_2^\dagger)^{n_2} / \sqrt{n_1!} \sqrt{n_2!}] |0, 0\rangle_{\hat{H}_0}$,

where $|0, 0\rangle_{\hat{H}_0}$ denotes the ground state. The corresponding eigenvalues are

$E_{\hat{H}_0}(n_1, n_2) = (n_1 + n_2 + 1) \omega_0$, where n_1 and n_2 are positive integers. Moreover, the

normalized spatial representation is expressed as

$$\langle \tilde{x}, \tilde{y} | n_1, n_2 \rangle_{\hat{H}_0} = \frac{1}{\sqrt{2^{n_1+n_2} \pi (n_1!)(n_2!)}} e^{-\frac{\tilde{x}^2 + \tilde{y}^2}{2}} H_{n_1}(\tilde{x}) H_{n_2}(\tilde{y}), \quad (2.1.3)$$

where $H_n(\cdot)$ is the Hermite polynomial of order n .

The general form of a 2D HO with the SU(2) coupling can be modeled as

$$\hat{H} = \hat{H}_0 + \Omega_1 \hat{J}_1 + \Omega_2 \hat{J}_2 + \Omega_3 \hat{J}_3, \quad (2.1.4)$$

where the coupling parameters Ω_i ($i=1,2,3$) are assumed to be real constants and

\hat{J}_i are the Casimir operators associated with the SU(2) Lie algebra and the

corresponding generators derived by Schwinger [48] are

$$\hat{J}_1 = \frac{1}{2}(\hat{a}_1^\dagger \hat{a}_2 + \hat{a}_2^\dagger \hat{a}_1), \quad (2.1.5a)$$

$$\hat{J}_2 = -\frac{i}{2}(\hat{a}_1^\dagger \hat{a}_2 - \hat{a}_2^\dagger \hat{a}_1), \quad (2.1.5b)$$

$$\hat{J}_3 = \frac{1}{2}(\hat{a}_1^\dagger \hat{a}_1 - \hat{a}_2^\dagger \hat{a}_2). \quad (2.1.5c)$$

The operators \hat{J}_i follow the angular-momentum commutation relation $[\hat{J}_i, \hat{J}_j] = i\hbar \varepsilon_{ijk} \hat{J}_k$ [48], where the Levi-Civita tensor ε_{ijk} equals +1 (-1) if (i, j, k) is an even (odd) permutation, and zero otherwise. With the dimensionless spatial variables,

$$\hat{J}_1 = \frac{1}{2}(\tilde{x} \tilde{y} + \tilde{p}_x \tilde{p}_y), \quad (2.1.6a)$$

$$\hat{J}_2 = \frac{1}{2}(\tilde{x} \tilde{p}_y - \tilde{y} \tilde{p}_x), \quad (2.1.6b)$$

$$\hat{J}_3 = \frac{1}{4}(\tilde{x}^2 + \tilde{p}_x^2 - \tilde{y}^2 - \tilde{p}_y^2). \quad (2.1.6c)$$

Before solving the quantum eigenstates of \hat{H} , let first investigate the classical representation of the Hamiltonian \hat{H} . The classical equation of motion for the Hamiltonian \hat{H} can be found to be

$$i \frac{d}{dt} \begin{bmatrix} v_1 \\ v_2 \end{bmatrix} = \begin{bmatrix} \omega_o + (\Omega_3 / 2) & (\Omega_1 - i\Omega_2) / 2 \\ (\Omega_1 + i\Omega_2) / 2 & \omega_o - (\Omega_3 / 2) \end{bmatrix} \begin{bmatrix} v_1 \\ v_2 \end{bmatrix}, \quad (2.1.7)$$

where $v_1 = \tilde{x} + i\tilde{p}_x$ and $v_2 = \tilde{y} + i\tilde{p}_y$. It is worth to mention that the equation of motion for the Hamiltonian \hat{H} in the classical system possesses the same form as the Schrödinger equation when considering the case of a 2-level system. By employing the SU(2) algebra, the general solution for Eq. (2.1.7) can be derived to be

$$\begin{bmatrix} v_1(t) \\ v_2(t) \end{bmatrix} = \begin{bmatrix} e^{-i\alpha/2} \cos(\beta/2) & -e^{-i\alpha/2} \sin(\beta/2) \\ e^{i\alpha/2} \sin(\beta/2) & e^{i\alpha/2} \cos(\beta/2) \end{bmatrix} \begin{bmatrix} u_1(t) \\ u_2(t) \end{bmatrix}, \quad (2.1.8)$$

where $\alpha = \tan^{-1}(\Omega_2/\Omega_1)$, $\beta = \tan^{-1}(\sqrt{\Omega_1^2 + \Omega_2^2}/\Omega_3)$, $u_1(t) = A_1 e^{-i(\omega_1 t - \phi_1)}$,
 $u_2(t) = A_2 e^{-i(\omega_2 t - \phi_2)}$ $\omega_1 = \omega_o + (\Omega/2)$, $\omega_2 = \omega_o - (\Omega/2)$, $\Omega = \sqrt{\Omega_1^2 + \Omega_2^2 + \Omega_3^2}$, A_1 ,
 A_2 , ϕ_1 , and ϕ_2 are decided by the initial conditions.

To explore the quantum eigenstates of the Hamiltonian \hat{H} , we employ the same SU(2) algebra as in the classical dynamics to define a new pair of operators

$$\begin{bmatrix} \hat{a}'_1 \\ \hat{a}'_2 \end{bmatrix} = \begin{bmatrix} e^{i\alpha/2} \cos(\beta/2) & e^{-i\alpha/2} \sin(\beta/2) \\ -e^{i\alpha/2} \sin(\beta/2) & e^{-i\alpha/2} \cos(\beta/2) \end{bmatrix} \begin{bmatrix} \hat{a}_1 \\ \hat{a}_2 \end{bmatrix}. \quad (2.1.9)$$

Substituting \hat{a}'_1 and \hat{a}'_2 into Eq. (2.1.4) according to the relation in Eq. (2.1.9), we thus obtain the Hamiltonian \hat{H} to be transformed into a separable 2D HO

$$\hat{H} = \left(\hat{a}'_1 \dagger \hat{a}'_1 + \frac{1}{2} \right) \omega_1 + \left(\hat{a}'_2 \dagger \hat{a}'_2 + \frac{1}{2} \right) \omega_2. \quad (2.1.10)$$

Therefore, the eigenstates and eigenvalues of the Hamiltonian \hat{H} yield to be $|n_1, n_2\rangle_{\hat{H}} = \left[(\hat{a}'_1 \dagger)^{n_1} (\hat{a}'_2 \dagger)^{n_2} / \sqrt{n_1! \sqrt{n_2!}} \right] |0, 0\rangle_{\hat{H}}$ and

$E_{\hat{H}}(n_1, n_2) = (n_1 + 1/2) \omega_1 + (n_2 + 1/2) \omega_2$, respectively. With the transformational relation in Eq. (2.1.9) and $|0, 0\rangle_{\hat{H}} = |0, 0\rangle_{\hat{H}_0}$, the eigenstates to the Hamiltonian \hat{H}

can be derived in terms of the Wigner d -coefficient [49]:

$$|n_1, n_2\rangle_{\hat{H}} = e^{iN\alpha/2} \sum_{m_1=0}^N e^{-im_1\alpha} d^2_{m_1-\frac{N}{2}, n_1-\frac{N}{2}} \left(\beta \right) |m_1, m_2\rangle_{\hat{H}_0}, \quad (2.1.11)$$

where $N = n_1 + n_2 = m_1 + m_2$ and

$$d^2_{m_1-\frac{N}{2}, n_1-\frac{N}{2}} \left(\beta \right) = \sqrt{m_1! (N - m_1)! n_1! (N - n_1)!}$$

$$\times \sum_{\nu=\max[0, m_1-n_1]}^{\min[N-n_1, m_1]} \frac{(-1)^\nu \left[\cos\left(\frac{\beta}{2}\right) \right]^{n_1+m_1-2\nu} \left[\sin\left(\frac{\beta}{2}\right) \right]^{n_2-m_1+2\nu}}{\nu!(N-n_1-\nu)!(m_1-\nu)!(n_1-m_1+\nu)!}. \quad (2.1.12)$$

The detailed derivation can be found in Appendix A. Evidently, the eigenstates $|n_1, n_2\rangle_{\hat{H}}$ can be expressed as a linear superposition of the set of $|m_1, m_2\rangle_{\hat{H}_0}$. Figure 2.1.1 and Fig. 2.1.2 depict the intensity distribution of $|n_1, n_2\rangle_{\hat{H}}$ for various indices (n_1, n_2) and values of (α, β) . Figure 2.1.1 and Fig. 2.1.2 are shown with the parameters $\beta = \pi/2$ and $\alpha = \pi/2$, respectively. It can be seen that the transformation from the HG to the LG modes can be continuously obtained by changing the parameter α or β , which suggests different extent of coupling effect. The intermediate states, the Ince-Gaussian modes, are accessibly acquired through the SU(2) algebra associated with the coupled isotropic HO. Notably, the LG modes presented in Fig. 2.1.2(e) and Fig. 2.1.2(e') possess fairly large orbital angular momentum per photon [19,20] of $l\hbar = 5\hbar$ and $l\hbar = 52\hbar$, respectively. Since light beams with well-defined orbital angular momentum have a number of developing applications [19,20], generation of such optical beams should be an important issue for further studies. Moreover, in Fig. 2.1.3, we present the comparison between the traveling-wave and the standing-wave forms of the eigenstates $|n_1, n_2\rangle_{\hat{H}}$ for $\beta = \pi/2$. The standing-wave forms are obtained by taking the real part of the eigenstates $|n_1, n_2\rangle_{\hat{H}}$.

2.1.2 Coherent States : Single Periodic Orbits

According to Eq. (2.1.8), we can obtain the classical orbits for \hat{H} with the parametric equations $\tilde{x}(t) = \text{Re}[\nu_1(t)]$ and $\tilde{y}(t) = \text{Re}[\nu_2(t)]$, where

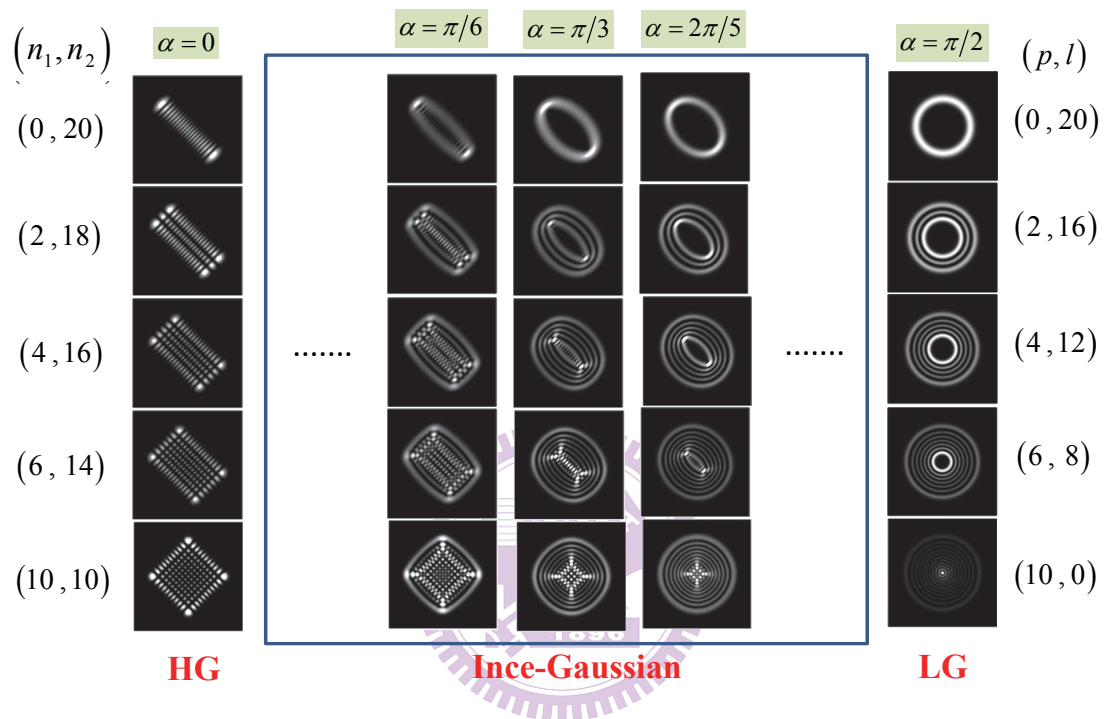


Fig. 2.1.1 The intensity distribution of the eigenstates $|n_1, n_2\rangle_{\hat{H}}$ with different indices (n_1, n_2) , various values of α values and constant value of $\beta = \pi/2$.

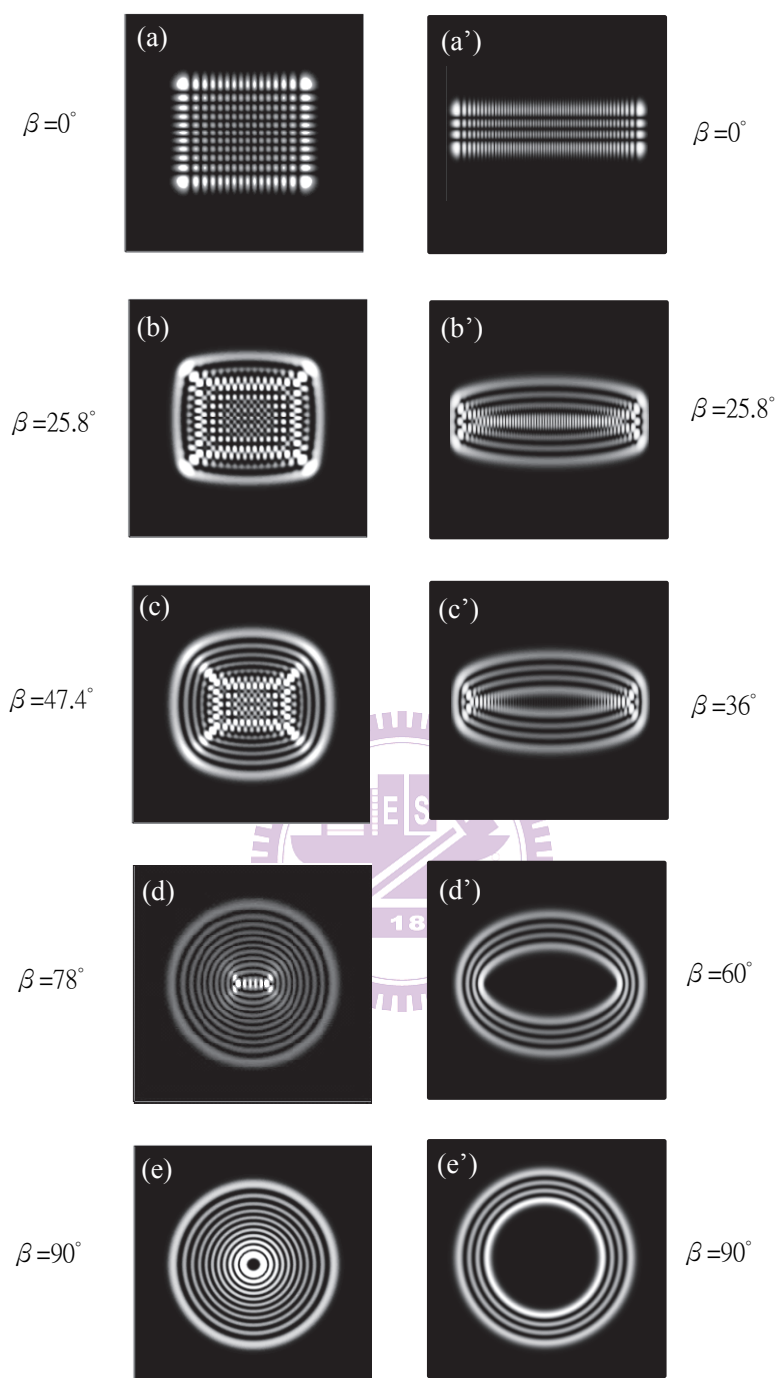
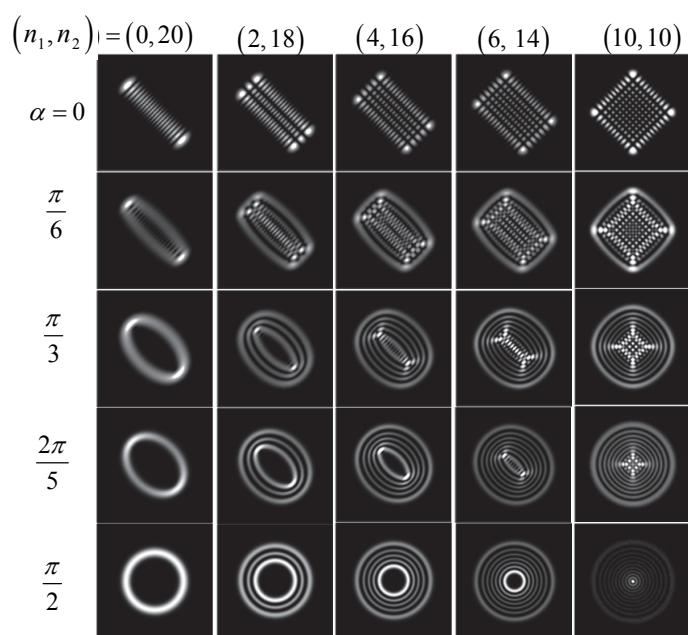
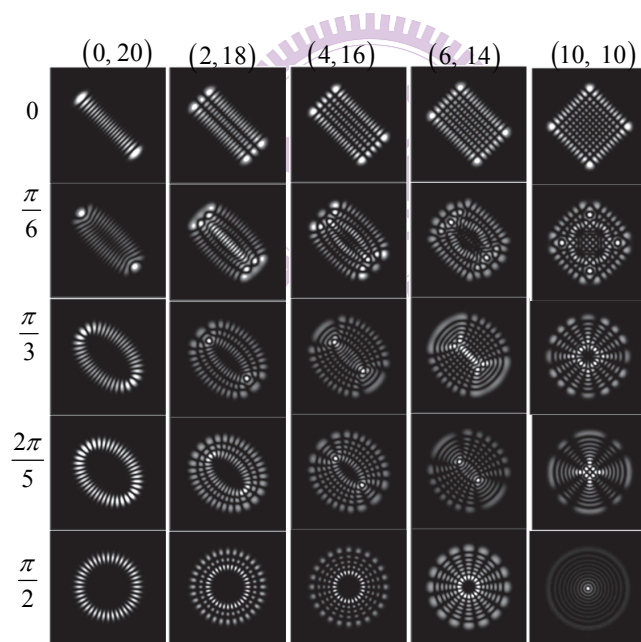


Fig. 2.1.2 The intensity distribution of the eigenstates $|n_1, n_2\rangle_{\hat{H}}$ with different indices (n_1, n_2) , various values of β and constant value of $\alpha = \pi/2$: (a)-(e) $(n_1, n_2) = (15, 10)$, (a')-(e') $(n_1, n_2) = (55, 3)$.



Traveling wave



Standing wave

Fig. 2.1.3 The intensity distribution of the eigenstates $|n_1, n_2\rangle_{\hat{H}}$ with different indices (n_1, n_2) , various values of α and constant value of $\beta = \pi/2$; (Upper) traveling-wave form; (Lower) standing-wave form.

$$\begin{cases} \tilde{x}(t) = A_1 \cos\left(\frac{\beta}{2}\right) \cos\left(\omega_1 t - \phi_1 - \frac{\alpha}{2}\right) - A_2 \sin\left(\frac{\beta}{2}\right) \cos\left(\omega_2 t - \phi_2 - \frac{\alpha}{2}\right) \\ \tilde{y}(t) = A_1 \sin\left(\frac{\beta}{2}\right) \cos\left(\omega_1 t - \phi_1 + \frac{\alpha}{2}\right) + A_2 \cos\left(\frac{\beta}{2}\right) \cos\left(\omega_2 t - \phi_2 + \frac{\alpha}{2}\right) \end{cases} \quad (2.1.13)$$

Figure 2.1.4 depicts the periodic orbits of the case $\omega_1/\omega_2 = 8/1$ for various α and β values with the parameters of $(A_1, A_2) = (35, 100)$ and $(\phi_1, \phi_2) = (-\pi, 0)$ according to Eq. (2.1.13). The periodic orbits are shown to be associated with a continuous transformation between Lissajous curves and hypotrochoids for differing values of α and β . In addition, Fig. 2.1.5 displays the periodic orbits the case of $\omega_1/\omega_2 = -9/1$ for different α and β values with the parameters of $(A_1, A_2) = (60, 150)$ and $(\phi_1, \phi_2) = (-\pi, 0)$ according to Eq. (2.1.13). The classical trajectories are found to be a continuous transformation between Lissajous figures and epitrochoids with varying values of α and β . It is obvious that a hypotrochoid or an epitrochoid depends on the ratio of ω_1/ω_2 to be positive or negative with $\alpha = \pi/2$ and $\beta = \pi/2$.

The periodic orbits for the Hamiltonian \hat{H} in the classical mechanics have been clearly demonstrated as mentioned above. Here we wonder whether the quantum states corresponding to the Schrödinger equation reveal the same morphologies localized on the periodic orbits. To construct such quantum states for mimicking the localized curves in classical dynamics, we apply the concepts of wave-packet coherent states first proposed by Schrödinger in 1926.

The wave-packet coherent states of 1D HO developed by Schrödinger are given by

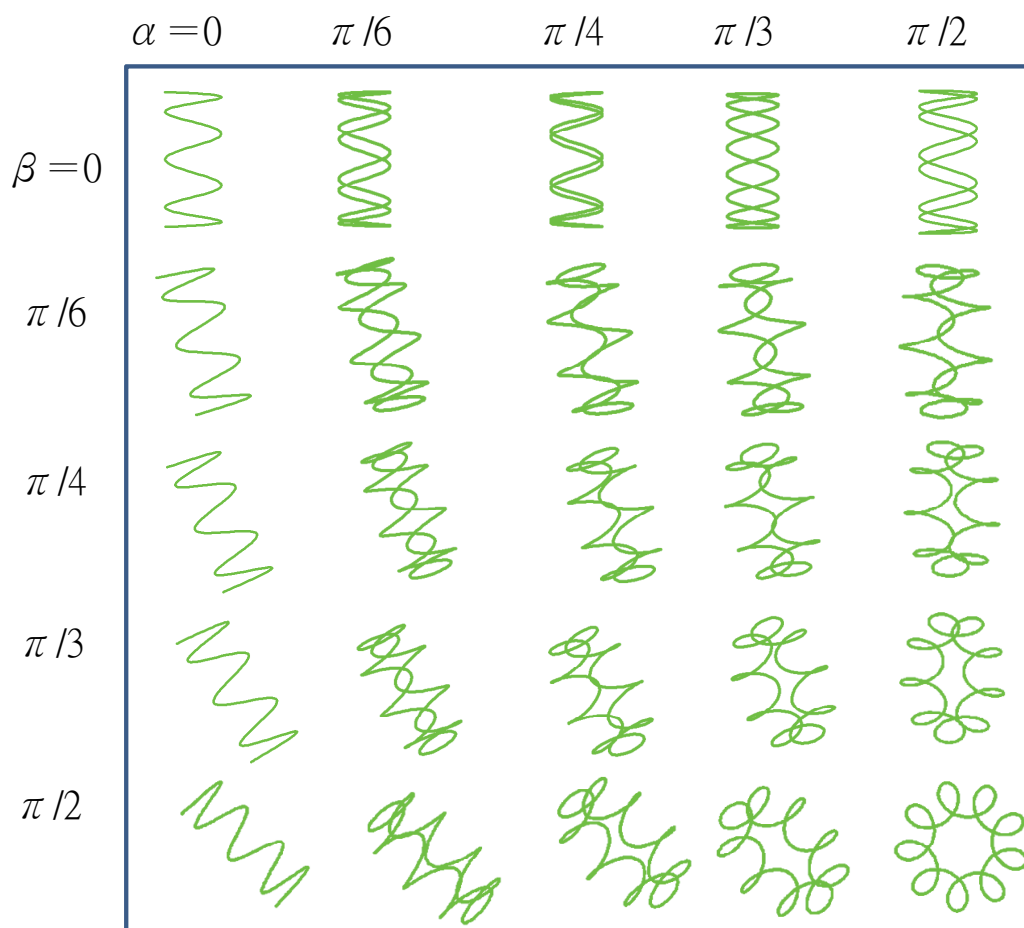


Fig. 2.1.4 Classical periodic orbits for the case $\omega_1/\omega_2 = 8/1$, $(A_1, A_2) = (35, 100)$, and $(\phi_1, \phi_2) = (-\pi, 0)$ corresponding to Eq. (2.1.13).

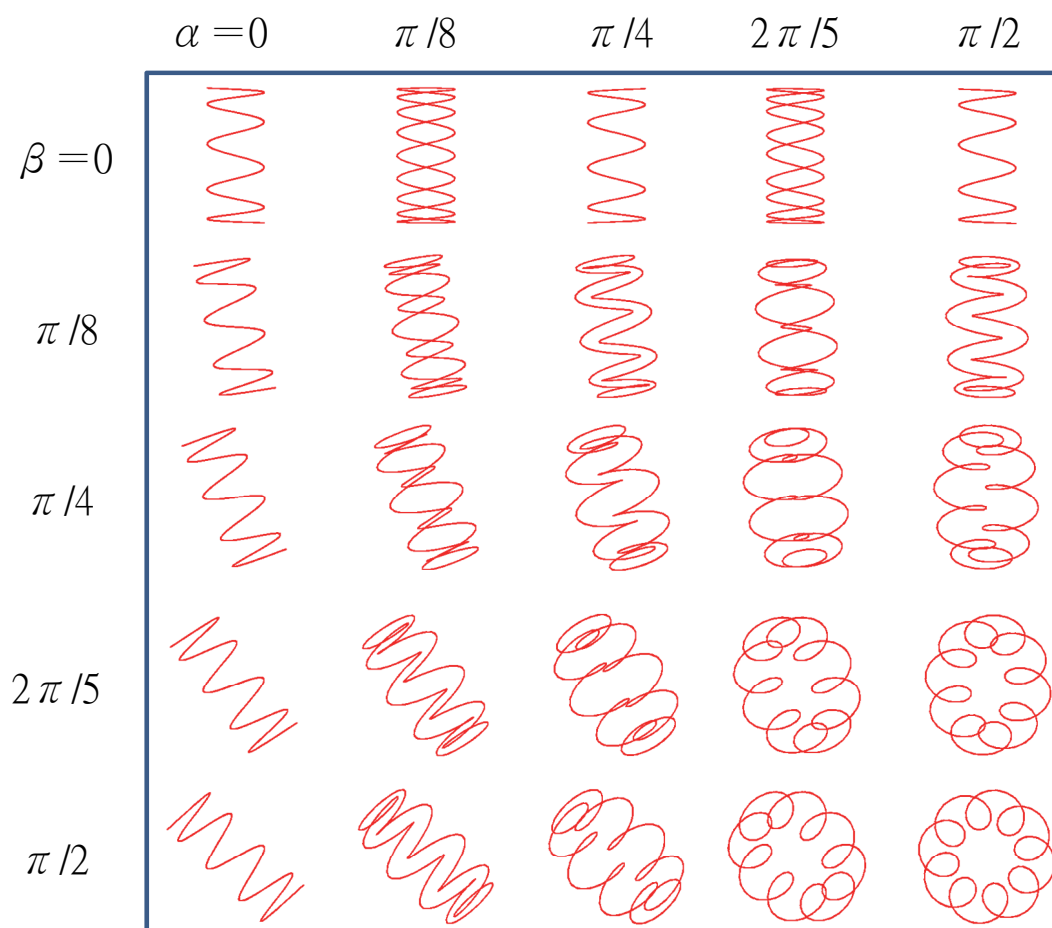


Fig. 2.1.5 Classical periodic orbits for the case $\omega_1/\omega_2 = -9/1$, $(A_1, A_2) = (60, 150)$, and $(\phi_1, \phi_2) = (-\pi, 0)$ corresponding to Eq. (2.1.13).

$$|\Psi(t; u)\rangle = e^{-i\frac{\omega_0 t}{2}} \sum_{n=0}^{\infty} \frac{u^n}{n!} e^{-\frac{|u|^2}{2}} (\hat{a}^\dagger)^n |0\rangle, \quad (2.1.14)$$

where $u = Ae^{-i(\omega_0 t - \phi)}$, A and ϕ are decided by the initial conditions of the orbits. By employing the generating function of the Hermite polynomials, the probability distributions of the Schrödinger coherent states can be derived to be

$$P(\tilde{x}, t; u) = |\langle \tilde{x} | \Psi(t; \mu) \rangle|^2 = \frac{1}{\sqrt{\pi}} \exp\left\{-[\tilde{x} - \sqrt{2} \operatorname{Re}(u)]^2\right\}. \quad (2.1.15)$$

It can be obviously seen that the center of the coherent state moves along the path of the classical trajectory $\tilde{x}(t) = \sqrt{2} \operatorname{Re}[u(t)] = \sqrt{2} A \cos(\omega t - \phi)$. In Eq. (2.1.10) we have performed that the coupled HO with Hamiltonian \hat{H} can be transformed into a separable 2D HO through the SU(2) algebra. The Schrödinger coherent states for a 2D coupled HO can be expressed as the product of two 1D wave-packet coherent states:

$$|\Psi(t; u_1, u_2)\rangle = e^{-i\frac{(\omega_1 + \omega_2)t}{2}} \left[\sum_{n_1=0}^{\infty} \sum_{n_2=0}^{\infty} e^{-\frac{(|u_1|^2 + |u_2|^2)}{2}} \frac{u_1^{n_1}}{n_1!} \frac{u_2^{n_2}}{n_2!} (\hat{a}_1^\dagger)^{n_1} (\hat{a}_2^\dagger)^{n_2} |0, 0\rangle_{\hat{H}} \right], \quad (2.1.16)$$

where $u_1(t) = A_1 e^{-i(\omega_1 t - \phi_1)}$ and $u_2(t) = A_2 e^{-i(\omega_2 t - \phi_2)}$. By substituting the ladder operators \hat{a}_1^\dagger and \hat{a}_2^\dagger with the transformational relations in Eq. (2.1.9), after cumbersome algebra, Eq. (2.1.16) is given by

$$|\Psi(t; v_1, v_2)\rangle = e^{-i\omega_0 t} \left[\sum_{m_1=0}^{\infty} \sum_{m_2=0}^{\infty} e^{-\frac{(|v_1|^2 + |v_2|^2)}{2}} \right]$$

$$\left. \frac{v_1^{m_1} v_2^{m_2}}{m_1! m_2!} (\hat{a}_1^\dagger)^{m_1} (\hat{a}_2^\dagger)^{m_2} |0,0\rangle_{\hat{H}_0} \right], \quad (2.1.17)$$

where $(u_1(t), u_2(t))$ and $(v_1(t), v_2(t))$ follow the same relations as presented in Eq. (2.1.8). According to Eq. (2.1.15) and Eq. (2.1.17), we find that the probability distribution of the coherent states $|\Psi(t; v_1, v_2)\rangle$ can be expressed as

$$P(\tilde{x}, \tilde{y}, t) = \left| \langle \tilde{x}, \tilde{y} | \Psi(t; v_1, v_2) \rangle \right|^2 = \frac{1}{\pi} \exp \left\{ - \left(\tilde{x} - \sqrt{2} \operatorname{Re}[v_1(t)] \right)^2 \right\} \\ \times \exp \left\{ - \left(\tilde{y} - \sqrt{2} \operatorname{Re}[v_2(t)] \right)^2 \right\}. \quad (2.1.18)$$

Equation (2.1.18) reveals that the coherent states $|\Psi(t; v_1, v_2)\rangle$ concentrate exactly on the same trajectories represented by the parametric equations in Eq. (2.1.13). To provide a comprehensive study in the corresponding quantum coherent states localized on the periodic orbits, we are here to find out the time independent stationary coherent states extracted out from the wave-packet coherent states $|\Psi(t; v_1, v_2)\rangle$.

Consider a general expression for the stationary coherent state, the wave-packet coherent states $|\Psi(t; v_1, v_2)\rangle$ can be expressed as the double finite sum with fairly large A_1 and A_2 values. For the corresponding 2D Poisson distribution, the probability of the coherent state $|\Psi(t; v_1, v_2)\rangle$ in the eigenstate $|n_1, n_2\rangle_{\hat{H}}$ can therefore be written as

$$P(n_1, n_2) = {}_{\hat{H}} \langle n_1, n_2 | \Psi(t; v_1, v_2) \rangle = \left(\frac{\bar{n}_1^{n_1}}{n_1!} e^{-\bar{n}_1} \right) \left(\frac{\bar{n}_2^{n_2}}{n_2!} e^{-\bar{n}_2} \right), \quad (2.1.19)$$

where \bar{n}_1 and \bar{n}_2 are the mean values for the associated quantum numbers and can

be given by $\bar{n}_1 = \langle \Psi | \hat{a}_1^\dagger \hat{a}_1 | \Psi \rangle = A_1^2$ and $\bar{n}_2 = \langle \Psi | \hat{a}_2^\dagger \hat{a}_2 | \Psi \rangle = A_2^2$. Since the values of the means \bar{n}_1 and \bar{n}_2 are sufficiently large, according to the central limit theorem, the distribution $P(n_1, n_2)$ becomes normally distributed and the standard deviations are given by $\sqrt{\bar{n}_1}$ and $\sqrt{\bar{n}_2}$. As a result, Eq. (2.1.17) can be rewritten as

$$|\Psi(t; \nu_1, \nu_2)\rangle = e^{-i\theta(t)} \left[\sum_{s_1=-[2\sqrt{\bar{n}_1}]}^{[2\sqrt{\bar{n}_1}]} \sum_{s_2=-[2\sqrt{\bar{n}_2}]}^{[2\sqrt{\bar{n}_2}]} \frac{e^{-is_1(\omega_1 t - \phi_1)}}{\sqrt{\sqrt{2\pi \bar{n}_1}}} e^{-\frac{s_1^2}{4\bar{n}_1}} \frac{e^{-is_2(\omega_2 t - \phi_2)}}{\sqrt{\sqrt{2\pi \bar{n}_2}}} e^{-\frac{s_2^2}{4\bar{n}_2}} |\bar{n}_1 + s_1, \bar{n}_2 + s_2\rangle_{\hat{H}} \right], \quad (2.1.20)$$

where $e^{-i\theta(t)} = e^{-i(\omega_1 + \omega_2)t/2} e^{-i\bar{n}_1(\omega_1 t - \phi_1)} e^{-i\bar{n}_2(\omega_2 t - \phi_2)}$ and $[a]$ is the Gaussian Bracket which signifies the nearest integer to a at the lower side. Considering the case for a commensurate HO with a frequency ratio of $\omega_1/\omega_2 = \pm q/p$, we let $\omega_1 = q\omega$ and $\omega_2 = \pm p\omega$, where p and q are relatively prime and positive integers. The eigenstates with indices (s_1, s_2) of the commensurate HO in Eq. (2.1.20) hence can be divided into subsets and expressed as $|\bar{n}_1 + pk_1 + \mu_1, \bar{n}_2 + qk_2 + \mu_2\rangle_{\hat{H}}$, where (k_1, k_2) are arbitrary nonnegative integers, and (μ_1, μ_2) are constants that $\mu_1 = 0, 1, \dots, p-1$ and $\mu_2 = 0, 1, \dots, q-1$. The coherent states in Eq. (2.1.20) can be derived to be

$$|\Psi(t; \nu_1, \nu_2)\rangle = e^{-i\theta(t)} \left[\sum_{\mu_1=0}^{p-1} e^{-i\mu_1(q\omega t - \phi_1)} \sum_{\mu_2=0}^{q-1} e^{-i\mu_2(\pm p\omega t - \phi_2)} \sum_{k_1=-[2\sqrt{\bar{n}_1}/p]}^{[2\sqrt{\bar{n}_1}/p]} \sum_{k_2=-[2\sqrt{\bar{n}_2}/q]}^{[2\sqrt{\bar{n}_2}/q]} \frac{e^{-ipk_1(q\omega t - \phi_1)}}{\sqrt{\sqrt{2\pi \bar{n}_1}}} e^{-\frac{(pk_1 + \mu_1)^2}{4\bar{n}_1}} \frac{e^{-iqk_2(\pm p\omega t - \phi_2)}}{\sqrt{\sqrt{2\pi \bar{n}_2}}} e^{-\frac{(qk_2 + \mu_2)^2}{4\bar{n}_2}} \times |\bar{n}_1 + pk_1 + \mu_1, \bar{n}_2 + qk_2 + \mu_2\rangle_{\hat{H}} \right], \quad (2.1.21)$$

with indices $k_1 = (s+k)/2$ and $k_2 = \pm(s-k)/2$, where the sign \pm of the index k is decided by the sign of $\omega_2 = \pm p\omega$ and the condition of nearly degeneracy, the coherent state $|\Psi(t; \nu_1, \nu_2)\rangle$ in Eq. (2.1.21) can hence be given by

$$|\Psi(t; \nu_1, \nu_2)\rangle = e^{-i\vartheta(t)} \left[\sum_{u_1=0}^{p-1} e^{-i\mu_1(q\omega t - \phi_1)} \sum_{u_2=0}^{q-1} e^{-i\mu_2(\pm p\omega t - \phi_2)} \sum_{s=-S}^S e^{-i2spq\omega t} e^{is(p\phi_1 \pm q\phi_2)} \left| \Psi_{\bar{n}_1, \bar{n}_2}^{\pm p, q}(\gamma) \right\rangle_{s, \mu_1, \mu_2} \right], \quad (2.1.22)$$

where $S = [2\sqrt{\bar{n}_1}/p + 2\sqrt{\bar{n}_2}/q]$ and the time independent stationary coherent state

$\left| \Psi_{\bar{n}_1, \bar{n}_2}^{\pm p, q}(\gamma) \right\rangle_{s, \mu_1, \mu_2}$ is given by

$$\left| \Psi_{\bar{n}_1, \bar{n}_2}^{\pm p, q}(\gamma) \right\rangle_{s, \mu_1, \mu_2} = \frac{1}{\sqrt{2\pi\sqrt{\bar{n}_1\bar{n}_2}}} \left[\sum_{k=L(s)}^{U(s)} e^{ik\gamma} e^{\frac{[p(s+k)+\mu_1]^2}{4\bar{n}_1}} e^{\frac{[\pm q(s-k)+\mu_2]^2}{4\bar{n}_2}} \left| \bar{n}_1 + p(s+k) + \mu_1, \bar{n}_2 \pm q(s-k) + \mu_2 \right\rangle_{\hat{H}} \right], \quad (2.1.23)$$

with $L(s) = \max(-[2\sqrt{\bar{n}_1}/p] - s, -[2\sqrt{\bar{n}_2}/q] + s)$ and

$U(s) = \min([2\sqrt{\bar{n}_1}/p] - s, [2\sqrt{\bar{n}_2}/q] + s)$. Note that it is valid for us to choose a

specific subset of $(\mu_1, \mu_2) = (0, 0)$ since the choice of the subset does not affect the

spatial morphology of the stationary states $\left| \Psi_{\bar{n}_1, \bar{n}_2}^{\pm p, q}(\gamma) \right\rangle_{s, \mu_1, \mu_2}$ in the classical limit (\bar{n}_1

and \bar{n}_2 large enough). Moreover, the amplitude coefficient of $\left| \Psi_{\bar{n}_1, \bar{n}_2}^{\pm p, q}(\gamma) \right\rangle_{s, \mu_1, \mu_2}$

dominates when the index s equals to zero. Thus, the stationary coherent state

$\left| \Psi_{\bar{n}_1, \bar{n}_2}^{\pm p, q}(\gamma) \right\rangle_{0, 0, 0}$ can be rewritten in a compact form:

$$|\Psi_{\bar{n}_1, \bar{n}_2}^{\pm p, q}(\gamma)\rangle_{0,0,0} = \frac{1}{\sqrt{2\pi\sqrt{\bar{n}_1\bar{n}_2}}} \sum_{k=-M}^M e^{iky} e^{\frac{(pk)^2}{4\bar{n}_1}} e^{\frac{(qk)^2}{4\bar{n}_2}} |\bar{n}_1 + pk, \bar{n}_2 \mp qk\rangle_{\hat{H}}, \quad (2.1.24)$$

where $M = \min\left(\left[2\sqrt{\bar{n}_1}/p\right], \left[2\sqrt{\bar{n}_2}/q\right]\right)$. The stationary coherent states in Eq. (2.1.24) suggest the periodic orbits that the wave-packet coherent states move along. Figure 2.1.6 depicts the transformation between the Lissajous curves and hypotrochoids for varying values of β with the parameters of $\omega_1/\omega_2 = 5/2$, $(\bar{n}_1, \bar{n}_2) = (9, 80)$, $\gamma = -\pi/4$, and $\alpha = \pi/2$. The continuous transformation between the Lissajous curves and the epitrochoids is clearly shown in Fig. 2.1.7 for different β values with the parameters of $\omega_1/\omega_2 = -5/2$, $(\bar{n}_1, \bar{n}_2) = (29, 60)$, $\gamma = \pi/4$, and $\alpha = \pi/2$. Moreover, Fig. 2.1.8 displays the transformation from Lissajous curves to hypotrochoids for various values of α with the parameters of $\omega_1/\omega_2 = -5/2$, $(\bar{n}_1, \bar{n}_2) = (29, 60)$, $\gamma = -\pi/2$, and $\beta = \pi/2$. Exploiting the concepts of the Schrödinger coherent states, we have successfully constructed the quantum states that mimic the classical dynamics in the coupled HOs. Via the SU(2) algebra, we also demonstrated the continuous transformation of the spatial morphologies between the two sort of distinct classical orbits, the Lissajous curves and the trochoids. The present results provide a comprehensive survey of the quantum-classical correspondence and might stimulate further ideas concerning the intriguing non-classical behavior in the mesoscopic regime.

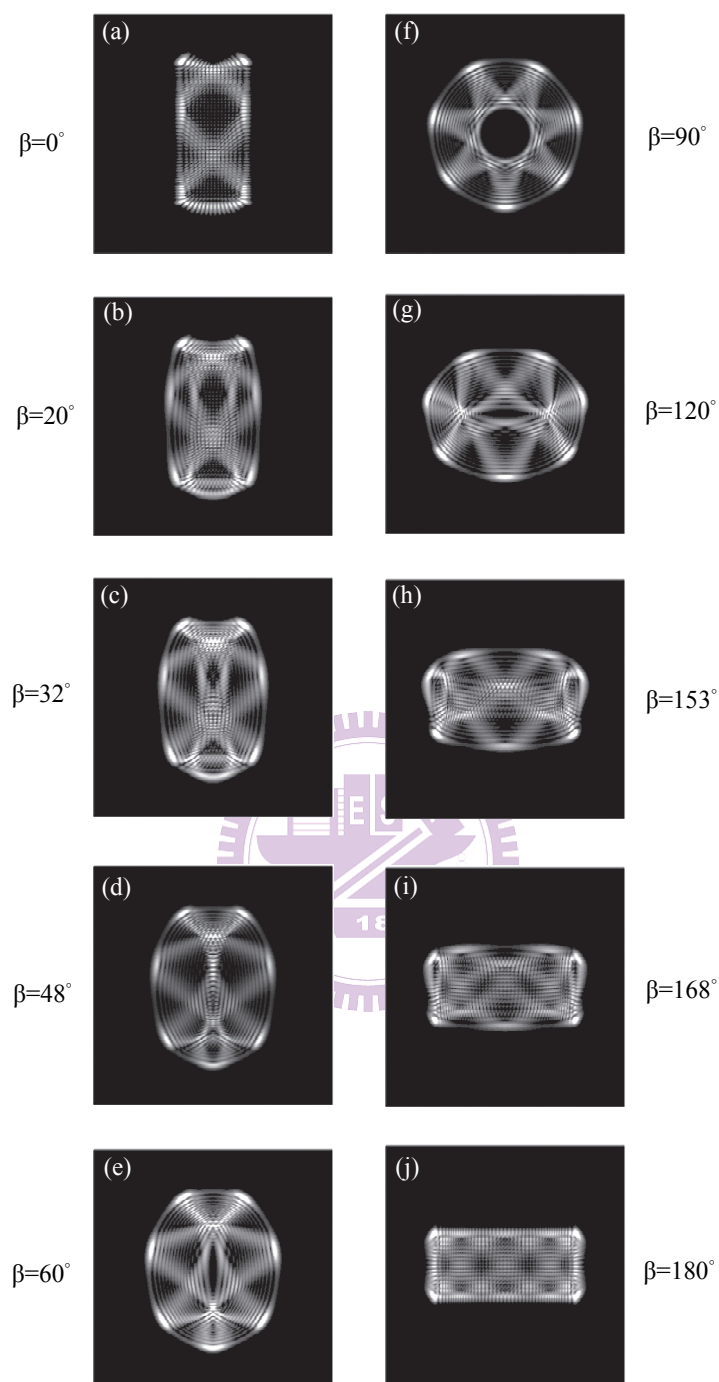


Fig. 2.1.6 Theoretical results for the intensity distribution of the stationary states $|\Psi_{\bar{n}_1, \bar{n}_2}^{\pm p, q}(\gamma)\rangle_{0,0,0}$ for varying values of β with the parameters of $\omega_1/\omega_2 = 5/2$, $(\bar{n}_1, \bar{n}_2) = (9, 80)$, $\gamma = -\pi/4$, and $\alpha = \pi/2$.

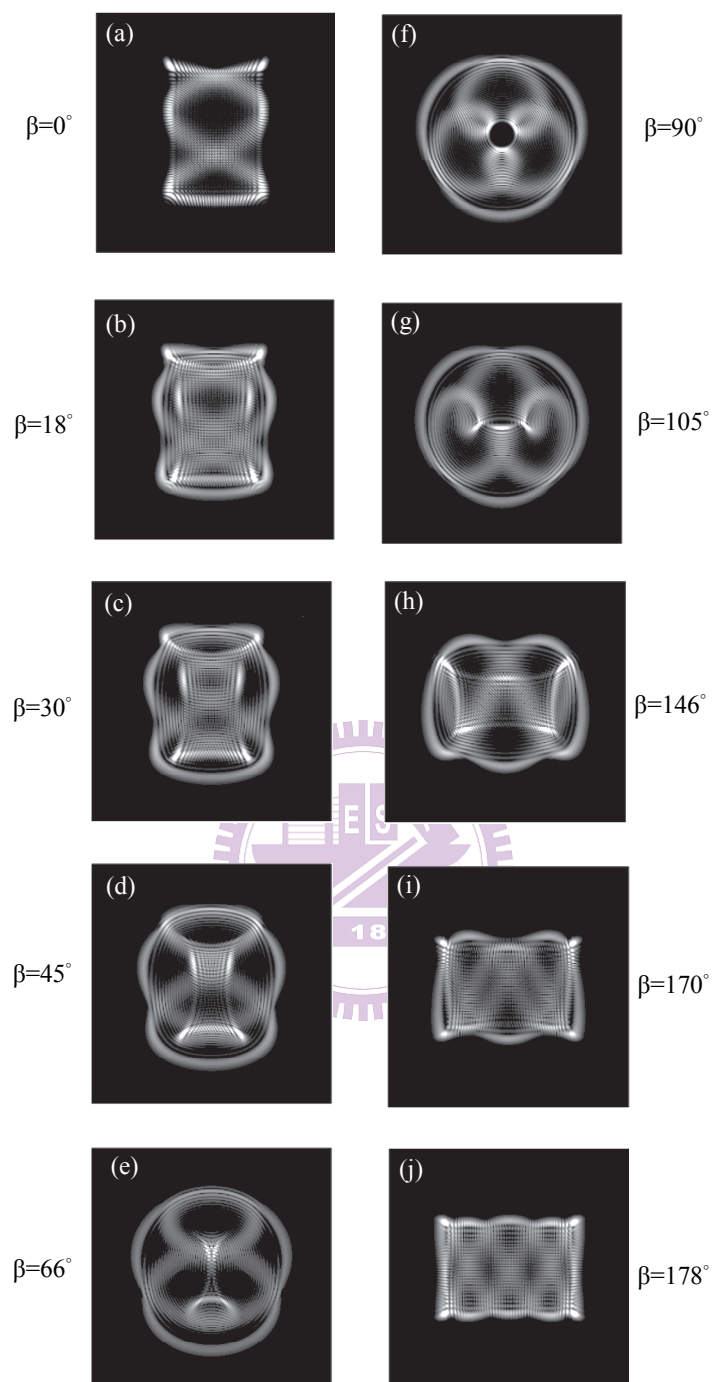


Fig. 2.1.7 Theoretical results for the intensity distribution of the stationary states $|\Psi_{\bar{n}_1, \bar{n}_2}^{\pm p, q}(\gamma)\rangle_{0,0,0}$ for different values of β with the parameters of $\omega_1/\omega_2 = -5/2$, $(\bar{n}_1, \bar{n}_2) = (29, 60)$, $\gamma = \pi/4$, and $\alpha = \pi/2$.

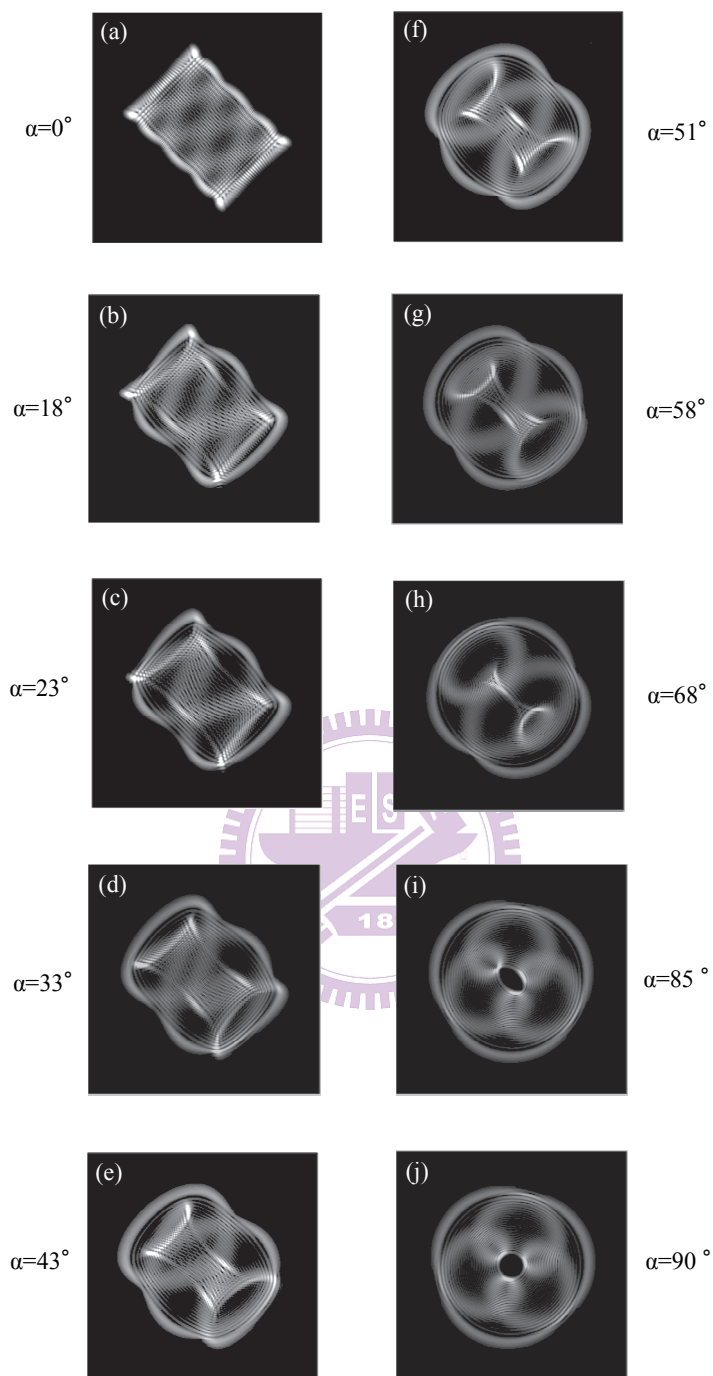


Fig. 2.1.8 Theoretical results for the intensity distribution of the stationary states $|\Psi_{\bar{n}_1, \bar{n}_2}^{\pm p, q}(\gamma)\rangle_{0,0,0}$ for different values of β with the parameters of $\omega_1/\omega_2 = -5/2$, $(\bar{n}_1, \bar{n}_2) = (29, 60)$, $\gamma = -\pi/2$, and $\beta = \pi/2$.

2.1.3 Coherent States : Multiple Periodic Orbits

In this section we start from the coupled commensurate HO with the Hamiltonian \hat{H} as derived in Eq. (2.1.10) and develop a quantum model by adding a new coupling term to the the coupled commensurate HO. We explore the eigenstates and find that the high-order spatial patterns are noticeably concentrated on Lissajous figures to trochoidal curves from single to multiple periodic orbits.

The general form of a two-dimensional (2D) commensurate HO comprising weak coupling term can be modeled as

$$\tilde{H} = \hat{H} + \hat{H}_c, \quad (2.1.25)$$

where \hat{H}_c signifies the SU(2) coupling term characterized by a vibration-rotational mechanism and the detail will be provided later. The Hamiltonian \hat{H} of the commensurate HO is given by $\hat{H} = \hat{H}_0 + \Omega_1 \hat{J}_1 + \Omega_2 \hat{J}_2 + \Omega_3 \hat{J}_3$ as has been shown in Eq. (2.1.4). By the use of the SU(2) algebra and in terms of the quantum ladder operators, the Hamiltonian has been transformed into Eq (2.1.10) with $\hat{H} = (\hat{a}'^\dagger \hat{a}' + 1/2)\omega_1 + (\hat{a}_2'^\dagger \hat{a}_2' + 1/2)\omega_2$, where $\omega_1 = q\omega$, $\omega_2 = p\omega$, ω is a common factor of the oscillation frequencies ω_1 and ω_2 , q and p are integers, and the ladder operators $\hat{a}_i'^\dagger$ and \hat{a}_i' ($i \in 1, 2$) follow the SU(2) transformation in Eq. (2.1.9).

The eigenstates of the commensurate HO can be divided into subsets given by $|n_1 p + \lambda_1, n_2 q + \lambda_2\rangle_{\hat{H}}$ as has been presented by Louck [46] and also discussed in section 2.1.2, where (n_1, n_2) are arbitrary nonnegative integers, and (λ_1, λ_2) are constants that $\lambda_1 = 0, 1, \dots, p-1$ and $\lambda_2 = 0, 1, \dots, q-1$. According to Eq. (2.1.11), the eigenstates $|n_1 p + \lambda_1, n_2 q + \lambda_2\rangle_{\hat{H}}$ can be written as

$$|n_1 p + \lambda_1, n_2 q + \lambda_2\rangle_{\hat{H}} = e^{iM\alpha/2} \sum_{s_1=0}^M e^{-is_1\alpha} d_{s_1-\frac{M}{2}, n_1 p + \lambda_1 - \frac{M}{2}}^{\frac{M}{2}}(\beta) |s_1, s_2\rangle_{\hat{H}_0}, \quad (2.1.26)$$

where $|s_1, s_2\rangle_{\hat{H}_0}$ are the eigenstates for the 2D isotropic HO given in Eq. (2.1.2),

$$M = n_1 p + \lambda_1 + n_2 q + \lambda_2 = s_1 + s_2, \quad \alpha = \tan^{-1}(\Omega_2/\Omega_1), \quad \text{and} \quad \beta = \tan^{-1}(\sqrt{\Omega_1^2 + \Omega_2^2}/\Omega_3).$$

It reveals the fact that the eigenstates have been divided into pq different subsets of states and the degeneracy holds when $n_1 + n_2$ is a constant N for fixed (λ_1, λ_2)

corresponding to the eigenvalues $E = \omega'[(n_1 + n_2) + 1/2p + 1/2q + \lambda_1/p + \lambda_2/q]$. For a

particular case $(p, q) = (1, 1)$ of the isotropic HO, it is evident that $\hat{H} = \omega'[2\hat{J} + 1]$,

where \hat{J} is the Casimir operator associated with the SU(2) Lie algebra and the corresponding generators derived by Schwinger [48] are shown in Eq. (2.1.5).

With the non-bijective canonical transformation, the commensurate HO can be mapped on to an isotropic one in a degenerate eigenspace [46]. The mapping suggests Schwinger's development of SU(2) symmetry represented by the canonically transformed ladder operators and leads to the analytical solutions to the Hamiltonian \hat{H} . Therefore, under the canonical transformation, the Hamiltonian in Eq. (2.1.10) can be transformed into

$$\hat{H} = \omega' \left[\left(\tilde{a}_1^\dagger \tilde{a}_1 + \frac{1}{2} \right) + \left(\tilde{a}_2^\dagger \tilde{a}_2 + \frac{1}{2} \right) \right], \quad (2.1.27)$$

where \tilde{a}_i and \tilde{a}_i^\dagger are the canonically transformed ladder operators which bear the relations [46]

$$\left. \begin{aligned} \tilde{a}_i^\dagger &= \sqrt{\frac{1}{\xi_i}(\hat{n}_i - \lambda_i)} \times [\hat{n}_i(\hat{n}_i - 1) \cdots (\hat{n}_i - \xi_i + 1)]^{-\frac{1}{2}} (\hat{a}_i^\dagger)^{\xi_i} \\ \tilde{a}_i &= \sqrt{\frac{1}{\xi_i}(\hat{n}_i - \lambda_i)} \times [\hat{n}_i(\hat{n}_i - 1) \cdots (\hat{n}_i - \xi_i + 1)]^{-\frac{1}{2}} (\hat{a}_i)^{\xi_i} \end{aligned} \right\}, \quad (2.1.28)$$

with number operator $\hat{n}_i = \hat{a}_i^\dagger \hat{a}_i$ and indices $(\xi_1, \xi_2) = (p, q)$. The operation of the

ladder operators on particular eigenstates for fixed (λ_1, λ_2) , for instance, are

$$\tilde{a}_1^\dagger |n_1 p + \lambda_1, n_2 q + \lambda_2\rangle_{\hat{H}} = \sqrt{n_1 + 1} |(n_1 + 1) p + \lambda_1, n_2 q + \lambda_2\rangle_{\hat{H}} \quad \text{and}$$

$$\tilde{a}_1 |n_1 p + \lambda_1, n_2 q + \lambda_2\rangle_{\hat{H}} = \sqrt{n_1} |(n_1 - 1) p + \lambda_1, n_2 q + \lambda_2\rangle_{\hat{H}}. \quad \text{Obviously, Eq. (2.1.27)}$$

has been converted into the same form as the isotropic HO when the degeneracy can exist for $n_1 + n_2 = N$ according to the eigenvalue $E = \omega'(n_1 + n_2 + 1)$ to the Hamiltonian \hat{H} . The generators of the SU(2) symmetry group can be rewritten in a way that makes them the generators responsible for the commensurate HO under consideration:

$$\tilde{J}_1 = (\tilde{a}_1^\dagger \tilde{a}_2 + \tilde{a}_2^\dagger \tilde{a}_1) / 2, \quad \tilde{J}_2 = (\tilde{a}_1^\dagger \tilde{a}_2 - \tilde{a}_2^\dagger \tilde{a}_1) / 2i, \quad \tilde{J}_3 = (\tilde{a}_1^\dagger \tilde{a}_1 - \tilde{a}_2^\dagger \tilde{a}_2) / 2. \quad (2.1.29)$$

The operators also satisfy the Lie commutation relation. Particularly, $\tilde{J}_1 = \hat{J}_1$, $\tilde{J}_2 = \hat{J}_2$, and $\tilde{J}_3 = \hat{J}_3$ for the special case of the isotropic HO with $(p, q) = (1, 1)$.

Let us now return to our formal considerations of the coupled HO of the Hamiltonian \tilde{H} given in Eq. (2.1.25). The Hamiltonian \hat{H}_c is expressed in the form of the SU(2) coupling interactions [44,45] and hence the Hamiltonian \tilde{H} can be modeled as

$$\tilde{H} = \hat{H} + \hat{H}_c = \hat{H} + \Omega'_1 \tilde{J}_1 + \Omega'_2 \tilde{J}_2 + \Omega'_3 \tilde{J}_3, \quad (2.1.30)$$

where Ω'_j ($j \in 1, 2, 3$) are constants indicating the coupling parameters with the assumption $\Omega'_j \leq \omega'$ for weak coupling. We would like to remark that, in view of the case $(p, q) = (1, 1)$ for the coupled isotropic HO, the wave functions have been demonstrated previously on a group theory level via the SU(2) transformation in section 2.1.1. Likewise, it enables us to derive the wave functions by employing the transformation of SU(2) symmetry group. It can be seen that Eq. (2.1.30) possesses

the same mathematical interpretation as Eq. (2.1.4). Therefore, the eigenstates with indices (m_1, m_2) for the Hamiltonian \tilde{H} can be directly obtained in terms of the Wigner d -coefficient [49]:

$$|m_1, m_2; \lambda_1, \lambda_2\rangle_{\tilde{H}} = e^{iN\alpha'/2} \sum_{n_1=0}^N e^{-in_1\alpha'} d_{n_1-N/2, m_1-N/2}^{N/2}(\beta') |n_1 p + \lambda_1, n_2 q + \lambda_2\rangle_{\tilde{H}}, \quad (2.1.31)$$

where

$$d_{n_1-N/2, m_1-N/2}^{N/2}(\beta') = \sqrt{n_1!(N-n_1)!m_1!(N-m_1)!} \times \sum_{v=\max[0, n_1-m_1]}^{\min[N-m_1, n_1]} \frac{(-1)^v [\cos(\beta'/2)]^{m_1+n_1-2v} [\sin(\beta'/2)]^{m_2-n_1+2v}}{v!(N-m_1-v)!(n_1-v)!(m_1-n_1+v)!}. \quad (2.1.32)$$

Evidently, the eigenstates $|m_1, m_2; \lambda_1, \lambda_2\rangle_{\tilde{H}}$ can be expressed as a linear superposition of the set of $|n_1 p + \lambda_1, n_2 q + \lambda_2\rangle_{\tilde{H}}$. Figures 2.1.9(a1)-2.1.9(a4) show distributions of the Wigner d -coefficient $|d_{n_1-N/2, m_1-N/2}^{N/2}(\beta')|^2$ with respect to n_1 for $m_1 = 0 \sim 3$, $N = 60$ and $\beta' = \pi/2$, which reveal the composition of $|m_1, m_2; \lambda_1, \lambda_2\rangle_{\tilde{H}}$ with eigenstates $|n_1 p + \lambda_1, n_2 q + \lambda_2\rangle_{\tilde{H}}$ of different orders. Figures 2.1.9(b1)-2.1.9(b4), 2.1.9(c1)-2.1.9(c4), and 2.1.9(d1)-2.1.9(d4) illustrate the corresponding eigenstates $|m_1, m_2; \lambda_1, \lambda_2\rangle_{\tilde{H}}$ for different indices (m_1, m_2) with $(p, q) = (2, 1)$, $(p, q) = (3, 1)$, and $(p, q) = (3, 2)$, respectively, and all with the parameters $(\lambda_1, \lambda_2) = (0, 0)$, $(\alpha', \beta') = (\pi/2, \pi/2)$, $(\alpha, \beta) = (0, 0)$, and $N = 60$.

Note that it is valid for us to choose a specific eigenspace of $(\lambda_1, \lambda_2) = (0, 0)$ since, in the classical limit (N large enough), [50] has confirmed that the choice of the

eigenspace does not affect the final results. Therefore, parameters (λ_1, λ_2) are set to be $(0,0)$ in the following discussions and we simplify the denotation of the eigenstates $|m_1, m_2; 0, 0\rangle_{\hat{H}}$ to $|m_1, m_2\rangle_{\hat{H}}$. Moreover, (α', β') are chosen for specific parameters. α' signifies an additional phase shift between the two HOs in x and y directions, and β' corresponds to the coupling strength arising from \hat{H}_c . The distribution shown in Fig. 2.1.10(a1)-2.1.10(a8) are varied with β' , which indicates different composition for the corresponding eigenstates $|m_1, m_2\rangle_{\hat{H}}$ as depicted in Fig. 2.1.10(b1)-2.1.10(b8) with $(p, q) = (2, 1)$, $\alpha' = \pi/2$, $(\alpha, \beta) = (0, 0)$, $m_1 = 1$, and $N = 60$. For $\beta' = 0$ and $\beta' = \pi$, the eigenstates can be seen to project precisely onto particular eigenstates $|p, q(N-1)\rangle_{\hat{H}}$ and $|p(N-1), q\rangle_{\hat{H}}$, respectively. While β' is determined, the conversion of α' can be illustrated as shown in Fig. 2.1.11(a1)-2.1.11(a5) with $m_1 = 1$, $\beta' = 0.4\pi$, $(\alpha, \beta) = (0, 0)$ and $N = 60$, and in Fig. 2.1.11(b1)-2.1.11(b5) with $m_1 = 3$, $\beta' = 0.74\pi$, $(\alpha, \beta) = (0, 0)$ and $N = 60$. The morphologies transform since different relative phases are introduced into the superposition of states $|m_1, m_2\rangle_{\hat{H}}$ with the set of states $|n_1 p, n_2 q\rangle_{\hat{H}}$.

Theoretical results disclose intriguing geometric patterns localized on an ensemble of periodic Lissajous orbits, which suggests a kind of quantum-classical analog. It is evident that the number of peaks associated with $|d_{n_1-N/2, m_1-N/2}^{N/2}(\beta')|^2$ is consistent with the number of Lissajous orbits in $|m_1, m_2\rangle_{\hat{H}}$ according to various m_1 . The fact implies each orbit of multi-Lissajous patterns is formed by the superposition of a particular group of the set $|n_1 p, n_2 q\rangle_{\hat{H}}$ with distribution centered on the

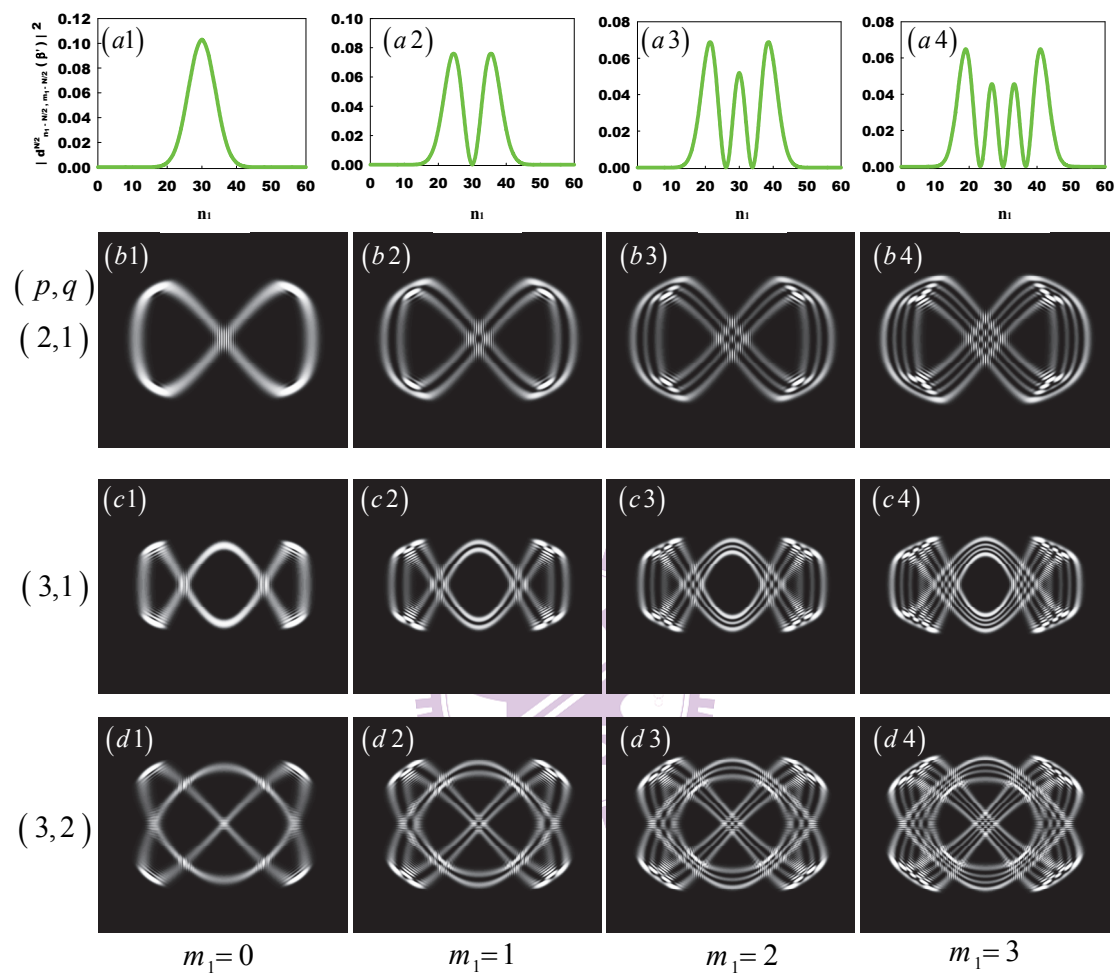


Fig. 2.1.9 (a1)-(a4) Numerical simulations of the Wigner d -coefficient with respect to n_1 for various m_1 ; (b1)-(d4) numerical wave patterns for the intensities of eigenstates $|m_1, m_2; 0, 0\rangle_{\bar{H}}$. Detailed description of the parameters; see text.

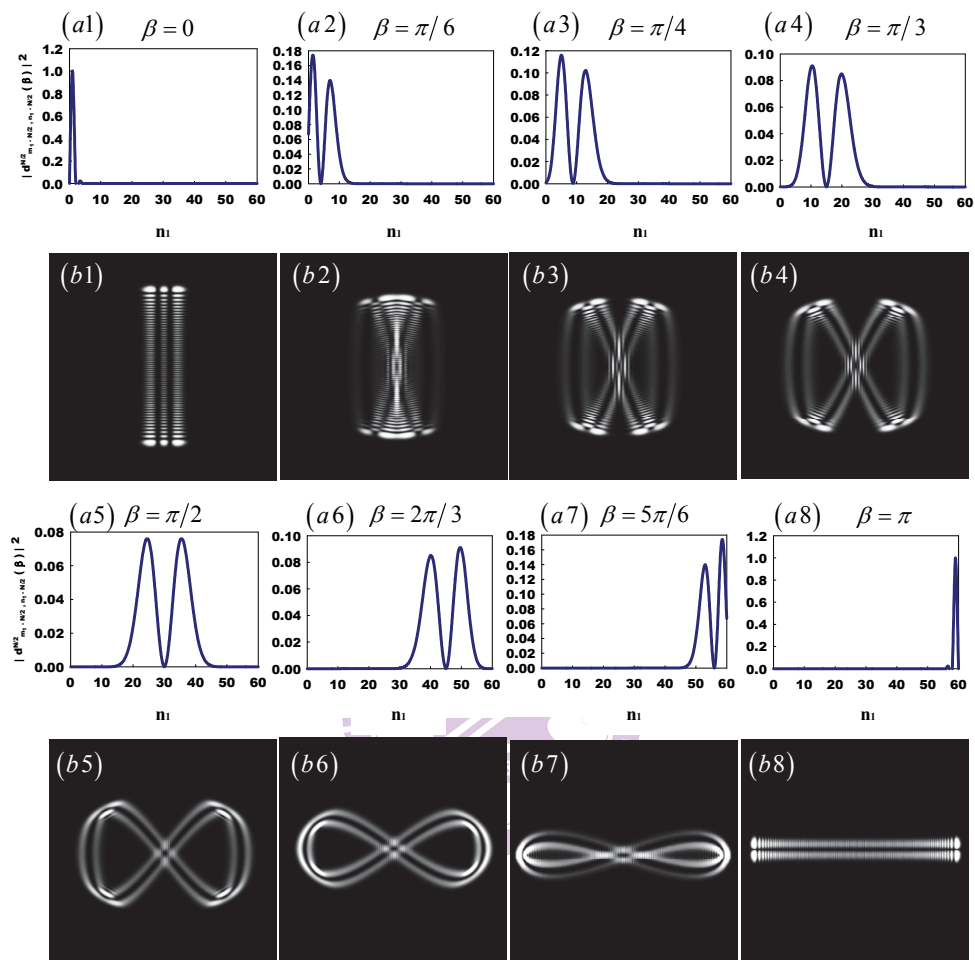


Fig. 2.1.10 (a1)-(a8) Numerical simulations of Wigner d -coefficient with respect to n_1 for various β ; (b1)-(b8) corresponding numerical wave patterns for the intensity distribution of eigenstates $|m_1, m_2\rangle_{\tilde{H}}$.

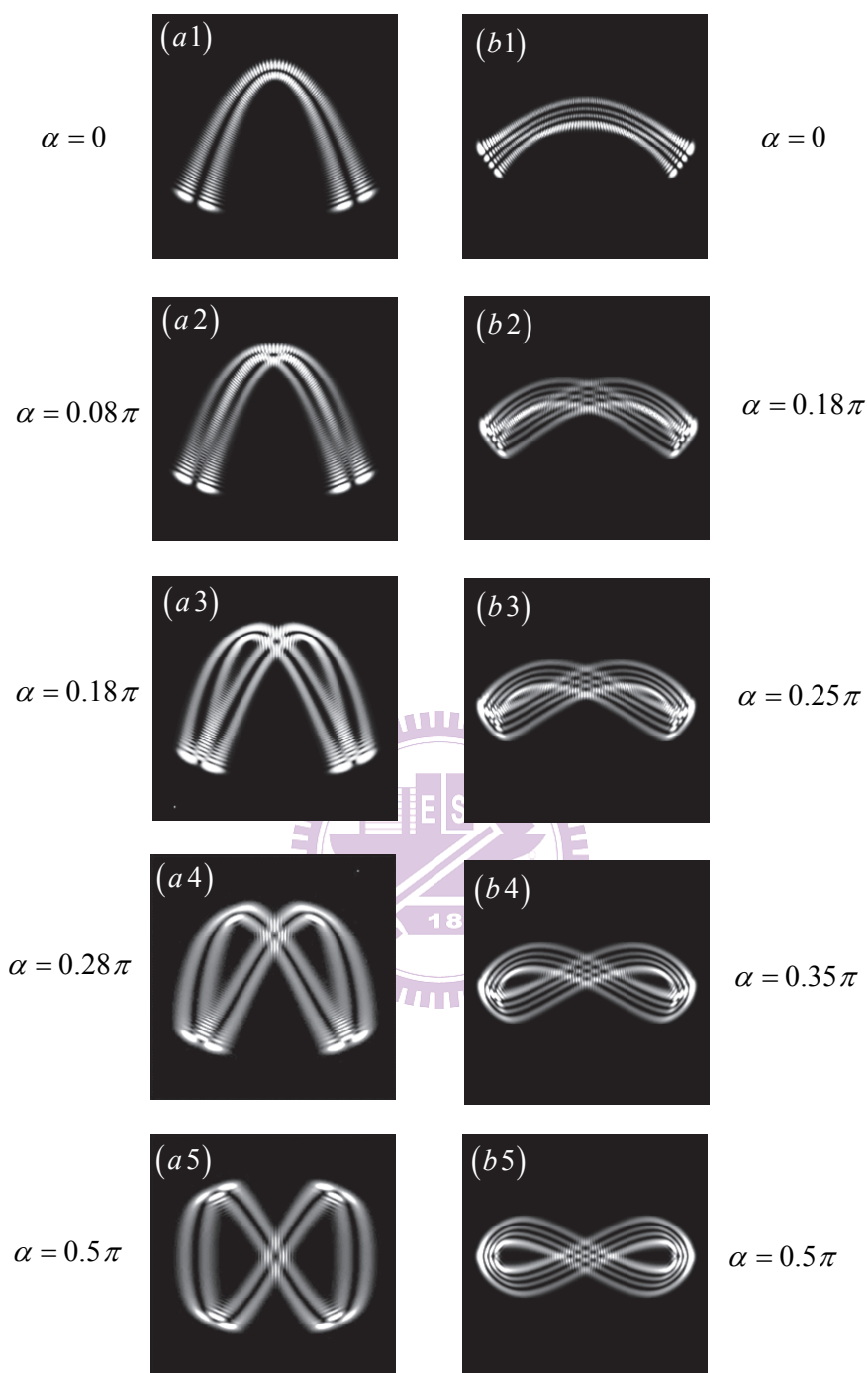


Fig. 2.1.11 Numerical wave patterns for the intensities of eigenstates $|m_1, m_2\rangle_{\hat{H}}$ with respect to varying α' ; (a1)-(a5) $\beta' = 0.4\pi$; (b1)-(b5) $\beta' = 0.74\pi$.

corresponding peak of $\left|d_{n_1-N/2, m_1-N/2}^{N/2}(\beta')\right|^2$. A relation $l = \min(m_1, m_2) + 1$ can be given, where l denotes the number of orbits. While the magnitude of $\min(m_1, m_2)$ becomes larger, the related excited states display more complex caustic-like geometric patterns as shown in Fig. 2.1.12 followed by the case in Fig. 2.1.9(b1)-2.1.9(b2). Additionally, the symmetry is held for $(m_1, m_2) \Leftrightarrow (m_2, m_1)$, e.g., eigenstates of $(m_1, m_2) = (26, 34)$ and $(m_1, m_2) = (34, 26)$ shown in Fig. 2.1.12(f) and 2.1.12(h) possess identical morphology for equal distribution $\left|d_{n_1-N/2, m_1-N/2}^{N/2}(\beta')\right|^2$. Though the same morphology is notified, the eigenstates (m_1, m_2) and (m_2, m_1) are characterized by distinct features of the quantum probability current $\bar{J}(x, y)$, where $\bar{J}(x, y) = \text{Im}(\Psi^* \bar{\nabla} \Psi)$ [49] and $\Psi_{m_1, m_2}(x, y) = \langle x, y | m_1, m_2 \rangle_{\bar{H}}$. Taking the cases of $(m_1, m_2) = (1, 59)$ and $(m_1, m_2) = (59, 1)$ as an example, it can be seen that the probability current $\bar{J}(x, y)$ flow in counter directions for the two states as depicted in Fig. 2.1.13(b) and 2.1.13(c). Note that the vector field $\bar{J}(x, y)$ has been normalized to $\bar{J}(x, y) / |\bar{J}(x, y)|$ for observing the detailed structures and the constants \hbar and particle mass are set to be unity.

Figure 2.1.14 further displays the phase structures for the case in Fig. 2.1.12(a) and 2.1.12(e). The enlarged figures of the box region in Fig. 2.1.14(a2) and 2.1.14(b2) are presented respectively in Fig. 2.1.14(a3) and 2.1.14(b3), where the complicated phase distribution indicates promising development in quantum physics such as quantum entanglement and quantum information as long as the quantum states $|m_1, m_2\rangle_{\bar{H}}$ can be accessibly prepared [51]. Furthermore, in Fig. 2.1.15, we

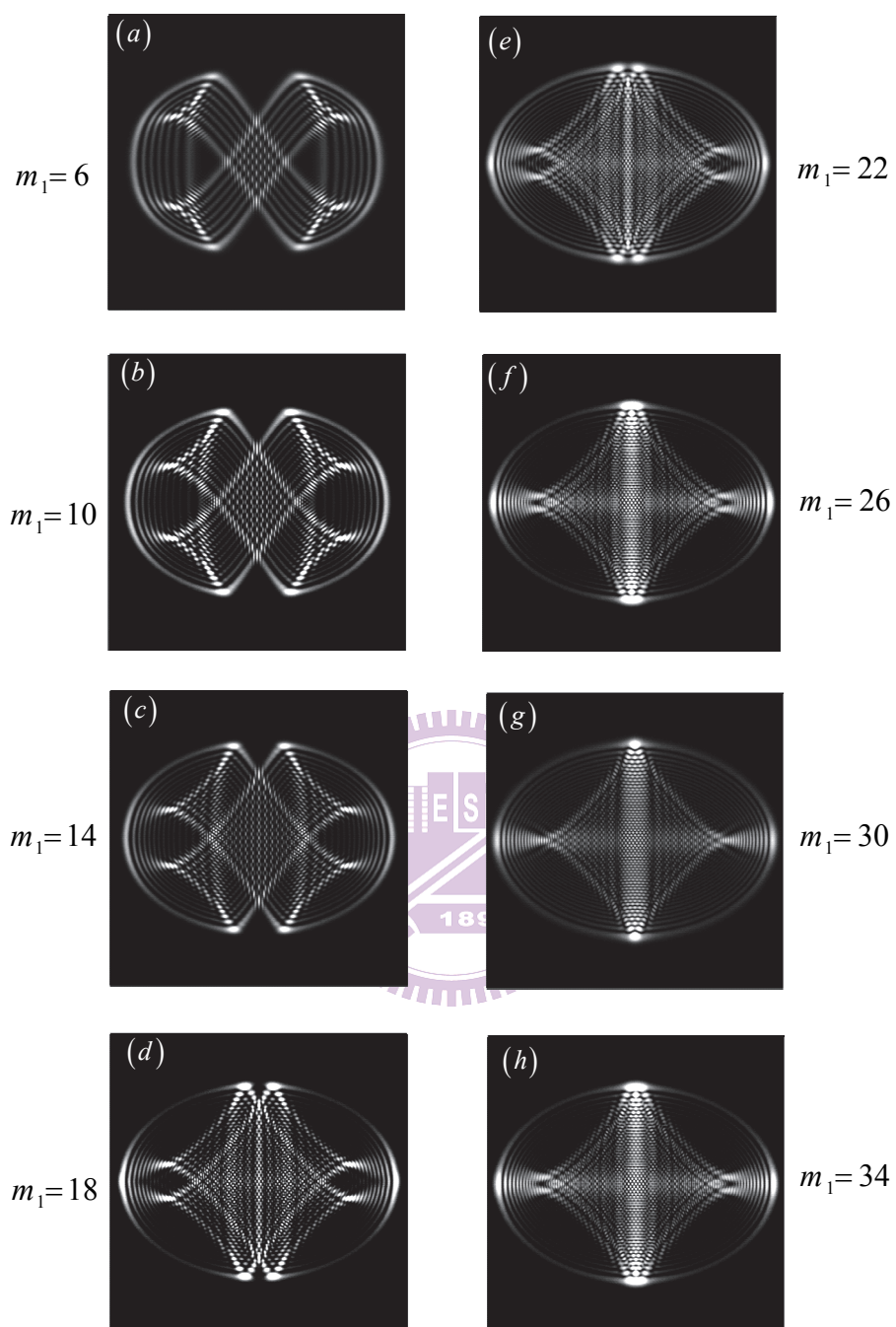


Fig. 2.1.12 Numerical wave patterns for higher indices m_1 followed by the case in Fig. 2.1.9(b1)-(b4).

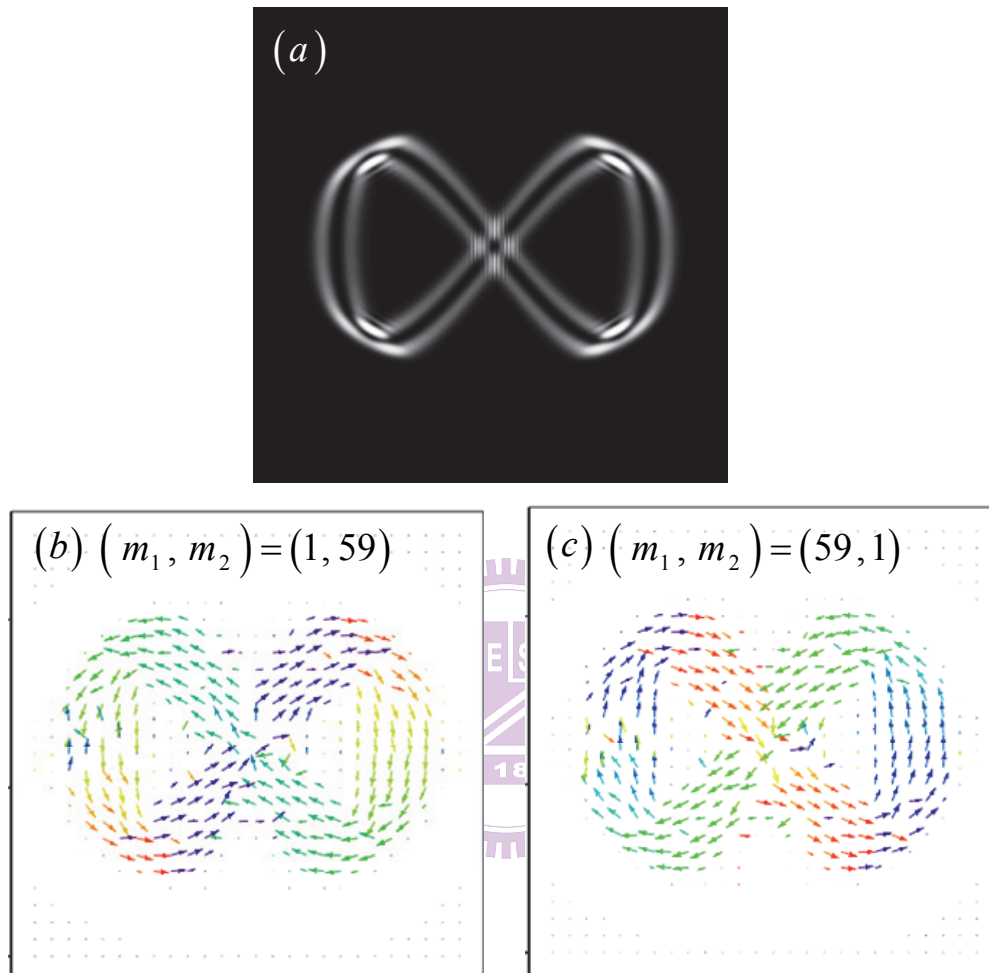


Fig. 2.1.13 (a) Numerical wave patterns for the intensities of eigenstates $|m_1, m_2\rangle_{\bar{H}}$ for $(m_1, m_2) = (1, 59)$ and $(m_1, m_2) = (59, 1)$; probability current $\vec{J}(x, y)$ for (b) $(m_1, m_2) = (1, 59)$, and (c) $(m_1, m_2) = (59, 1)$.

the numerical calculations of $|m_1, m_2\rangle_{\hat{H}}$ for different (p, q) where $(p, q) = (3, 2)$, and $(\alpha', \beta') = (\pi/2, \pi/2)$ for Fig. 2.1.15(a), $(p, q) = (3, 1)$, and $(\alpha', \beta') = (\pi/2, \pi/2)$ for Fig. 2.1.15(b), $(p, q) = (4, 3)$, and $(\alpha', \beta') = (0, \pi/2)$ for Fig. 2.1.15(c), and $(p, q) = (5, 2)$, and $(\alpha', \beta') = (\pi/2, \pi/2)$ for Fig. 2.1.15 (d), and all with $(\alpha, \beta) = (0, 0)$, $m_1 = 1$, and $N = 60$. Moreover, Fig. 2.1.16 depicts the transverse patterns for multiple Lissajous orbits in Fig. 2.1.15(a) for varying α' .

We have provided comprehensive analyses for the condition of $(\alpha, \beta) = (0, 0)$ on the above, i.e. the examples for multiple Lissajous orbits have been thoroughly investigated. More intriguingly, consider the case for $(\alpha, \beta) \neq (0, 0)$, the eigenstates of the coupled commensurate HO can be found to transform continuously from multiple Lissajous orbits to the multiple trochoidal orbits as depicted in Fig. 2.1.17. It is noted that the intensity distribution in Eq. (2.1.31) has been modified here to be

$$|m_1, m_2; \lambda_1, \lambda_2; \bar{n}_1, \bar{n}_2\rangle_{\hat{H}} = e^{iN\alpha'/2} \left[\sum_{n_1=0}^N e^{-in_1\alpha'} d_{n_1-N/2, m_1-N/2}^{N/2}(\beta') \right. \\ \left. |\bar{n}_1 + n_1 p + \lambda_1, \bar{n}_2 \mp n_2 q + \lambda_2\rangle_{\hat{H}} \right], \quad (2.1.33)$$

where \bar{n}_1 and \bar{n}_2 are the initial values for the associated quantum numbers and the sign \mp of the index $n_2 q$ is decided by the general representation for $\omega_2 = \pm p\omega$.

As presented in section 2.1.2, the localization on the classical structure is more prominent as the number of quanta increases. Therefore, without limiting the initial values to be $(\bar{n}_1, \bar{n}_2) = (0, 0)$, \bar{n}_1 and \bar{n}_2 are introduced here for the general expression of the localized trajectories associated with fairly large quantum numbers. Note that the degeneracy is still hold for Eq. (2.1.33) under the modification. Figures

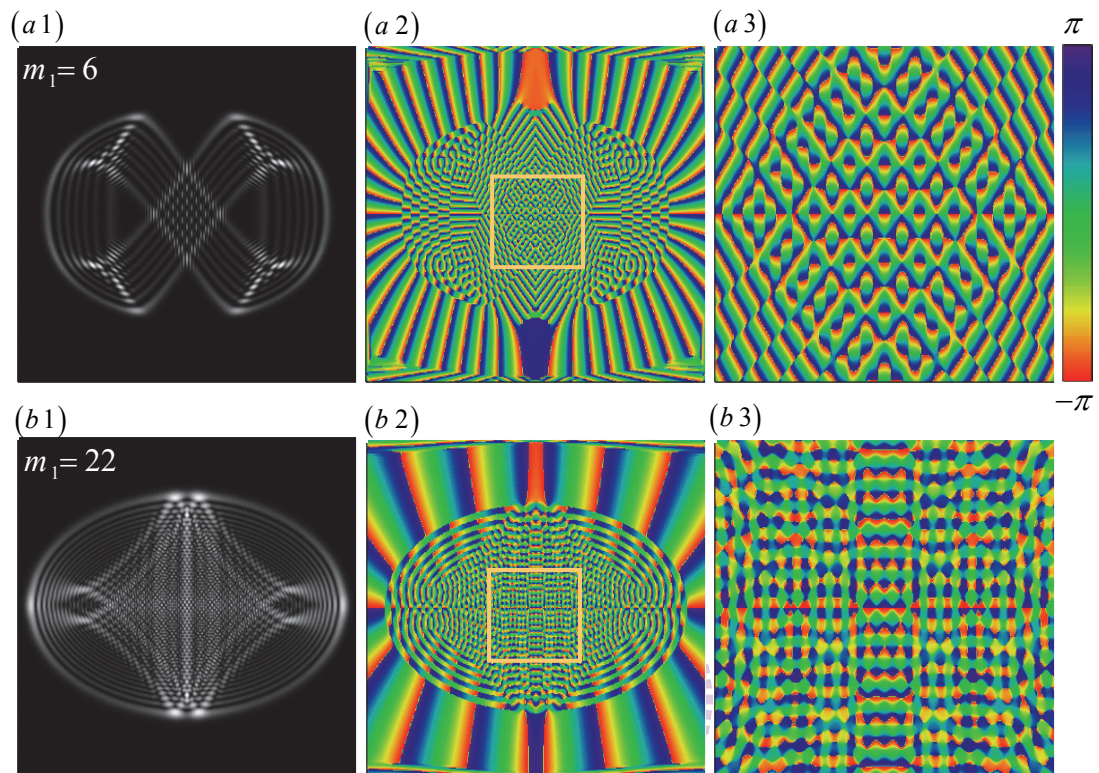


Fig. 2.1.14 (a1), (b1) Theoretical results in Fig. 2.1.12(a) and 2.1.12(e); (a2), (b2) phase distribution of (a1) and (b1), respectively; (a3), (b3) enlarged figures of the box region in (a2) and (b3), respectively.

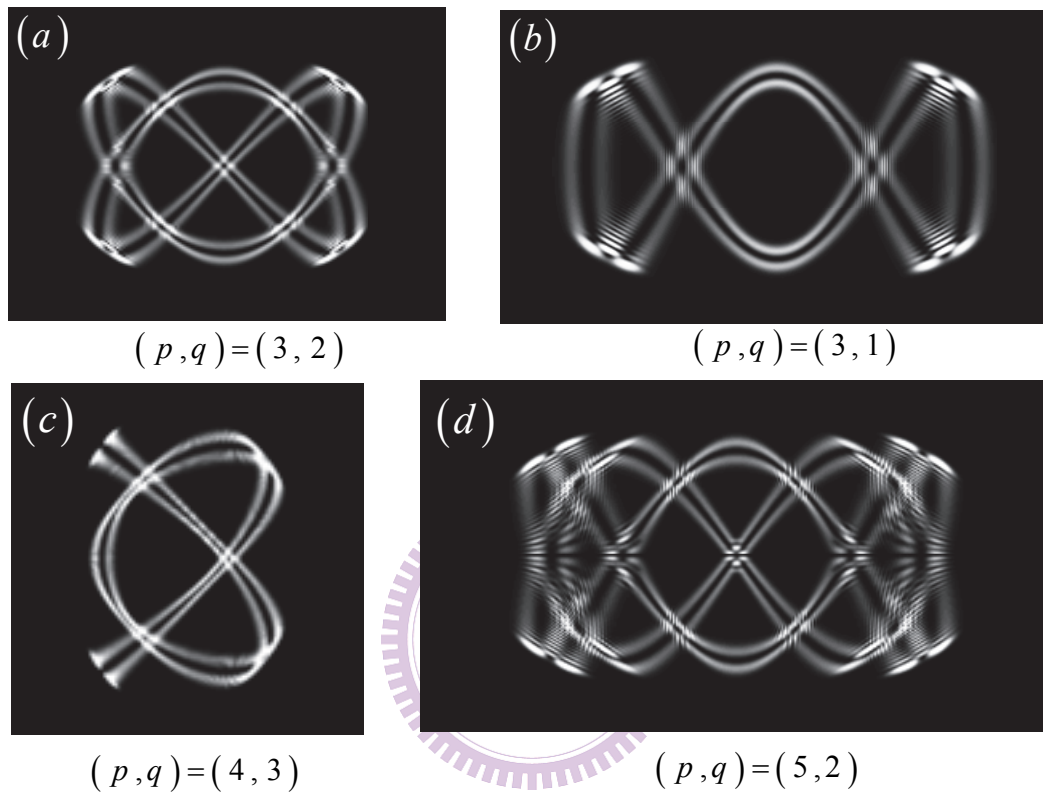


Fig. 2.1.15 Numerical wave patterns for the intensity distribution of $|m_1, m_2\rangle_{\tilde{H}}$ with different indices (p, q) .

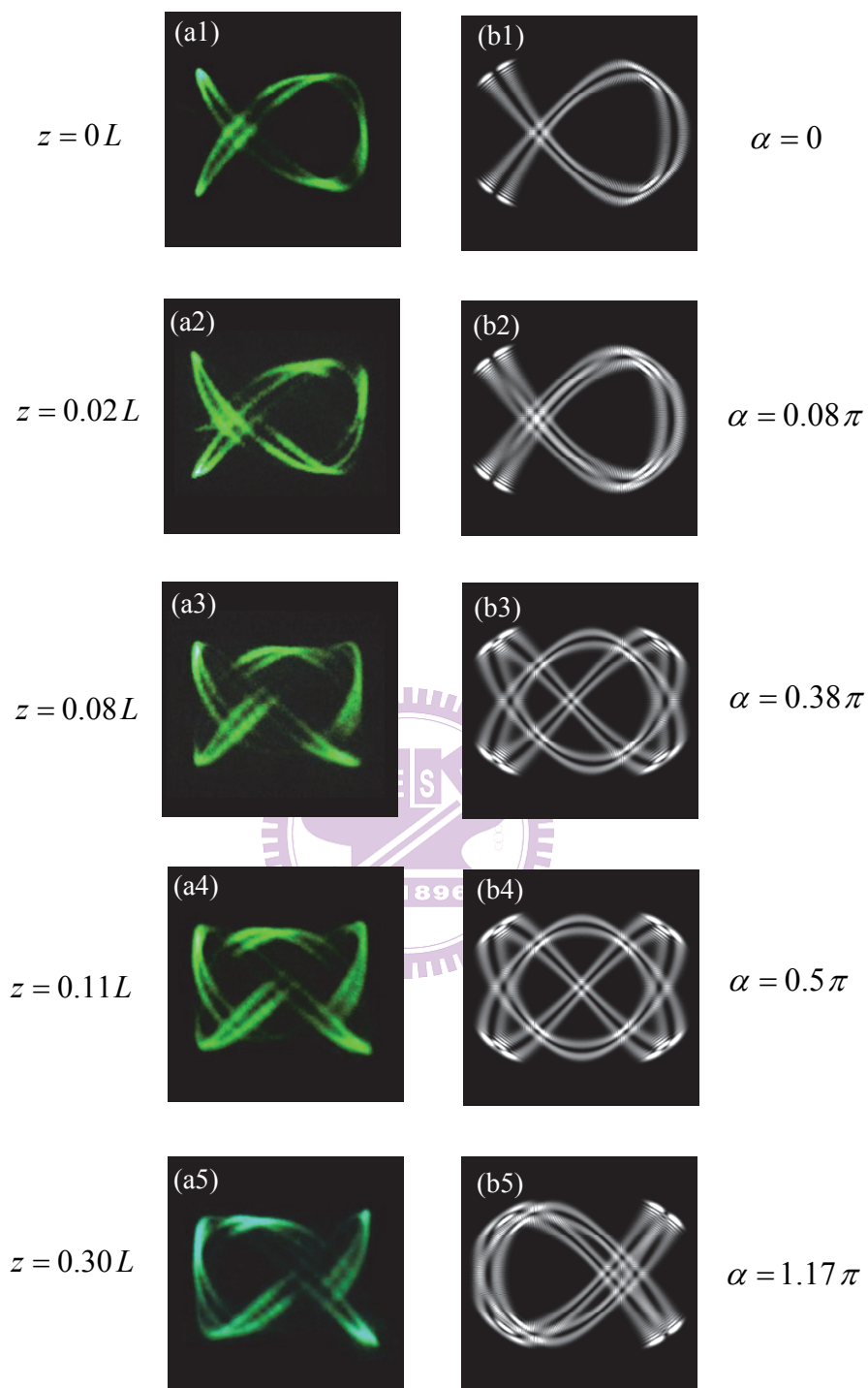


Fig. 2.1.16 (a1)-(a5) Experimental wave patterns. (b1)-(b5) Numerical wave patterns for the intensity distribution of $|m_1, m_2\rangle_{\tilde{H}}$ with $(p, q) = (3, 2)$ and varying values of α' .

2.1.17(a1)-2.1.17(e1) display the intensity distribution of $|m_1, m_2; \lambda_1, \lambda_2; \bar{n}_1, \bar{n}_2\rangle_{\tilde{H}}$ for varying values of β with the parameters $\omega_1/\omega_2 = 1/4$, $(\bar{n}_1, \bar{n}_2) = (60, 20)$, $(\lambda_1, \lambda_2) = (0, 0)$, $N=7$, $m_1 = 1$, $(\alpha', \beta') = (-\pi/4, 0)$, and $\alpha = \pi/2$. Figures 2.1.17(b1)-2.1.17(b2) show the intensity distribution of $|m_1, m_2; \lambda_1, \lambda_2; \bar{n}_1, \bar{n}_2\rangle_{\tilde{H}}$ for varying values of β with the parameters $\omega_1/\omega_2 = 2/5$, $(\bar{n}_1, \bar{n}_2) = (40, 28)$, $(\lambda_1, \lambda_2) = (0, 0)$, $N=5$, $m_1 = 1$, $(\alpha', \beta') = (\pi/4, 0)$, and $\alpha = \pi/2$. It can be seen that for $(\alpha, \beta) = (\pi/2, \pi/2)$ the eigenstates to the coupled commensurate HO are concentrated on the multiple trochoidal orbits. The eigenstates reveal a continuous transformation from the multiple Lissajous orbits to the multiple trochoidal curves for β changing from 0 to $\pi/2$.

As we will see in section 2.2.4, the correlated optical modes can be successfully generated in an astigmatic large-Fresnel-number laser cavity [52]. The certification is based on the reconciliation between the wave equation for laser transverse modes in the paraxial approximation and the Schrödinger equation for the 2D quantum confined systems [9,11,29]. Most importantly, Nienhuis *et al* [9] has clarified high correlation between the quantum operator algebra and manipulation in the laser cavity. Consequently, based on the acts of the quantum operators, we are able to generate the analogous wave patterns by the correlated operation in a laser resonator. The presented research will not be restricted to the theoretical viewpoint of quantum physics and, intriguingly, practical correspondence will be explicitly provided with optical waves.

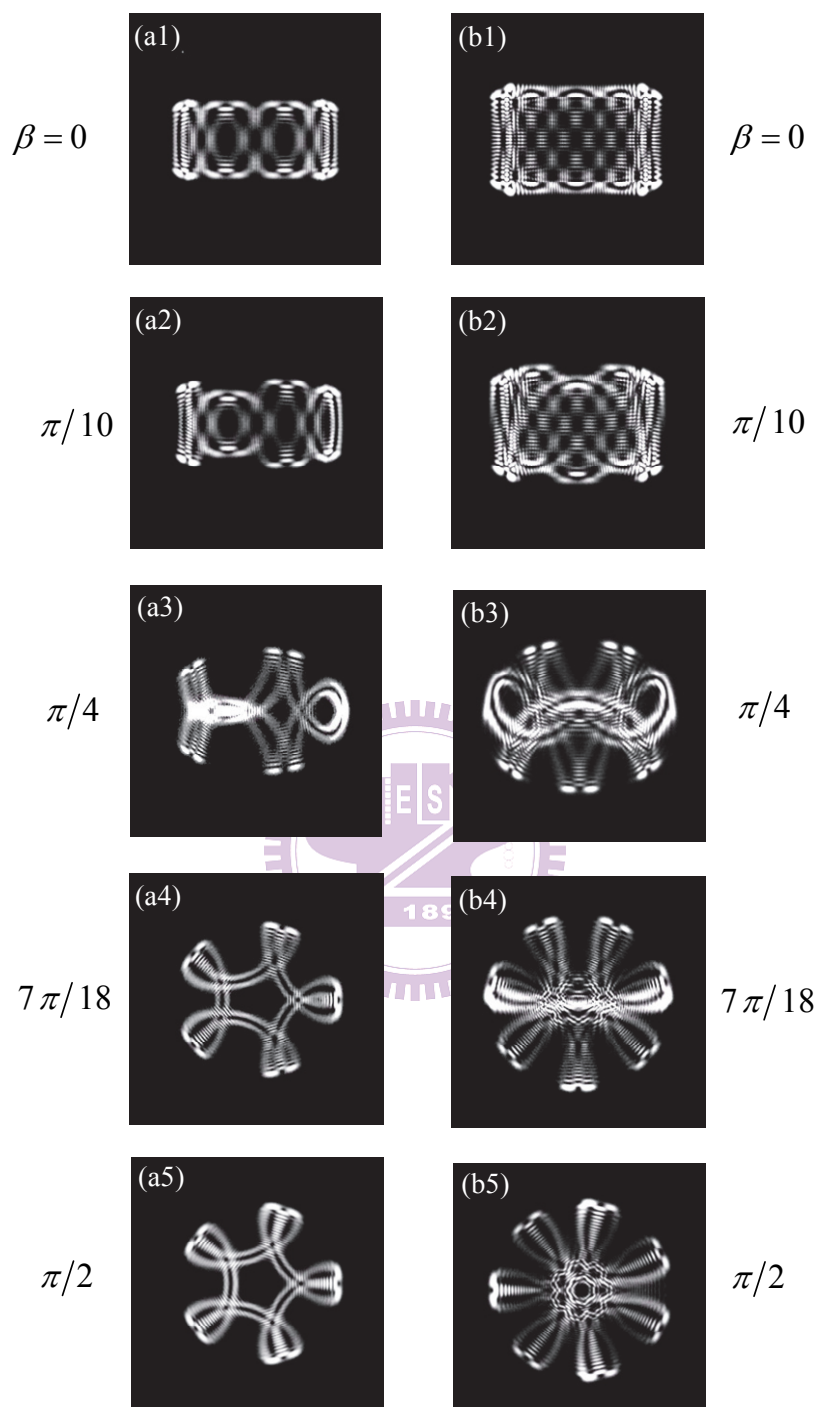


Fig. 2.1.17 Numerical results of the intensity distribution for $|m_1, m_2; \lambda_1, \lambda_2; \bar{n}_1, \bar{n}_2\rangle_{\tilde{H}}$ with various values of β . Detailed description of the parameters, see text.

2.2 Analogous Optical Experiments

2.2.1 Experimental Setup

Figure 2.2.1 depicts the experimental setup for transforming the laser modes through cylindrical lenses. The present laser cavity was composed of a spherical mirror and a large-aperture gain medium. The spherical mirror was a 10-mm radius-of-curvature concave mirror with antireflection coating at the pumping wavelength on the entrance face ($R < 0.2\%$), high-reflection coating at lasing wavelength ($R > 99.8\%$), and high-transmission coating at the pumping wavelength on the other surface ($T > 95\%$). The gain medium was an a -cut 2.0 at. % Nd:YVO₄ crystal with the length of 2 mm and the cross section of $8 \times 8 \text{ mm}^2$. One planar surface of the laser crystal was coated for antireflection at the pumping and lasing wavelengths; the other surface was coated to be an output coupler with the reflectivity of 99%. The pump source was a 3-W 809-nm fiber-coupled laser diode with a core diameter of 100 μm . A coupling lens was used to focus the pump beam into the laser crystal with a large off-axis displacement. The well-known transverse HG modes are emitted by most laser cavities and are formally identical to the eigenstates of 2D quantum HO [53]. For localized laser patterns, it has been found that the longitudinal-transverse coupling and the mode-locking effect in large-Fresnel-number spherical laser cavities usually drive the laser modes to be the coherent waves that are transversely concentrated on the Lissajous figures with the relative phase continuously varying with the longitudinal direction [11]. The generated laser mode was re-imaged into a cylindrical-lens mode converter to perform the beam transformation. The focal length of the cylindrical lenses was $f = 25 \text{ mm}$; the distance was precisely adjusted to be $\sqrt{2}f$ for the operation of the $\pi/2$ converter. To image the transformed transverse

pattern, the transformed laser beam was directly projected on a paper screen at a distance of ~50 cm behind the cylindrical mode converter and the scattered light was captured by a digital camera.

In the following sections we are going to discuss the beam transformation of the laser modes emitted from the laser resonator to be converted through the cylindrical-lens mode converter.

2.2.2 Eigenmodes : General Huygens' Integral

We first derive a general form for the laser modes to be converted via an ABCD system by exploiting the Huygens integral to investigate the case concerning the transverse HG modes to be transformed through the cylindrical-lens mode converter. It can be found that the conversion of the laser modes possess identical mathematical interpretation to the quantum states via the SU(2) transformation in section 2.1.1

In free space, Huygens' integral in one transverse dimension for propagation through a distance L can be given by [53]

$$u(x_2, z_2) = \sqrt{\frac{j}{L\lambda_0}} \int_{-\infty}^{\infty} u(x_1, z_1) \exp[-jk\rho(x_1, x_2)] dx_1, \quad (2.2.1)$$

where $\rho(x_1, x_2) = \sqrt{L^2 + (x_2 - x_1)^2}$ is the optical path length, also called the *eikonal* function for the optical ray propagate from (x_1, z_1) to $(x_1, z_2 = z_1 + L)$, $k = 2\pi/\lambda_0$ is the wave number and λ_0 is the wavelength of the light in free space. For a general consideration that the optical ray travels through optical elements building up the ABCD system of length L , the optical path length under the paraxial approximation can be derived to be [53]

$$\rho(x_1, x_2) = L + \frac{(Ax_1^2 - 2x_1x_2 + Dx_2^2)}{2B}. \quad (2.2.2)$$

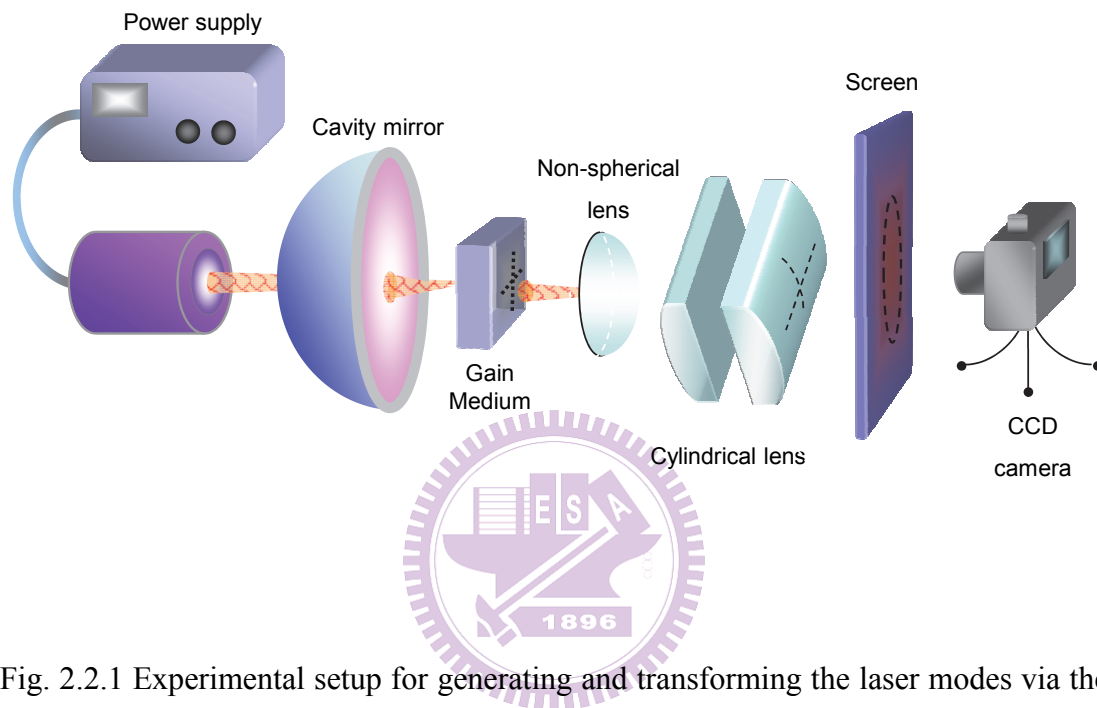


Fig. 2.2.1 Experimental setup for generating and transforming the laser modes via the cylindrical-lens mode converter.

Therefore, the general Huygens' integral associated with an ABCD system can be rewritten as

$$u(x_2, z_2) = \sqrt{\frac{j}{B\lambda_0}} \exp(-jkL) \times \int_{-\infty}^{\infty} u(x_1, z_1) \exp\left[-j \frac{\pi(Ax_1^2 - 2x_1x_2 + Dx_2^2)}{B\lambda_0}\right] dx_1. \quad (2.2.3)$$

Consider an input beam of a high-order HG mode in the form [53]

$$u_n(x_1, z_1) = \sqrt{\frac{\sqrt{2}}{2^n n! \omega_1 \sqrt{\pi}}} H_n\left(\frac{\sqrt{2} x_1}{\omega_1}\right) \exp\left(-j \frac{\pi x_1^2}{\lambda_1 q_1}\right). \quad (2.2.4)$$

where $H_n(\cdot)$ is the Hermite polynomial of order n . Note that

$1/q_1 \equiv (1/R_1) - j(\lambda_1/\pi \omega_1^2)$, where R_1 is the radius of curvature for the input beam,

ω_1 signifies the beam radius at z_1 , and λ_1 is the wavelength in the medium where

the beam is currently located and here we assume $\lambda_1 \approx \lambda_0$ for simplicity. Employing

the generating function for the Hermite polynomials

$\exp(2\xi t - t^2) = \sum_{n=0}^{\infty} [H_n(\xi) t^n / n!]$ and the identity $\int_{-\infty}^{\infty} \exp(-ax^2) dx = \sqrt{\pi/a}$ we

can obtain the amplitude distribution of $u_n(x_2, z_2)$ in the form

$$u_n(x_2, z_2) = \exp(-jkL) \sqrt{\frac{\sqrt{2}}{2^n n! \omega_1 \sqrt{\pi}}} \left(\frac{1}{A+B/q_1}\right)^{n+1/2} \times \left(\frac{\omega_2}{\omega_1}\right)^n H_n\left(\frac{\sqrt{2} x_2}{\omega_2}\right) \exp\left(-j \frac{\pi x_2^2}{\lambda_0 q_2}\right), \quad (2.2.5)$$

with $1/q_2 \equiv (1/R_2) - j(\lambda_0/\pi \omega_2^2)$, where R_2 is the radius of curvature for the

output beam, $\omega_2 = \omega_1 \sqrt{(A+B/q_1)^2 + j[2B\lambda_0(A+B/q_1)/\pi\omega_1^2]}$ signifies the beam

radius at z_2 , and q_2 follows the relation $1/q_2 = (C + D/q_1)/(A + B/q_1)$. It is worth to mention that the term $[1/(A + B/q_1)]^{n+1/2}$ is a complex value which can be rewritten as $|1/(A + B/q_1)|^{n+1/2} \exp[-j(n + 1/2)\phi]$ where $\exp[-j(n + 1/2)\phi]$ suggests the Gouy phase shift. Equation (2.2.5) is the general form for a high-order HG mode traveling through an arbitrary ABCD system. For a high-order HG mode with two transverse dimensions, Eq. (2.2.5) can be modified as

$$\begin{aligned}
 u_{n,m}(x_2, y_2, z_2) = & \exp(-jkL) \left(\frac{\omega_{2x}}{\omega_{1x}} \right)^n \left(\frac{\omega_{2y}}{\omega_{1y}} \right)^m \sqrt{\frac{1}{2^{n+m-1} (n+m)! \pi \omega_{1x} \omega_{1y}}} \\
 & \times \left(\frac{1}{A_x + B_x/q_{1x}} \right)^{n+1/2} \left(\frac{1}{A_y + B_y/q_{1y}} \right)^{m+1/2} H_n \left(\frac{\sqrt{2} x_2}{\omega_{2x}} \right) H_m \left(\frac{\sqrt{2} y_2}{\omega_{2y}} \right) \\
 & \times \exp \left(-j \frac{\pi x_2^2}{\lambda_0 q_{2x}} \right) \exp \left(-j \frac{\pi y_2^2}{\lambda_0 q_{2y}} \right), \quad (2.2.6)
 \end{aligned}$$

where the subscript x or y denotes the transverse direction for the corresponding parameter. Without astigmatism, the Gouy phase shift can be given by $\exp[-j(n + m + 1)\phi]$. Since there is induced astigmatism for the light beam propagating via the cylindrical-lens mode converter, the parameters are to be considered separately into the x and y directions.

Furthermore, consider a rotated HG mode passing through an ABCD system such as a cylindrical-lens mode converter as depicted in Fig. 2.2.2, the output beam in Eq. (2.2.6) can be modified as $u_{n,m}(\xi_2, \eta_2, z_1)$, where the coordinates (ξ, η) for the optical beam follow the relation:

$$\begin{cases} \xi_2 = x_2 \cos \theta + y_2 \sin \theta \\ \eta_2 = x_2 (-\sin \theta) + y_2 \cos \theta \end{cases} \quad (2.2.7)$$

It can be seen that the formulae in Eq. (2.2.7) are the general expressions for the

coordinates (x_2, y_2) of a point to be rotated by an angle θ . Substitute Eq. (2.2.6) and Eq. (2.2.7) into the generating function for the Hermite polynomial, after cumbersome algebra (Appendix B), the output beam for the rotated HG mode can be derived to be

$$u_{n,m}(\xi_2, \eta_2, z_2) = \sum_{s=0}^N d_{s-\frac{N}{2}, n-\frac{N}{2}}^{\frac{N}{2}}(\theta) u_{s, N-s}(x_2, y_2, z_2), \quad (2.2.8)$$

where $N = m + n$, θ represents the rotated angle of the input mode relative to the principal axes of the cylindrical lenses as shown in Fig. 2.2.2, and $d_{s-\frac{N}{2}, n-\frac{N}{2}}^{\frac{N}{2}}(\theta)$ is just the Wigner d -coefficient in Eq. (2.1.12). Equation (2.2.8) reveals that the rotated HG mode can be expanded by a set of high-order HG modes without rotation and with the distribution weighting of the Wigner d -coefficient. It can be seen that Eq. (2.2.8) has the similar form to Eq. (2.1.11), which implies that one could find an appropriate ABCD system for the realization of the conversion between the HG and the LG modes presented in section 2.1.1. In this thesis, we choose the cylindrical-lens mode converter as our equipment for the beam transformation. As a result, we define the ABCD system in the range between the the gain medium ($z=0$) and the observation plane at z_2 . Based on the arrangement for the cylindrical-lens mode converter as mentioned in section 2.2.1, we have successfully performed the beam transformation between the HG and the LG modes in Fig. 2.2.3. Figure 2.2.3(a)-2.2.3(e) show the far-field patterns obtained by passing a rotated HG mode at various angles with indices $(n, m) = (15, 10)$ through the cylindrical-lens mode converter. Fig. 2.2.3(a')-2.2.3(e') display the experimental results of the far-field patterns generated by inputting the rotated HG mode at different angles with indices $(n, m) = (55, 3)$. It can be informed that the experimental observations shown in Fig. 2.2.3 are in good

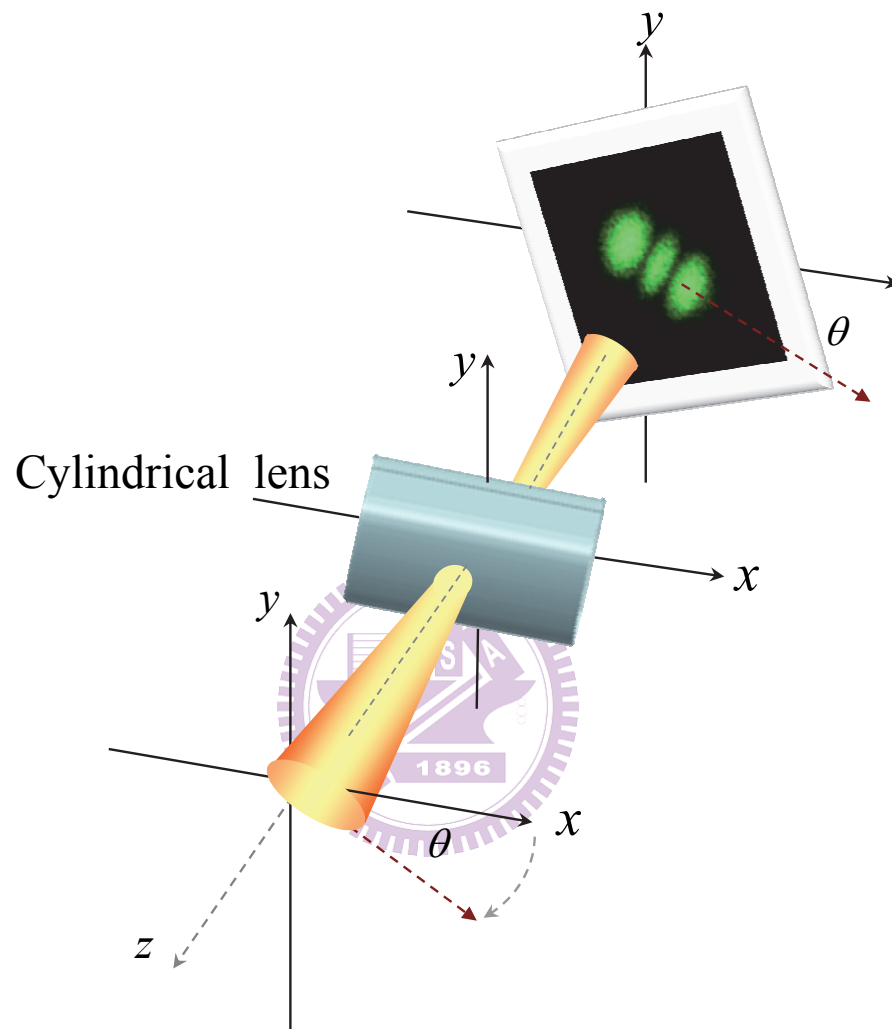


Fig. 2.2.2 Experimental scheme for a rotated HG mode propagating through a cylindrical-lens mode converter.

agreement with the theoretical results illustrated in Fig. 2.1.2 associated with the eigenstates to the coupled HO. The quantum states are successfully realized when we find a corresponding optical system. Therefore, the investigation suggests the possibility for the manifestation of the beam transformation between localized optical patterns that related to the quantum coherent states discussed in section 2.1.2.

2.2.3 Coherent Modes: Single Periodic Orbits

In this section, we first discuss the wave functions of the optical coherent wave emitted from a large-Fresnel-number spherical laser resonator. Furthermore, we exploit the the general Huygens integral mentioned in previous section to explore the transformation of the spatial morphologies from the optical Lissajous states to the optical trochoidal states. We further employ the optical Lissajous modes and a cylindrical-lens mode converter to realize the spatial transformation. The present investigation manifests an intriguing non-classical behavior of the coherent optical waves.

The optical coherent wave is a superposition of degenerate laser modes and can provide a general description for a laser system exhibiting ray behavior. One aim of our work is to explore the spatial geometry of the optical coherent wave related to the HG and LG modes. The free-space wave function of a HG mode with longitudinal index n_3 , transverse indices n_1 and n_2 in Cartesian coordinates (x, y, z) is given by [9]

$$\Phi_{n_1, n_2, n_3}^{(HG)}(x, y, z) = \Phi_{n_1, n_2}^{(HG)}(x, y, z) e^{i(n_1 + n_2 + 1)\theta_G(z)} e^{-i\zeta_{n_1, n_2, n_3}(x, y, z)}, \quad (2.2.9)$$

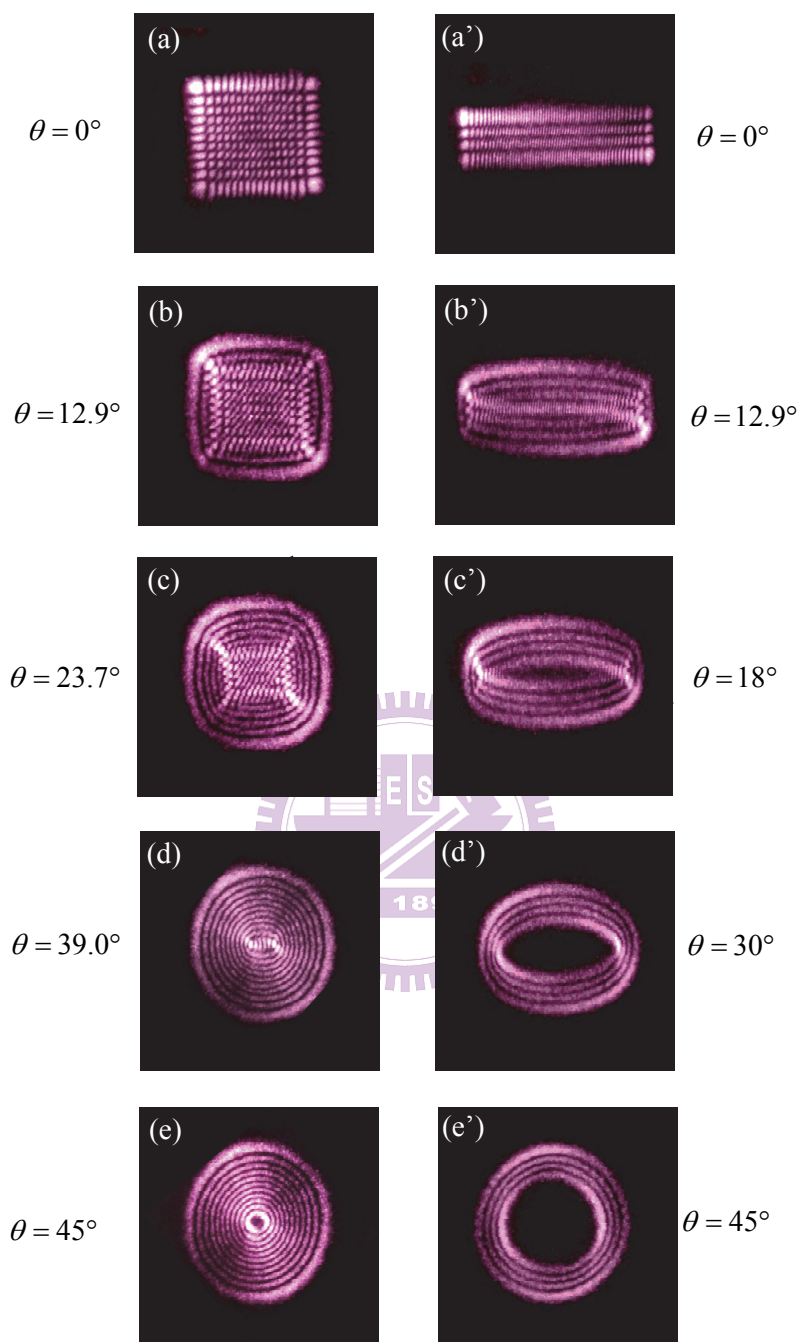


Fig. 2.2.3 Output far-field patterns for the rotated HG modes at various angles passing through the cylindrical-lens mode converter; (a)-(e) transformed far-field patterns for a rotated HG mode of indices $(n, m) = (15, 10)$; (a')-(e') transformed far-field patterns for a rotated HG mode of indices $(n, m) = (55, 3)$.

where

$$\Phi_{n_1, n_2}^{(HG)}(x, y, z) = \frac{1}{\sqrt{2^{n_1+n_2} \pi n_1! n_2!}} \frac{\sqrt{2}}{w(z)} \times H_{n_1} \left(\frac{\sqrt{2} x}{w(z)} \right) H_{n_2} \left(\frac{\sqrt{2} y}{w(z)} \right) \exp \left[-\frac{x^2 + y^2}{w(z)^2} \right], \quad (2.2.10)$$

$w(z) = w_0 \sqrt{1 + (z/z_R)^2}$, $\zeta_{n_1, n_2, n_3}(x, y, z) = k_{n_1, n_2, n_3} z \left[1 + (x^2 + y^2)/2(z^2 + z_R^2) \right]$, w_0 is the beam radius at the waist, and $z_R = \pi w_0^2 / \lambda$ is the Rayleigh range, $H_n(\cdot)$ are the Hermite polynomials, k_{n_1, n_2, n_3} is the wave number, and $\theta_G(z) = \tan^{-1}(z/z_R)$ is the Gouy phase. In terms of the effective length L , the wave number k_{n_1, n_2, n_3} is given by

$$k_{n_1, n_2, n_3} L = \pi \left[n_3 + (n_1 + n_2) (\Delta f_T / \Delta f_L) \right], \quad (2.2.11)$$

where $\Delta f_L = c/2L$ is the longitudinal mode spacing and Δf_T is the transverse mode spacing. When the ratio $\Delta f_T / \Delta f_L$ is close to a simple fractional, it has been evidenced that the longitudinal-transverse coupling usually leads to the frequency locking among different transverse modes with the help of different longitudinal orders [11]. Consequently, when the mode-spacing ratio $\Delta f_T / \Delta f_L$ is locked to a rational number P/Q , the group of the HG modes $\Phi_{n_1+pk, n_2 \mp qk, n_3+sk}^{(HG)}$ with $k = \dots, -2, -1, 0, 1, 2, \dots$ can be found to constitute a family of frequency degenerate states, provided that the given integers (p, q, s) obey the equation $s + (p \mp q)(P/Q) = 0$. For convenience, the integers p and q are taken to be positive. The equation $s + (p \mp q)(P/Q) = 0$ indicates that $p \mp q$ needs to be an integral multiple of Q , i.e. $p \mp q = K \times Q$, where K is an integer.

With the coherent-state representation presented in section 2.1.2 and Ref. [11], the optical coherent wave formed by the family of the degenerated HG modes

$\Phi_{n_1+pk, n_2 \mp qk, n_3+sk}^{(HG)}$ can be expressed as

$$\left| \Psi_{\bar{n}_1, \bar{n}_2, \bar{n}_3}^{\pm p, q, s}(\gamma) \right\rangle = \frac{1}{\sqrt{2\pi\sqrt{\bar{n}_1\bar{n}_2}}} \sum_{k=-M}^M e^{ik\gamma} e^{\frac{(pk)^2}{4\bar{n}_1}} e^{\frac{(qk)^2}{4\bar{n}_2}} \left| \Phi_{\bar{n}_1+pk, \bar{n}_2 \mp qk, \bar{n}_3+sk}^{(HG)} \right\rangle, \quad (2.2.12)$$

where $M = \min\left(\left[2\sqrt{\bar{n}_1}/p\right], \left[2\sqrt{\bar{n}_2}/q\right]\right)$, the parameter $\gamma = p\phi_1 \mp q\phi_2$ is the relative phase between various HG modes at $z = 0$, ϕ_1 and ϕ_2 are the phase factors related to the wave pattern, and \bar{n}_1 , \bar{n}_2 , and \bar{n}_3 are the mean orders. With the expression of Eq. (2.2.9), the HG coherent wave can be expressed as

$$\left| \Psi_{\bar{n}_1, \bar{n}_2, \bar{n}_3}^{\pm p, q, s}(\gamma) \right\rangle = \left| \Psi_{\bar{n}_1, \bar{n}_2}^{\pm p, q}(\gamma) \right\rangle e^{i(\bar{n}_1+\bar{n}_2+1)\theta_G(z)} e^{-i\zeta_{\bar{n}_1, \bar{n}_2, \bar{n}_3}(x, y, z)}, \quad (2.2.13)$$

with

$$\left| \Psi_{\bar{n}_1, \bar{n}_2}^{\pm p, q}(\gamma) \right\rangle = \frac{1}{\sqrt{2\pi\sqrt{\bar{n}_1\bar{n}_2}}} \left[\sum_{k=-M}^M e^{ik\gamma} e^{\frac{(pk)^2}{4\bar{n}_1}} e^{\frac{(qk)^2}{4\bar{n}_2}} \times e^{ik(p \mp q)\theta_G(z)} \left| \Phi_{\bar{n}_1+pk, \bar{n}_2 \mp qk}^{(HG)} \right\rangle \right]. \quad (2.2.14)$$

The wave pattern of the coherent state $\left| \Psi_{\bar{n}_1, \bar{n}_2}^{\pm p, q}(\gamma) \right\rangle$ has been shown to be localized on the Lissajous parametric surface: $x(\vartheta, z) = \text{Re}[X(\vartheta, z)]$; $y(\vartheta, z) = \text{Re}[Y(\vartheta, z)]$, where $X(\vartheta, z) = \sqrt{\bar{n}_1} w(z) e^{i[q\vartheta - \theta_G(z) - \phi_1]}$, $Y(\vartheta, z) = \sqrt{\bar{n}_2} w(z) e^{i[\pm p\vartheta - \theta_G(z) - \phi_2]}$, $0 \leq \vartheta \leq 2\pi$ and $-\infty \leq z \leq \infty$. Explicitly, the Lissajous parametric surface is formed by the Lissajous curves with the phase factor varying with the position z . Note that these Lissajous orbits are invariant with respect to changes in the phases ϕ_1 and ϕ_2 , provided that the quantity $\gamma = p\phi_1 \mp q\phi_2$ is conserved modulo 2π .

It had been experimentally realized in optics that a HG mode could be

transformed with cylindrical lenses into an Ince-Gaussian (IG) or a LG mode as shown in section 2.2.2. As discussed above, the coherent states formed by the HG modes represent the quantum Lissajous states that display the spatial morphologies concentrating on the Lissajous figures. The stationary Lissajous states $|\Psi_{\bar{n}_1, \bar{n}_2}^{\pm p, q}(\gamma)\rangle$ have been analogously generated from various degenerate laser cavities for several hundred different (p, q) [11]. It is intriguing to explore the change of the spatial morphology for a Lissajous coherent state passing through cylindrical lenses that transforms each HG component into the corresponding output mode. Here we apply the technique associated with the general Huygens' integral in two transverse dimensions and take the Lissajous coherent waves in Eq. (2.2.13) as the input mode. The general expression for a Lissajous coherent state traveling through an arbitrary ABCD system in terms of the spatial representation hence can hence be given by

$$U_{\bar{n}_1, \bar{n}_2}^{\pm p, q}(x_2, y_2, z_2; \gamma) = \frac{1}{\sqrt{2\pi\sqrt{\bar{n}_1\bar{n}_2}}} \left[\sum_{k=-M}^M e^{ik\gamma} e^{\frac{(pk)^2}{4\bar{n}_1}} e^{\frac{(qk)^2}{4\bar{n}_2}} \times u_{\bar{n}_1+pk, \bar{n}_2\mp qk}(x_2, y_2, z_2) \right], \quad (2.2.15)$$

where $u_{\bar{n}_1+pk, \bar{n}_2\mp qk}(x_2, y_2, z_2)$ is the general form for the HG mode in Eq. (2.2.6), and $U_{\bar{n}_1, \bar{n}_2}^{\pm p, q}(x_2, y_2, z_2; \gamma)$ represents the output coherent wave observed at the plane of z_2 .

Generally, consider a rotated Lissajous laser mode to be transformed via an ABCD system, the Eq. (2.2.15) can be modified as

$$U_{\bar{n}_1, \bar{n}_2}^{\pm p, q}(\xi_2, \eta_2, z_2; \gamma) = \frac{1}{\sqrt{2\pi\sqrt{\bar{n}_1\bar{n}_2}}} \left[\sum_{k=-M}^M e^{ik\gamma} e^{\frac{(pk)^2}{4\bar{n}_1}} e^{\frac{(qk)^2}{4\bar{n}_2}} \times u_{\bar{n}_1+pk, \bar{n}_2\mp qk}(\xi_2, \eta_2, z_2) \right], \quad (2.2.16)$$

where

$$u_{\bar{n}_1+pk, \bar{n}_2 \mp qk}(\xi_2, \eta_2, z_2) = \sum_{s=0}^{N_k} d_{s-\frac{N_k}{2}, \bar{n}_1+pk-\frac{N_k}{2}}^{\frac{N_k}{2}}(\theta) u_{s, N_k-s}(x_2, y_2, z_2), \quad (2.2.17)$$

with $N_k = \bar{n}_1 + \bar{n}_2 + pk \mp qk$. Eq. (2.2.17) comes from Eq. (2.2.8) which demonstrates the transformation of a rotated HG modes traveling through an ABCD system. It can be seen that Eq. (2.2.16) possesses the same mathematical interpretation as Eq. (2.1.24). Therefore, we can find a corresponding ABCD system to realize the transformational relation for the quantum coherent states illustrated in section 2.1.2. Employing the arrangement for the cylindrical-lens mode converter as mentioned in section 2.2.1, we have successfully demonstrated the continuous transformation between the Lissajous and the trochoidal curves with the input of a rotated Lissajous laser mode at various angles. Figure 2.2.4 displays the experimental results of the the output beam $|U_{\bar{n}_1, \bar{n}_2}^{\pm p, q}(x_2, y_2, z_2; \gamma)|^2$ generated by passing the Lissajous laser mode of positive sign through the cylindrical lenses. The spatial morphologies of the laser modes can be clearly seen to be transformed from Lissajous figures to hypetrochoidal curves. Figures 2.2.5 shows the experimental results of the output beam $|U_{\bar{n}_1, \bar{n}_2}^{\pm p, q}(x_2, y_2, z_2; \gamma)|^2$ by passing the Lissajous laser mode of negative sign through the cylindrical lenses. Instead of hypetrochoids, the spatial morphologies of the laser modes are transformed from Lissajous figures to epitrochoidal curves due to the negative sign of ω_1/ω_2 . It is evident that the experimental observations in Fig. 2.2.4 and Fig. 2.2.5 are in excellent agreement with the theoretical results demonstrated in Fig. 2.1.6 and 2.1.7, respectively. The parameter β in Eq. (2.1.24) and the rotation angle θ in Eq. (2.1.16) are found to obey the relation $\theta = \beta/2$. Moreover, Fig. 2.2.6 exhibits various Lissajous patterns with positive sign and their hypetrochoidal counterparts. Figure 2.2.7 shows several Lissajous patterns with negative sign and their

corresponding epitrochoidal curves.

2.2.4 Coherent Modes : Multiple Periodic Orbits

In section 2.1.3, we have explored the eigenstates for the coupled commensurate HO with the $SU(2)$ algebra and found that the high-order spatial patterns are noticeably concentrated on Lissajous figures and trochoidal curves from single to multiple periodic orbits. In this section, we demonstrate the analogous experimental results corresponding to the multi-trajectory quantum states discussed in section 2.1.3. The three-dimensional (3D) coherent lasing modes with transverse patterns corresponding to single Lissajous figures have been methodically generated in degenerate cavities with a large off-axis tightly focused pumping scheme [11,52]. Here we verified that the 3D coherent lasing waves can be manipulated to form more intricate transverse patterns corresponding to multiple Lissajous orbits as found in the quantum eigenstates of the developed model. The number of the Lissajous orbits in the lasing transverse pattern is experimentally confirmed to be proportional to the pumping spot size. More importantly, the role of the phase factor introduced by the $SU(2)$ coupling interactions can be nicely manifested from the propagating property of the lasing modes. Furthermore, the transformation between the multiple Lissajous orbits and the multiple trochoidal orbits is performed with the cylindrical-lens mode converter. We expect that the findings of controlling lasing transverse modes with spatial patterns to be related to quantum states could open new attractive issues in quantum physics and optical pattern formations.

The experiment mainly consists of a laser resonator, a pumping source, a mode converter and an imaging system as shown in Fig. 2.2.1. The length of the present resonator can be set to form various degenerate cavities in which a resonance

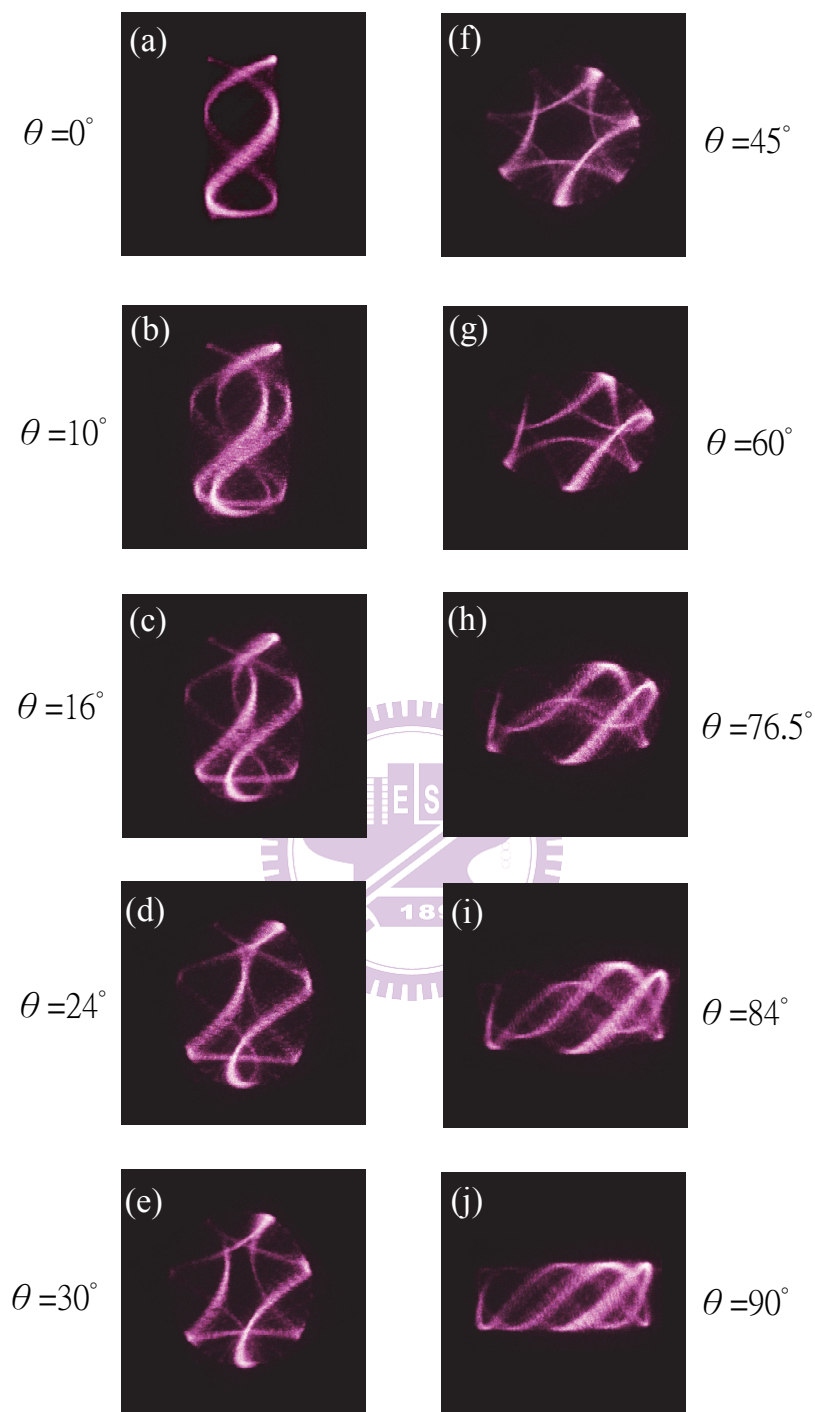


Fig. 2.2.4 Experimental results of the output beam $|U_{\vec{n}_1, \vec{n}_2}^{\pm p, q}(x_2, y_2, z_2; \gamma)|^2$ generated by passing the rotated Lissajous laser mode of positive sign through the cylindrical lenses.

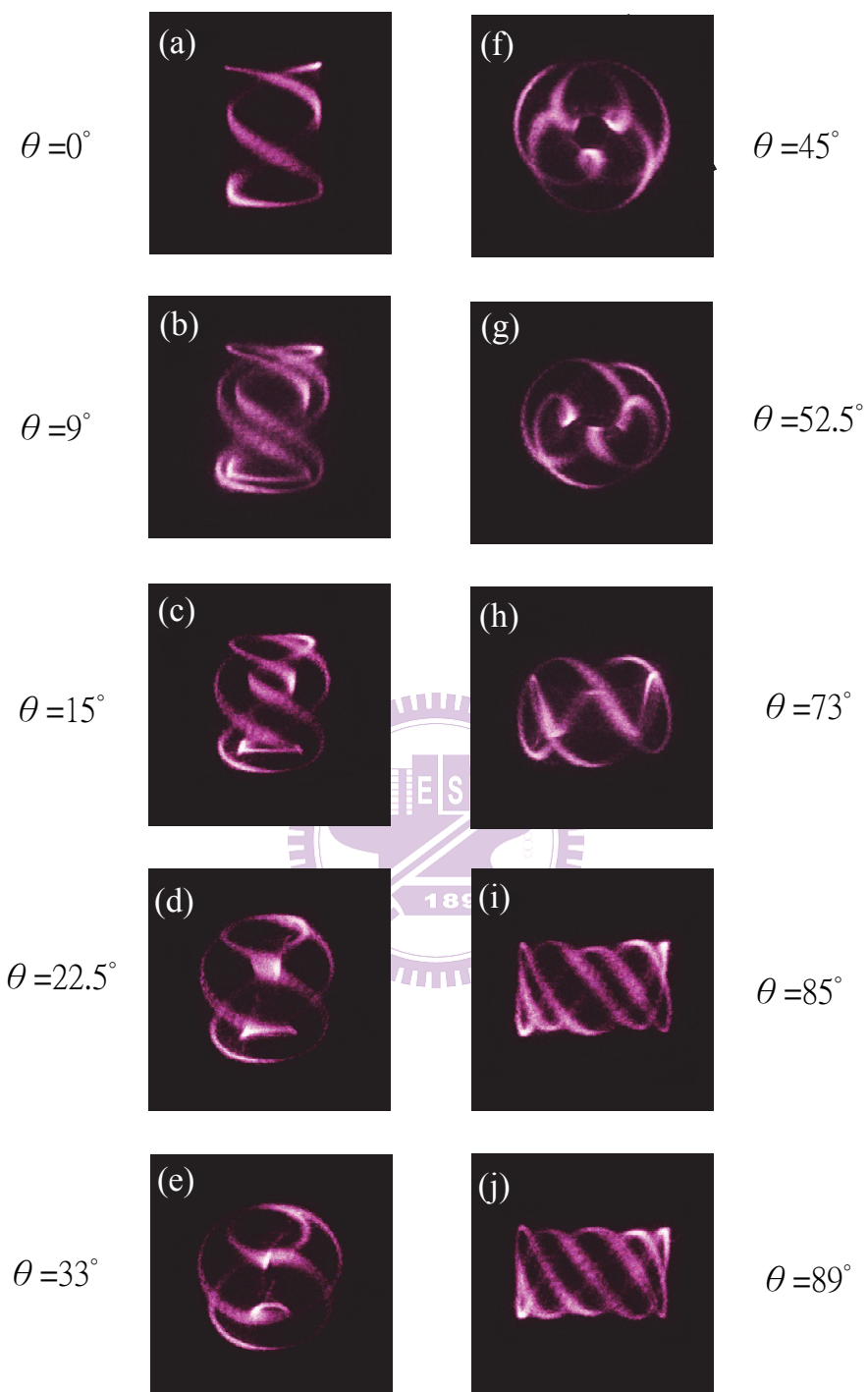


Fig. 2.2.5 Experimental results of the output beam $|U_{\vec{n}_1, \vec{n}_2}^{\pm p, q}(x_2, y_2, z_2; \gamma)|^2$ generated by passing the rotated Lissajous laser mode of negative sign through the cylindrical lenses.

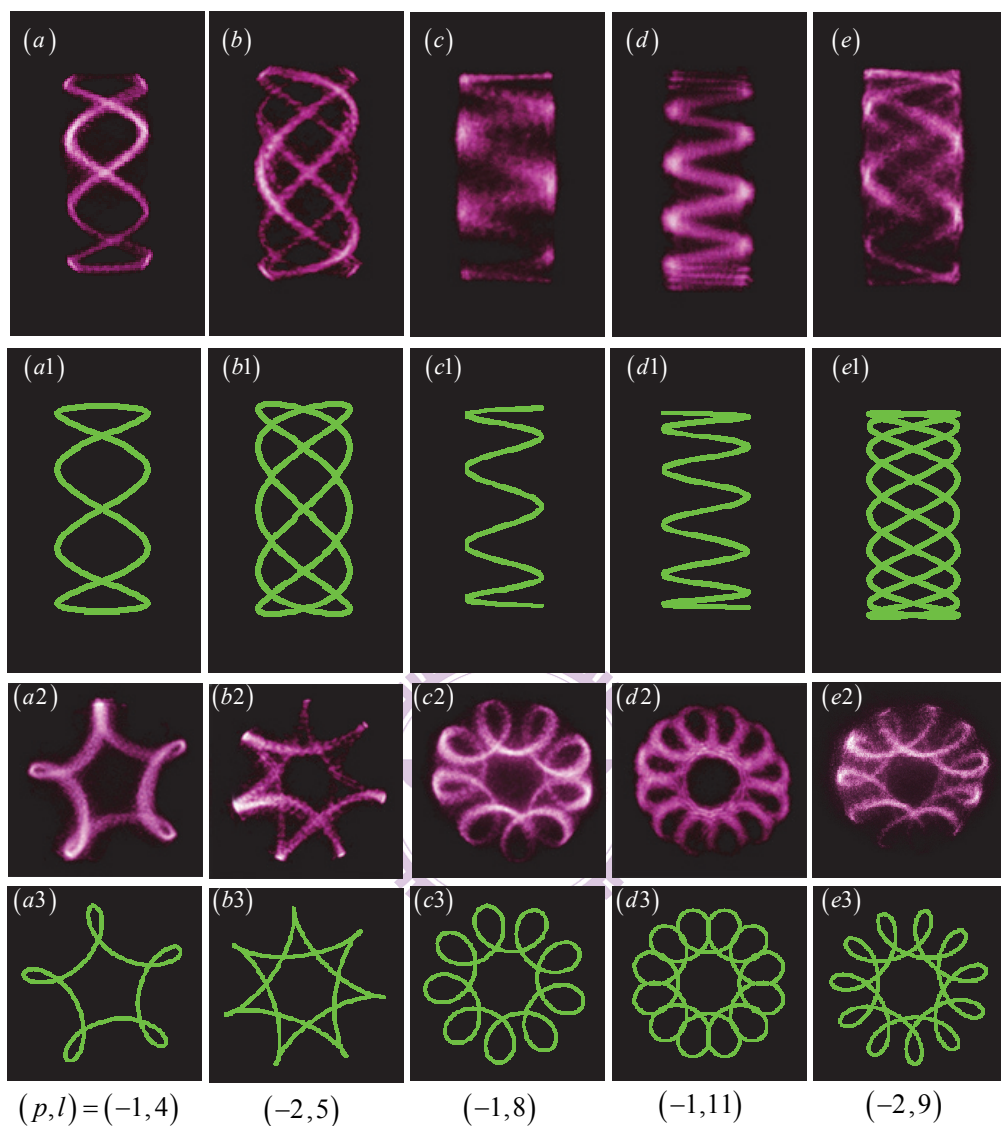


Fig. 2.2.6 (a)-(e) Input Lissajous laser modes. (a1)-(e1) corresponding classical Lissajous curves. (a2)-(e2) Output hypotrochoidal laser modes, (a3)-(e2) corresponding classical hypotrochoidal curves.

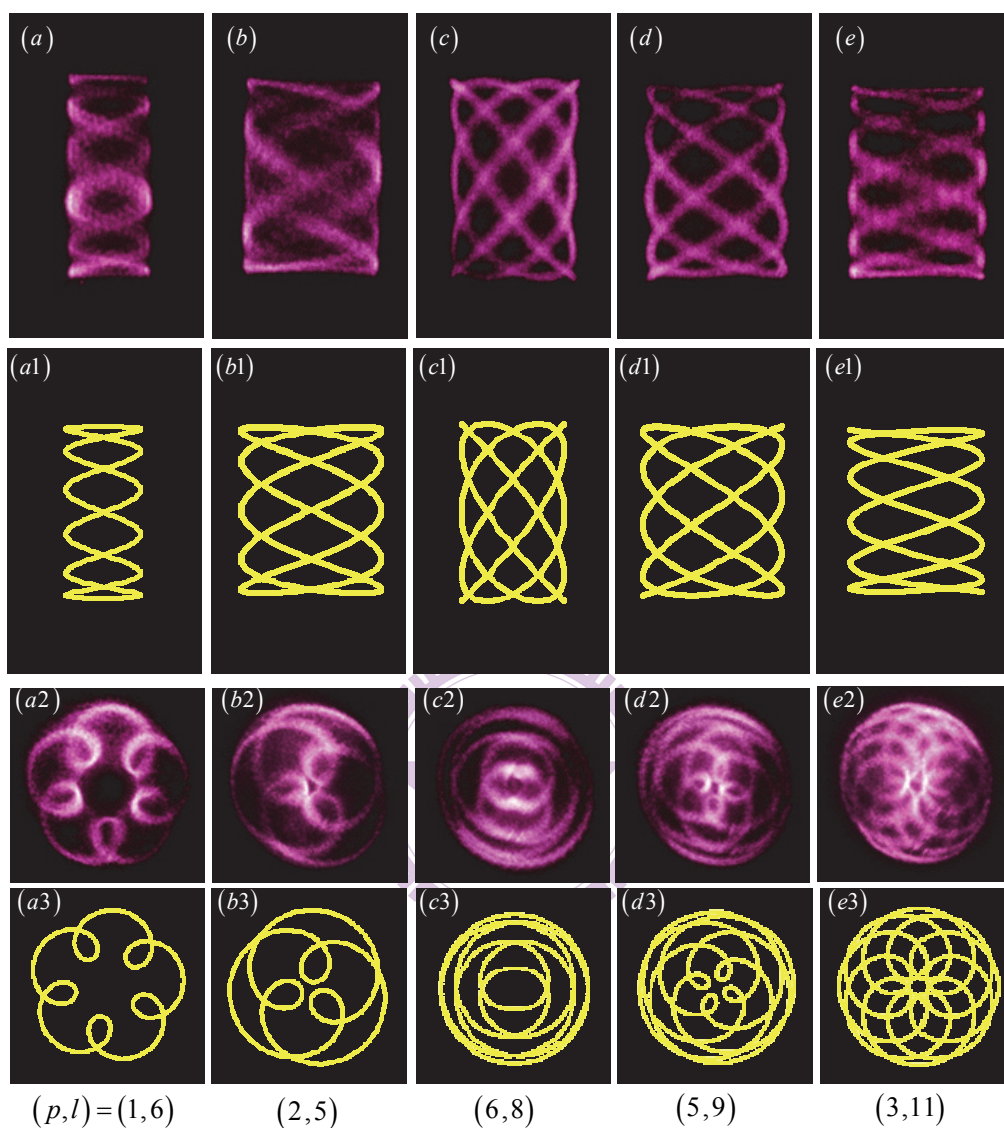


Fig. 2.2.7 (a)-(e) Input Lissajous laser modes. (a1)-(e1) corresponding classical Lissajous curves. (a2)-(e2) Output epitrochoidal laser modes, (a3)-(e3) corresponding classical epitrochoidal curves.

frequency with a high-order transverse mode is equal to another resonance frequency with the fundamental transverse modes [53]. Figures 2.2.8(a)-2.2.8(d) depict the experimental observations for the cavity length L of 7.5 mm with the pumping size to be approximately 50-100 μm . It can be seen that the experimental observations agree very well with the numerical results in Fig. 2.1.9(b1)- 2.1.9(b4), which confirms our theoretical analysis that groups of eigenstates can be excited simultaneously to compose the corresponding Lissajous patterns. Note that the indices (p,q) are determined from the cavity length L and the degenerate conditions [11]. We verify that the number of the Lissajous orbits in the lasing transverse pattern is governed by the spot size of the pumping beam. The larger the pumping size is, the more the number of Lissajous orbits can be effectively excited.

In section 2.1.3, we have demonstrated the effect of the parameter β' on the degree of coupling mechanism and the distribution related to the superposed eigenstates $|m_1, m_2\rangle_{\hat{H}}$ for the states $|n_1 p + \lambda_1, n_2 q + \lambda_2\rangle_{\hat{H}}$. In a laser resonator, the influence of β' corresponds to the amount of astigmatism arising from the off-axis pumping. While β' is chosen, the parameter α' can be realized as the Gouy phase shift [11,54] which differs along the propagation direction for Gaussian beams. As shown in Fig. 2.2.9, the transverse patterns of different positions along the propagation direction are visibly consistent with the theoretical results in Fig. 2.1.11 for the evolution of multiple Lissajous orbits. Obviously, a 3D evolutionary parametric surface can be exploited to interpret the transformation of the spatial patterns inside the cavity. The same clarification for single periodic Lissajous figures had been primarily provided [11] to show noticeable localization on the 3D parametric surface by observing the tomographic transverse patterns inside the cavities. Note that Fig. 2.2.9(a1)-2.2.9(a5), and Fig. 2.2.9(b1)-2.2.9(b5) are generated with off-axis pumping

$(\Delta x, \Delta y) = (0.21 \text{ mm}, 0.10 \text{ mm})$, and $(\Delta x, \Delta y) = (0.57 \text{ mm}, 0.10 \text{ mm})$, where $(\Delta x, \Delta y)$ are measured relative to the optical axis of the laser cavity and an objective lens is employed to reimage the near-field patterns on the screen. In Fig. 2.2.10(a)-2.2.10(d), the far-field patterns are observed at $L=9.0 \text{ mm}$, $L=4.9 \text{ mm}$, $L=6.1 \text{ mm}$, and $L=7.4 \text{ mm}$, respectively. Moreover, Fig. 2.2.11(a1)-2.2.11(a5) show the transverse patterns along the propagation direction of $(p, q) = (3, 2)$ in Fig. 2.2.10(a). The good agreement with the theoretical results presented in Fig. 2.1.15 and Fig. 2.1.16 suggests that our quantum operator model of the coupled commensurate HO is applicable to the ubiquitous laser modes.

In previous discussion, we have successfully generated the multiple Lissajous orbits with a large-Fresnel-number spherical laser resonator to analogously explore the eigenstates to the coupled commensurate HO as presented in section 2.1.3. Here we employ the cylindrical-lens mode converter to transform the obtained multiple Lissajous orbits and to reconstruct the relation in Fig. 2.1.17. The field distribution for the output beam can be obtained from the expression in Eq. (2.1.33):

$$U_{\bar{n}_1, \bar{n}_2, \lambda_1, \lambda_2}^{\pm p, q}(\xi_2, \eta_2, z_2; \gamma) = e^{iM\alpha'/2} \left[\sum_{n_1=0}^M e^{-in_1\alpha'} d_{n_1-M/2, m_1-M/2}^{M/2}(\beta') \right. \\ \left. \times u_{\bar{n}_1+n_1p+\lambda_1, \bar{n}_2+n_2q+\lambda_2}(\xi_2, \eta_2, z_2) \right], \quad (2.2.18)$$

where

$$u_{\bar{n}_1+n_1p+\lambda_1, \bar{n}_2+n_2q+\lambda_2}(\xi_2, \eta_2, z_2) = \sum_{s=0}^N d_{s-\frac{N}{2}, \bar{n}_1+n_1p+\lambda_1-\frac{N}{2}}^{\frac{N}{2}}(\theta) u_{s, N-s}(x_2, y_2, z_2), \quad (2.2.19)$$

with $M = n_1 + n_2$ and $N = \bar{n}_1 + n_1p + \lambda_1, \bar{n}_2 + n_2q + \lambda_2$. Figure 2.2.12 shows the experimental observation of the multiple Lissajous orbits and their trochoidal counterparts. Figure 2.2.12(a') displays the epitrochoidal orbits transformed from Fig.

2.2.12(a) with the negative sign of $\omega_1/\omega_2 = -1/2$. Fig. 2.2.12(b'), Fig. 2.2.12(c'), and Fig. 2.2.12(d') exhibit the multiple hypotrochoids corresponding to the multiple Lissajous orbits in Fig. 2.2.12 (b), Fig. 2.2.12(c), and Fig. 2.2.12(d) with the positive sign of $\omega_1/\omega_2 = 1/3$, $\omega_1/\omega_2 = 2/5$, and $\omega_1/\omega_2 = 1/4$, respectively.



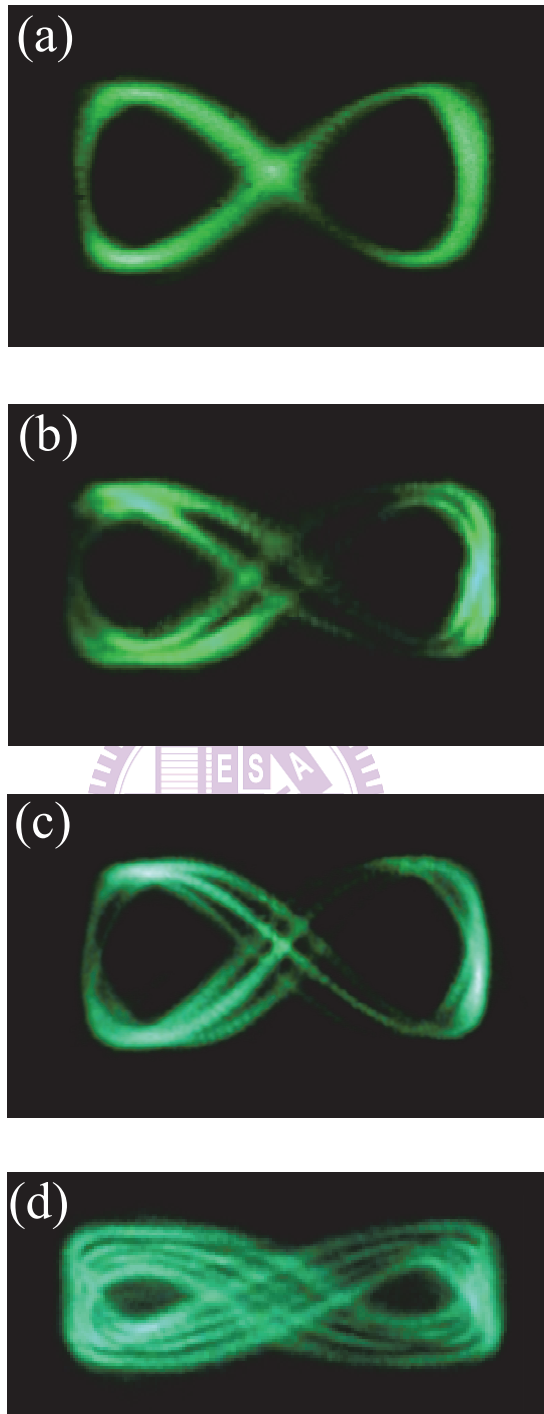


Fig. 2.2.8 Experimental far-field patterns corresponded to the numerical results in Fig. 2.1.9(b1)-2.1.9(b4).

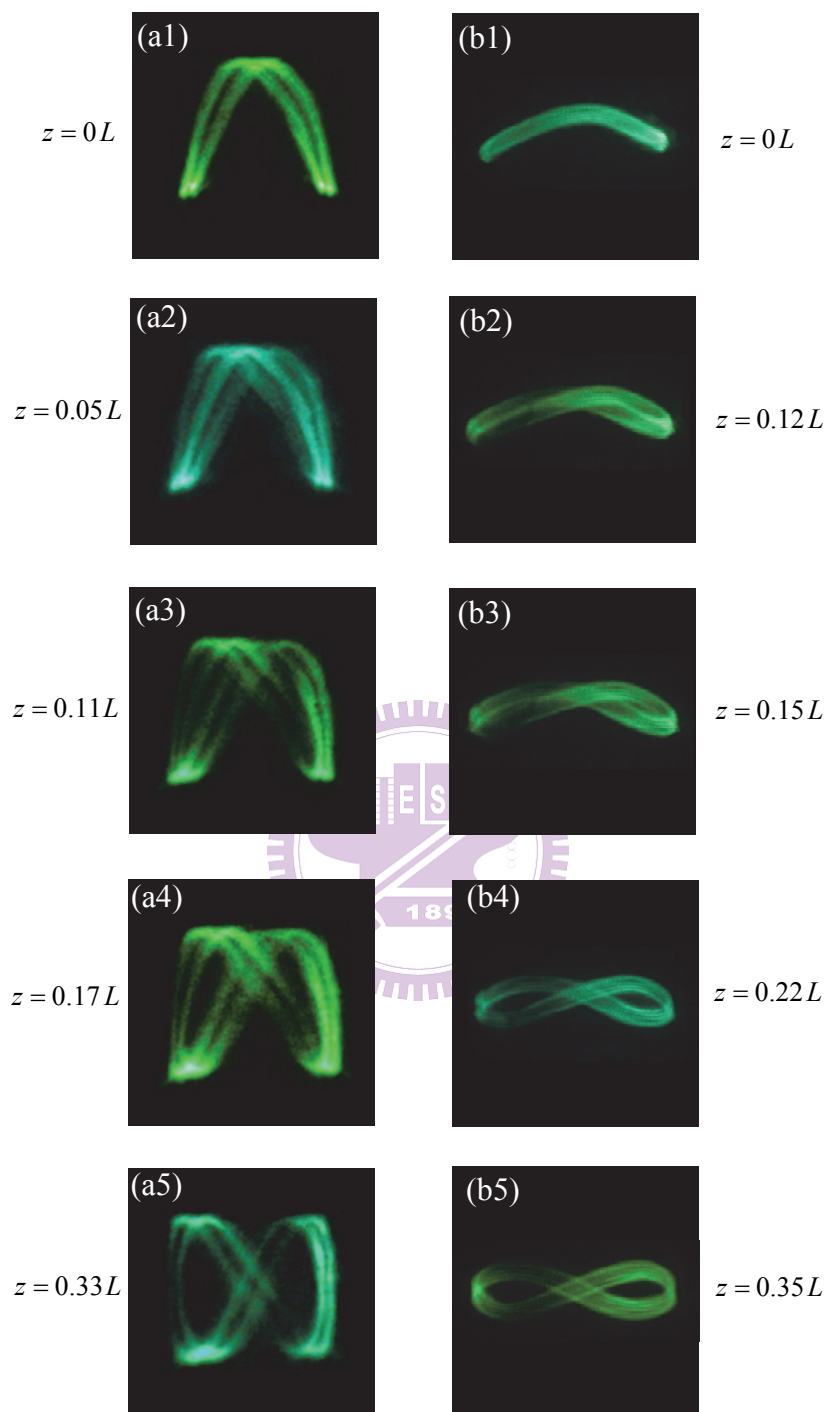


Fig. 2.2.9 Experimental tomographic transverse patterns observed along the propagation direction from the beam waist; (a1)-(a5) $(\Delta x, \Delta y) = (0.21 \text{ mm}, 0.10 \text{ mm})$; (b1)-(b5) $(\Delta x, \Delta y) = (0.57 \text{ mm}, 0.10 \text{ mm})$.

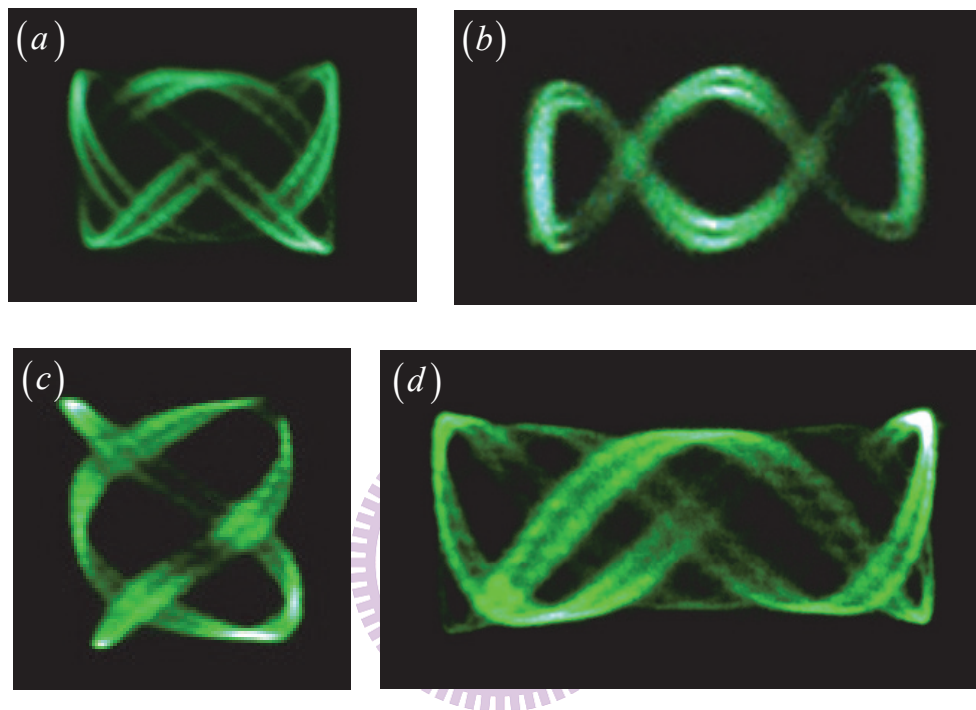


Fig. 2.2.10 Experimental results corresponded to the theoretical analysis. Detailed description of the parameters; see text.

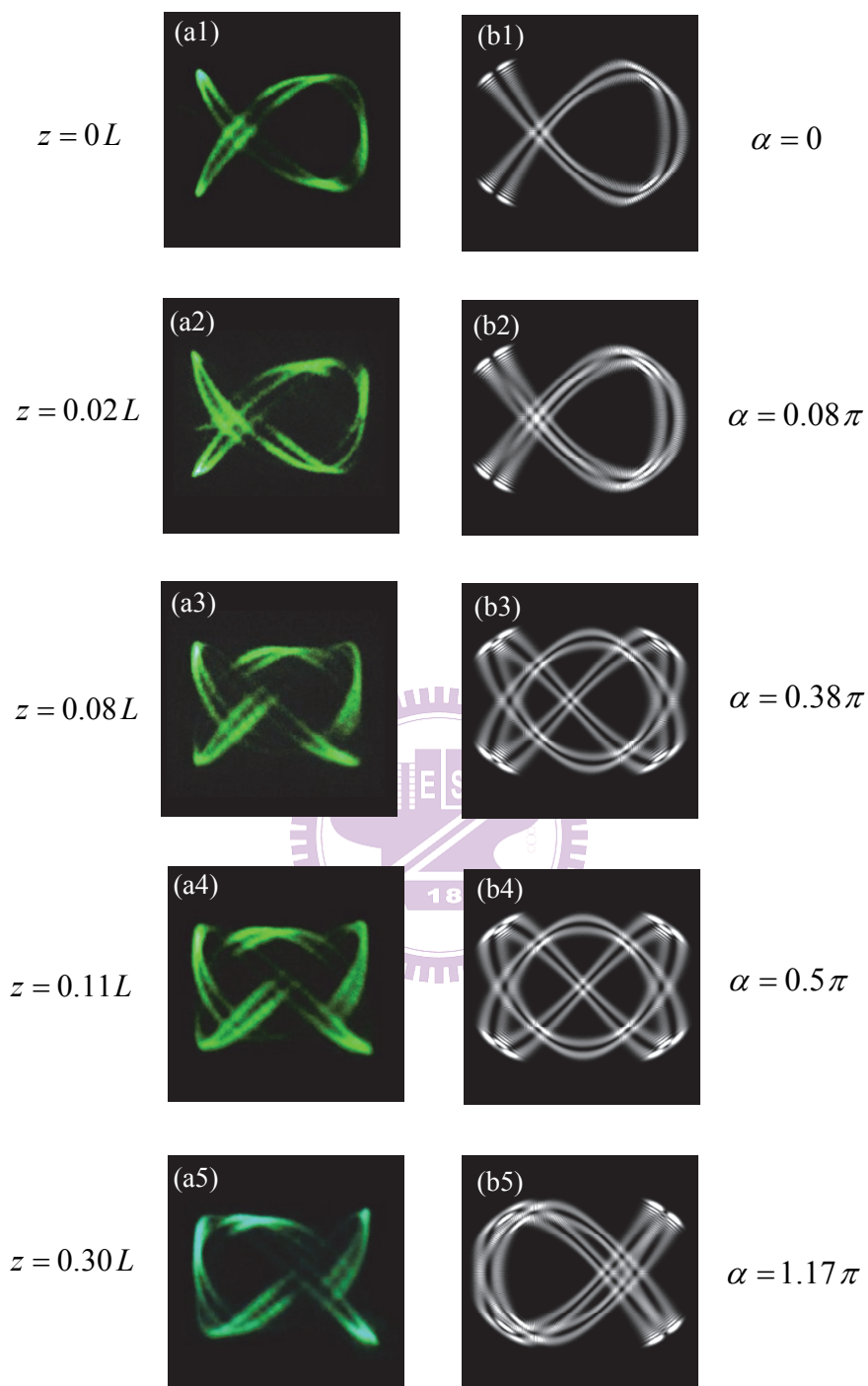


Fig. 2.2.11 (a1)-(a5) Experimental tomographic transverse patterns observed along the propagation direction from the beam waist for $(p, q) = (3, 2)$. (b1)-(b5) Corresponding numerical calculations according to Eq. 2.1.31.

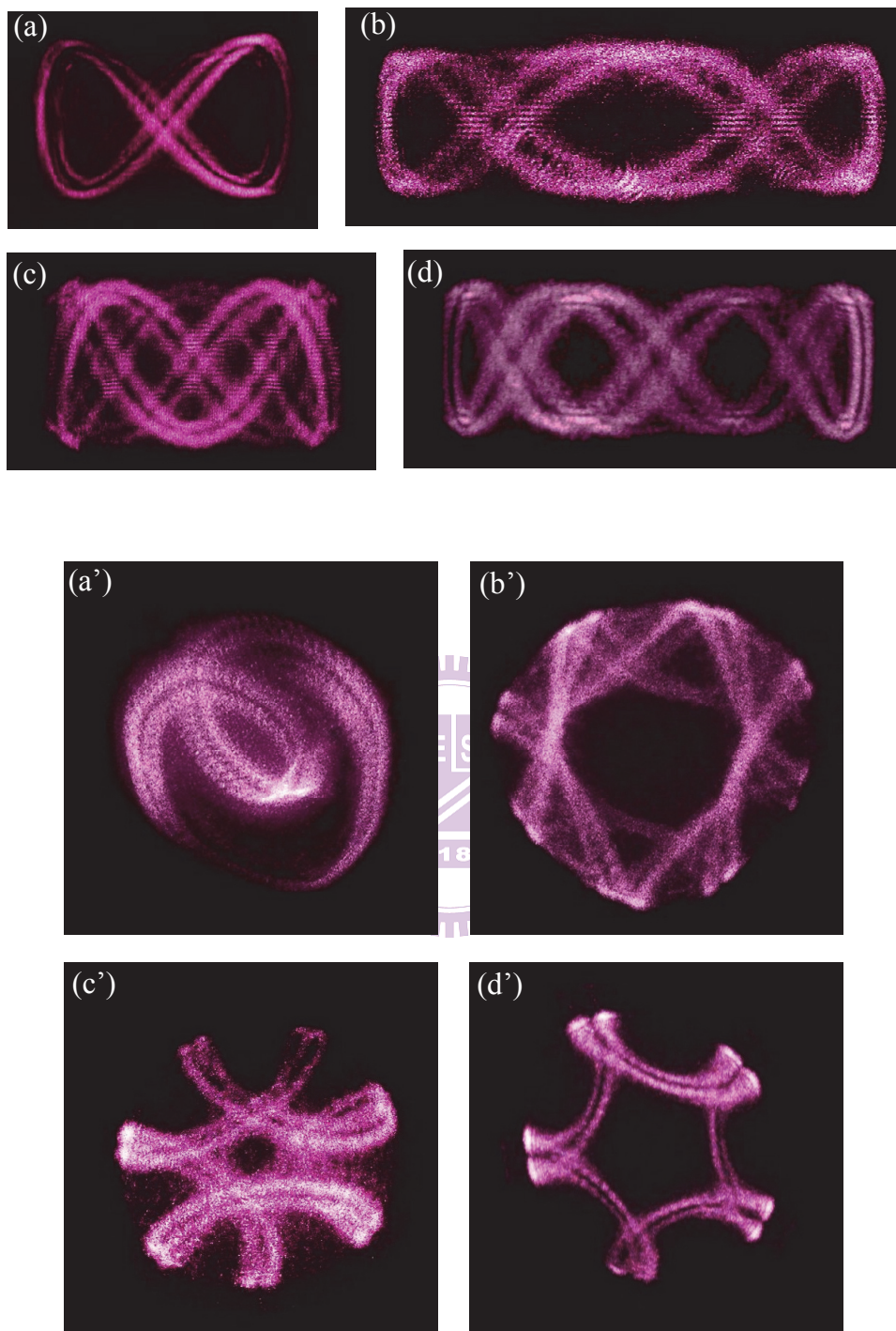


Fig. 2.2.12 (a)-(d) Input multiple Lissajous laser modes. (a')-(d') Output multiple trochoidal laser modes. For detailed descriptions for the parameters, see the text.

2.3 Extension Topic : Generation of Optical Vortex Array

2.3.1 Introduction

In recent decades, optical vortices (OVs) characterized by their distinct features [55] have gained increasing importance in the study of singular optics [56], light and matter interaction [55,57,58], and quantum optics [59]. Since an OV is defined as the phase singularity with vanishing intensity of a helical-phased light beam, the azimuthally circulated phase term implies the orbital angular momentum (OAM) carried by the light beam [60]. For practical interest, the characteristics associated with the OAM inspire great applications on optical tweezers [55,57,58], optical testing [61], image processing [62,63], quantum entanglement [59], and nonlinear optics [64].

Several approaches have been adopted to generate a single OV, such as mode conversions by astigmatic lenses [64,65], spiral phase plates [66], computer generated holograms [67], and optical wedges [68]. Since Hermite-Gaussian (HG) modes can be emitted by most laser cavities and are well-known eigenstates for the 2D quantum harmonic oscillator [9], via the mode conversion, a HG mode has been widely used to create a single OV [65-67] hold by a traveling-wave Laguerre Gaussian (LG) mode features azimuthally phased term $\exp(il\phi)$, where l is known as the topological charge of the vortex. The transformational relation has also been confirmed theoretically by using a Fresnel integral [15] or quantum operators connected the two complete sets of HG and LG states [69].

Aside from an isolated OV, a network of OVs can be created by means of interferometry and lead to a novel type of vortex structure. For instance, intriguing manifestations were shown corresponding to the two-dimensional (2D) optical vortex

array [70] and 3D topology of optical vortex lines [71] by superposing several plane waves. Exploiting a thin-slice solid state laser, [72] demonstrated the generation of vortex array beams by the interference of emitted Ince-Gaussian modes. Distinguished from an isolated OV, optical vortex array related to a network of vortices is especially useful in optical metrology [73], microlithography [74], quantum processing [59], micro-optomechanical pumps manipulation [75], and investigating nonlinear propagation of array of singularities [76].

In this section, a novel method is carried out to produce the optical vortex array by the transformation of a standing-wave LG mode (the so-called “*flower-like*” [77] LG mode). Generation of the flower-like LG modes has been provided experimentally by utilizing a large-aperture CO₂ laser [78], a solid-state laser cavity compounded of nonlinear medium [77,79,80], and a vertical-cavity surface-emitting semiconductor laser [81]. Unlike a traveling-wave LG mode, a flower-like LG mode, formed by coherent superposition of a pair of traveling-wave ones that carry the same topological charges while counter rotational wave fronts, possesses no OV and has been concerned especially in the study of pattern formation [77,79-81]. Therefore, it is fascinating and practical to raise the issue for the creation of optical vortex array by the use of the flower-like LG modes. To illustrate the feasibility, we verify firstly that a flower-like LG mode can be transformed from a set of “*crisscrossed*” HG modes theoretically. The optical vortex array is shown to be located at the cross section of the crisscrossed HG modes established by coherent superposition of a TEM_{*n,m*} mode and a TEM_{*m,n*} mode with well-defined relative phase α , where (*n,m*) designate the transverse indices in x-y directions. Since the transformational relation has been confirmed to show excellent analogy to the mode conversion of a $\pi/2$ -cylindrical-lens mode converter ($\pi/2$ -CLMC) [69], the investigation enables us to generate the optical vortex array experimentally by transforming the accessible flower-like LG modes

through the $\pi/2$ -CLMC. More importantly, adjustability of the relative phase α is qualitatively displayed in this paper by rotating the mode converter at various angles. In all, we expect the creation and exploration of the vortex light beams in our work may inspirit a more thorough study in the vortex structure and its further applications.

2.3.2 Transformation of Fundamental Laser Modes

HG modes and LG modes are complete orthonormal sets that each can well describe any amplitude distribution by an appropriate complex superposition. Besides, they are eigenmodes that can be emitted by most laser resonators. Due to comprehensive studies and accessibility of the eigenmodes, it can be understood that it is useful to create and investigate the 2D optical vortex array by concerning those well-known eigenmodes. As a result, it may be necessary to provide firstly a brief overview of the eigenmodes and their transformational relationship.

The profile of a HG mode in terms of the Cartesian coordinates (x, y, z) with transverse indices (m, n) under paraxial approximation of the wave equation is given by [74]

$$\Psi_{n,m}^{(HG)}(x, y, z) = \psi_{n,m}^{(HG)}(x, y, z) e^{i(n+m+1)\theta_G(z)} e^{-i\xi(x, y, z)}, \quad (2.3.1)$$

where

$$\psi_{n,m}^{(HG)}(x, y, z) = \frac{C_{n,m}^{(HG)}}{w(z)} e^{-\frac{x^2+y^2}{w(z)^2}} H_n\left(\frac{\sqrt{2}}{w(z)}x\right) H_m\left(\frac{\sqrt{2}}{w(z)}y\right), \quad (2.3.2)$$

with $\xi(x, y, z) = kz \left[1 + (x^2 + y^2)/2(z^2 + z_R^2)\right]$, $C_{n,m}^{(HG)} = (2^{n+m-1} \pi n! m!)^{-1/2}$,

$w(z) = w_0 \sqrt{1 + (z/z_R)^2}$, w_0 is the beam radius at the waist, and $z_R = \pi w_0^2 / \lambda$ is

the Rayleigh range. $H_n(\cdot)$ is the Hermite polynomial of order n , k is the wave

number, and $\theta_G(z) = \tan^{-1}(z/z_R)$ is the Gouy phase. Likewise, the wavefunction of a LG mode characterized by its azimuthal and radial symmetry associated with a helical phase front $e^{il\phi}$ can be written in terms of the cylindrical coordinates (r, ϕ, z) with radial index p and azimuthal index l as [74]

$$\Psi_{p,l}^{(LG)}(r, \phi, z) = \psi_{p,l}^{(LG)}(r, \phi, z) e^{i(2p+|l|+1)\theta_G(z)} e^{-i\xi(r, \phi, z)}, \quad (2.3.3)$$

where

$$\psi_{p,l}^{(LG)}(r, \phi, z) = \frac{C_{p,l}^{(LG)}}{w(z)} (-1)^p \left(\frac{\sqrt{2}r}{w(z)} \right)^{|l|} L_p^{|l|} \left(\frac{2r^2}{w(z)^2} \right) e^{-\frac{r^2}{w(z)^2}} e^{il\phi}, \quad (2.3.4)$$

where $L_p^l(\cdot)$ is the associated Laguerre polynomial of azimuthal index l and radial

index p , $\xi(r, \phi, z) = kz \left[1 + r^2/2(z^2 + z_R^2) \right]$, and

$C_{p,l}^{(LG)} = \sqrt{2p! / [(1 + \delta_{0,l})(p + |l|)! \pi]}$ with $\delta_{0,l} = 1$ for $l = 0$. Note that the azimuthal indices with different sign convention (l and $-l$) denote the equal and opposite topological charge $\pm l\hbar$ of the LG modes which implies the OAM possessed by the light beam.

Most important of all, the conversion of the Gaussian modes, which has been demonstrated and verified in detail by [15,69], can be expressed in the following with a left-right-double arrow “ \Leftrightarrow ” signifying the transformational relation

$$\psi_{p,l}^{(LG)}(r, \phi, z) \Leftrightarrow \psi_{n,m}^{(HG)}(x, y, z), \quad (2.3.5a)$$

$$\psi_{p,-l}^{(LG)}(r, \phi, z) \Leftrightarrow \psi_{m,n}^{(HG)}(x, y, z), \quad (2.3.5b)$$

where $p = \min(n, m)$, $l = m - n$, and the relation $2p + l = n + m$ is hold for the conservation of transverse order under transformation. Explicitly, LG modes of opposite topological charges can be given by the transformation of a HG mode and its

replica rotated at 90 degrees as shown in Eq. (2.3.5). To clarify the results, simplicity is added by using the Poincaré-sphere resemblance [82] since the transformation of the LG and HG modes can be well mapped on the Poincaré-sphere that has been verified to be an effective tool in dealing with the conversion of polarization states [83].

2.3.3 Formation of Optical Vortex Array

To make these formal considerations more meaningful, return to our concern of the 2D optical vortex array. Our goal is to create the OAM state of a network of lattices by superposing two crisscrossed HG modes of the same order N with a well-defined relative phase α . Hence, the wavefunction of the superposed state composed of the HG modes can straightforwardly be written as

$$\Omega_{n,m}(x,y,z,\alpha) = \frac{1}{\sqrt{2}} \left[\psi_{n,m}^{(HG)}(x,y,z) + e^{-i\alpha} \psi_{m,n}^{(HG)}(x,y,z) \right], \quad (2.3.6)$$

where α indicates the relative phase between the crisscrossed HG modes. To determine the OVs, it should be noted that they are defined as the phase singularities where the real and imaginary components of the scalar field $\Omega_{n,m}(x,y,z,\alpha)$ are both zero and possess the characteristic of zero intensity in the vortex core [84,85]. In other words, the resulting vortices are dark points in intersects of the nodal lines corresponding to the respective HG modes of the state $\Omega_{n,m}(x,y,z,\alpha)$ with relative phase α apart from an integral multiple of π . An illustration of $|\Omega_{0,11}(x,y,z,\alpha)|^2$ is depicted in Fig. 2.3.1 with various relative phase α ranging from 0 to 2π and it can be seen the intensity distribution in the cross-section is altered accordingly. Despite this, Fig. 2.3.1 also reveals the nature that $|\Omega_{n,m}(x,y,z,\alpha)|^2$ is repeated within every period of 2π phase shift.

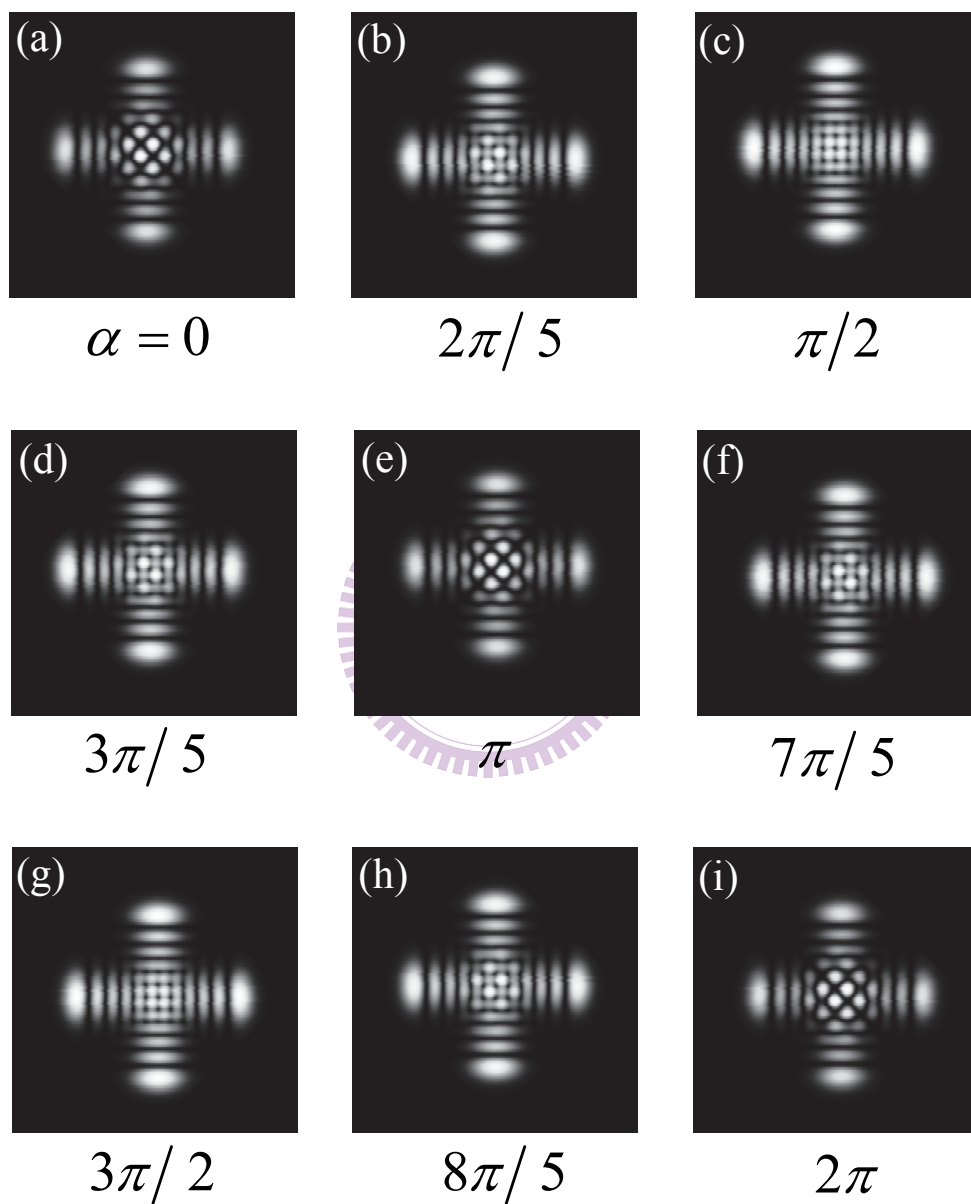
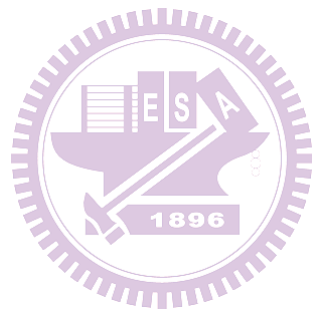


Fig. 2.3.1 Theoretical results of $|\Omega_{0,11}(x, y, z, \alpha)|^2$ of various relative phases.



For comprehensive demonstration of the vortex structure, Fig. 2.3.2 depicts the phase distribution of the state $\Omega_{0,11}(x, y, z, \pi/2)$. Though there are all 11×11 singularities which situate at the crisscrossed positions of the nodal lines as depicted in Fig. 2.3.2(b), the available OVs for practical use of particle trapping with stronger intensity distribution around [55] are estimated at 5×5 in total within the cross section. The enlarged figure of the box region in Fig. 2.3.2(b) is shown in Fig. 2.3.2(c) where the black and red dots mark the vortex positions of counter rotational phase fronts. It is conspicuously illustrated in Fig. 2.3.2(d) by plotting the transverse linear momentum density \mathbf{p}_\perp of a linear polarized light beam [60]

$$\mathbf{p}_\perp = i\omega \frac{\varepsilon_0}{2} (\Omega^* \nabla_\perp \Omega - \Omega \nabla_\perp \Omega^*), \quad (2.3.7)$$

where $\mathbf{p}_\perp = (p_x, p_y)$, $\nabla_\perp = (\partial/\partial x, \partial/\partial y)$, ω relates to the frequency of the light beam and ε_0 represents the permittivity of free space. Note that the vector field \mathbf{p}_\perp has been normalized to $\mathbf{p}_\perp/|\mathbf{p}_\perp|$ for observing the detailed structures. Since the helical wave fronts signify the OAM carried by the light beam, the swirls in Fig. 2.3.2(d) shows the evidence that the superposed state $\Omega_{0,11}(x, y, z, \pi/2)$ certainly form an OAM state associated with the vortex array. From quantum perspective, preparing such superposed OAM states has become an important issue concerning quantum entanglement and quantum information [59]. Thus, it is crucial to arrange feasible experimental techniques for creating and investigating the superposed states.

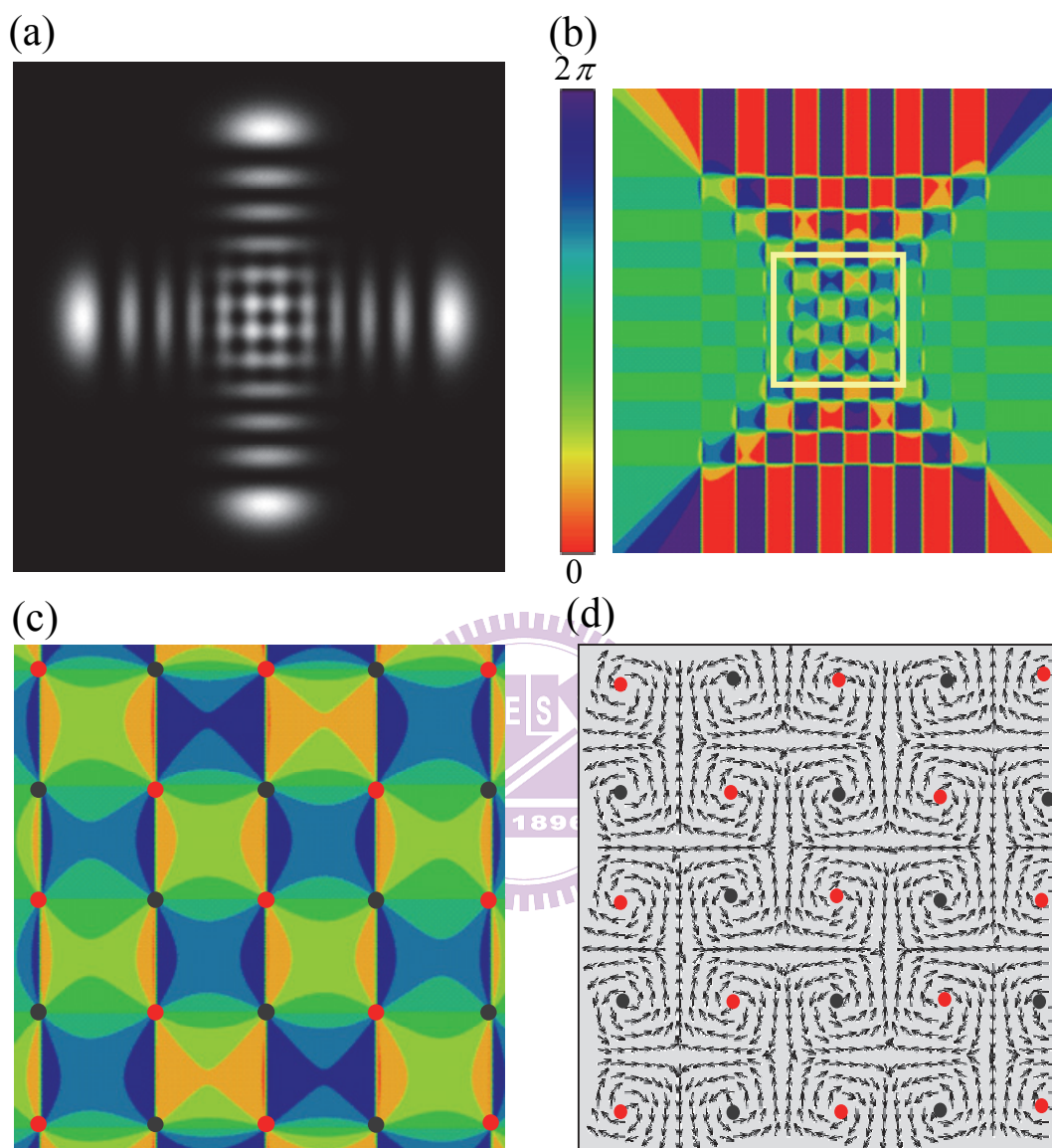


Fig. 2.3.2 (a) Theoretical results of $\Omega_{0,11}(x, y, z, \pi/2)$. (b) Phase distribution of (a). (c) Enlarged figure of the box region in (b). (d) probability current \mathbf{p}_\perp for the box region in (b) of $\Omega_{0,11}(x, y, z, \pi/2)$.

2.3.4 Formation of Flower Laguerre-Gaussian Modes

To develop an available experimental configuration to generate the superposed state $\Omega_{n,m}(x,y,z,\alpha)$, an inspiration is provided by the transformational relation written in Eq. (2.3.5). Likewise, we can obtain a coherent superposed state $\Phi_{p,l}(r,\phi,z,\alpha)$ according to the discussion at the very start, i.e.

$$\Omega_{n,m}(x,y,z,\alpha) \Leftrightarrow \Phi_{p,l}(r,\phi,z,\alpha), \quad (2.3.8)$$

where, with a little algebraic manipulation, the superposed state $\Phi_{p,l}(r,\phi,z,\alpha)$ can be expressed in the form

$$\begin{aligned} \Phi_{p,l}(r,\phi,z,\alpha) = & e^{-\frac{i\alpha}{2}} \frac{C_{p,l}^{(LG)}}{w(z)} (-1)^p \left(\frac{\sqrt{2}r}{w(z)} \right)^{|l|} L_p^{|l|} \left(\frac{2r^2}{w(z)^2} \right) e^{-\frac{r^2}{w(z)^2}} \\ & \times \cos \left[l \left(\phi + \frac{\alpha}{2l} \right) \right]. \end{aligned} \quad (2.3.9)$$

It therefore appears that a new family of superposed state $\Phi_{p,l}(r,\phi,z,\alpha)$ is established and can be decomposed into two LG modes of opposite topological charges $\pm l$ with identical relative phase α . Compared to the traveling-wave LG mode in Eq. (2.3.4), the expression explicitly shows distinct intensity distribution of $\cos \left[l \left(\phi + \alpha / 2l \right) \right]$ in azimuthal angle which forms the flower-like [77] LG mode of $2l$ nodes in azimuthal and possess no OAM at all. Besides, the intensity distribution of $\Phi_{p,l}(r,\phi,z,\alpha)$ can be seen to rotate with its profile remains the same followed by the variation of α as depicted in Fig. 2.3.3 of a specific case $(p,l)=(0,11)$ related to $\Omega_{0,11}(x,y,z,\alpha)$. It is worth to mention that, with the help of the arrows illustrated

in Fig. 2.3.3, the state $\Phi_{0,11}(r, \phi, z, \alpha)$ is visualized obviously to rotate by an angle $\alpha/2l = 2\pi/22$ through a period of 2π phase retardation. The investigation reveals the fact that the superposed state $\Omega_{n,m}(x, y, z, \alpha)$ can be repeated while the flower-like LG mode $\Phi_{p,l}(r, \phi, z, \alpha)$ rotates by $2\pi/2l$ which is exactly the angle between consecutive peaks. Experimentally, this result provides the key to qualitatively controlling the relative phase α between the crisscrossed HG modes that will be presented in the next section.

2.3.5 Experimental Setup

The experimental configuration can be separated mainly into three parts according to particular purposes as depicted in Fig. 2.3.4. The microchip solid state laser cavity presented in Fig. 2.3.4(a) is utilized to generate the flower-like LG mode discussed on the above as an input mode to be transformed via the $\pi/2$ -CLMC. The second part at the external cavity is consisted of a non-spherical lens and the $\pi/2$ -CLMC to convert the emitted LG mode into the crisscrossed HG modes as shown in Fig. 2.3.4(b). The last part in Fig. 2.3.4(c) corresponds apparently to the detection scheme. Furthermore, detailed experimental arrangements are provided in the following.

It can be seen that the laser resonator is composed of a gain medium and a spherical mirror. The laser medium is an a-cut 2.0-at. % Nd:YVO4 crystal with a length of 2 mm and the cross section $3 \times 3 \text{ mm}^2$. One side of the Nd:YVO4 crystal is coated for partial reflection at 1064 nm and the other is for antireflection at 1064 nm. The radius of curvature of the cavity mirror is $R = 25 \text{ cm}$ and its reflectivity is 97% at 1064 nm. The pump source is an 808 nm fiber-coupled laser diode with pump core of 100 μm in radius, a numerical aperture of 0.16, and a maximum output power of 1 W.

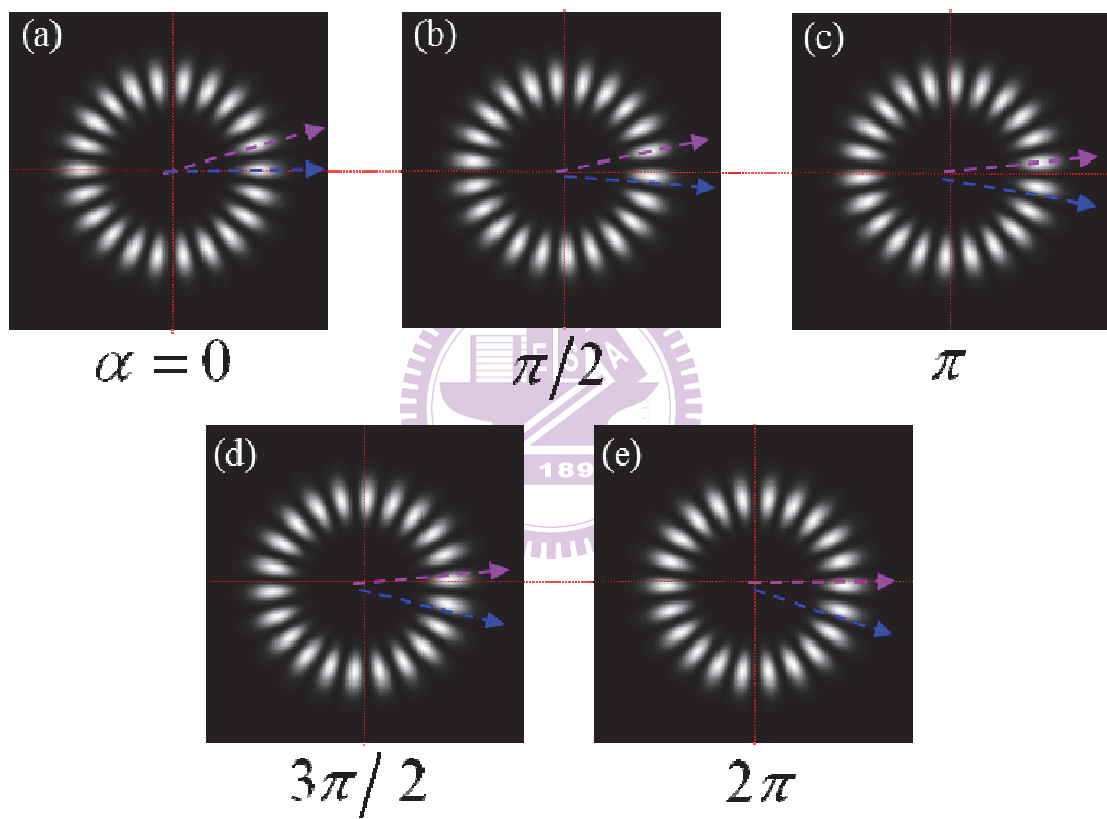
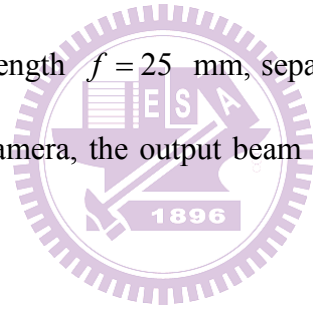


Fig. 2.3.3 Theoretical results of superposed state $|\Phi_{0,11}(r, \phi, z, \alpha)|^2$ of various relative phases.

A focusing lens with focal length of 20 mm and 90 % coupling efficiency is used to reimage the pump beam into the laser crystal. To produce a high-order flower-like LG mode, which are processed from the astigmatism and imperfection dominated by the cylindrical symmetric laser cavity, the valid key point is using a doughnut pump profile and defocusing the standard fiber-coupled diode [85]. The pump spot radius is controlled to be around 50-200 μm . The effective cavity length is set in the range of 1-1.5 cm. A non-spherical lens with focal length $f = 40$ mm mounted on a translation stage is exploited to provide the mode matching condition by collimating the input light beam in the midway between the following cylindrical lenses. The flower-like LG modes generated by the laser cavity are converted into the crisscrossed HG modes by passing through a rotatable $\pi/2$ -CLMC comprised of two identical cylindrical lenses with focal length $f = 25$ mm, separated by $\sqrt{2} f$. To observe the far-field pattern via a CCD camera, the output beam is directly projected to a paper screen.



2.3.6 Experimental Results and Discussions

According to the previous sections, considering the correspondence of the transformational relation depicted in Fig. 2.3.5(a) and the mode conversion through the $\pi/2$ -CLMC, we therefore utilize a rotatable $\pi/2$ -CLMC to convert the accessible flower-like LG mode emitted by the laser cavity into the crisscrossed HG modes as shown in Fig. 2.3.5(b). Figures 2.3.6(a)-(j) further display the experimental results of an input flower-like LG mode with $(p,l) = (0,11)$ and the corresponding output crisscrossed HG modes associated with various rotating angles θ of the $\pi/2$ -CLMC. Since the output HG modes are always at 45 degrees relative to the principal axes of the cylindrical lenses, it can be seen that the superposed HG modes

rotate by the same angle θ as the mode converter. With attention to the cross section of the crisscrossed HG modes, the intensity distribution can be informed to alter accordingly with the rotating angle of the mode converter. Analogously, compared to the theoretical illustration of the superposed state $\Omega_{0,11}(x, y, z, \alpha)$ as depicted in Fig. 2.3.1, the obtained experimental results in Fig. 2.3.6(b)-(j) are in good agreement with the theoretical realization in Fig. 2.3.1(a)-(i) and are connected by the relation $\theta = \alpha/2l$. In essence, the manifestation of the correlation $\theta = \alpha/2l$ is none other than the geometric rotating angle of the input LG mode relative to the principal axes of the mode converter as if it was fixed. That is, the fulfillment can be understood based on our previous discussion of the superposed state $\Phi_{0,11}(r, \phi, z, \alpha)$ according to different relative phase α as shown in Fig. 2.3.3, which identically exhibits the behavior of geometric rotation by the angle $\alpha/2l$. As a result, we have successfully verified the transformational relation demonstrated in the preceding analysis by exploiting the rotatable $\pi/2$ -CLMC experimentally. In other words, the 2D optical vortex array embedded in the crisscrossed HG mode has been finally generated by the method of mode conversion with a $\pi/2$ -CLMC. What needs to be emphasized especially is the controllable relative phase α between the two crisscrossed HG modes, which can be qualitatively altered by rotating the $\pi/2$ -CLMC at various angle. Since the relative phase has been confirmed to be the decisive factor that contributes to the formation of the phase singularities according to the above investigation, the adjustability of the relative phase in the experiment appears to be absolutely crucial to the production of the OAM state. For practical consideration, the investigation reveals the possibility of particle manipulation in two-transverse-dimension for the developing applications as it can be informed from Fig. 2.3.6(b) that the resulting vortices with fixed relative positions are simultaneously

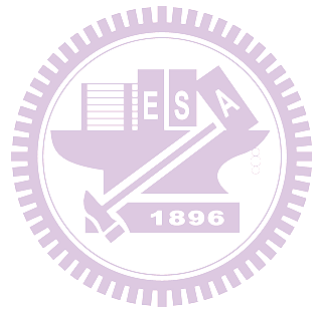
rotated with the CLMC by an angle θ . Moreover, since the Gaussian beams satisfy the property of bilinear transformation [53], which indicates that the profiles are preserved under propagation in free space through the Fourier transformation, the resulting vortex array can maintain its spatial distribution while being focused. Namely, it enables us to quantitatively determine the features of the optical vortex array that focused into the optical traps.

In addition to constructing the optical vortex array that embedded in the superposed state $\Omega_{n,m}(x,y,z,\alpha)$ with vanishing transverse index p illustrated on the above, we are now considering more complicated vortex structures determined by increasing transverse index l with multi-ring LG modes. As an illustration, Fig. 2.3.7(b) demonstrates the theoretical results of superposed states $\Omega_{1,10}(x,y,z,\pi/2)$, $\Omega_{2,10}(x,y,z,\pi/2)$, and $\Omega_{3,10}(x,y,z,\pi/2)$ with non-vanishing transverse index p corresponding to the flower-like LG modes of $\Phi_{1,9}(r,\phi,z,\pi/2)$, $\Phi_{2,8}(r,\phi,z,\pi/2)$, and $\Phi_{3,7}(r,\phi,z,\pi/2)$ as shown in Fig. 2.3.7(a). To make it clear, the associated phase distribution is demonstrated in Fig. 2.3.7(c) which explicitly shows the variation of the position of the singularities defined by the points of intersection. Since several methods have been adopted to generate the multi-ring LG modes [77-81], our investigation may provoke further application for the creation of the exotic vortex structures by transforming the available higher-order LG modes through the mode converter.

2.3.7 Summary

In conclusion, we successfully create the optical vortex array by employing the flower-like LG modes. Theoretically, we firstly verify that the flower-like LG mode

can be transformed from the crisscrossed HG modes embedded with the optical vortex array. According to excellent correspondence of the transformational relation and the mode conversion of the $\pi/2$ -CLMC, we further confirm our assertion by converting the available flower-like LG modes through the $\pi/2$ -CLMC. Importantly, the relative phase of the crisscrossed HG modes can be controlled qualitatively by rotating the rotatable mode converter at various angles. We anticipate the present result and method to be an inspiration for novel application and more sophisticated study related to the fascinating features of optical vortices.



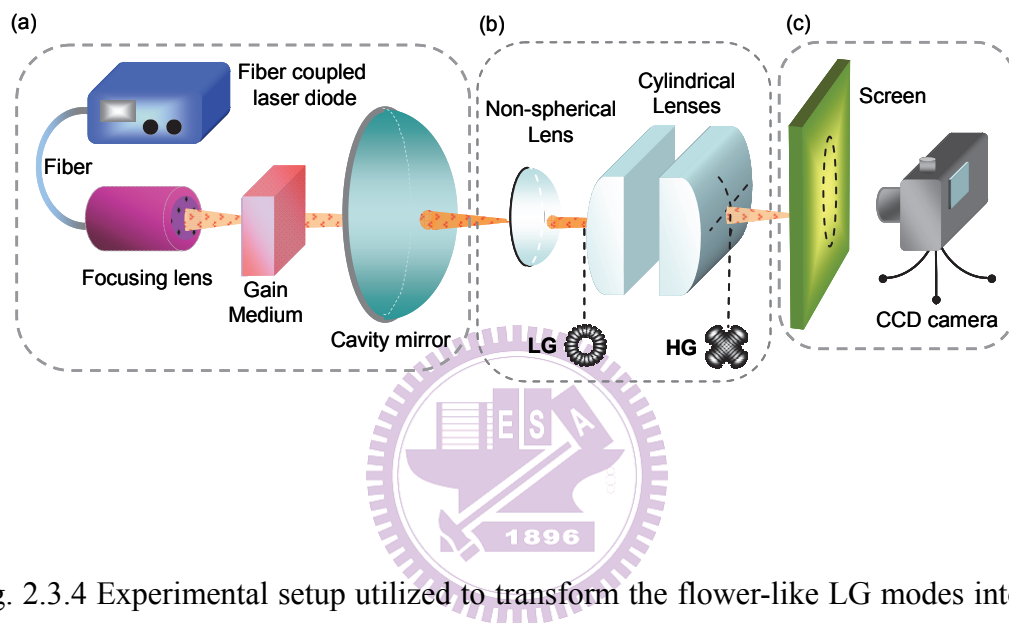


Fig. 2.3.4 Experimental setup utilized to transform the flower-like LG modes into the crisscrossed HG modes with the cylindrical lenses.

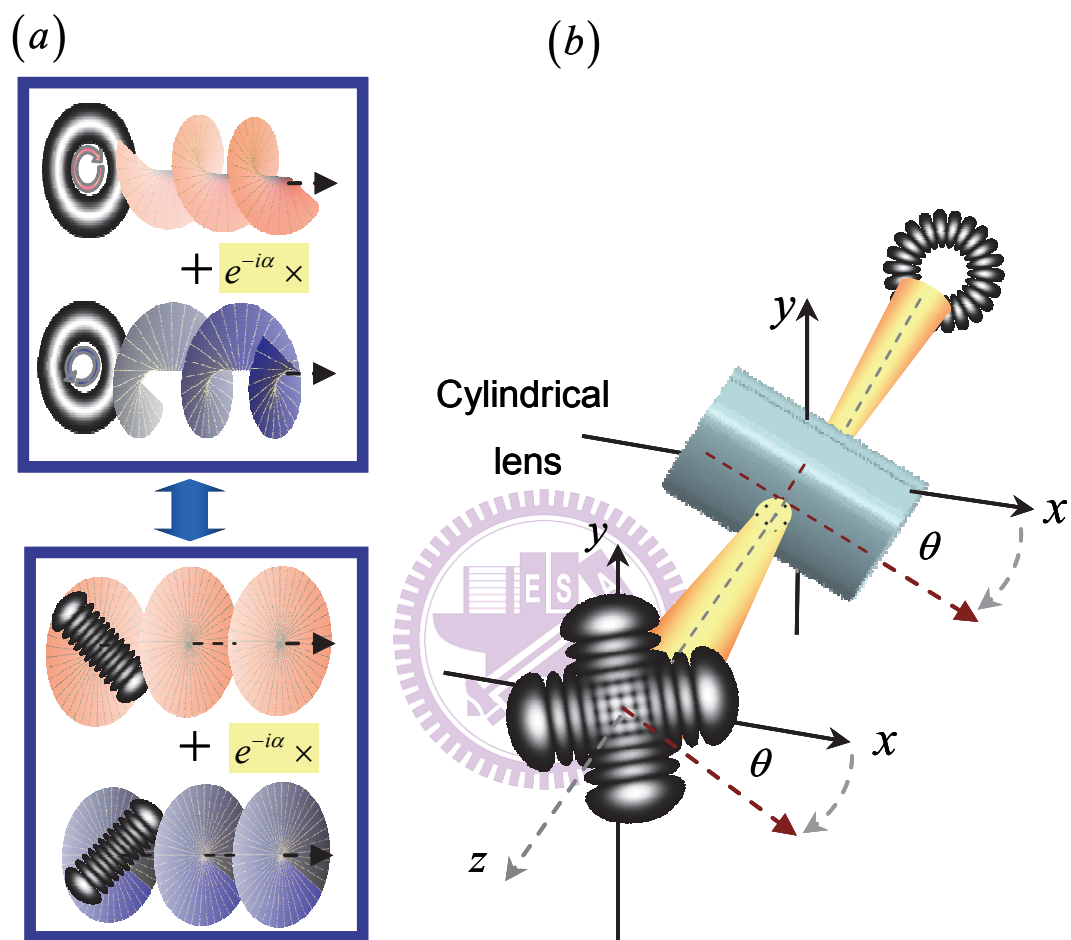


Fig. 2.3.5 (a) Diagram for the transformational relation of a flower-like LG mode and the crisscrossed HG modes. (b) Operational scheme for the rotation of the mode converter.

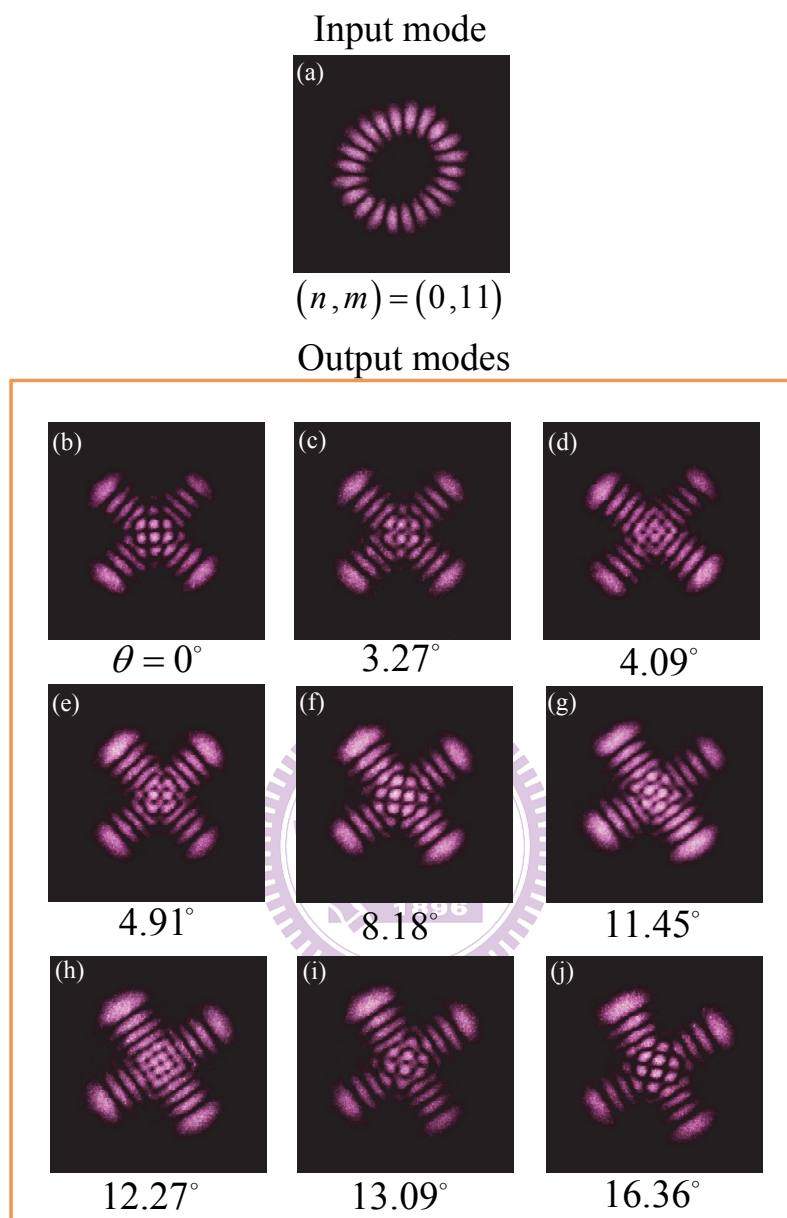


Fig. 2.3.6 Experimental results of an input LG mode with $(p, l) = (0, 11)$ and the corresponding crisscrossed HG modes while rotating the CLMC.

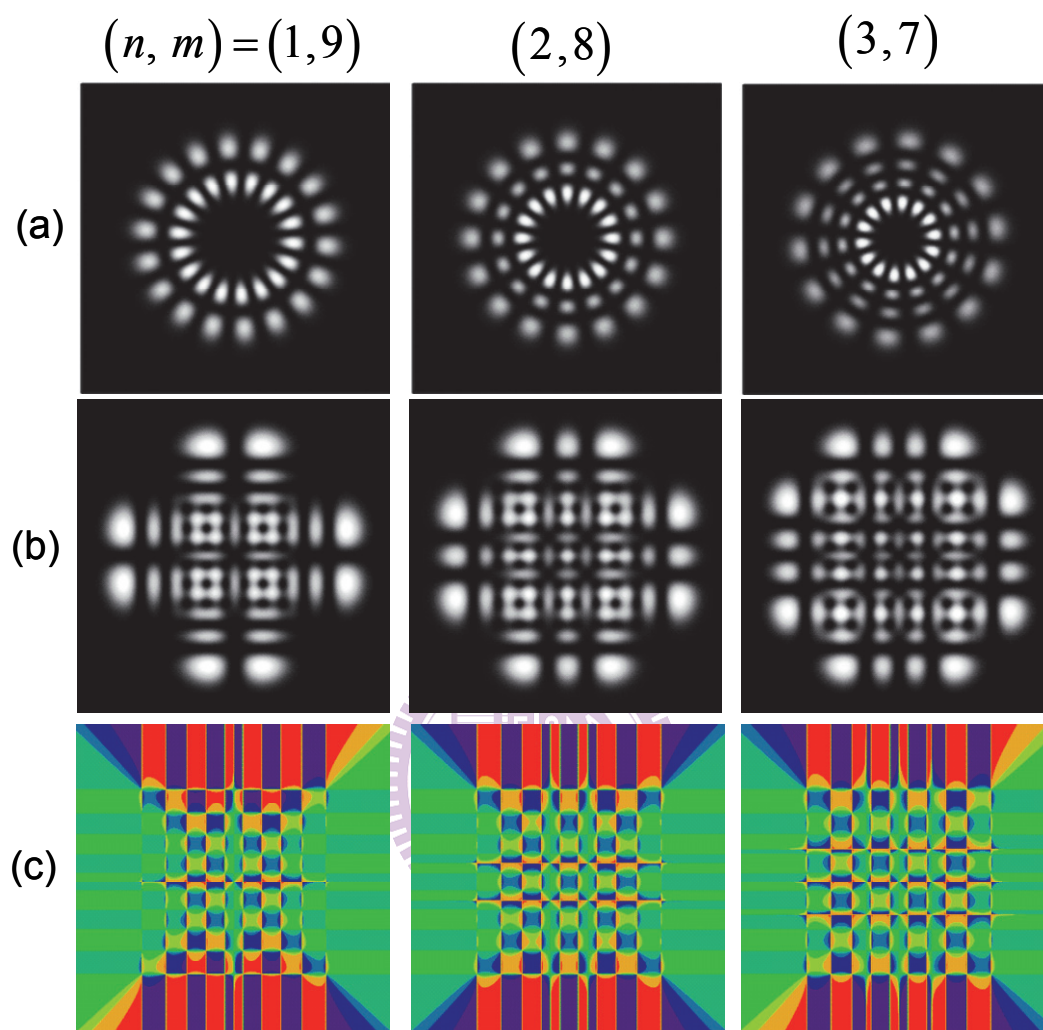


Fig. 2.3.7 Theoretical analysis: (a) LG modes with non-vanishing radial index p . (b) The resulting modes converted from the LG modes. (c) Phase distribution corresponding to (b).

Reference

- [1] D. Dragoman and M. Dragoman, *Prog. Quantum Electron.* 23, 131 (1999).
- [2] D. Dragoman and M. Dragoman, *Quantum-Classical Analogies* (Springer, Berlin, 2004).
- [3] S. Longhi, *Laser & Photon. Rev.* 3, 243 (2009)
- [4] K. Wagner et al., *Science* 321, 541 (2008)
- [5] J. Fu et al., *Phys. Rev. A* 70, 042313 (2004)
- [6] N. K. Langford et al., *Phys. Rev. Lett.* 93, 053601 (2004).
- [7] M. Lassen et al., *Phys. Rev. Lett.* 98, 083602 (2007).
- [8] G. F. Calvo and A. Picón, *Phys. Rev. A* 77, 012302 (2008).
- [9] G. Nienhuis and L. Allen, *Phys. Rev. A* 48, 656 (1993).
- [10] G. F. Calvo, A. Picón, and R. Zambrini, *Phys. Rev. Lett.* 100, 173902 (2008).
- [11] Y. F. Chen, T. H. Lu, K. W. Su, and K. F. Huang, *Phys. Rev. Lett.* 96, 213902 (2006).
- [12] C. Lena, D. Delande, and J. C. Gay, *Europhys. Lett.*, 15, 697-702 (1991).
- [13] T. H. Lu et al., *Phys. Rev. Letts.* 101, 233901 (2008).
- [14] M. S. Soskin and M. V. Vasnetsov, *Singular optics*, in: E. Wolf (Ed.). *Prog. Opt.* 42, 219 (2001).
- [15] E. Abramochkin and V. Volostnikov, *Opt. Commun.* 83, 123 (1991).
- [16] M. W. Beijersbergen et al., *Opt. Commun.* 96, 123 (1993).
- [17] D. Akamastu and M. Kozuma, *Phys. Rev. A* 67, 023803 (2003).
- [18] J. Leach, M. J. Padgett, S. M. Barnett, S. Franke-Arnold, and J. Courtial, *Phys. Rev. Lett.* 88, 0257901 (2002).
- [19] H. He et al., *Phys. Rev. Letts.* 75, 826 (1995).
- [20] D. G. Grier, "A revolution in optical manipulation," *Nature* 424, 810-816 (2003).

- [21] Quantumlike Models and Coherent effects, edited by R. Fedele and P. K. Shukla (World Scientific, Singapore, 1995).
- [22] New Perspectives in Physics of Mesoscopic Systems: Quantumlike Descriptions and Macroscopical Coherent Phenomena, edited by S. De Martino, S. De Nicola, S. De Siena, R. Fedele, and G. Miele (World Scientific, Singapore, 1995).
- [23] V. I. Karpman, Nonlinear Waves in Dispersive Media (Pergamon Press, Oxford, 1975).
- [24] G. P. Agrawal, Nonlinear Fiber Optics (Academic Press, San Diego, 1995).
- [25] M. A. Leontovich, *Izv. Akad. Nauk SSSR*, 8, 16 (1944).
- [26] M. A. Leontovich and V. A. Fock, *Zh. Éksp. Teor. Fiz.*, 16, 557 (1946).
- [27] D. Gloge and D. Marcuse, *J. Opt. Soc. Am. A* 59, 1629 (1969).
- [28] R. Fedele, M. A. Man'ko, V. I. Man'ko, and V. G. Vaccaro, *Physica Scripta*. 68, 377 (2003).
- [29] N. B. Rex, H. E. Tureci, H. G. L. Schwefel, R. K. Chang, and A. D. Stone, *Phys. Rev. Lett.* 88, 094102 (2002).
- [30] K. F. Huang, Y. F. Chen, H. C. Lai, and Y. P. Lan, *Phys. Rev. Lett.* 89, 224102 (2002).
- [31] T. Gensty, K. Becker, I. Fischer, W. Elsäßer, C. Degen, P. Debernardi, and G. P. Bava, *Phys. Rev. Lett.* 94, 233901 (2005).
- [32] Y. F. Chen, K. W. Su, T. H. Lu, and K. F. Huang, *Phys. Rev. Lett.* 96, 033905 (2006).
- [33] R. Fedele and V. I. Man'ko, *Phys. Rev. E*. 58, 992 (1998).
- [34] R. Fedele and V. I. Man'ko, *Phys. Rev. E*. 60, 6042 (1999).
- [35] M. Moshinsky, *Phys. Rev.* 88, 625 (1952).
- [36] S. Godoy, *Phys. Rev. A* 65, 042111 (2002).
- [37] C. C. Chen, Y. T. Yu, Ross C. C. Chen, Y. J. Huang, K. W. Su, Y. F. Chen, and K.

- F. Huang, Phys. Rev. Lett. 101, 044101 (2009).
- [38] O. Dippel, P. Schmelcher, and L. S. Cederbaum, Phys. Rev. A 49, 4415 (1994)
- [39] P. K. Bhaduri, S. Li, K. Tanaka, and J. C. Waddington, J. Phys. A: Math. Nucl. Gen. 27, L553 (1994).
- [40] B. L. Johnson and G. Kirczenow, Europhys. Lett. 51, 367 (2000).
- [41] S. G. Nilsson, Mat.-Fys. Medd. Dan. Vidensk. Selsk. 29 (1955).
- [42] W. D. Heiss and R. G. Nazmitdinov, Phys. Rev. Lett. 73, 1235 (1994).
- [43] R. G. Nazmitdinov, Phys. Part. Nucl. 40, 71 (2009).
- [44] G. S. Agarwal and J. Banerji, J. Phys. A: Math. Gen. 39, 11503 (2006)
- [45] Y. F. Chen, Phys. Rev. A 83, 032124 (2011)
- [46] J. D. Louck, M. Moshinsky, and K. B. Wolf, J. Math. Phys. 14, 692 (1973).
- [47] J. D. Louck, M. Moshinsky, and K. B. Wolf, J. Math. Phys. 14, 692 (1973).
- [48] J. S. Schwinger and B. G. Englert, Quantum mechanics: symbolism of atomic measurements (Springer 2001).
- [49] J. J. Sakurai Modern Quantum Mechanics (Addison-Wesley 1994).
- [50] M. S. Kumar and B. Dutta-Roy, J. Phys. A: Math. Theor. 41 075306 (2008).
- [51] A. Vaziri, G. Weihs, and A. Zeilinger, J. Opt. B: Quantum Semicalss. Opt. 4, S47 (2002).
- [52] T. H. Lu, Y. C. Lin, H. C. Liang, Y. J. Huang, Y. F. Chen, and K. F. Huang, Opt. Lett. 35, 345 (2010).
- [53] A. E. Siegman, Lasers (University Science, 1986).
- [54] T. D. Visser, and E. Wolf, Opt. Commun. 283, 3371 (2010).
- [55] K. T. Gahagan and G. A. Swartzlander, Jr. Opt. Lett. 21, 827-829 (1996).
- [56] M. S. Soskin, M. V. Vasnetsov, Prog. Opt. 42, 219-276 (2001).
- [57] N. B. Simpson, K. Dholakia, L. Allen, and M. J. Padgett, Opt. Lett. 22, 52-54

- (1997).
- [58] H. Adachi, S. Akahoshi, and K. Miyakawa, *Phys. Rev. A* 75, 063409 (2007).
- [59] A. Mair, A. Vaziri, G. Weihs, and A. Zeilinger, *Nature* 412, 313 (2001).
- [60] L. Allen, M.W. Beijersbergen, R.J.C. Spreeuw, J.P. Woerdman, *Phys. Rev. A* 45 8185-8189 (1992).
- [61] P. Senthilkumaran, *Appl. Opt.* 42, 6314-6320 (2003).
- [62] G. Gibson, J. Courtail, and M. J. Padgett, *Opt. Express* 12, 5448-5456 (1996).
- [63] K. Crabtree, J. A. Davis, and I. Moreno, *Appl. Opt.* 43, 1360-1367 (2004).
- [64] K. Dholakia, N. B. Simpson, M. J. Padgett, and L. Allen, *Phys. Rev. A* 54 R3742 (1996).
- [65] M. W. Beijersbergen, L. Allen, H. Vanderveen, J. P. Woerdman, *Opt. Commun.* 96 123-132 (1993).
- [66] M. W. Beijersbergen, R. P. C. Coerwinkel, M. Kristensen, J. P. Woerdman, *Opt. Commun.* 112 321-327 (1994).
- [67] N. R. Heckenberg, R. McDuff, C. P. Smith, and A. G. White, *Opt. Lett.* 17, 211-233 (1992).
- [68] Y. Izdebskaya, V. Shvedov, and A. Volyar, *Opt. Lett.* 30, 2472. (2005)
- [69] Y. F. Chen, Y. C. Lin, K. F. Huang., and T. H. Lu, *Phys. Rev. A* 82, 043801 (2010).
- [70] S. Vyas, and P. Senthilkumaran, *Appl. Opt.* 46, 2893-2898 (2007).
- [71] K. O'Holleran, and M. J. Padgett, *Opt. Express* 14, 3039-3044 (2006).
- [72] K. Otsuka, and S. C. Chu, *Opt. Lett.* 34, 10-12 (2009).
- [73] J. Masajada, *Opt. Commun.* 239, 373-381 (2004).
- [74] M. D. Levenson, T. Ebihura, G. Dai, Y. Morikawa, N. Hyashi, and S. M. Tan, *J. Microlithogr. Microfabr. Microsyst.* 3, 293-304 (2004).
- [75] K. Ladavac, and D. G. Grier, *Opt. Express* 12, 1144-1149 (2004).

- [76] G. H. Kim, J. H. Jeon, Y. C. Noh, K. H. Ko, H. J. Moon, J. H. Lee, and J. S. Chang, *Opt. Commun.* 147, 131-137 (1998).
- [77] G. Grynberg, A. Maitre, and A. Petrossian, *Phys. Rev. Lett.* 72 2378-2382 (1994).
- [78] C. Green, G. B. Mindlin, E. J. D'Angelo, H. G. Solari, and J. R. Tredicce, *Phys. Rev. Lett.* 65, 3124-3127 (1990)
- [79] Y. F. Chen, T. H. Lu, and K. F. Huang, "Phys. Rev. Lett. 97, 233903 (2006).
- [80] M. P. Thirugnanasambandam, Yu. Senatsky, and K. Ueda, *Laser Phys. Lett.* 7, 637-643 (2010).
- [81] S. F. Pereira, M. B. Willemsen, M. P. van Exter, and J.P. Woerdman, *Appl. Phys. Lett.* 73, 2239 (1998)
- [82] M. J. Padgett and J. Courtial, *Opt. Lett.* 24, 430-432 (1999).
- [83] M. Born and E. Wolf, *Principles of Optics* (Pergamon, New York, 1980).
- [84] G. A. Swartzlander, Jr., *Opt. Lett.* 17, 789-791 (1992).
- [85] Y. F. Chen, and Y. P. Lan, *Phys. Rev. A* 63, 063807 (2001).

Chapter 3

Generation of Resonant Geometric Modes in Quantum Circular Billiards and Light Pipes

3.0 Introduction

Helically phased light beams are well known to have an azimuthal phase form of $\exp(im\phi)$ and carry an orbital angular momentum (OAM) of $m\hbar$ per photon, where m is an integer [1,2]. The OAM or optical vortex of light has been exploited in a variety of applications, such as trapping [3,4] and rotating [5] of micron and submicron objects in hydrodynamics and biology, stellar coronagraphy [6], image processing [7], quantum cryptography [8], phase contrast microscopy [9], and spiral interferometry [10]. Helically phased beams with small OAM can be generated with several different techniques, such as transformation from Hermite-Gaussian modes by lens converters [11], generation from Gaussian beams by spiral phase plates [12], creation by synthesized holograms [13], generation through spatial light modulation by liquid crystal cells [14], and creation with light diffraction on dielectric wedges [15]. Nowadays, generation of light beams with huge OAM is an important and interesting task for potential applications including demonstration of opto-mechanical effects and trapping of cold atoms [16].

Bessel beams emerge as propagation invariant solutions of the Helmholtz equation in a cylindrical waveguide and carry a well-defined OAM associated with

their spiral wave fronts [17]. In ray dynamics, the transverse confinement of a cylindrical waveguide can be regarded as a circular billiard for light. The periodic orbits of a circular billiard can be characterized by the indices (p,q) , where q is the number of turning points at the boundary during one period, and p is the number of windings during one period [18]. The average OAM of light for each periodic orbit (p,q) can be given by $\hbar(k_t R_0)$, where R_0 is the shortest distance to the circular center and k_t is the transverse wave number. This indicates that it is possible to employ the geometric modes of cylindrical waveguides to generate light beams with large OAM. Even though very high order Bessel beams have been demonstrated using cylindrical waveguides and whispering gallery resonators [16], generation of geometric modes with huge OAM has not been realized yet. Moreover, since light interferences are profoundly relevant to the underlying ray dynamics [19-21], it will be scientifically interesting to explore light beams with huge OAM from the feature of ray-wave correspondence that is analogous to the classical-quantum correspondence [22].

In this section we first explore the subtle relationship between geometric modes and high order Bessel modes for manifesting the OAM in the ray-wave correspondence. We further develop a systematic method to generate various geometric modes with huge OAM from a large aperture cylindrical waveguide. More importantly, we also employ the free-space propagation of the geometric modes emerging from the cylindrical waveguide to analogously emulate the transient dynamics of quantum states suddenly released from quantum billiards.

3.1 Quantum Circular Billiards

3.1.1 Eigenstates

The normalized eigenstates $\psi_{m,n}(r,\phi)$ in polar coordinates for a circular billiard of radius R are given by

$$\psi_{m,n}(r,\phi) = \frac{1}{\sqrt{\pi R J_{m+1}(k_{m,n}R)}} J_m(k_{m,n}r) e^{im\phi}, \quad (3.1.1)$$

where $m \in \mathbb{Z}$, $n \in \mathbb{N}$, and J_m is the Bessel function of the first kind and order m as depicted in Fig. 3.1.1. The corresponding eigenvalues $k_{m,n}$ are determined by the boundary condition at the circular boundary, i.e. $J_m(k_{m,n}R) = 0$ and the quantum numbers m, n correspond to the quantization of the azimuthal and radial oscillations of the wave, respectively. In a cylindrical waveguide, $k_{m,n}$ is the transverse component of the total wave number k . For large quantum numbers, the eigenvalues $k_{m,n}$ can be determined with the Wentzel-Kramers-Brillouin (WKB) method to be given by $\sqrt{k_{m,n}^2(R^2 - R_o^2)} - m \cos^{-1}(R_o/R) = (n + 3/4)\pi$, where R_o is the distance of closest approach of the wave to the center of the billiard. The relationship between R_o and $k_{m,n}$ is given by the expression for OAM: $m\hbar = R_o(\hbar k_{m,n})$. In ray dynamics, the shortest distance to the origin R_o for the periodic orbits (p,q) is given by $R_o = R \cos(p\pi/q)$. With this expression, the quantization condition from the WKB method can be written as $k_{m,n} R \sin(p\pi/q) = [m(p/q) + n + (3/4)]\pi$. This quantization condition reveals that the group of the eigenstates $\psi_{m_o+q\kappa, n_o-p\kappa}$ with $\kappa \in \mathbb{Z}$ and $m_o \gg |q\kappa|$ constitutes a family of nearly degenerate states and forms an energy shell in the neighborhood of the central eigenstate ψ_{m_o, n_o} , which indicates the appearance of a sharp peak in the density of states [23].

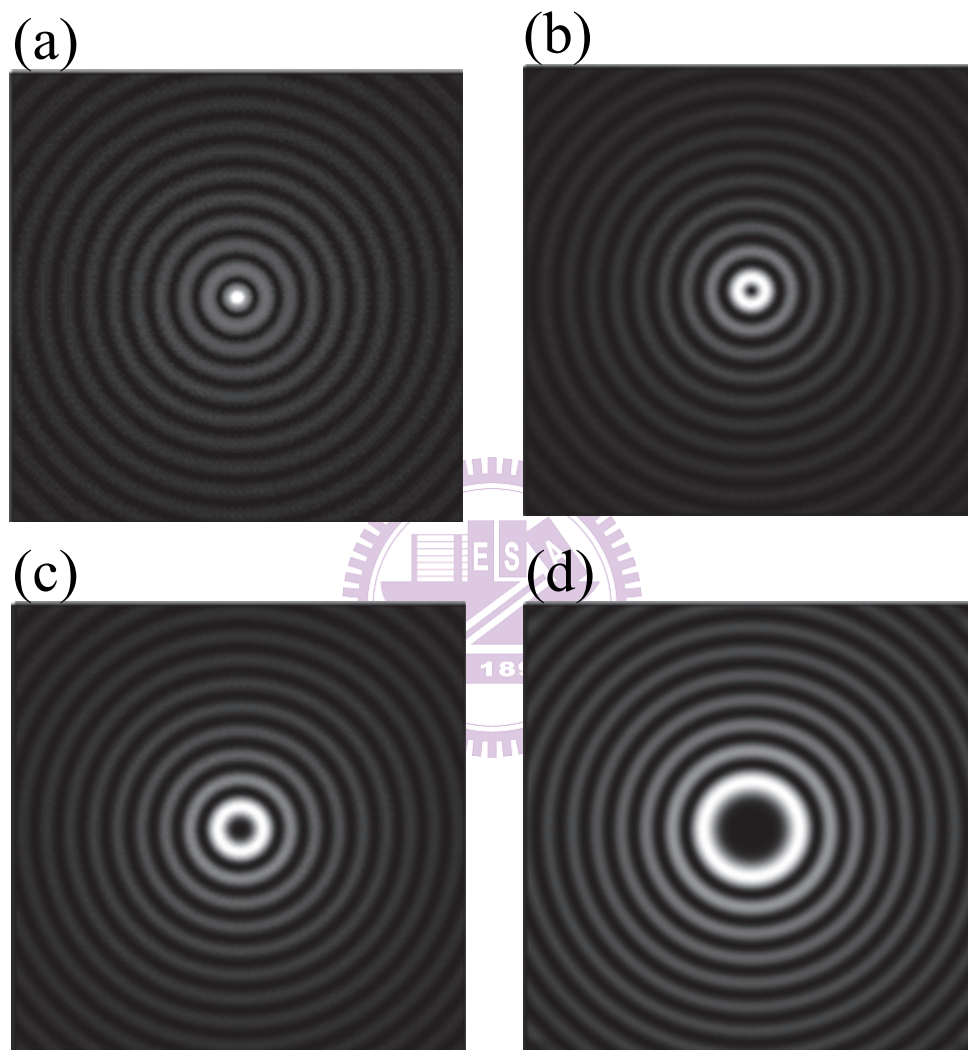


Fig. 3.1.1 Numerical results of Bessel functions with different orders: (a)-(d) are $m=0$, $m=1$, $m=2$, and $m=3$, respectively.

3.1.2 Coherent States

In terms of the representation of stationary coherent state [24,25], the resonant modes localized on the periodic orbits can be expressed as a coherent superposition of the eigenstates belonging to the same shell of the spectrum:

$$\Psi_{m_o, M}^{p, q}(r, \phi; \phi_o) = (2M + 1)^{-1/2} \sum_{\kappa=-M}^M e^{i q \kappa \phi_o} \psi_{m_o + q \kappa, n_o - p \kappa}(r, \phi), \quad (3.1.2)$$

where ϕ_o is related to the starting position of periodic orbits and $(2M + 1)$ is the total number of Bessel modes. For a sufficient large m_o , the larger the number M is, the more localized the resonant mode $\Psi_{m_o, M}^{p, q}(r, \phi; \phi_o)$ is on the orbital trajectories. It is intriguing that even $M=1$ the resonant modes $\Psi_{m_o, M}^{p, q}(r, \phi; \phi_o)$ are conspicuously localized on the periodic orbits. In brief, the interference between nearly degenerate eigenmodes is extremely efficient to form the resonant geometric modes. The efficient interference leads the resonant geometric modes to play an important role in numerous mesoscopic systems [18-22]. Figure 3.1.2 shows the numerical patterns calculated by using Eq. (3.1.2) with $M=3$ and $\phi_o=0$, where the values of the order parameter m_o are 200 and 100 for the results in Figs. 3.1.2(a)-3.1.2(d) and Figs. 3.1.2(e)-3.1.2(h), respectively. Note that the chosen values for m_o , ϕ_o and M are not particular but only for clear presentation. It can be seen that the numerical patterns for the resonant geometric modes are well localized on the periodic orbits. Since the Bessel beams with the azimuthal phase term of $\exp(im\phi)$ carry OAM [16], the resonant geometric modes naturally possess considerable average OAM. The average OAM of the geometric mode $\Psi_{m_o, M}^{p, q}(r, \phi; \phi_o)$ can be straightforwardly verified to be $m_o \hbar$.

Although the numerical patterns of resonant modes $\Psi_{m_o, M}^{p, q}(r, \phi; \phi_o)$ are clearly

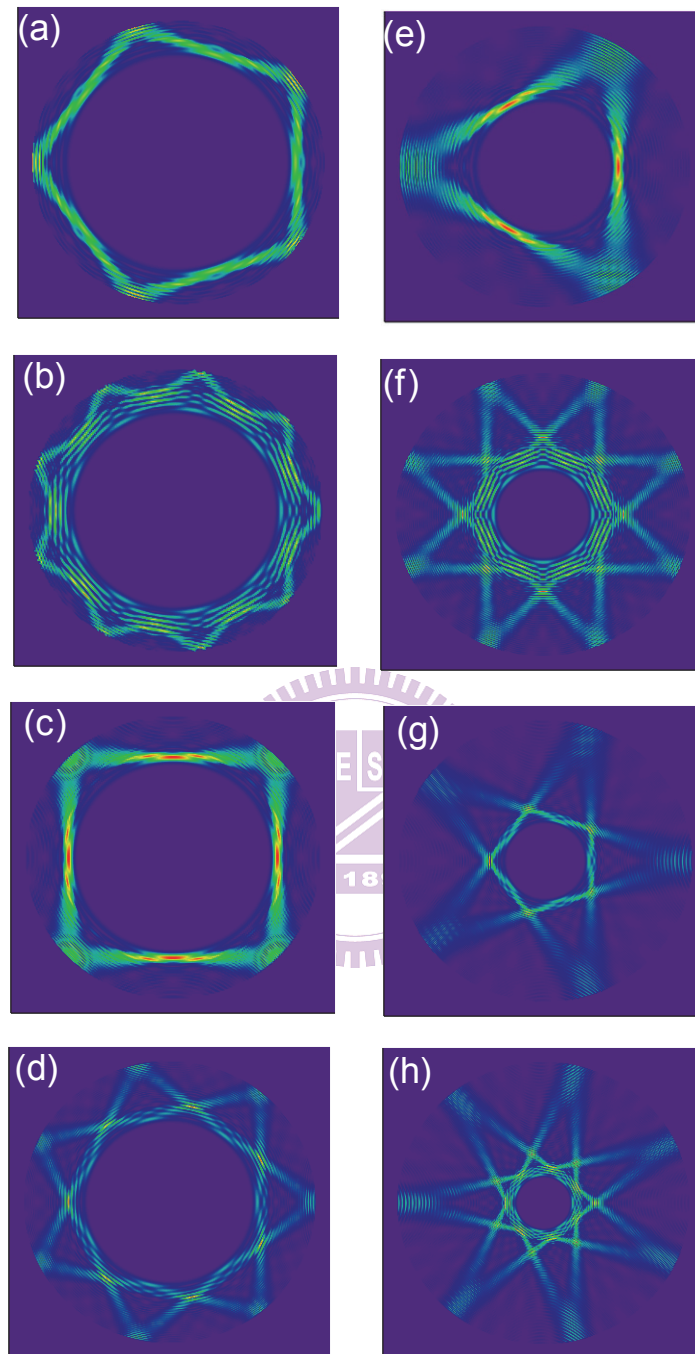


Fig. 3.1.2 Numerically calculated patterns with Eq. (3.1.2) and using $M=3$ and $\theta_o=0$. The values of the order parameter m_o are 200 and 100 for the results in Figs. 3.1.2(a)-3.1.2(d) and Figs. 3.1.2(e)-3.1.2(h), respectively.

concentrated on the periodic orbits, it is pedagogically useful and important to explore the ray-wave correspondence in an explicit way. Next, we use the properties of the Bessel function to construct the relationship between the Bessel beams and geometric modes. Using the boundary condition $J_m(k_{m,n}R) = 0$ and the asymptotic form of the Bessel function, $J_m(z) \approx \sqrt{2/(\pi z)} \cos[z - (2m+1)\pi/4]$ for $z \rightarrow \infty$ and, we can obtain $J_{m+1}(k_{m,n}R) \approx \sqrt{2/(\pi k_{m,n}R)}$ for the large indices. With this result and the Bessel's integral representation, the high-order Bessel modes $\psi_{m,n}(r, \phi)$ can be expressed as

$$\psi_{m,n}(r, \phi) = \sqrt{\frac{k_{m,n}}{2R}} \frac{1}{2\pi} \int_{-\pi}^{\pi} e^{ik_{m,n}r \sin \phi} e^{im(\phi - \varphi)} d\varphi . \quad (3.1.3)$$

In substitution of Eq. (3.1.3) into Eq. (3.1.2), the resonant modes $\Psi_{m_o, M}^{p, q}(r, \phi; \phi_o)$ is given by

$$\Psi_{m_o, M}^{p, q}(r, \varphi; \varphi_o) = \sqrt{\frac{k_{m_o, n_o}}{(2M+1)R}} \frac{1}{2\sqrt{2}\pi} \times \int_{-\pi}^{\pi} e^{ik_{m_o, n_o}r \sin \phi} e^{-im_o(\phi - \varphi)} \sum_{\kappa=-M}^M e^{-iq\kappa(\phi - \varphi - \varphi_o)} d\phi . \quad (3.1.4)$$

Changing the integration variable from φ to α with $\varphi - \phi - \phi_o = \alpha$ and resetting the integration bounds on the circle angle, Eq. (3.1.4) can be written

$$\Psi_{m_o, M}^{p, q}(r, \varphi; \varphi_o) = \sqrt{\frac{(2M+1)k_{m_o, n_o}}{2R}} \frac{e^{-im_o\varphi_o}}{2\pi} \times \int_{-\pi}^{\pi} e^{ik_{m_o, n_o}r \sin(\alpha + \varphi + \varphi_o)} e^{-im_o\alpha} D_M(q\alpha) d\alpha , \quad (3.1.5)$$

where $D_M(q\alpha) = (2M+1)^{-1} \sum_{\kappa=-M}^M e^{-i\kappa q\alpha}$ is the Dirichlet kernel. Since $D_M(q\alpha)$ is a periodic pulse function with period $2\pi/q$, the integration of Eq. (3.1.5) on the circle angle can be divided into q segments with the integration interval between $-\pi/q$ and π/q . Hence Eq. (3.1.5) can be written as

$$\Psi_{m_o, M}^{p, q}(r, \varphi; \varphi_o) = \sqrt{\frac{(2M+1)k_{m_o, n_o}}{2R}} \frac{e^{-im_o\varphi_o}}{2\pi} \times \sum_{s=0}^{q-1} \left\{ \int_{-\pi/q}^{\pi/q} e^{ik_{m_o, n_o} r \sin\left(\alpha + \varphi + \varphi_o - \frac{2\pi s}{q}\right)} e^{-im_o\left(\alpha - \frac{2\pi s}{q}\right)} D_M(q\alpha) d\alpha \right\}. \quad (3.1.6)$$

For $(2M+1)q \gg 1$, the Dirichlet kernel $D_M(q\alpha)$ displays a narrow peak concentrated in a small region of $-\Delta \leq \alpha \leq \Delta$, where $\Delta = \pi/[q(2M+1)]$. Since the effective integral range of α in Eq. (3.1.6) is rather limited, the factor $\sin[\alpha + \theta + \theta_o - (2\pi s/q)]$ for small α can be reasonably approximated as $\alpha \cdot \cos[\theta + \theta_o - (2\pi s/q)] + \sin[\theta + \theta_o - (2\pi s/q)]$. For obtaining a close form, we also approximate the function $D_M(q\alpha)$ as a gate function that is 0 outside the interval $[-\Delta, \Delta]$ and unity inside it. With these approximations and $k_{m_o, n_o} = m_o/R_o$, Eq. (3.1.6) can be analytically integrated as

$$\Psi_{m_o, M}^{p, q}(r, \varphi; \varphi_o) = \sqrt{\frac{m_o}{2RR_o}} \frac{e^{-im_o\varphi_o}}{q\sqrt{(2M+1)}} \left\{ \sum_{s=0}^{q-1} e^{im_o \left[\frac{r}{R_o} \sin\left(\varphi + \varphi_o - \frac{2\pi s}{q}\right) + \frac{2\pi s}{q} \right]} \times \text{sinc} \left(\frac{m_o}{R_o} \frac{\pi}{q(2M+1)} \left[r \cos\left(\varphi + \varphi_o - \frac{2\pi s}{q}\right) - R_o \right] \right) \right\}, \quad (3.1.7)$$

where $\text{sinc}(x) = \sin(x)/x$ is the sinc function. From the property of the sinc function, the wave function $\Psi_{m_o, M}^{p, q}(r, \phi; \phi_o)$ can be manifestly deduced to be concentrated on the set of straight lines: $r \cos[\phi + \phi_o - (2\pi s/q)] = R_o$ with $s = 0, 1, \dots, q-1$ that coincide

with the periodic orbit in a circular billiard.

3.1.3 Transient Dynamics of Released Coherent States

In quantum mechanics, the free time evolution of the quantum state $\psi(x, y)$ suddenly released at time $t_0 = 0$ can be in terms of the 2D free propagator $K(x, y, t; x', y', t_0)$ [26, 27] and expressed as

$$\psi(x, y, t) = \int dy' \int dx' K(x, y, t; x', y', t_0) \psi(x', y'), \quad (3.1.8)$$

where

$$K(x, y, t; x', y', t_0) = \frac{m}{2\pi i \hbar (t - t_0)} \exp \left\{ \frac{i m [(x - x')^2 + (y - y')^2]}{2 \hbar (t - t_0)} \right\}. \quad (3.1.9)$$

Thus the quantum state $\psi(x, y, t)$ can be written as

$$\psi(x, y, t) = \frac{m}{2\pi i \hbar t} \int dy' \int dx' \exp \left\{ \frac{i m [(x - x')^2 + (y - y')^2]}{2 \hbar t} \right\} \psi(x', y'). \quad (3.1.10)$$

3.2 Analogous Optical Experiments

3.2.1 Experimental Setup

Cylindrical waveguides and whispering gallery resonators have been employed to generate very high order Bessel beams [16]. Here we exploit a large-aperture cylindrical waveguide with the precise coupling scheme to systematically generate resonant geometric modes with large OAM. Figure 3.2.1(a) depicts the experimental setup. A linearly polarized Gaussian laser beam of wavelength at 532 nm was used as an incident light source. A beam expander was employed to reduce the beam divergence less than 0.1 mrad. A lens with the focal length of 25 mm was used to focus the laser beam into the cylindrical waveguide. Figure 3.2.1(b) depicts the

central angle of incidence θ_0 and the effective spreading range $\Delta\theta$ in the longitudinal section of the cylindrical waveguide. The transverse path length of a ray with the angle of incidence θ_0 through the waveguide is given by $L_T = L \tan\theta_0$, where L is the length of the waveguide. For the angle bandwidth $\Delta\theta$, the range of the transverse path length can be found to be $\Delta L_T = (L \sec^2 \theta_0) \Delta\theta$. To form a complete transverse orbit (p,q) , the range ΔL_T needs to be greater than the orbital length $L_{p,q} = 2qR \sin(p\pi/q)$. Namely, the geometric condition is given by $(\sec^2 \theta_0) \Delta\theta \geq 2q(R/L) \sin(p\pi/q)$. A smaller aspect ration R/L can lead to the formation of geometric modes with smaller angle bandwidth. Here we use the cylindrical waveguide with $R=0.75$ mm and $L=295$ mm. Figure 3.2.1(c) depicts the off-axis distance R_0 of the incident beam and the effective azimuthal spreading $\Delta\phi$ in the transverse section of the cylindrical waveguide. A movable pinhole with an adjustable diameter was placed behind the beam expander to control the incident angle θ_0 and the off-axis distance R_0 of the laser beam. The pinhole diameter was adjusted to obtain the desired bandwidth $\Delta\theta$ and $\Delta\phi$.

3.2.2 Coherent Modes

We experimentally confirmed that the geometric mode with index (p,q) can be completely generated when the off-axis distance R_0 is close to the value of $R \cos(p\pi/q)$. The transverse near-field pattern at the output facet of the cylindrical waveguide was projected on a screen and was imaged by a CCD camera. We controlled the incident angle to be approximately $\theta_0 = 10^\circ$ and changed the off-axis distance R_0 to generate various geometric modes with indices (p,q) corresponding to the theoretical results shown in Fig. 3.1.2. Figure 3.2.2 shows the near-field patterns

for observed geometric modes. The experimental patterns are in good agreement with the numerical patterns showing in Fig. 3.1.2. With $\theta_o = 10^\circ$ and R_o for different geometric modes with indices (p, q) , the average OAM can be calculated as $\langle m \rangle = k \tan \theta_o \times R \cos(p\pi/q)$, where k is the wave number of the incident beam.

Consequently, it can be found that the average OAM ranges from $348 \hbar$ to $1264 \hbar$.

3.2.3 Propagation of Coherent Modes

Another extended intriguing topic is to investigate the free-space propagation of the geometric mode because it can be analogous to the time evolution of a suddenly released 2D quantum-billiard waves. The optical wave $\psi(x, y)$ emerges from the output end of the light pipe at $z=0$ to the free space in the direction of the $+z$ axis can be described with the Fresnel transformation:

$$\psi(x, y, z) = \frac{i e^{-ikz}}{\lambda z} \int dy' \int dx' \exp\left\{-\frac{ik}{2z} [(x-x')^2 + (y-y')^2]\right\} \psi(x', y') \quad (3.2.1)$$

Comparing Eqs. (3.1.10) and (3.2.1) it is evident that the time evolution of a 2D quantum state is equivalent to the Fresnel transformation of a near-field optical wave with the substitution of $t \rightarrow z$ and $m/\hbar \rightarrow 2\pi/\lambda$, where λ is the optical wavelength. Figure 3.2.3 illustrates the experimental (upper row) and numerical (lower row) patterns for the geometric modes $\Psi_{m_o, M}^{p, q}(r, \phi; \phi_o)$ for the case of $(p, q) = (2, 5)$ in the free-space propagation. Numerical patterns can be clearly seen to agree very well with experimental results. It is also worth noting that the free-space propagation of the geometric mode displays not only the feature of ray streamlines but also the spiral characteristics. The spiral feature confirms the existence of OAM that comes from the traveling-wave nature of the geometric modes in the azimuthal axis.

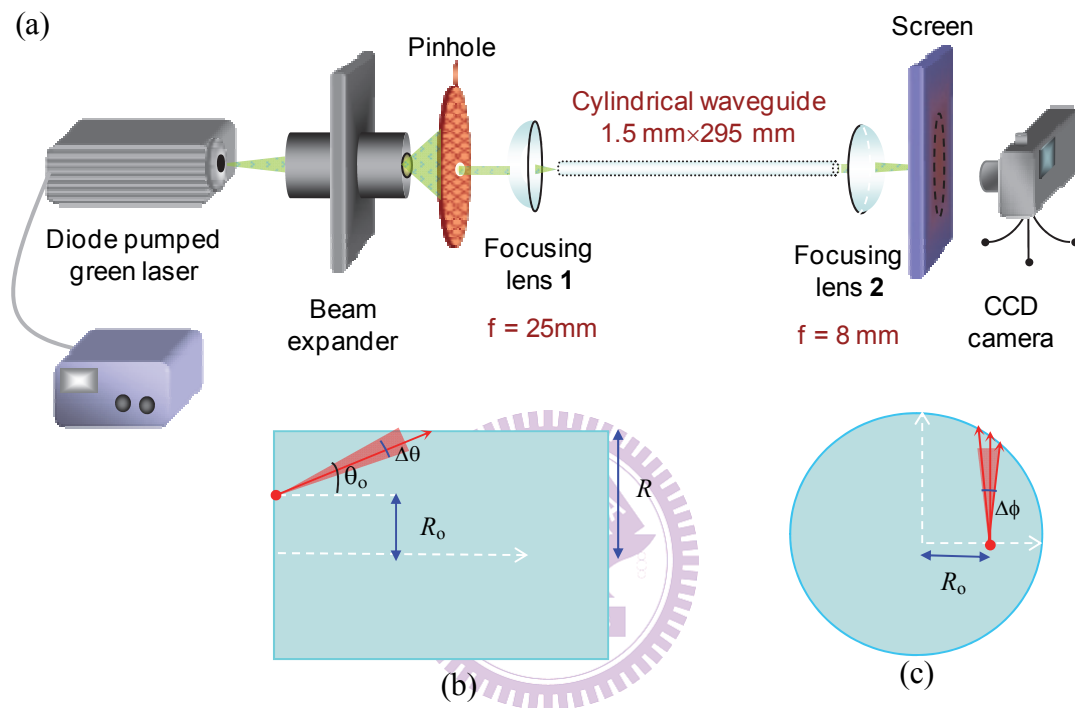


Fig. 3.2.1 (a) Experimental setup for generating the resonant geometric modes from a cylindrical waveguide; (b) longitudinal section of the cylindrical waveguide, showing the central angle of incidence θ_0 and the effective spreading range $\Delta\theta$; (c) transverse section, showing the off-axis distance R_0 of the incident beam and the effective azimuthal spreading $\Delta\phi$.

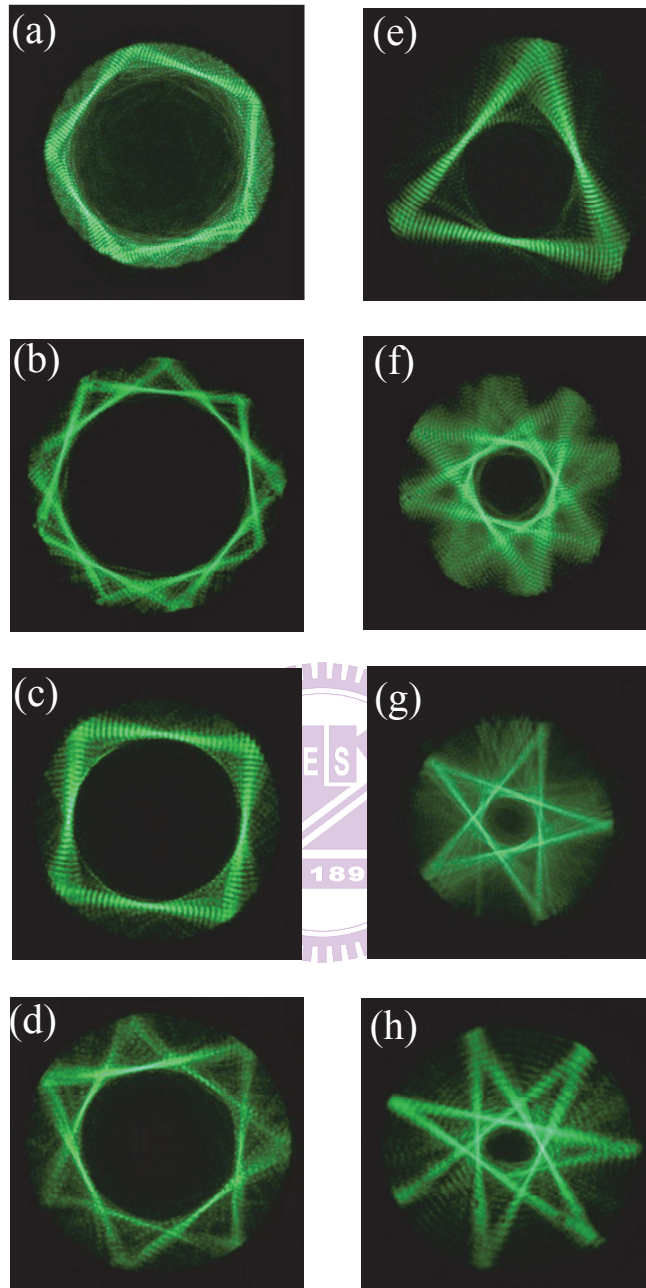


Fig. 3.2.2 Experimental transverse near-field patterns for the observed geometric modes corresponding to the numerical patterns shown in Fig. 3.1.2.

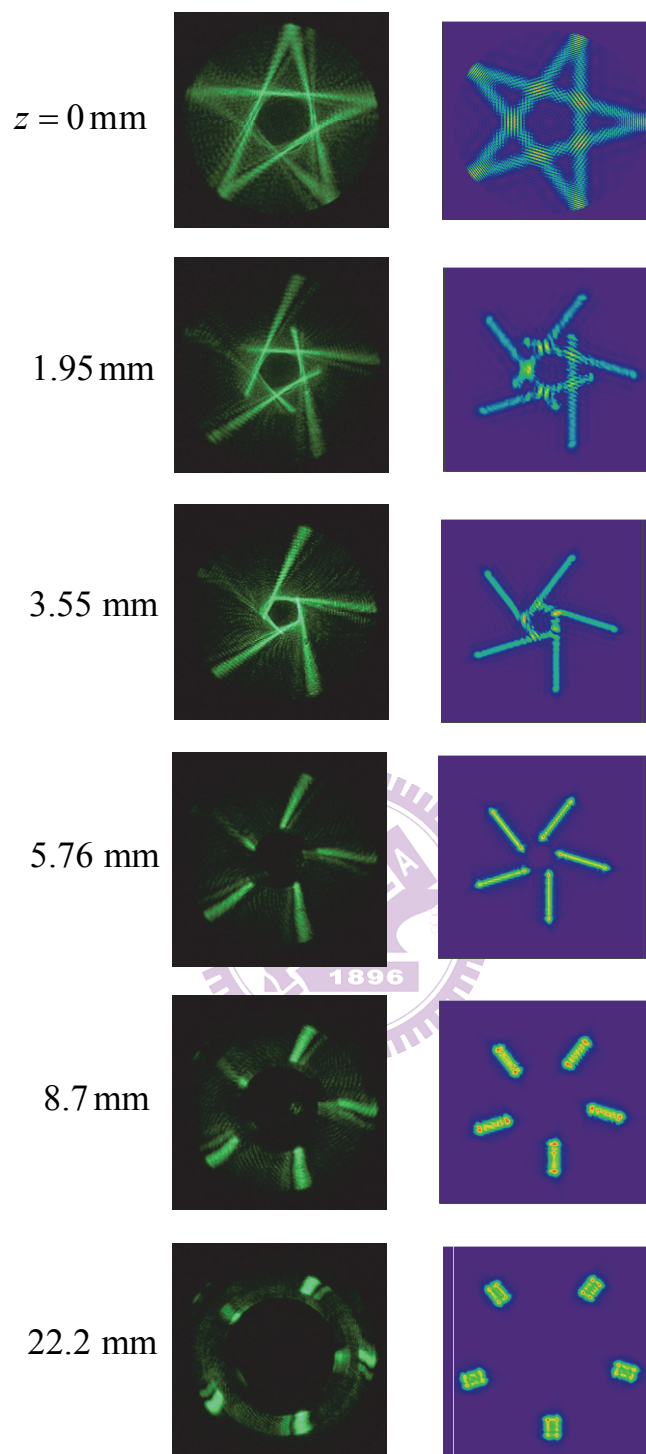


Fig. 3.2.3 Experimental (upper row) and numerical (lower row) patterns for the quasiscattered optical modes for the case of $(p, q) = (2, 5)$ in the free-space propagation.

3.2.4 Spiral Patterns

Spiral patterns characterized by their fascinating structures have been investigated in various systems of different fields such as biological [28], chemical [29], physical [30-34], and optical [35,36] systems. It is also found that the spirals appear in heart muscle during the heart diseases [37-39] such as the cardiac arrhythmia and fibrillation.

In this section, we demonstrate the observation of the optical spiral patterns with the high-order geometric modes emitted from the light pipe. The experimental configuration is the same as the one in Fig. 3.2.1. The propagation for various high-order geometric modes traveling from the end facet ($z=0$) of the light pipe to the far field are clearly displayed in Fig. 3.2.4 to Fig. 3.2.6. It should be noted that

these attracting figures are generated with the input angle $\theta_0 \approx 10^\circ$ and with different off-axis distances R_0 . Figure 3.2.4 and Fig. 3.2.5 show the experimental observations of the high-order geometric modes with indices $(p, q) = (6, 25)$, and $(p, q) = (21, 62)$, respectively. For the case in Fig. 3.2.6, the intricate structure of the geometric mode has caused difficulty in directly recognizing the indices (p, q) . Even so, with the relation $R_0 = R \cos(p\pi/q)$, we can derive the ratio p/q with $R_0/R = 0.48$ to be

$p/q = \left[\cos^{-1}(R_0/R) \right] / \pi = 0.34$ according to the experimental result. It can be seen

that the spiral patterns are distinctly formed through the propagation. The far-field patterns also show that the effective spreading range $\Delta\theta$ should be quantized and the effective azimuthal spreading range $\Delta\phi$ in the transverse section of the light pipe is continuously distributed. The quantization for $\Delta\theta$ can be obtained from the theoretical interpretation since the available incident angles are governed by the boundary condition of the light pipe. Moreover, the inner and the outer intensity

distribution of the far-field spiral patterns suggest the lower and higher values of the transverse component of the wave number, respectively. The outer intensity distribution of the far-field spiral pattern also implies the more number of times the light beams are reflected by the wall of the light pipe. During the propagation, it can be obviously observed that the light beams corresponding to different transverse components of the wave number are divided into layers and ultimately form the spirals. More complex spiral patterns with irregular trajectories can be observed in Fig. 3.2.7 and Fig 3.2.8. Since the presented optical spiral patterns are reproducible, robust, and stable, it is useful for further exploration of the intriguing features of the spirals.



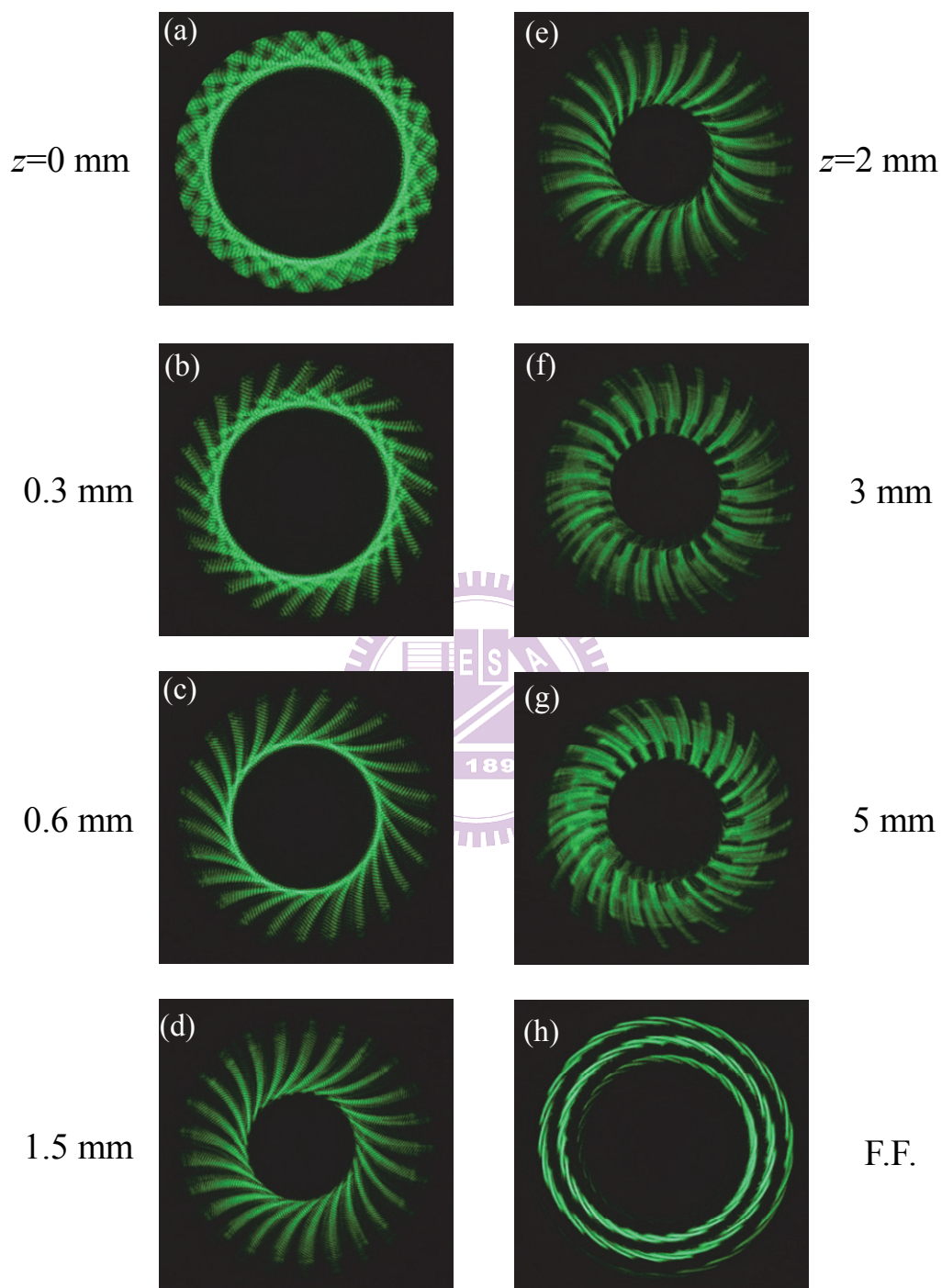


Fig. 3.2.4 Experimental patterns for the optical geometric modes for the case of $(p, q) = (6, 25)$ in the free-space propagation.

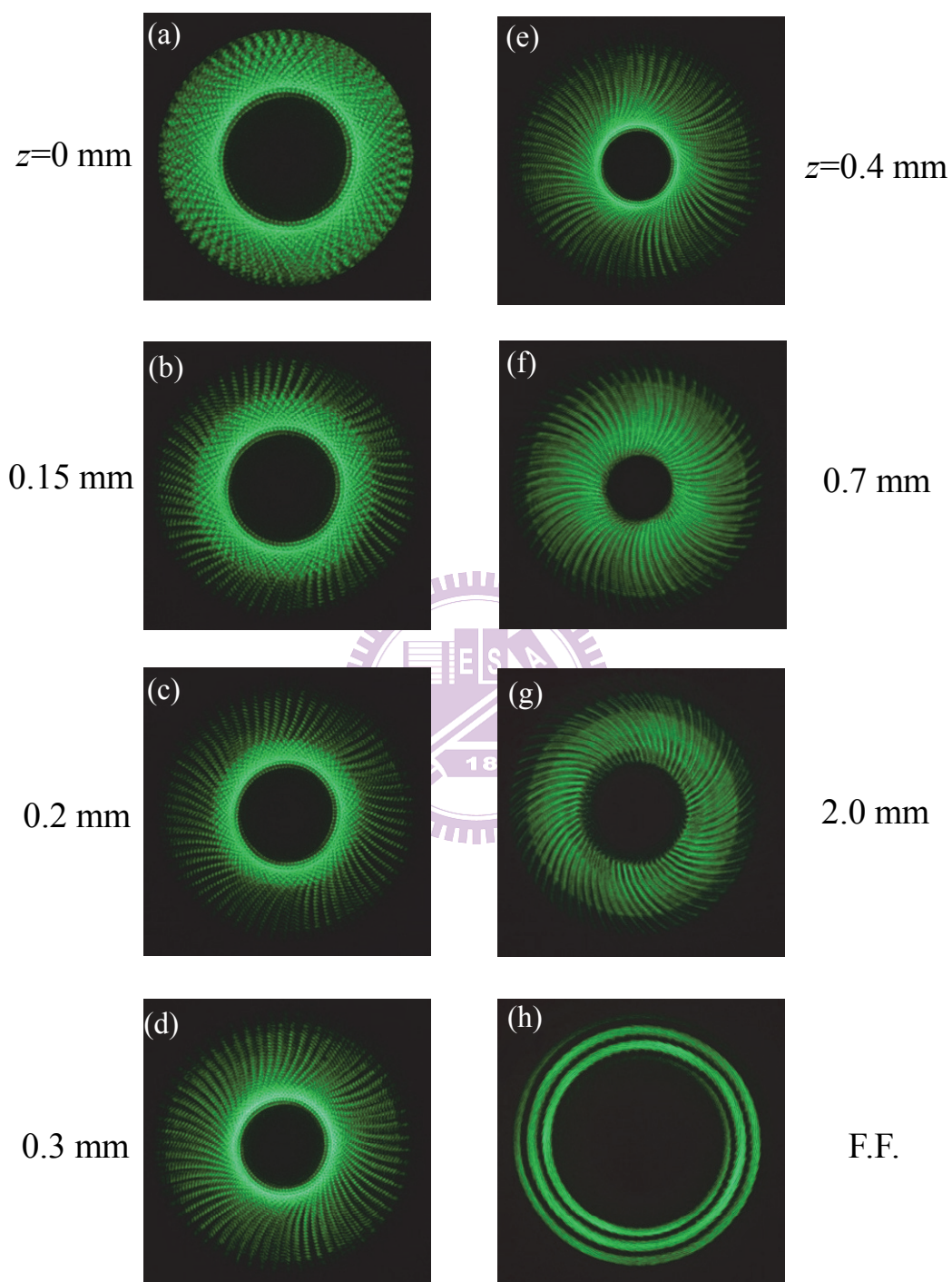


Fig. 3.2.5 Experimental patterns for the optical geometric modes for the case of $(p, q) = (21, 62)$ in the free-space propagation.

\

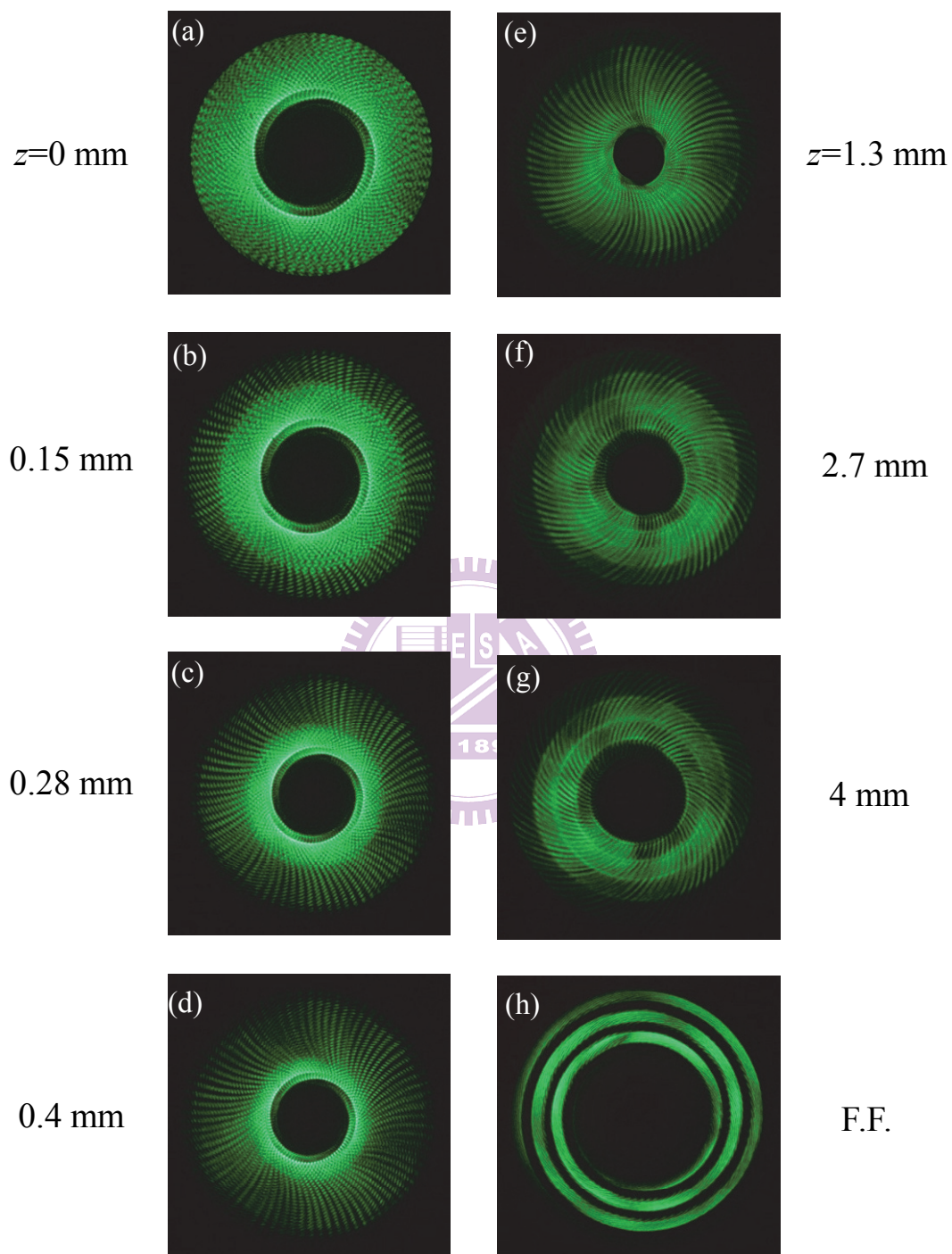


Fig. 3.2.6 Experimental patterns for the optical geometric modes for the case of $p/q = 0.34$ in the free-space propagation.

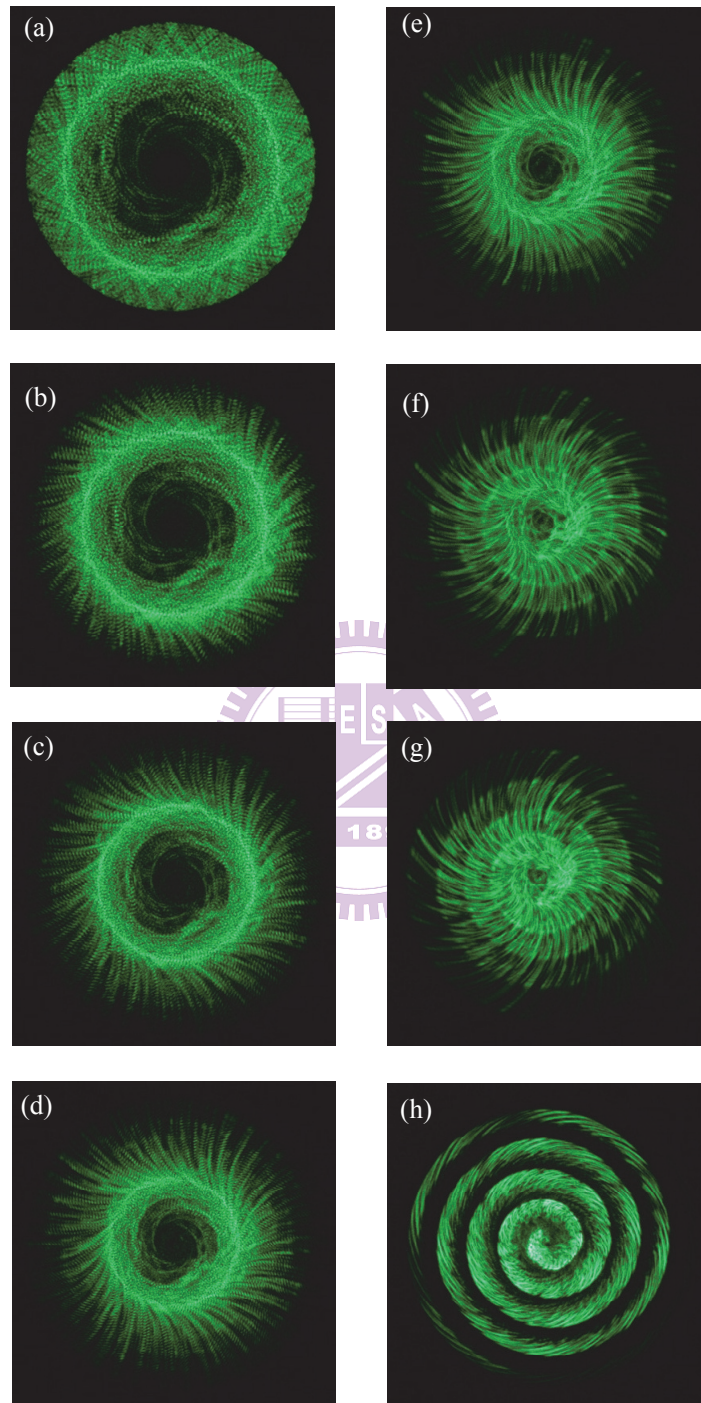


Fig. 3.2.7 Experimental patterns for the spiral patterns with irregular trajectories in the free-space propagation.

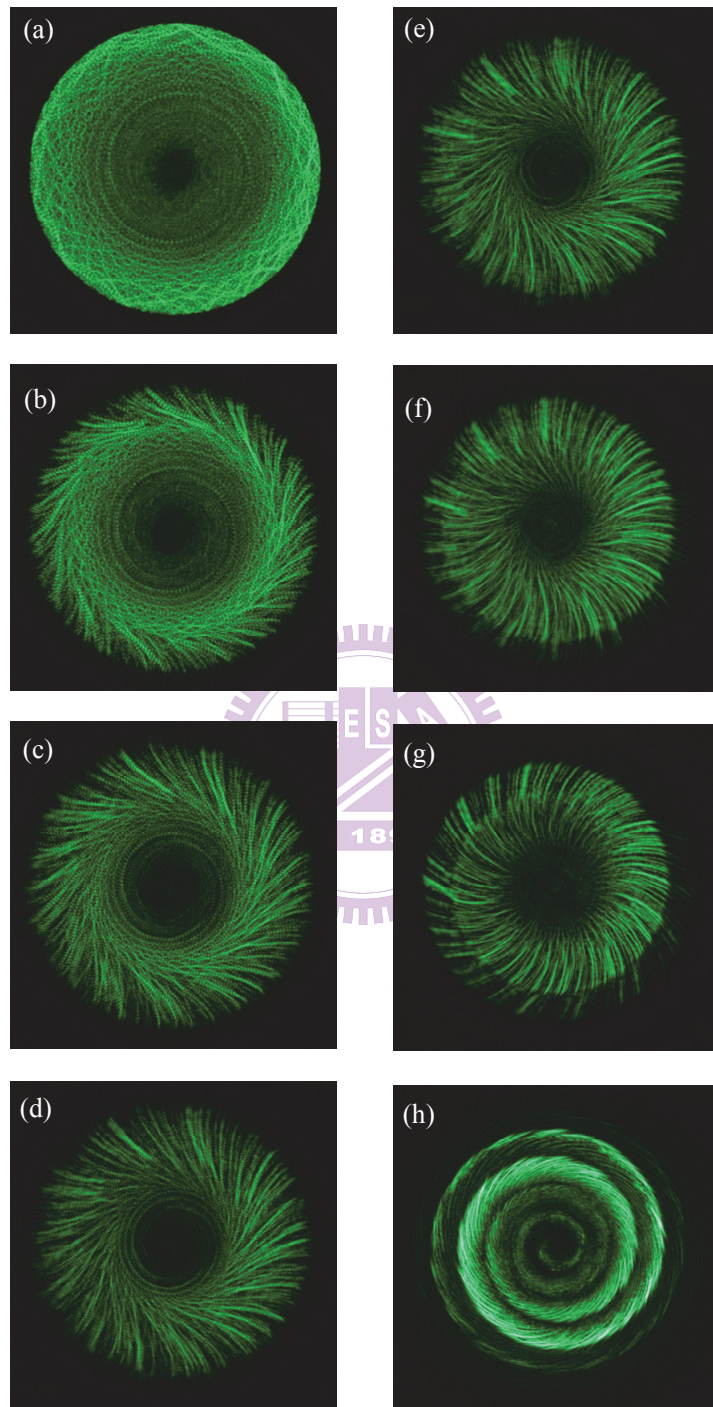


Fig. 3.2.8 Experimental patterns for the spiral patterns with irregular trajectories in the free-space propagation.

Reference

- [1] J. F. Nye and M. V. Berry, Proc. R Soc. London Ser. A 336, 165 (1974).
- [2] M. S. Soskin and M. V. Vasnetsov, Prog. Opt. 42, 219 (2001).
- [3] K. T. Gahagan, G. A. Swartzlander Jr., Opt. Lett. 21, 827 (1996).
- [4] M. Dienerowitz, M. Mazilu, P. J. Reece, T. F. Krauss, and K. Dholakia, Opt. Express 16, 4991 (2008).
- [5] J.M. Macdonald, G. Spalding, and K. Dholakia, Nature 426, 421 (2003).
- [6] G. A. Swartzlander Jr., Opt. Lett. 26, 497 (2001).
- [7] K. Crabtree, J. A. Davis, and L. Moreno, Appl. Opt. 43, 1360 (2004).
- [8] J. M. Hickmann, E. J. S. Fonseca, W. C. Soares, and S. Chávez Cerda, Phys. Rev. Lett. 105, 053904 (2010).
- [9] S. Fürhapter, A. Jesacher, S. Bernet, and M.R. Marte, Opt. Express 13, 689 (2005).
- [10] A. Jesacher, S. Fürhapter, S. Bernet, and M. R. Marte, J. Opt. Soc. Am. A 23, 1400 (2006).
- [11] E. Abramochkin and V. Volostnikov, Opt. Commun. 83, 123 (1991).
- [12] M. W. Beijersbergen, R. P. C. Coerwinkel, M. Kristensen, and J. P. Woerdman, Opt. Commun. 112, 321 (1994).
- [13] V. Yu. Bazhenov, M. S. Soskin, and M. V. Vasnetsov, J. Mod. Opt. 39, 985 (1992).
- [14] Y. J. Liu, X. W. Sun, D. Luo, and Z. Raszewsk, Appl. Phys. Lett. 92, 101114 (2008).
- [15] Ya. V. Izdebskaya, V. G. Shvedov, and A. V. Volyar, Opt. Lett. 30, 2472 (2005).
- [16] A. B. Matsko, A. A. Savchenkov, D. Strekalov, and L. Maleki, Phy. Rev. Lett. **95**, 143904 (2005).

- [17] J. Durnin, J. J. Miceli, and J. H. Eberly, *Phys. Rev. Lett.* **58**, 1499 (1987).
- [18] M. Brack and R. K. Bhaduri: *Semiclassical Physics*. (Westview Press, Boulder CO, USA 2003)
- [19] J. Wiersig and M. Hentschel, *Phys. Rev. Lett.* **100**, 033901 (2008).
- [20] C. Gmachl, F. Capasso, E. E. Narimanov, J. U. Nöckel, A. D. Stone, J. Faist, D. L. Sivco, A. Y. Cho, *Science* **280**, 1556 (1998).
- [21] N. B. Rex, H. E. Tureci, H. G. L. Schwefel, R. K. Chang, and A. D. Stone, *Phys. Rev. Lett.* **88**, 094102 (2002).
- [22] I. V. Zozoulenko and K. F. Berggren, *Phys. Rev. B* **56**, 6931 (1997).
- [23] W. A. De Heer, *Rev. Mod. Phys.* **65**, 611 (1993).
- [24] Y. F. Chen, T. H. Lu, K. W. Su, and K. F. Huang, *Phys. Rev. Letts.* **96**, 213902 (2006).
- [25] V. Bužek and T. Quang, *J. Opt. Soc. Am. B* **6**, 2447 (1989).
- [26] M. Moshinsky, *Phys. Rev.* **88**, 625 (1952).
- [27] S. Godoy, *Phys. Rev. A* **65**, 042111 (2002).
- [28] J. D. Murray, *Mathematical Biology* (Springer, Berlin, 1993).
- [29] A. N. Zaikin and A. M. Zhabotinsky, *Nature* **225**, 535 (1970).
- [30] M. Assenheimer and V. Steinberg, *Phys. Rev. Lett.* **70**, 3888 (1993);
- [31] M. Assenheimer and V. Steinberg, *Nature* **367**, 345 (1994).
- [32] M. C. Cross and P. Hohenberg, *Rev. Mod. Phys.* **65**, 851 (1993).
- [33] S. V. Kiyashko, L. N. Korzinov, M. I. Rabinovich, and L. S. Tsimring, *Phys. Rev. E* **54**, 5037 (1996).
- [34] John R. de Bruyn, B. C. Lewis, M. D. Shattuck, and Harry L. Swinney, *Phys. Rev. E* **63**, 041305 (2001).
- [35] S. Longhi, *Phys. Rev. E*, **63**, 055202 (2001).
- [36] E. G. Abramochkin, and V. G. Volostnikov, *Physics - Uspekhi* **47**, 1177 (2004).

- [37] F. X. Witkowski, L. J. Leon, P. A. Penkoske, W. R. Giles, M. L. Spano, W. L. Ditto and A. T. Winfree, *Nature*, 392, 78, (1998).
- [38] V. Panfilov, *Chaos* **8**, 57 (1998).
- [39] D. T. Kim, Y. Kwan, J. J. Lee, T. Ikeda, T. Uchida, K. Kamjoo, Y. Kim, J. J. C. Ong, C. A. Athill, T. Wu, L. Czer, H. S. Karagueuzian, and P. Chen, *Chaos* **8**, 137 (1998).



Chapter 4

Formation of Centrally Focused Beam via Intracavity Second Harmonic Generation

4.0 Introduction

Traveling-wave Laguerre-Gaussian $TEM_{p,l}$ ($LG_{p,l}$) modes display intriguing physics and have developing technology applications, where p and l are the indices in radial and azimuthal directions of the traveling-wave $LG_{p,l}$ modes. In 1992, Allen *et. al* have shown that the traveling-wave $LG_{p,l}$ modes with an azimuthal phase term $e^{il\phi}$ possess well-defined orbital angular momentum of $l\hbar$ per photon [1]. Since then, the optical beams with orbital angular momentum have been intensively studied in a variety of fields [2-5]. Unlike the traveling-wave $LG_{p,l}$ modes, standing-wave $LG_{p,l}$ modes are characterized by their flower-like profiles [6] and possess no net orbital angular momentum. It has been confirmed that the flower-like LG modes are formed by a coherent superposition of two traveling-wave $LG_{p,l}$ modes that carry the same topological charges l while with counter rotational wave fronts ($+l, -l$) [7]. The production of high-order standing-wave $LG_{p,l}$ modes has been reported in a large-aperture CO_2 laser [8], optically pumped [9] and electrically pumped [10] vertical-cavity surface emitting semiconductor lasers (VCSELs), and a solid-state laser cavity compounded of nonlinear medium [6,11-13]. The attractive features of the SLG modes lead to rich studies in the pattern formation [6,11-13] and recent research on the generation of the two-dimensional optical vortex array [7].

Besides the investigations into the optical properties of the traveling-wave $LG_{p,l}$ modes at fundamental wavelengths, Allen *et. al* reported further studies in the frequency doubling of the traveling-wave $LG_{p,l}$ modes through the second-harmonic generation (SHG) [14,15]. The second-harmonic wave is shown to be decomposed into a number of traveling-wave $LG_{p,l}$ modes with different indices. Since the components of different indices give rise to a varying Gouy phase shift between the modes, the resulting intensity distribution of the second-harmonic wave changes its profile during propagation. Hasegawa and Shimizu disclosed the same physical picture with frequency-doubled Hermite-Gaussian (HG) modes which are described as a coherent superposition of the orthonormal HG bases with different orders [16]. It can be noted that the second-harmonic waves can no longer be illustrated as a simple traveling-wave LG mode or HG mode. The wave interference of constituent modes with corresponded Gouy phase shift results in the interesting structures of the second-harmonic waves through propagation. The experiments for the generation of the frequency-doubled modes were carried out in the extracavity configurations of the SHG [14-16]. However, limited to the conversion efficiency of the extracavity scheme, the experiments only revealed the results concerning the SHG for the low-order fundamental modes. On the other hand, though the SHG for the essential optical modes has been thoroughly studied, frequency doubling of the standing-wave $LG_{p,l}$ modes that characterized by their highly-symmetric and fascinating structures has not been investigated as yet.

In this chapter we present the mode transformation of the high-order standing-wave $LG_{0,l}$ modes when undergoing the SHG. We theoretically validated that the frequency-doubled modes can be expressed as the interference between a set of traveling-wave $LG_{p,0}$ modes and a standing-wave $LG_{0,2l}$ mode with differing Gouy phase shift. We found that, through the second-harmonic process, a centrally focused

beam was formed along the propagation direction. The location of the maximum intensity on the longitudinal axis was numerically calculated to vary among the standing-wave LG modes of different orders. To generate such a centrally focused beam, we performed the experiment in a diode-pumped solid state laser with intracavity SHG. We employed a doughnut-shaped pump profile [11] to produce the highly-symmetric standing-wave $LG_{0,l}$ modes of varying orders for frequency doubling. The intracavity scheme with higher conversion efficiency enables the realization of the frequency conversion for the high-order standing-wave $LG_{0,l}$ modes. Since focused beams have great importance on practical uses [17-19], the presented centrally focused beam might have the potential for further applications.

4.1 Theoretical Analyses

4.1.1 Wave Functions of Laguerre-Gaussian Flower Modes

Under the paraxial approximation, one of the attracting solutions to the Helmholtz equation in terms of the cylindrical coordinates (r, ϕ, z) is the traveling-wave $LG_{p,l}$ modes. The profiles of the traveling-wave $LG_{p,l}$ modes with radial indices p and azimuthal indices l at frequency ω can be written as [20],

$$\Psi_{p,l}^{(\omega)}(r, \phi, z) = (-1)^p \frac{N_{p,l}}{w(z)} \left(\frac{\sqrt{2}r}{w(z)} \right)^{|l|} L_p^{|l|} \left(\frac{2r^2}{w(z)^2} \right) \exp(il\phi) \exp\left(-\frac{r^2}{w(z)^2}\right) \times \exp[-i\xi(r, \phi, z)] \exp[i(2p + |l| + 1)\theta_G(z)]. \quad (4.1.1)$$

Here $\theta_G(z) = \tan^{-1}(z/z_R)$ is the Gouy phase, $\xi(r, \phi, z) = kz \left[1 + r^2/2(z^2 + z_R^2) \right]$, k is the wave number, $z_R = k w_0^2/2$ is the Rayleigh range, w_0 is the beam radius at

$z=0$, $w(z) = w_0 \sqrt{1 + (z/z_R)^2}$ is the spot size at z ,

$N_{p,l} = \sqrt{2} p! / (1 + \delta_{0,l}) \pi (|l| + p)!$ is the constant for normalization where $\delta_{0,l} = 1$ for $l = 0$, and $L_p^{|l|}(\cdot)$ is the associated Laguerre polynomial of integer indices l and p in azimuthal and radial directions, respectively. The indices l can be zero, positive, or negative and $p \geq 0$.

The standing-wave $LG_{p,l}$ mode is verified to be the coherent superposition of a pair of traveling-wave $LG_{p,l}$ modes with equal but opposite topological charges $\pm l \hbar$ [7]. Based on the validation, the field distributions of the standing-wave $LG_{0,l}$ modes can be immediately obtained

$$\Phi_{p,l}^{(\omega)}(r, \phi, z, \alpha) = \frac{1}{2} [\Psi_{p,l}^{(\omega)}(r, \phi, z) + e^{-i\alpha} \Psi_{p,-l}^{(\omega)}(r, \phi, z)], \quad (4.1.2)$$

where α ranging from 0 to 2π signifies the relative phase between the two traveling-wave LG modes. Substitute Eq. (4.1.1) into Eq. (4.1.2), the coherent state $\Phi_{p,l}^{(\omega)}(r, \phi, z, \alpha)$ can be expressed as

$$\begin{aligned} \Phi_{p,l}^{(\omega)}(r, \phi, z, \alpha) = & (-1)^p \frac{N_{p,l}}{w(z)} \left(\frac{\sqrt{2}r}{w(z)} \right)^{|l|} \frac{L_p^{|l|}}{p!} \left(\frac{2r^2}{w(z)^2} \right) \\ & \times \cos \left[l \left(\phi + \frac{\alpha}{2l} \right) \right] \exp \left(-i \frac{\alpha}{2} \right) \exp \left(-\frac{r^2}{w(z)^2} \right) \\ & \times \exp \left[i(2p + |l| + 1) \theta_G(z) \right] \exp \left[-i\xi(r, \phi, z) \right]. \quad (4.1.3) \end{aligned}$$

Equation (4.1.3) reveals the distinct intensity distribution with $\cos^2 [l(\phi + \alpha/2l)]$ which suggests the flower-like profiles of the standing-wave $LG_{p,l}$ modes with $2l$ nodes in the azimuthal direction. The profiles of $|\Phi_{p,l}^{(\omega)}(r, \phi, z, \alpha)|^2$ can be found to rotate by an angle $\alpha/2l$ during a period of 2π retardation, where α are decided by initial conditions of the system. In the following, we focus our attention on the standing-wave $LG_{0,l}$ modes with vanishing radial indices, i.e. $p = 0$. For $p = 0$, the

associated Laguerre polynomial reduces to a constant and is independent of r . Figure 4.1.1 displays the intensity distribution of several high-order standing-wave $LG_{0,l}$ modes with different azimuthal indices l . The relative phases α are $-\pi/1.3$, $-\pi/1.3$, π , π , $-\pi$, 0 , $\pi/4$, π for Fig. 4.1.1(a)-4.1.1(h), respectively.

4.1.2 Second-harmonic Laguerre-Gaussian Flower Modes

Next we consider the standing-wave $LG_{0,l}$ modes when undergoing the phase-matching SHG. To simplify the analysis further, we assume that there is no absorption and neglect the depletion of the input wave. Under these conditions, the amplitude of the frequency-doubled field can be obtained to be proportional to the square of the fundamental field [14-16]. That is, the frequency-doubled field for the standing-wave $LG_{0,l}$ mode at the beam waist, $z=0$, is given by

$$E_{0,l}^{(2\omega)}(r, \phi, 0, \alpha) = D \left[\Phi_{0,l}^{(\omega)}(r, \phi, 0, \alpha) \right]^2, \quad (4.1.4)$$

where D is a constant related to the conversion efficiency in the second-harmonic process. It follows that the transformational relations $k' = 2k$ and $w'(z) = w(z)/\sqrt{2}$ ($w'_0 = w_0/\sqrt{2}$) are satisfied during the SHG, where k' and $w'(z)$ represent the wave number and the spot size of the frequency-doubled beam, respectively. Based on the relations, Eq. (4.1.4) becomes

$$E_{0,l}^{(2\omega)}(r, \phi, 0, \alpha) = D e^{-i\alpha} \frac{1}{2^{|l|} \pi |l|!} \left(\frac{1}{w'_0} \right)^2 \left(\frac{\sqrt{2}r}{w'_0} \right)^{2|l|} e^{-\frac{r^2}{w_0'^2}} \cos^2 \left[l \left(\phi + \frac{\alpha}{2l} \right) \right]. \quad (4.1.5)$$

To understand the second-harmonic process due to the wave interference of the corresponding components, we here provide further analysis for the frequency-doubled field, $E_{0,l}^{(2\omega)}(r, \phi, 0, \alpha)$. By substituting $\cos^2 \left[l \left(\phi + \frac{\alpha}{2l} \right) \right]$ with

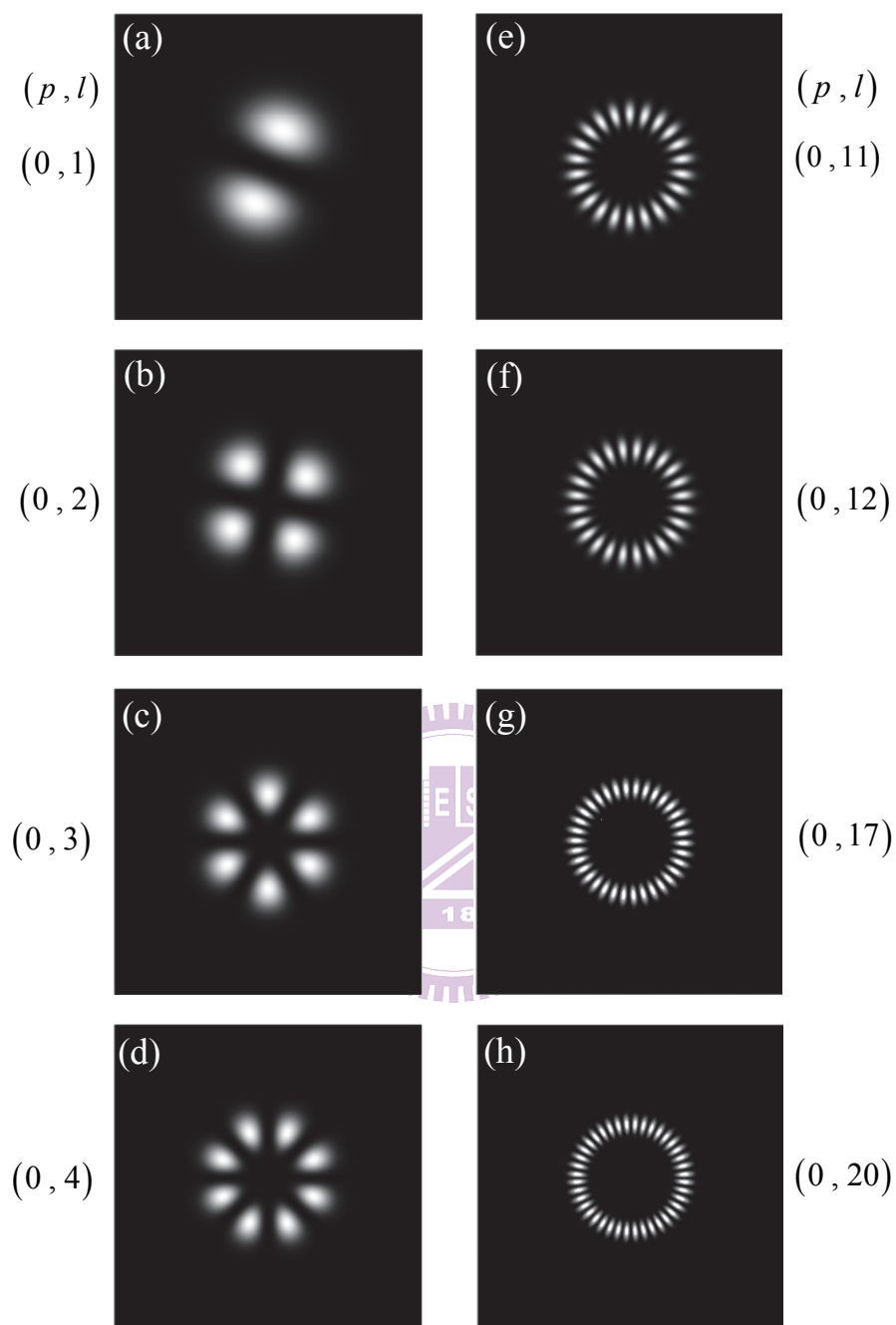


Fig. 4.1.1 (a)-(h) Theoretical results for the fundamental standing-wave $LG_{0,l}$ modes of different orders corresponding to the intensity distributions $|\Phi_{0,l}^{(\omega)}(r, \phi, z, \alpha)|^2$ at far field. For detailed description of the parameters; see the text.

its explicit expression according to the double-angle formula, $E_{0,l}^{(2\omega)}(r, \phi, 0, \alpha)$ in Eq.

(4.1.5) can be decomposed into two terms. Expanding $(\sqrt{2}r/w'_0)^{2|l|}$ in series of the

Laguerre polynomials [21]

$$x^{|l|} = |l|! \sum_{n=0}^{|l|} \binom{|l|}{n} (-1)^n L_n(x), \quad (4.1.6)$$

where $x = (\sqrt{2}r/w'_0)^2$ in our consideration and $\binom{|l|}{n} = \frac{|l|!}{n!(|l|-n)!}$ is the

binomial coefficient, we thus obtain that

$$E_{0,l}^{(2\omega)}(r, \phi, 0, \alpha) = \frac{D}{2^{|l|+1} \sqrt{\pi} w'_0} \times \left\{ \exp(-i\alpha) \sum_{n=0}^{|l|} \binom{|l|}{n} \Psi_{n,0}^{(2\omega)}(r, \phi, 0) + \frac{\sqrt{(2|l|)!}}{\sqrt{2}|l|!} \Phi_{0,2l}^{(2\omega)}(r, \phi, z, 2\alpha) \right\}. \quad (4.1.7)$$

It can be seen that the second-harmonic wave $E_{0,l}^{(2\omega)}(r, \phi, 0, \alpha)$ can be expanded by

the normalized set of the frequency-doubled traveling-wave $LG_{p,0}$ modes and the

standing-wave $LG_{0,2l}$ mode corresponding to Eq. (4.1.1) and Eq. (4.1.2) with $z = 0$

and w_0 replaced by w'_0 . Considering the general form for the second-harmonic

wave when propagating along the z direction, we can derive the z -dependent

expression for $E_{0,l}^{(2\omega)}$ from Eq. (4.1.7) as follows

$$E_{0,l}^{(2\omega)}(r, \phi, z, \alpha) = \frac{D}{2^{|l|+1} \sqrt{\pi} w'_0} \exp[-i\xi(r, \phi, z)] \times \left\{ \exp(-i\alpha) \sum_{n=0}^{|l|} \binom{|l|}{n} \Psi_{n,0}^{(2\omega)}(r, \phi, z) \exp[-i(2n+1)\theta_G(z)] \right\}$$

$$+ \left. \frac{\sqrt{(2|l|)!}}{\sqrt{2}|l|!} \Phi_{0,2l}^{(2\omega)}(r, \phi, z, 2\alpha) \exp[-i(2|l|+1)\theta_G(z)] \right\}. \quad (4.1.8)$$

Figure 4.1.2 demonstrates the theoretical results of the far-field patterns for the second-harmonic waves $E_{0,l}^{(2\omega)}(r, \phi, z, \alpha)$ corresponding to the fundamental waves displayed in Fig. 4.1.1. It can be noted that a Bessel-like profile due to the first term in Eq. (4.1.8) is formed at the center of the frequency-doubled beam. On the other hand, the flower-like structure whose azimuthal index l is doubled through the second-harmonic process is mainly contributed by the last term in Eq. (4.1.8).

4.1.3 Propagation of Second-harmonic Waves

In Fig. 4.1.3, we present the propagation of the frequency-doubled beam from the beam waist ($z=0$) for the fundamental standing-wave $LG_{0,12}$ mode according to Fig. 4.1.2(f). Figure 4.1.3(a) illustrates the side view of the second-harmonic wave along the z direction to reveal the formation of the centrally focused beam. The corresponding transverse intensity profiles at different longitudinal positions are depicted in Fig. 4.1.3(b)-4.1.3(i) where the fine multilayer structure is clearly visible at the center of the focused beam. A single standing-wave $LG_{0,l}$ mode propagates without changing its profile, only with a beam divergence determined by the size of the beam waist and the Rayleigh range. However, the second-harmonic wave exhibits the revolution along the longitudinal axis to form a centrally focused beam, which resulted from the interference of several LG modes with the corresponding Gouy phase shift.

Furthermore, Fig. 4.1.4(a)-4.1.4(d) display the side views of various centrally focused beams propagating along the longitudinal axis with indices $(p, l) = (0, 6)$,

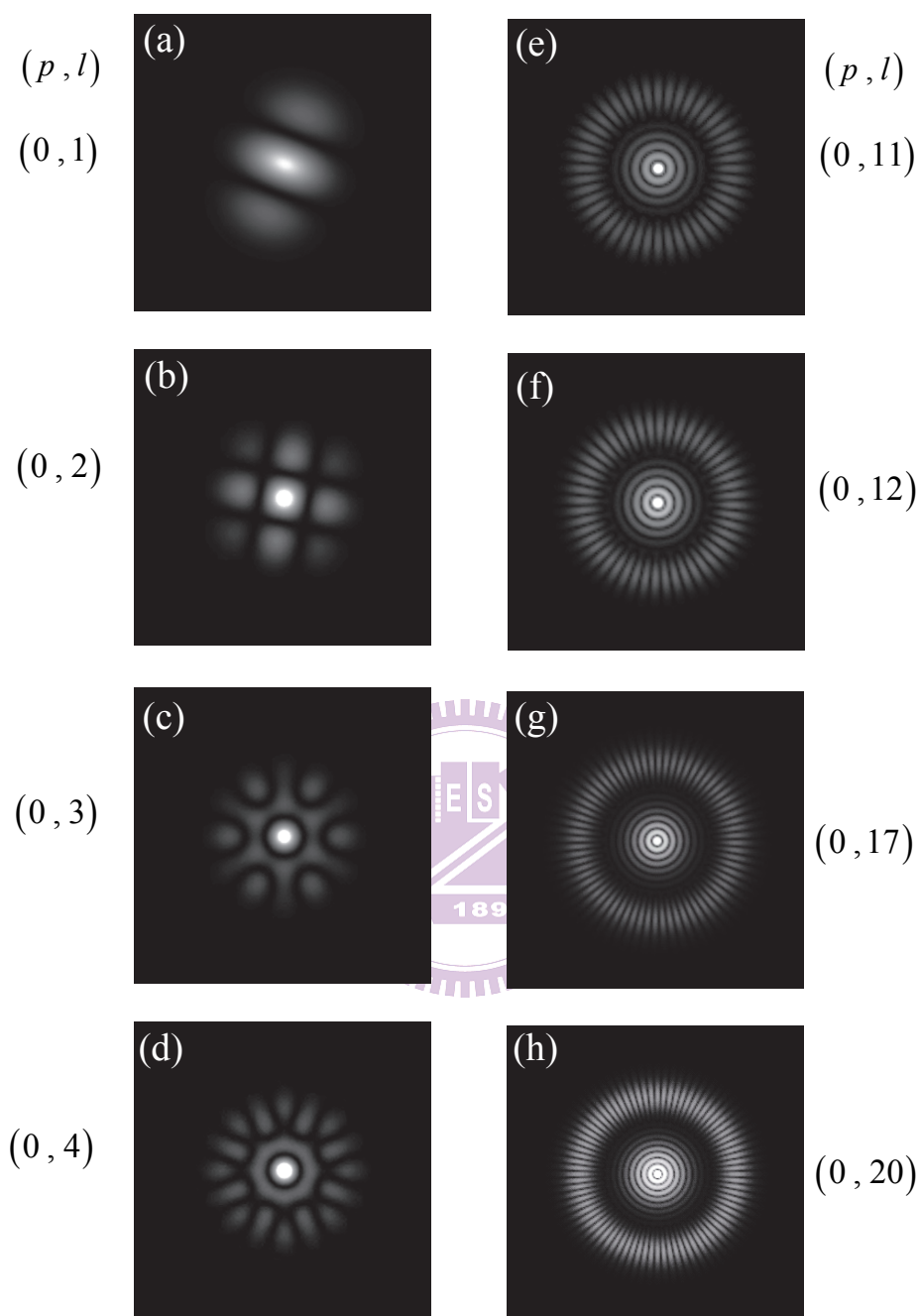


Fig. 4.1.2 (a)-(h) Theoretical simulations for the second-harmonic waves of intensity distributions $|E_{0,l}^{(2\omega)}(r, \phi, z, \alpha)|^2$ corresponding to Fig. 4.1.1.

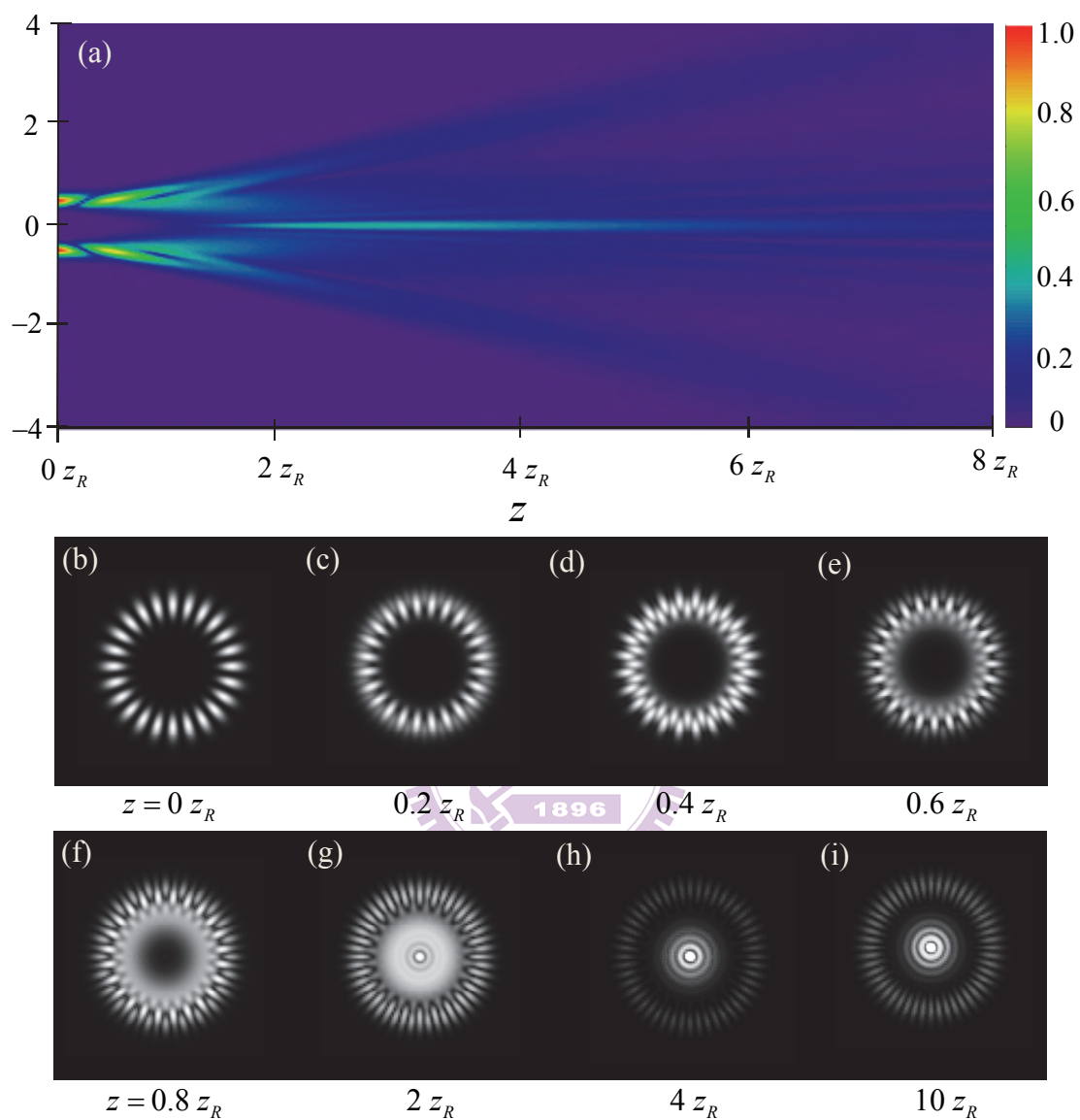


Fig. 4.1.3 (a) The side view of the frequency-doubled beam $|E_{0,12}^{(2\omega)}(r, \phi, z, \alpha)|^2$ as it propagates from the beam waist, (b) corresponding transverse intensity profiles.

$(p, l) = (0, 12)$, $(p, l) = (0, 20)$, and $(p, l) = (0, 40)$, respectively. The maximum intensity of the central profiles marked by the dashed lines is numerically calculated to vary among the fundamental standing-wave $LG_{0,l}$ modes of different orders. The maximum intensity are located at $z = 1.8 z_R$, $2.5 z_R$, $3.4 z_R$, and $4.7 z_R$ for Fig. 4.1.4(a)-4.1.4(d), respectively. As the order of the fundamental standing-wave $LG_{0,l}$ mode gets higher, the distance from the beam waist to the position of the maximum intensity becomes larger. The focusing phenomena of optical waves have great importance for applications such as optical trapping [17-18], and optical manufacturing [19]. Therefore, it might be useful to generate such centrally focused beams characterized by their inherent focusing phenomena through the SHG.

4.2 Experimental Observations

4.2.1 Experimental Setup

The schematic diagram for the experimental setup of a diode-pumped Nd:YVO₄ laser with a KTP crystal as an intracavity SHG medium is illustrated in Fig. 4.2.1. The experimental configuration was designed for the SHG at 532 nm from the fundamental wavelength at 1064 nm. The laser medium is an a-cut 2.0-at. % Nd:YVO₄ crystal with a length of 2 mm and the cross section $10 \times 10 \text{ mm}^2$. The SHG medium is a 10-mm-long KTP crystal with a cutting angle ($\theta=90^\circ$ and $\phi=23.5^\circ$) to satisfy the type II SHG phase matching condition. Both sides of the Nd:YVO₄ and KTP crystals were coated for antireflection at 1064 nm ($R < 0.2\%$). In addition, they were wrapped with indium foil and mounted in a water-cooled copper block. The front mirror is a 250-mm radius-of-curvature concave mirror with antireflection

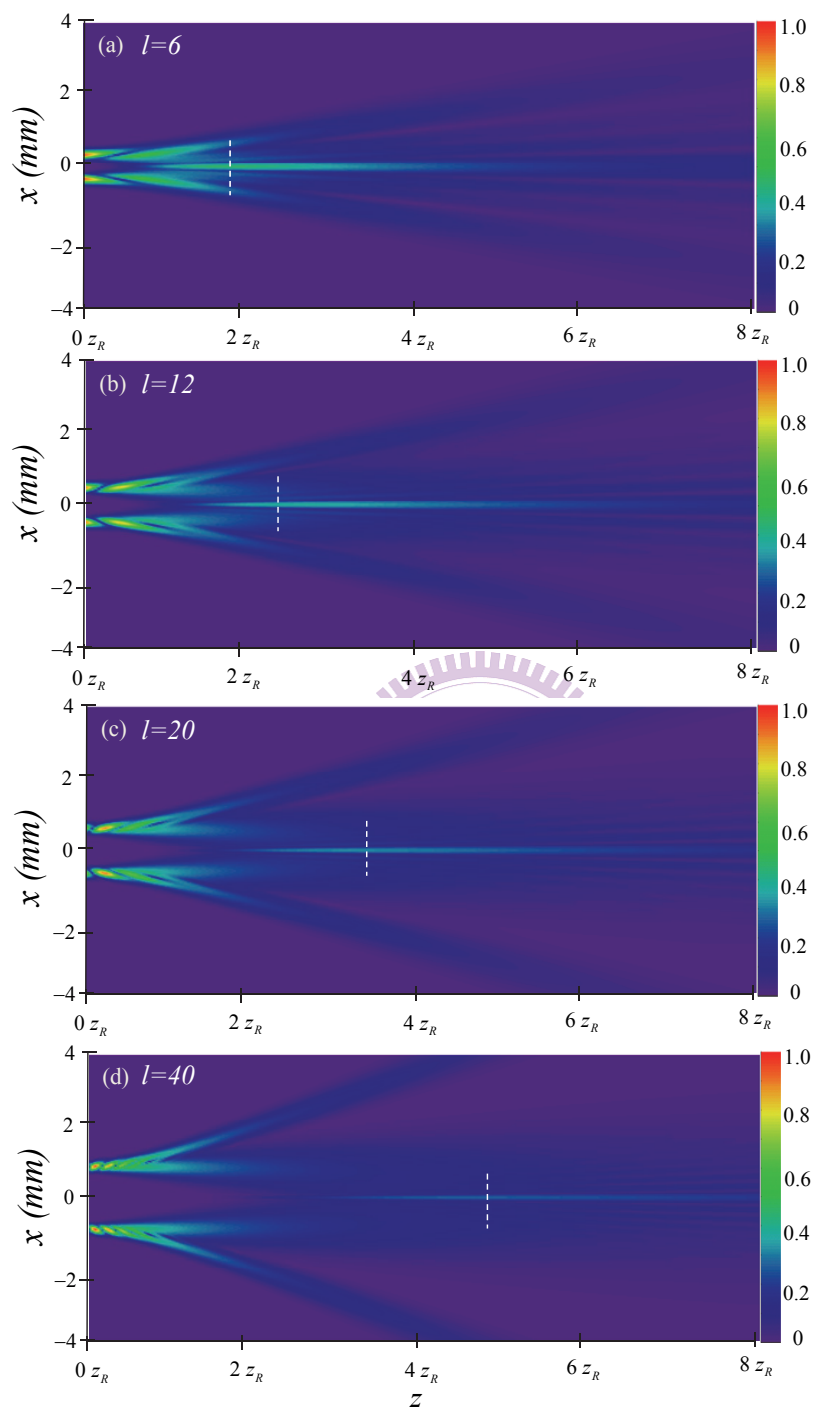


Fig. 4.1.4 (a)-(d) The side views of the frequency-doubled beams with different orders.

($R < 0.2\%$) coating at 808 nm on the entrance surface ($R < 0.2\%$), and high-reflection coating at 1064 ($R > 99.8\%$) nm and 532 nm ($R > 99\%$) on the other surface. The output coupler is a flat mirror with partial-reflection coating at 1064 nm ($R = 98\%$) and high-transmission coating at 532 nm ($T > 85\%$). The pump source is an 808 nm fiber-coupled laser diode with pump core of 100 μm in radius, a numerical aperture of 0.16, and a maximum output power of 1 W. A focusing lens with focal length of 25 mm and 85% coupling efficiency was used to reimage the pump beam into the laser medium. To generate the high-order standing-wave $\text{LG}_{0,l}$ modes of different orders, we employed a doughnut-shaped pump profile and defocused the standard fiber-coupled diode [11]. The standing-wave $\text{LG}_{0,l}$ modes of varying orders correspond to differing sizes of the pump profiles. The pump spot sizes were controlled to be at 50 – 200 μm . The overall cavity length is nearly 80 mm. According to the experimental scheme, the beam radius of the fundamental TEM_{00} mode can be calculated to be around 141 μm . The difference of the beam radius between adjacent standing-wave $\text{LG}_{0,l}$ modes is of the order 40 μm . The conversion efficiency for the standing-wave $\text{LG}_{0,0}$ mode from the diode laser incident power to the SHG output is about 12% . Moreover, filters placed after the laser cavity allow either the fundamental or the second-harmonic wave to be chosen and projected onto a screen. The projected patterns were observed through a CCD camera.

4.2.2 Generation of Centrally Focused Beams

Figure 4.2.2 and Fig. 4.2.3 display respectively the far-field patterns of a variety of fundamental standing-wave $\text{LG}_{0,l}$ modes and their frequency-doubled counterparts. The experimental observations show good agreement with the theoretical results as illustrated in Fig. 4.1.1 and Fig. 4.1.2. Moreover, the formation of the centrally focused beam corresponding to Fig. 4.1.3 has been confirmed via the measurement of

the transverse intensity profiles at different z planes as shown in Fig. 4.2.4. The experimental tomographic transverse patterns are found to be in accordance with the theoretical simulations in Fig. 4.1.3. It is worth to mention that the focusing phenomenon is a linear interference of the wave itself as we have validated in previous section and not the result of the nonlinear self-focusing effect. Since focused beams have always been a subject of practical interest, the second-harmonic waves presented here might be utilized for further applications.



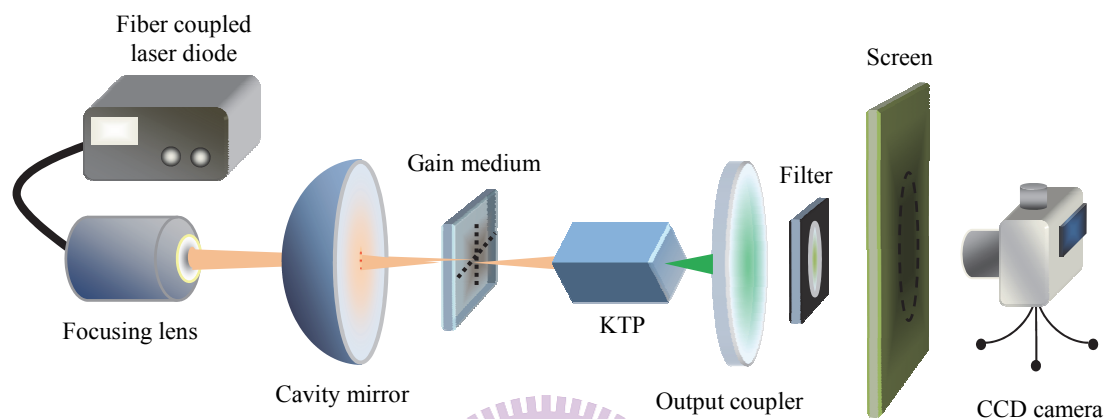
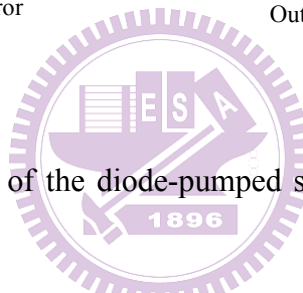


Fig. 4.2.1 Experimental setup of the diode-pumped solid-state laser with intracavity SHG.



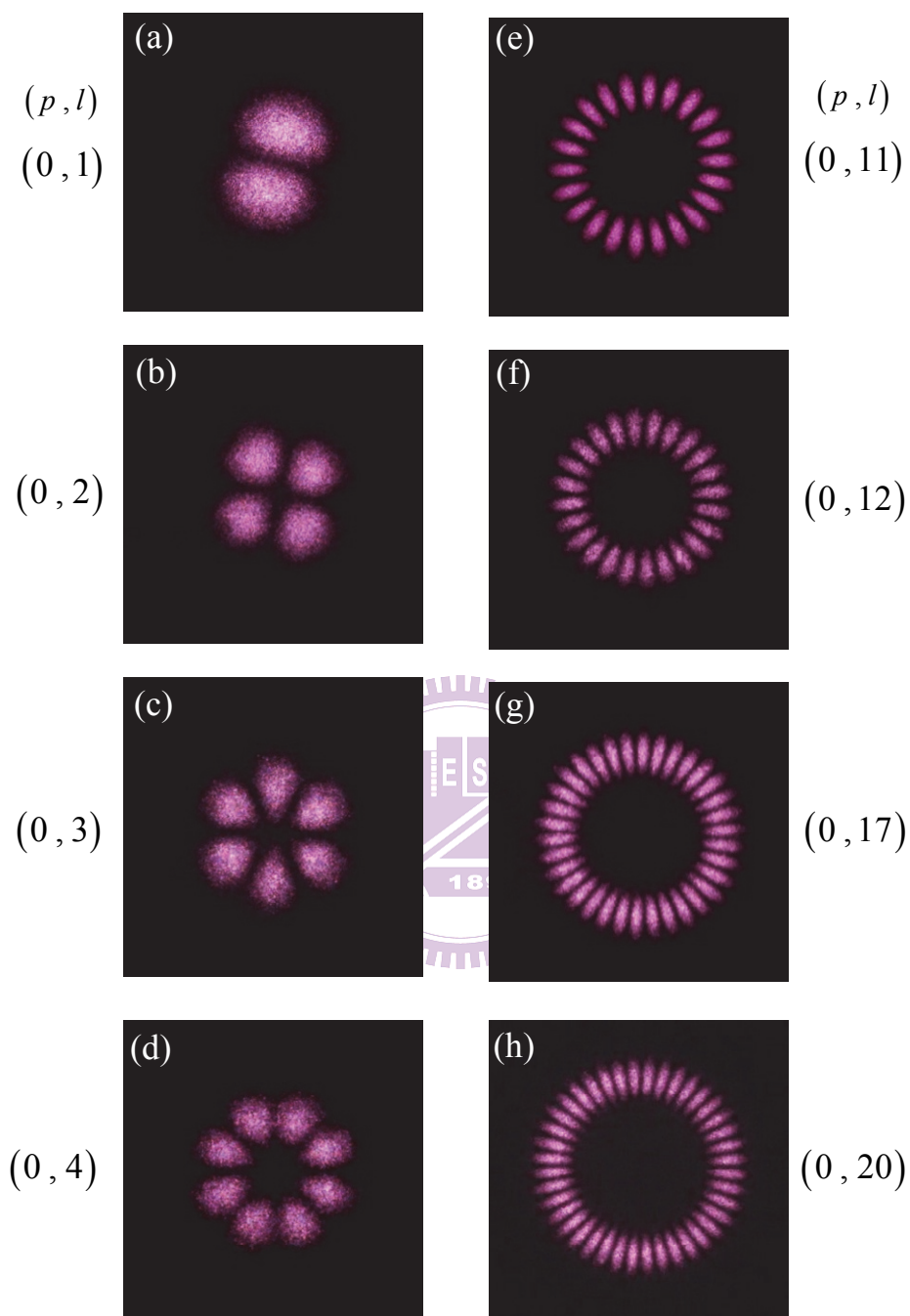


Fig. 4.2.2 Observed far-field patterns of the standing-wave $LG_{0,l}$ modes at the fundamental wavelength.

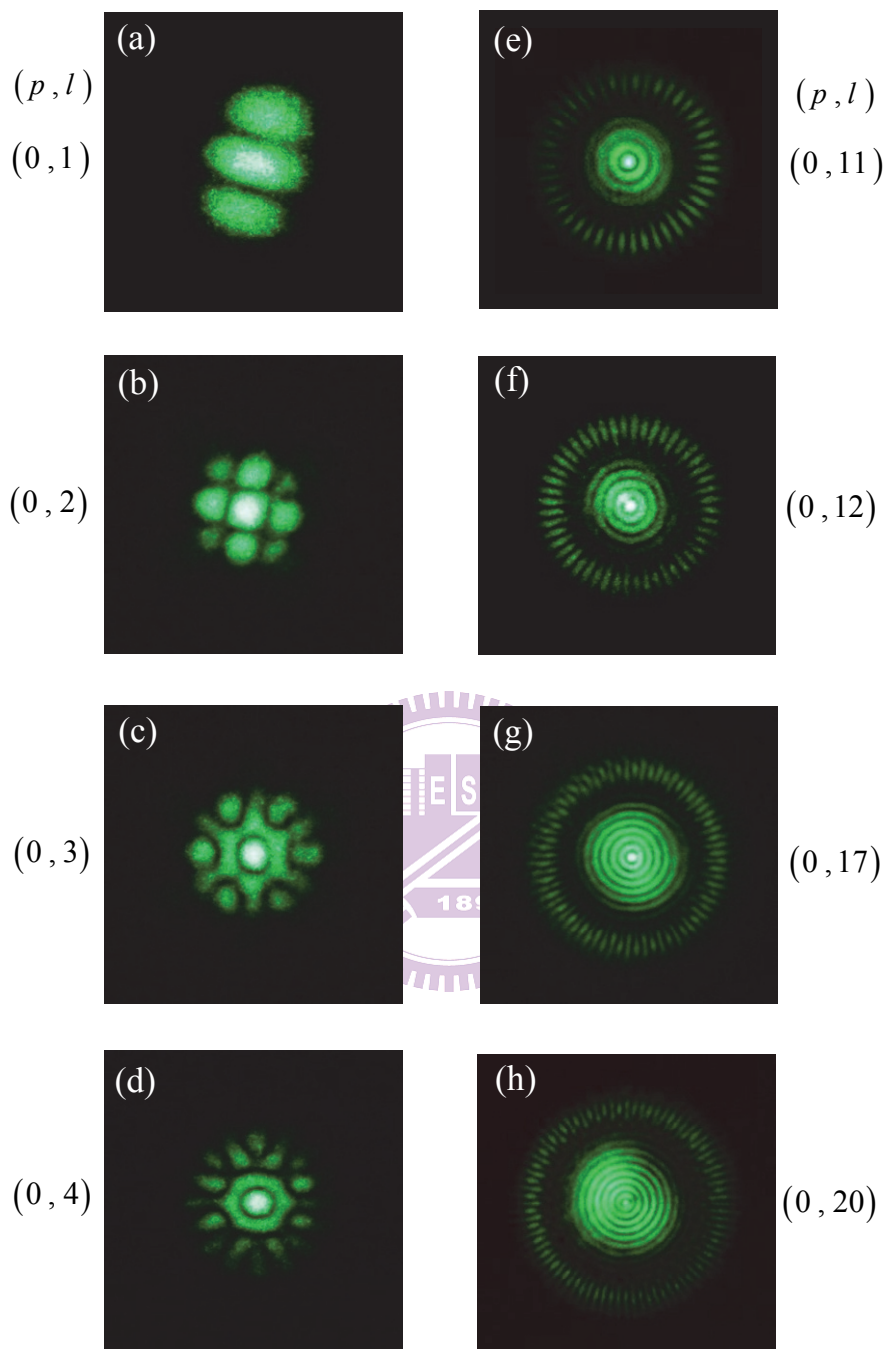


Fig. 4.2.3 Frequency-doubled counterparts of the fundamental standing-wave $LG_{0,l}$ modes in Fig. 4.2.2.

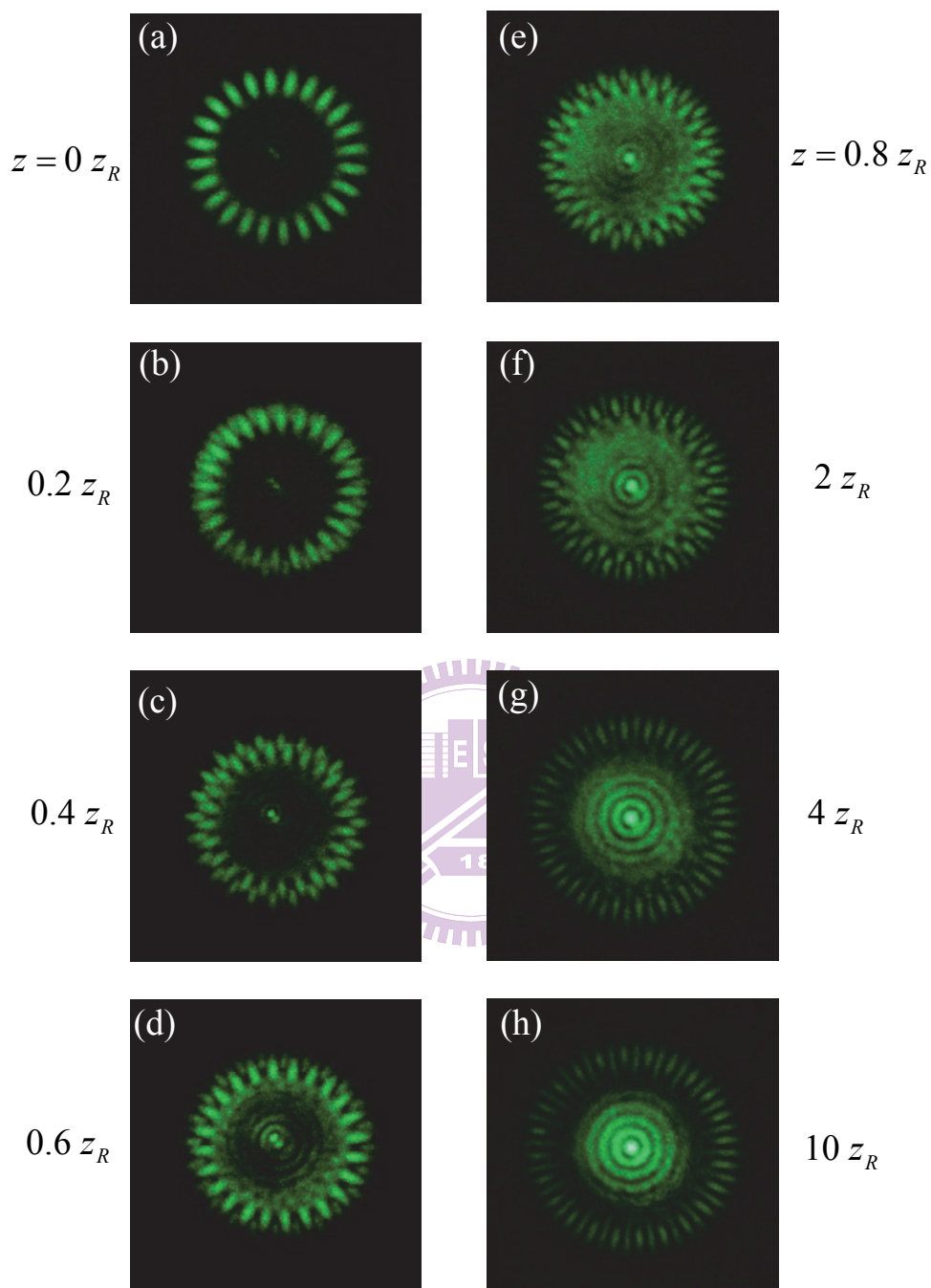
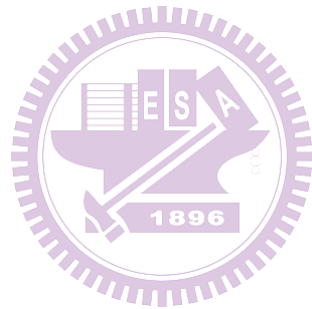


Fig. 4.2.4 Observed transverse intensity profiles along the longitudinal axis.

Reference

- [1] L. Allen, M.W. Beijersbergen, R.J.C. Spreeuw, J.P. Woerdman, Phys. Rev. A **45** 8185 (1992).
- [2] K. T. Gahagan and G. A. Swartzlander, Jr. Opt. Lett. **21**, 827 (1996).
- [3] H. Adachi, S. Akahoshi, and K. Miyakawa, Phys. Rev. A **75**, 063409 (2007).
- [4] A. Mair, A. Vaziri, G. Weihs, and A. Zeilinger, Nature **412**, 313 (2001).
- [5] P. Senthilkumaran, Appl. Opt. **42**, 6314 (2003).
- [6] G. Grynberg, A. Maitre, and A. Petrossian, Phys. Rev. Lett. **72** 2378 (1994).
- [7] Y. C. Lin, T. H. Lu, K. F. Huang, and Y. F. Chen, Opt. Express **19** 10293 (2011).
- [8] C. Green, G. B. Mindlin, E. J. D'Angelo, H. G. Solari, and J. R. Tredicce, Phys. Rev. Lett. **65**, 3124 (1990).
- [9] S. F. Pereira, M. B. Willemsen, M. P. van Exter, and J.P. Woerdman, Appl. Phys. Lett. **73**, 2239 (1998).
- [10] Q. Deng, H. Deng, and D. G. Deppe, Opt. Lett. **22**, 463 (1997).
- [11] Y. F. Chen, and Y. P. Lan, Phys. Rev. A **63**, 063807 (2001).
- [12] M. P. Thirugnanasambandam, Yu. Senatsky, and K. Ueda, Laser Phys. Lett. **7**, 637 (2010).
- [13] A. Ito, Y. Kozawa, and S. Sato, J. Opt. Soc. Am. A **27**, 2072 (2010).
- [14] K. Dholakia, N. B. Simpson, and M. J. Padgett, Phys. Rev. A **54**, R3742 (1996).
- [15] J. Courtial, K. Dholakia, L. Allen, and M. J. Padgett, Phys. Rev. A **56**, 4193 (1997).
- [16] T. Hasegawa, and T. Shimizu, Opt. Commun. **160**, 103 (1999).
- [17] A. Ashkin and J. M. Dziedzic, Science **235**, 1517 (1987).
- [18] P. Zhang, J. Prakash, Z. Zhang, M. S. Mills, N. K. Efremidis, D. N. Christodoulides, and Z. Chen, Opt. Lett. **36** 2883 (2011).

- [19] D. G. Papazoglou, N. K. Efremidis, D. N. Christodoulides, and S. Tzortzakis, *Opt. Lett.* **36** 1842 (2011).
- [20] A. E. Siegman, *Lasers* (University Science, 1986).
- [21] N. N. Lebedev and R. A. Silverman, *Special functions and their applications*, (Prentice-Hall, 1965).



Chapter 5

Weak Localization in Disordered Systems with Conical Second Harmonic Generation

5.0 Introduction

Wave localization, which originally results from the peculiar interference of waves scattered by disorders, is an intriguing phenomenon beyond diffusion theory and transfer treatment [1-3]. Since the fundamental processes of scattering and interference are identical for classical and quantum waves, the phenomena of wave localization have been extensively investigated in different physical systems [4-7]. Recent developments have led to much interest in various disordered media specified by weak (WL) [8-14] or strong localization (SL) [5,15-17]. It could be found [1-17] that the localization phenomenon is still an important issue and deserves further investigations.

Theoretical analyses and experimental observations for the disordered wave functions are the straightforward procedures to determine the extent of wave localization. Numerous theoretical models [18-22] have been constructed to explore the extent of wave localization. Recently, the nonlinear sigma models based on the supersymmetry theory have been employed to investigate the statistical properties of disordered wave functions [22]. The zero-dimensional (0D) nonlinear sigma model has been shown to be equivalent to the random matrix method [22] in the diffusive limit of disordered systems. In the weakly disordered systems, the wave functions are

widely spread over space, corresponding to the so-called extended states. With the one-dimensional (1D) nonlinear sigma model, the density distributions of the extended states can be expressed as an analytical formula related to the well-known Porter-Thomas (P-T) distribution [23]. On the other hand, the wave functions of the strongly disordered systems display log-normal asymptotic forms and long-tail characteristics in the density distributions [24,25], corresponding to the so-called pre-localized states. Fal'ko and Efetov [20] developed the reduced version of the nonlinear sigma model (RV-NLS model) to analyze the long-tail density distributions of the pre-localized states. Although the RV-NLS model seems to be applicable to quantify the varying extent of WL, detailed comparisons with experimental observations have not been performed as yet.

In experiments, the disordered wave functions were measured in a microwave cavity to show the influence of chaos and localization in disordered quantum billiards [13]. In 2006, Chen et al. [26] demonstrated the spatial structure of two-dimensional (2D) disordered wave functions from exploring the near-field patterns of conical second harmonic generation (SHG) in a GdCa₄O(BO) (GdCOB) nonlinear crystal with moderate defect domains. So far, experimental results for the disordered wave functions only covered a partial WL regime and did not provide a comprehensive analysis of the transition from extended to pre-localized states.

In this chapter we experimentally generate the 2D disordered wave functions by systematically scanning a GdCOB nonlinear crystal in the conical SHG process to explore the characteristics of WL. We numerically confirm that the RV-NLS model can provide statistical analyses to agree very well with the experimental wave functions with various localizations. Furthermore, we find that the density distributions of the disordered wave functions can be analytically expressed as the chi-square distributions with fractional parameters. Since the parameters in the formal

expression of chi-square distributions are only integers for the integral degrees of freedom [27], we use the terminology of *fractional* chi-square distribution to distinguish the difference. Finally, we construct the relationship between the RV-NLS model and the fractional chi-square distributions to reveal the characteristics of the fractional degrees of freedom in the disordered wave functions. Although the present results focus on the regime of WL, the fractional chi-square distribution might be useful for the full crossover of localization. We also believe that the present model can be employed to study the degree of localization in various disordered systems [8-14] such as scattering powder, cold atoms, randomized laser materials, liquid crystal, scattered systems, microcavities, and graphene.

5.1 Experimental Observations

5.1.1 Experimental Setup and Results


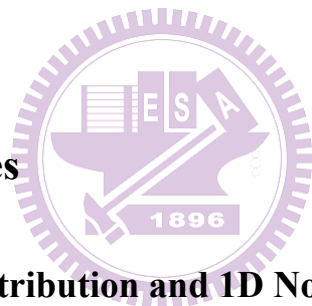


Figure 5.1.1 shows the experimental setup that is a diode-pumped actively Q-switched Nd: YAG laser with intracavity SHG in the GdCOB crystal. The gain medium is a 0.8-at. % Nd³⁺:YAG crystal with a length of 10 mm. The GdCOB crystal was cut for type I frequency doubling in the XY planes ($\theta = 90^\circ$, $\varphi = 46^\circ$) with a length of 2 mm and a cross section of 3 mm \times 3 mm. All crystals were coated for antireflection ($R < 2\%$) at 1064 nm on their both sides. The radius of curvature of the concave-front mirror is 50 cm with coating of antireflection ($R < 0.2\%$) at 808 nm, high-reflection ($R > 99.8\%$) at 1064 nm, and 532 nm on the entrance side and high-transmission ($T > 90\%$) at 808 nm on the other side. The output coupler is a planar mirror with coating of high-reflection ($R > 99.8\%$) at 1064 nm and high-transmission at 532 nm ($T > 85\%$). The pump source is a 10 W 808 nm fiber-coupled laser diode with a core diameter of 800 μm . A focusing lens with a focal length of 2.5 cm and 90% coupling

efficiency was employed to reimage the pump beam into the laser gain medium. The acoustic-optic Q switch with a length of 30 mm has coating with antireflection at 1064 nm on both sides and is driven at a 27.12-MHz center frequency with 15.0 W of rf power. An object lens was used to reimage the near-field patterns on the screen.

It has been shown that GdCOB crystals possess various random defect domains which can be used to generate the intensities $|\Psi(\vec{r})|^2$ of 2D disordered wave functions in the SHG process [26]. Here we find that the extent of random defect domains significantly depend on the transverse position of the GdCOB crystal. With this feature, we can scan all transverse positions of the GdCOB crystal to generate a variety of disordered wave functions from extended to pre-localized states as shown in Figs. 5.1.2(a)-5.1.2(f).

5.2 Statistical Analyses



5.2.1 Porter-Thomas Distribution and 1D Nonlinear Sigma Model

To determine the extent of localization, the density probability distribution $P(|\Psi(\vec{r})|^2)$ is illustrated to specify the localization of wave functions. For extended states in quantum chaotic systems, random-matrix method and equivalent 0D nonlinear σ model have been verified to give good explanations of universal statistic behaviors with the P-T distribution [22]. For weakly disordered systems, density probability of the normalized disordered wave functions can be expressed with 1D nonlinear σ model as [19,22,26]

$$P_{1D}(I) = P_{PT}(I) \left[1 + (\text{IPR} - 3) \left(\frac{1}{8} - \frac{1}{4}I + \frac{1}{24}I^2 \right) \right], \quad (5.2.1)$$

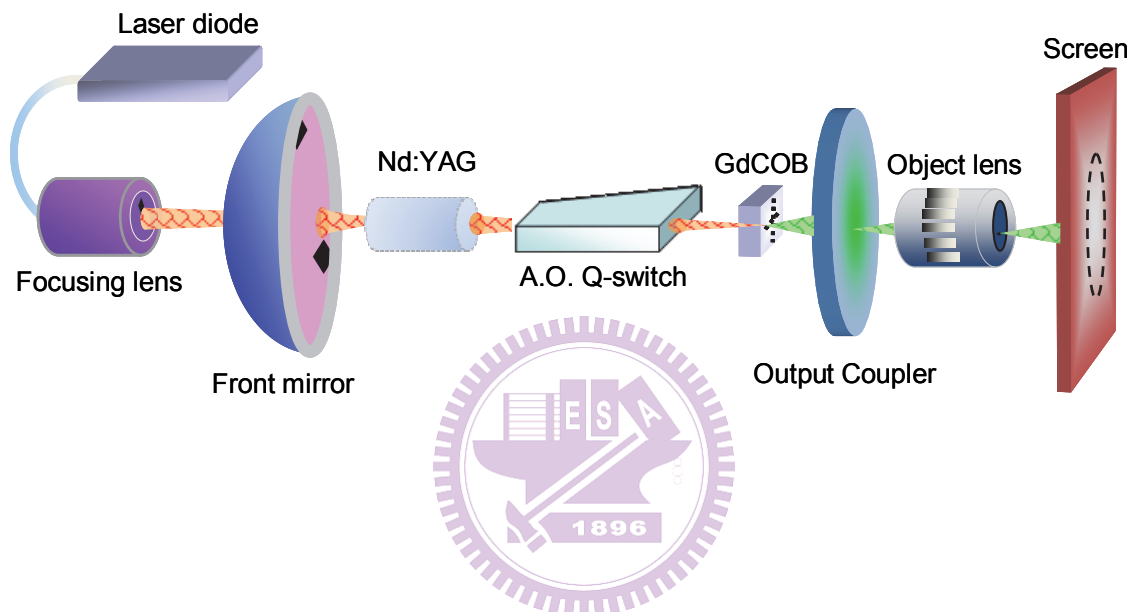


Fig. 5.1.1 Experimental setup for the generation of disordered wave functions with the diode-pumped Q-switched Nd:YAG laser of intracavity SHG in the GdCOB crystal.

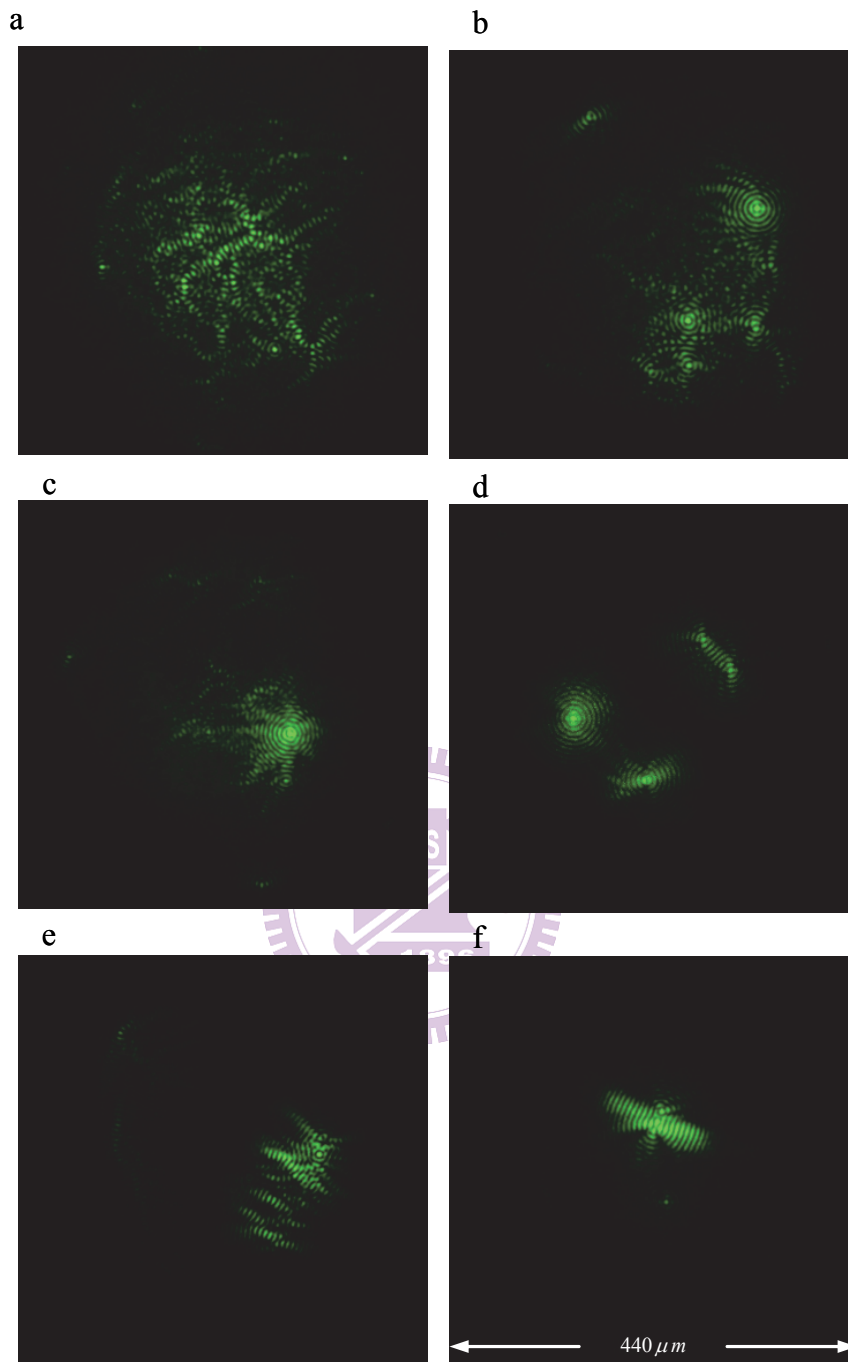


Fig. 5.1.2 (a)-(f) Experimental observation of near-field wave patterns measured at different transverse positions of the GdCOB crystal.

where $P_{PT}(I) = \exp(-I/2)/\sqrt{2\pi I}$ is the expression of the P-T distribution, and $IPR = \int I^2 d^2r$ is the inverse participation ratio associated with the extent of localization. For P-T distribution, the IPR can be directly achieved to be $IPR = \int_0^\infty I^2 P_{PT}(I) dI = 3.0$ indicating the chaotic systems. The larger the IPR value, the stronger the extent of localization is. As a result, the IPR values for disordered systems are greater than 3.0 in general. The IPR values for the experimental data in Fig. 5.2.1(a) and 5.2.1(b) are 3.3 and 5.72, respectively. Evidently, the fitting curve of 1D nonlinear σ model is validated to be consistent with the experimental data which displays small deviation to the P-T distribution in Fig. 5.2.1(a). However, as depicted in Fig. 5.2.1(b), the use of the perturbative result according to the 1D nonlinear σ model is violated obviously in the region where the deviation from the P-T distribution is considerable. Negative quantities of the density distribution $P(I)$ can be obtained for IPR values greater than 7.0. We numerically confirm that the 1D nonlinear σ model is only appropriate for the disordered wave function with $IPR < 5.5$. For stronger disorder, higher densities of the distribution functions decay more slowly in the region where 1D nonlinear σ models break down. Therefore, a more appropriate model should be given to clarify the varying extent of localization.

5.2.2 Reduced Version of the Nonlinear Sigma Model

In the following, we employ the experimental data to testify the RV-NLS model that is developed to quantitatively specify different regimes of localization. The RV-NLS model indicated by a dimensionless parameter g is given by [20,22]

$$P_\sigma(I; g) = \frac{A}{\sqrt{I}} \exp\left[-g\left(\frac{z(I)}{2} + \frac{z(I)^2}{4}\right)\right], \quad (5.2.2)$$

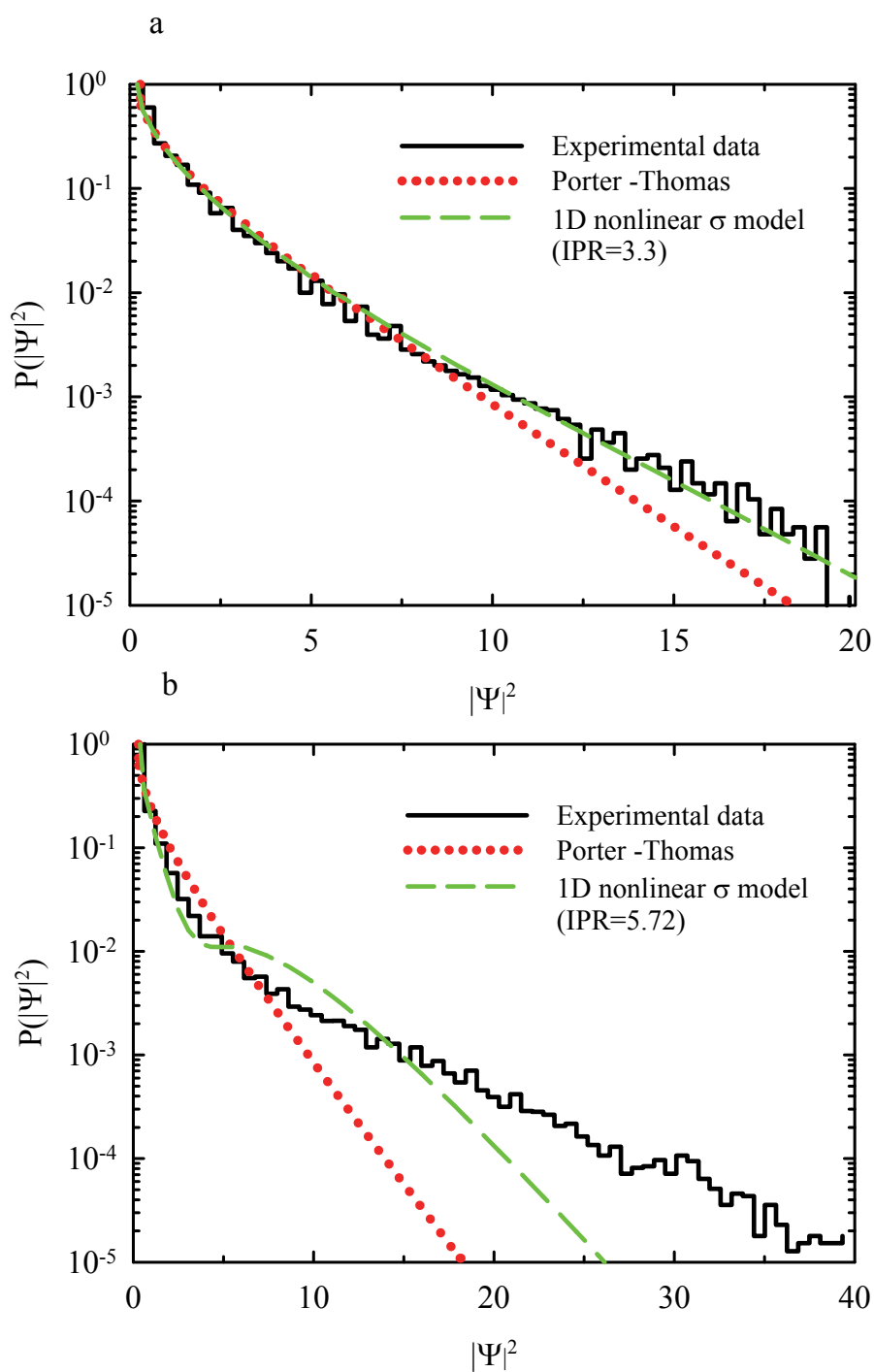


Fig. 5.2.1 (a)-(b) The density distribution $P(I)$ according to experimental data in Fig. 5.1.2(a) and 5.1.2(c), respectively.

where A is a normalized constant, $z(I)$ could be solved numerically according to the relation $z e^z = I/g$, and g is the dimensionless conductance [2,3] used to identify the degree of localization. The parameter g is also called the “Thouless number” which first proposed by Thouless in the discussion on the scaling theories of localization [2,3]. The dimensionless conductance g is adopted by the scaling theory as its only parameter and depends on the dimensionality of the system. For 2D case, $g \sim kl / \ln(L/l)$ [2] where k is the wave vector, $k = 2\pi/\lambda$, l signifies the value of mean free path, and L denotes the size of the system. The formal definition of g is $g \equiv G(L)/(e^2/2\hbar)$ (Ref. 2) where $G(L)$ is the conductance of a hypercube of size L^d , d relates to the dimensionality, \hbar is Plank’s constant, and e is the electronic charge. In the diffusive limit of $g \gg 1$, the density distribution reveals a universality of the statistics of localized waves. The value of g is substantially decreased due to WL which is the precursor of Anderson localization (SL) of $g \approx 1$ [28]. In other words, the scaling parameter g can be exploited to specify the extent of localization for the experimental results. Figures 5.2.2(a)- 5.2.2(f) depict the numerical results of the RV-NLS model for the best fits to the wave patterns shown in Figs. 5.1.2(a)-5.1.2(f), where the values of g are found to be 33, 11, 5.5, 3.5, 2.3, and 1.1, respectively. It can be seen that the density distributions generated with the RV-NLS model agree very well with the experimental results for all cases. Actually, K. B. Efetov [22] has once bought up the idea that the RV-NLS model can be applied to explain the statistical behavior for the disordered wave functions in a microwave cavity [13]. Employing the laser system with the conical SHG operation, we have verified here the practicability of the RV-NLS model in another disordered system. The fact implies possible extension of RV-NLS model on the studies of different extent of localization in various kinds of disordered systems.

5.2.3 Fractional Chi-square Distribution

Besides the verification of the RV-NLS model, we originally find that the chi-square distributions with fractional parameters can satisfactorily describe the experimental results. The analytic expression of the chi-square distributions is given by [27]

$$P_{CS}(I; \nu) = \Gamma(\nu/2)^{-1} (\nu I/2)^{\nu/2} I^{-1} e^{-\nu I/2}, \quad (5.2.3)$$

where $\nu > 0$ is a parameter referred to the number of degrees of freedom and $\Gamma(\nu/2)^{-1}$ is the gamma function which serves to normalize the density distributions $P_{CS}(I; \nu)$. The P-T distribution $P_{PT}(I)$ is the chi-square distribution with one degree of freedom, i.e. $P_{CS}(I; \nu = 1)$ [23]. In addition, the exponential distribution $\exp(-I)$ can be referred to the chi-square distribution with two degrees of freedom, i.e. $P_{CS}(I; \nu = 2)$. Even though there is no conceptual difficulty to extend an integer value of ν to a non-integer, it has not been confirmed that whether non-integer degrees of freedom have any applications in nature. As shown in Figs. 5.2.2(a)–5.2.2(f), the chi-square distributions with $0.06 \leq \nu < 1$, almost identical to the features of the RV-NLS model, can excellently illustrate the experimental results. The values of ν for experimental wave patterns in Figs. 5.1.2(a)–5.1.2(f) are 0.774, 0.54, 0.32, 0.20, 0.126, and 0.06, respectively. The evidence shows that the tails of the density distribution decay more slowly at small values of ν and the degree of localization becomes larger while the values of ν decrease rapidly. The investigation yields a clear result that the fractional chi-square distribution could be a powerful procedure for analyzing the statistical properties of the localization phenomena. It is well-known that the non-integer dimensionality is an important property of most fractals. Our exploration reveals that non-integer or fractional parameters are also valid concepts in statistical distributions of disordered wave functions.

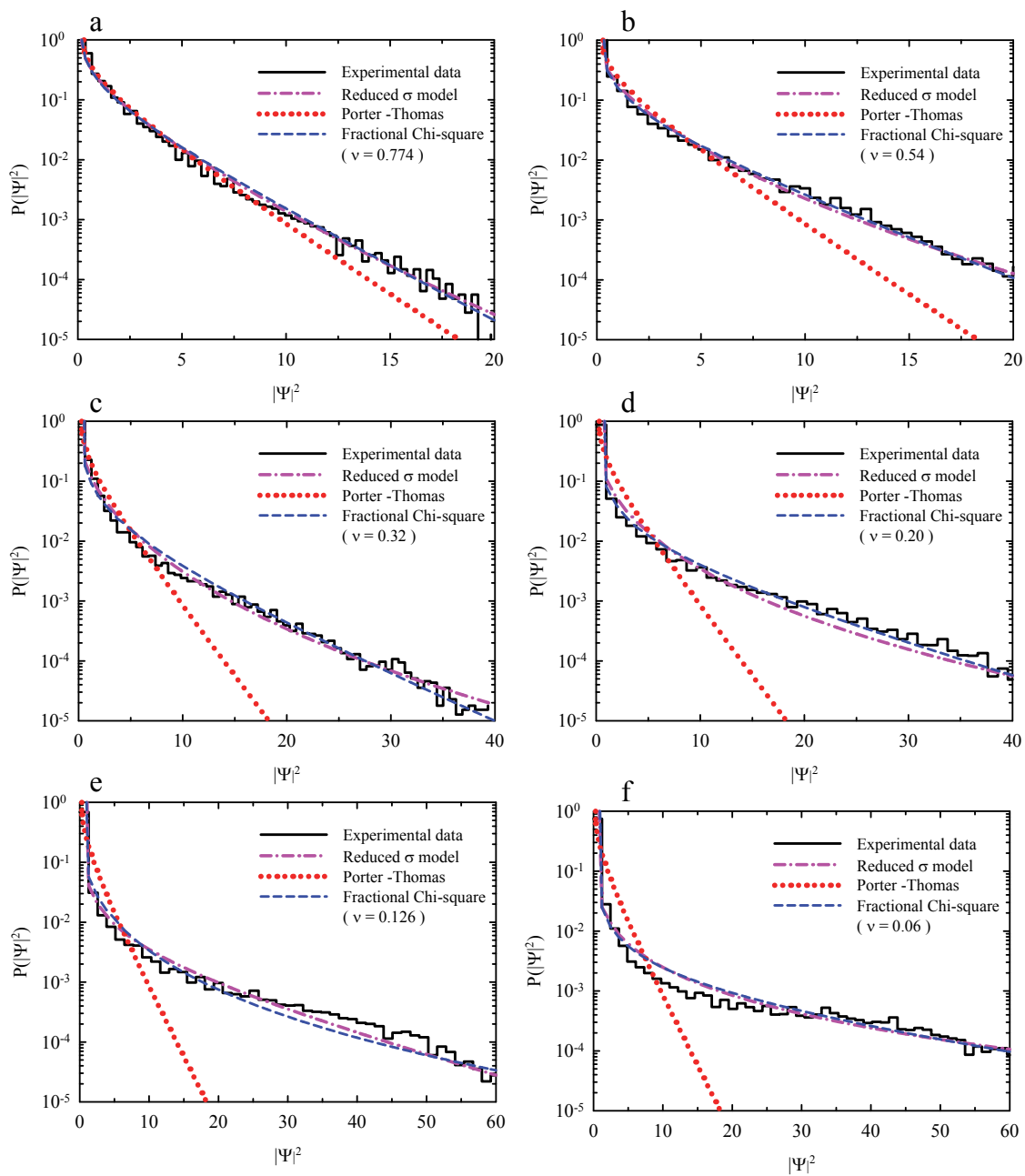
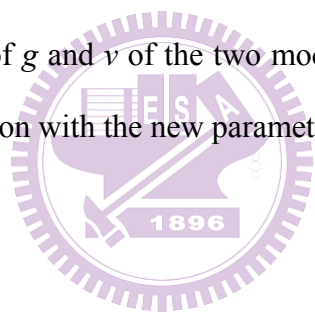


Fig. 5.2.2 (a)-(f) Experimental and theoretical density distributions $P(I)$ corresponding to experimental data in Fig. 5.1.2(a)-5.1.2(f), respectively.

5.2.4 Relation between Statistical Models

The validity and equivalence between the density distributions $P_{CS}(I; \nu)$ and $P_{\sigma}(I; g)$ imply that the two parameters ν and g are related. The relationship between ν and g according to the experimental results is marked with blue dots in Fig. 5.2.3. We employ an empirical form of $\nu = 1 - \exp[-0.08 g^{0.85}]$ to express the relationship between ν and g , as depicted with a solid line in Fig. 5.2.3. The empirical expression indicates the two properties: one is $\nu \rightarrow 1$ as $g \rightarrow \infty$ to indicate no WL effects and the other is $\nu_c \approx 0.06$ with $g \approx 1$ to signify the SL threshold. In other words, the statistical properties for the WL and SL effects can be manifested with the the chi-square distributions with the parameters in the region of $\nu_c \leq \nu < 1$ and $0 \leq \nu < \nu_c$, respectively. Taking the familiar parameter g as a standard of scaling, the careful mapping of g and ν of the two models helps to clarify the regime of different extent of localization with the new parameter ν .



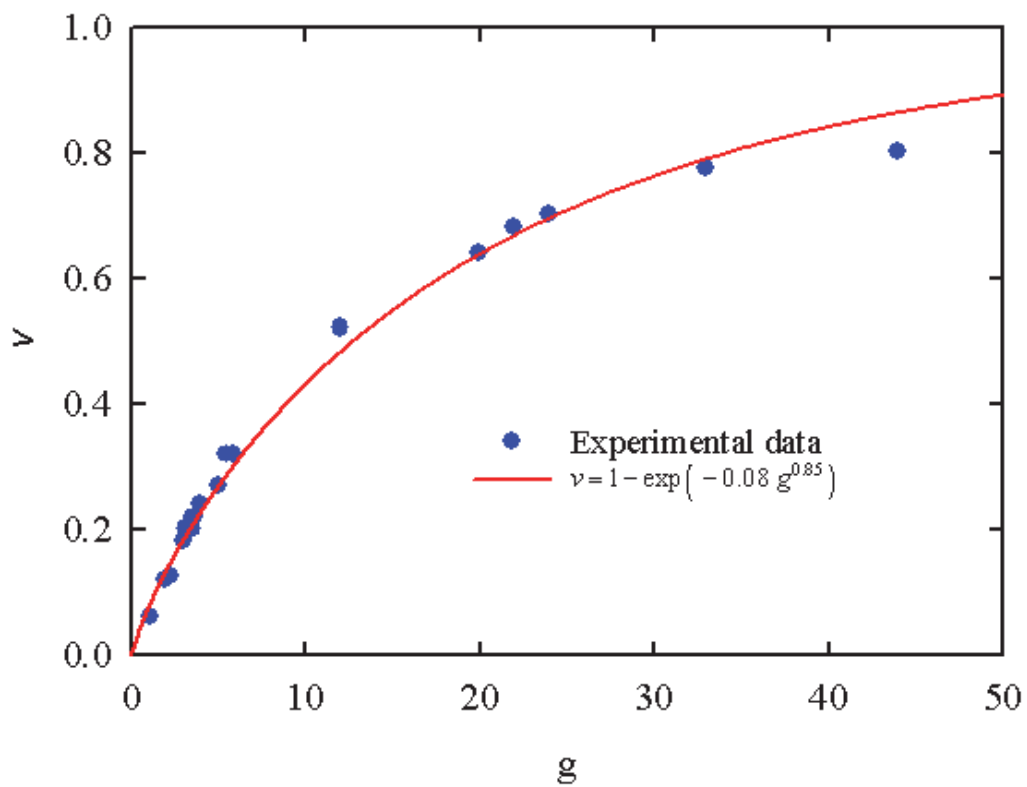


Fig. 5.2.3 Blue dots: The relation between ν and g according to the experimental data.
Red line: Empirical form for the relationship between ν and g .

Reference

- [1] P. W. Anderson, Phys. Rev. **109**, 1492 (1958).
- [2] E. Abrahams, P. W. Anderson, D. C. Licciardello, and T. V. Ramakrishnan, Phys. Rev. Lett. **42**, 673 (1979).
- [3] P. W. Anderson, D. J. Thouless, E. Abrahams, and D. S. Fisher, Phys. Rev. B **22**, 3519 (1980).
- [4] M. Kaveh, M. Rosenbluh, I. Edrei, and I. Freund, Phys. Rev. Lett. **57**, 2049 (1986).
- [5] J. Billy, V. Josse, Z. Zho, A. Bernard, B. Hambrecht, P. Lugan, D. Clément, L. Sanchez-Palencia, P. Bouyer, and A. Aspect, Nature, **453**, 891 (2008).
- [6] D. Laurent, O. Legrand, P. Sebbah, C. Vanneste, and F. Mortessagne, Phys. Rev. Lett. **99**, 253902 (2007).
- [7] H. Hu, A. Strybulevych, J. H. Page, S. E. Skipetrov, and B. A. Van Tiggelen, Nature, **4**, 945 (2008).
- [8] D. S. Wiersma, M. P. van Albada, B. A. van Triggelen, and A. Lagendijk, Phys. Rev. Lett. **74**, 4193 (1995).
- [9] P. E. Wolf, and G. Maret, Phys. Rev. Lett. **55**, 2696 (1985).
- [10] G. Labeyrie, F. De Tomasi, J. C. Bernard, C. A. Muller, C. Miniatura, and R. Kaiser, Phys. Rev. Lett. **83**, 5266 (1999).
- [11] R. Sapienza, S. Mujumdar, C. Cheung, A. G. Yodh, and D. Wiersma, Phys. Rev. Lett. **92**, 033903 (2004).
- [12] F. V. Tikhonenko, D. W. Horsell, R. V. Gorbachev, and A. K. Savchenko, Phys. Rev. Lett. **100**, 056802 (2008).
- [13] A. Kudrolli, V. Kidambi, and S. Sridhar, Phys. Rev. Lett. **75**, 822 (1995).
- [14] M. Gurioli, F. Bogani, L. Cavidli, H. Gibbs, G. Khitrova, and D. S. Wiersma,

- Phys. Rev. Lett. **94**, 183901 (2005).
- [15] S. John, Phys. Rev. Lett. **58**, 2486 (1987).
- [16] T. Schwartz, G. Bartal, S. Fishman, and M. Segev, Nature, **446**, 52 (2007).
- [17] G. Roati, C. D'Errico, L. Fallani, M. Fattori, C. Fort, M. Zaccanti, G. Modugno, M. Modugno, and M. Inguscio, Nature, **453**, 895 (2008).
- [18] A. D. Mirlin, and Y. V. Fyodorov, J. Math. A: Math. Gen. **26**, L551 (1993).
- [19] Y. V. Fyodorov, and A. D. Mirlin, Phys. Rev. B, **51**, 13 403 (1995).
- [20] V. I. Fal'ko, and K. B. Efetov, Phys. Rev. B, **52**, 17 413 (1995).
- [21] A. D. Mirlin, Phys. Rev. B, **53**, 1186 (1996).
- [22] K. B. Efetov, *Supersymmetry in Disorder and Chaos* (Cambridge University Press, Cambridge, 1997).
- [23] C. E. Porter, and R. G. Thomas, Phys. Rev. **104**, 483 (1956).
- [24] I. I. Kogan, C. Mudry, and A. M. Tsvelik, Phys. Rev. Lett. **77**, 707 (1996).
- [25] A. Ossipov, T Kottos, and T. Geisel, Phys. Rev. E, **65**, 055209 (2002).
- [26] Y. F. Chen, K. W. Su, T. H. Lu, and K. F. Huang, Phys. Rev. Lett. **96**, 033905 (2006).
- [27] G. G. Roussas, *A Course in Mathematical Statistics* (Academic Press, California, 1997).
- [28] A. Lagendijk, B. van Tiggelen, and D. S. Wiersma, Phys. Today, **62**, 24 (2009).

Chapter 6

Summary and Future Work

6.1 Summary

In section 2.1.1, we have theoretically derived the eigenstates of the coupled isotropic HO, which reveals the continuous transformation from the HG to the LG states. In section 2.2.2, we have performed the analogous optical experiment to systematically reconstruct the transformational relation between the HG and LG modes with a cylindrical-lens mode converter. In section 2.1.2, we have verified that the spatial morphologies of the Lissajous states can be continuously transformed into the trochoidal states with spatial morphologies corresponding to the trochoidal curves by converting the HG components into the corresponding LG modes. In section 2.2.3, we have further exploited the optical Lissajous modes and a $\pi/2$ cylindrical lens mode converter to perform the spatial transformation in analogous way and to generate the intermediate optical modes between the optical Lissajous and trochoidal modes. Experimental realization confirmed a notable method to generate the spatial coherent states with various orbital morphologies. The present method is expected to be constructive for investigating the spatial transformation of optical coherent waves. In section 2.1.3, we have systematically investigated the quantum signatures of the eigenstates corresponding to the coupled commensurate HO with $SU(2)$ coupling interactions. The eigenstates are shown to be concentrated on the multiple periodic orbits that transform from the multiple Lissajous orbits to the multiple trochoidal orbits. In section 2.2.4, we have explored the analogous observation of the laser

transverse modes from large-Fresnel-number degenerate cavities via varying pumping size. It has been experimentally verified that the 3D coherent lasing waves corresponding to the quantum states with multiple Lissajous orbits can be systematically generated by enlarging the pumping spot size. We also employ the propagating property of the lasing modes to manifest the role of the phase factor introduced by the $SU(2)$ coupling interactions. Moreover, we apply the cylindrical-lens mode converter to confirm the transformational relation between the multiple Lissajous orbits and the multiple trochoidal orbits. Section 2.3 is the further extension of section 2.1 and 2.2. We develop a novel method of creating optical vortex array by the conversion of a standing-wave Laguerre-Gaussian (LG) mode. Theoretically, by employing the transformational relation, the standing-wave LG mode is verified to be transformed from a pair of crisscrossed Hermite-Gaussian (HG) modes, embedded with optical vortex array, consists of a $TEM_{n,m}$ mode and a $TEM_{m,n}$ mode. Due to close correspondence between the transformational relation and the mode conversion of astigmatic lenses, we successfully generate the optical vortex array by transforming a standing-wave LG mode into the crisscrossed HG modes via a $\pi/2$ cylindrical lens mode converter. The investigation may provide useful insight in the study of the vortex light beam and its further applications.

In chapter 3, we have exploited the Bessel's integral to analytically manifest the ray-wave correspondence between high-order Bessel beams and geometric modes in circular billiards. We also experimentally demonstrated that the Bessel-related geometric modes can be strikingly generated by utilizing a large-aperture cylindrical waveguide with controlling the extent of the incident angle. Moreover, we demonstrated that the free-space propagation of the output beam emerging from the cylindrical waveguide could be used to investigate the transient dynamics of the geometric modes. We believe that the present investigation can provide an important

insight into quantum physics and wave optics.

In chapter 4, we have theoretically demonstrated the mode transformation of the high-order standing-wave $LG_{0,l}$ modes when undergoing the phase-matching SHG. The SHG for the standing-wave $LG_{0,l}$ modes has been verified to cause the formation of the centrally focused beams which propagate with their transverse intensity profiles changed. The theoretical analysis reveals that the revolution of the centrally focused beam along the longitudinal axis results from the interference of a set of traveling-wave $LG_{p,0}$ and a standing-wave $LG_{0,2l}$ modes according to different Gouy phase shift. Furthermore, we have employed a diode-pumped solid-state laser with intracavity SHG to carry out the experiment. By controlling the spot sizes of the doughnut-shaped pump profiles, we have effectively generated the high-order standing-wave $LG_{0,l}$ modes of varying orders for frequency-doubling. The experimental results of the second-harmonic waves are shown to be in good agreement with the theoretical analysis. Our studies might provide some useful insights into the wave functions for the nonlinear conversion.

In chapter 5 we have experimentally generated the optical patterns from the conical SHG process to investigate the disordered wave functions with different extents of WL from extended to pre-localized states. It has been numerically confirmed that the statistical characteristics of experimental disordered wave functions can be explained very well with the RV-NLS model. Furthermore, we have found that the fractional chi-square distributions are nearly equivalent to the distributions of the RV-NLS model. With this result, the concept of the fractional degrees of freedom can be used to manifest the extent of localization for the disordered wave functions. It is believed that the present work can bring more insight into the localization phenomena of diverse disordered systems.

6.2 Future work

In chapter 4, we have thoroughly investigated the formation of the centrally focused beam with the second-harmonic generation (SHG) of a high-order Laguerre-Gaussian mode. It can be found that the obtained second-harmonic waves characterized by their intricate structures reveal fairly different morphologies to the input fundamental waves. The intriguing observations stimulate our interests in the SHG for the localized coherent waves as discussed in chapter 2. However, the restriction of the conversion efficiency for the SHG of such a high-order laser mode might cause the major difficulty in carrying out the experiment. Once we can overcome the limitation, it could be expected that the second-harmonic coherent waves associated with the input localized modes might display considerably complicated configurations.



Appendix A

Derivation of the Eigenstates to the Harmonic Oscillator with SU(2) Coupling

The Hamiltonian for a two-dimensional (2D) isotropic harmonic oscillator with SU(2) coupling can be given by

$$\hat{H} = \hat{H}_0 + \Omega_1 \hat{J}_1 + \Omega_2 \hat{J}_2 + \Omega_3 \hat{J}_3. \quad (\text{A.1})$$

In terms of the dimensionless spatial representation, (A.1) can be rewritten as

$$\begin{aligned} \hat{H} = & \frac{1}{2}(\tilde{x}^2 + \tilde{p}_x^2 + \tilde{y}^2 + \tilde{p}_y^2)\omega_0 + \frac{\Omega_1}{2}(\tilde{x}\tilde{y} + \tilde{p}_x\tilde{p}_y) + \frac{\Omega_2}{2}(\tilde{x}\tilde{p}_y - \tilde{y}\tilde{p}_x) \\ & + \frac{\Omega_3}{4}(\tilde{x}^2 + \tilde{p}_x^2 - \tilde{y}^2 - \tilde{p}_y^2). \end{aligned} \quad (\text{A.2})$$

$$\hat{H} \rightarrow \hat{H}'$$

Try to eliminate the second term with Ω_1 , we employ the following transformation for the operators:

$$\begin{cases} \tilde{x} = \tilde{x}' \cos \phi + \tilde{p}_x' \sin \phi \\ \tilde{y} = \tilde{y}' \cos \phi - \tilde{p}_y' \sin \phi \end{cases}, \quad \begin{cases} \tilde{p}_x = -\tilde{x}' \sin \phi + \tilde{p}_x' \cos \phi \\ \tilde{p}_y = \tilde{y}' \sin \phi + \tilde{p}_y' \cos \phi \end{cases}, \quad (\text{A.3})$$

where $2\phi = \tan^{-1}(\Omega_2/\Omega_1)$. Substitute Eq. (A.3) into Eq. (A.2), the Hamiltonian in

Eq. (A.2) hence can be written as

$$\begin{aligned} \hat{H}' = & \frac{1}{2}(\tilde{x}'^2 + \tilde{p}_x'^2 + \tilde{y}'^2 + \tilde{p}_y'^2)\omega_0 + \frac{\sqrt{\Omega_1^2 + \Omega_2^2}}{2}(\tilde{x}'\tilde{y}' + \tilde{p}_x'\tilde{p}_y') \\ & + \frac{\Omega_3}{4}(\tilde{x}'^2 + \tilde{p}_x'^2 - \tilde{y}'^2 - \tilde{p}_y'^2). \end{aligned} \quad (\text{A.4})$$

$$\hat{H}' \rightarrow \hat{H}''$$

Try to eliminate the third term with Ω_3 in \hat{H}' :

$$\begin{cases} \tilde{x}' = \tilde{x}'' \cos \theta - \tilde{y}'' \sin \theta \\ \tilde{y}' = \tilde{x}'' \sin \theta + \tilde{y}'' \cos \theta \end{cases} \quad \begin{cases} \tilde{p}_x' = \tilde{p}_x'' \cos \theta - \tilde{p}_y'' \sin \theta \\ \tilde{p}_y' = \tilde{p}_x'' \sin \theta + \tilde{p}_y'' \cos \theta \end{cases}, \quad (\text{A.5})$$

where $2\theta = \tan^{-1}\left(\sqrt{\Omega_1^2 + \Omega_2^2}/\Omega_3\right)$. Substituting Eq. (A.5) into (A.4), we obtain that

$$\begin{aligned} \hat{H}'' &= \frac{1}{2}(\tilde{x}''^2 + \tilde{p}_x''^2 + \tilde{y}''^2 + \tilde{p}_y''^2)\omega_0 + \frac{\Omega}{4}(\tilde{x}''^2 + \tilde{p}_x''^2 - \tilde{y}''^2 - \tilde{p}_y''^2) \\ &= \frac{1}{2}(\hat{x}''^2 + \hat{p}_x''^2)\omega_1 + \frac{1}{2}(\hat{y}''^2 + \hat{p}_y''^2)\omega_2, \end{aligned} \quad (\text{A.6})$$

where $\Omega = \sqrt{\Omega_1^2 + \Omega_2^2 + \Omega_3^2}$, $\omega_1 = \omega_0 + \Omega/2$, and $\omega_2 = \omega_0 - \Omega/2$. Obviously, the eigenvalues and eigensates $|n_1, n_2\rangle_{\hat{H}''}$ in terms of the spatial representation for

\hat{H}'' can be given by

$$E_{n_1, n_2} = \left(n_1 + \frac{1}{2}\right)\hbar\omega_1 + \left(n_2 + \frac{1}{2}\right)\hbar\omega_2, \quad (\text{A.7})$$

and

$$\Psi_{n_1, n_2}(x'', y'') = \frac{1}{\sqrt{2^{n_1} n_1!} \sqrt{\pi}} \frac{1}{\sqrt{2^{n_2} n_2!} \sqrt{\pi}} H_{n_1}(x'') e^{-\frac{x''^2}{2}} H_{n_2}(y'') e^{-\frac{y''^2}{2}}, \quad (\text{A.8})$$

Solve \hat{H} :

We have already got the solutions of \hat{H}'' . Such transformations in Eq. (A.3), and (A.5) enable us to simplify the question with the well-known eigenstates Hermite-Gaussian states of the uncoupled Hamiltonian \hat{H}'' . At the end, we will show that the eigenstates of the coupled oscillator can be expressed as the superposition of Hermite-Gaussian states. Now let us back to our question in the beginning with the 2D coupled harmonic oscillator—solving the eigenstates and eigenvalues of it. Furthermore, using the ladder operators may help us explicitly figure out the question. The ladder operators can be given by

$$\begin{cases} \tilde{x}'' = \frac{1}{\sqrt{2}}(\hat{a}'' + \hat{a}''^\dagger) \\ \tilde{p}_x'' = \frac{i}{\sqrt{2}}(\hat{a}''^\dagger - \hat{a}'') \end{cases}, \quad \begin{cases} \tilde{y}'' = \frac{1}{\sqrt{2}}(\hat{b}'' + \hat{b}''^\dagger) \\ \tilde{p}_y'' = \frac{i}{\sqrt{2}}(\hat{b}''^\dagger - \hat{b}'') \end{cases}. \quad (\text{A.9})$$

Equations (A.5) can be rewritten in the form of the ladder operators:

$$\begin{cases} \hat{a}''^\dagger = (\hat{a}'^\dagger \cos \theta + \hat{b}'^\dagger \sin \theta) \\ \hat{b}''^\dagger = (-\hat{a}'^\dagger \sin \theta + \hat{b}'^\dagger \cos \theta) \end{cases}. \quad (\text{A.10})$$

Since the ground state $|0,0\rangle$ is invariant under transformation of the coordinate, it is obvious that $|0,0\rangle_{\hat{H}''} = |0,0\rangle_{\hat{H}'}$. Therefore, the eigenstates $|n_1, n_2\rangle_{\hat{H}''}$ can be written as

$$\begin{aligned} |n_1, n_2\rangle_{HO}'' &= \frac{(\hat{a}''^\dagger)^{n_1}}{\sqrt{n_1!}} \frac{(\hat{b}''^\dagger)^{n_2}}{\sqrt{n_2!}} |0,0\rangle_{\hat{H}''} \\ &= \frac{(\hat{a}''^\dagger)^{n_1}}{\sqrt{n_1!}} \frac{(\hat{b}''^\dagger)^{n_2}}{\sqrt{n_2!}} |0,0\rangle_{\hat{H}'} \\ &= \frac{(\hat{a}'^\dagger \cos \theta + \hat{b}'^\dagger \sin \theta)^{n_1} (-\hat{a}'^\dagger \sin \theta + \hat{b}'^\dagger \cos \theta)^{n_2}}{\sqrt{n!} \sqrt{(N-n)!}} |0,0\rangle_{\hat{H}'}, \end{aligned} \quad (\text{A.11})$$

where $n_1 + n_2 = N$, $n_1 = n$, $n_2 = N - n$, and N is a constant. This condition is required for the energy degeneracy. Furthermore, we use the Binomial series to expand Eq. (A.11):

$$\begin{aligned} &|n_1, n_2\rangle_{\hat{H}''} \\ &= \sum_{v_1} \sum_{v_2} \frac{C_{v_1}^n (\hat{a}'^\dagger \cos \theta)^{v_1} (\hat{b}'^\dagger \sin \theta)^{n-v_1} C_{v_2}^{N-n} (-\hat{a}'^\dagger \sin \theta)^{v_2} (\hat{b}'^\dagger \cos \theta)^{N-n-v_2}}{\sqrt{n!} \sqrt{(N-n)!}} |0,0\rangle_{\hat{H}'} \\ &= \sum_{s=0}^N \sum_v \frac{C_{s-v}^n (\hat{a}'^\dagger \cos \theta)^{s-v} (\hat{b}'^\dagger \sin \theta)^{n-s+v} C_v^{N-n} (-\hat{a}'^\dagger \sin \theta)^v (\hat{b}'^\dagger \cos \theta)^{N-n-v}}{\sqrt{n!} \sqrt{(N-n)!}} |0,0\rangle_{\hat{H}'} \\ &= \sum_{s=0}^N \sum_v (-1)^v \frac{\sqrt{n!} \sqrt{(N-n)!} (\cos \theta)^{N-n+s-2v} (\sin \theta)^{n-s+2v} (\hat{a}'^\dagger)^s (\hat{b}'^\dagger)^{N-s}}{(s-v)!(n-s+v)!(N-n-v)!v!} |0,0\rangle_{\hat{H}'} \end{aligned}$$

$$= \sum_{s=0}^N d_{s-\frac{N}{2}, n-\frac{N}{2}}^{\frac{N}{2}}(2\theta) |s, N-s\rangle_{\hat{H}'}, \quad (\text{A.12})$$

where $v_1 = s - v$, $v_2 = v$, $v_1 + v_2 = s$ ($s = 0 \dots N$), $C_k^n = n! / [(n-k)!k!]$, and the

Wigner d -coefficient is given by

$$d_{s-\frac{N}{2}, n-\frac{N}{2}}^{\frac{N}{2}}(2\theta) = \sqrt{s!} \sqrt{(N-s)!} \sqrt{n!} \sqrt{(N-n)!} \\ \times \sum_{v=\max[0, s-n]}^{\min[N-n, s]} \frac{(-1)^v (\cos \theta)^{N-s+n-2v} (-\sin \theta)^{s-n+2v}}{(n-v)!(s-n+v)!(N-s-v)!v!}. \quad (\text{A.13})$$

Similarly, according to Eq. (A.3), the ladder operators can be obtained to be

$$\begin{cases} \hat{a}'^\dagger = \hat{a}^\dagger e^{-i\phi} \\ \hat{b}'^\dagger = \hat{b}^\dagger e^{i\phi} \end{cases}. \quad (\text{A.14})$$

Substitute Eq. (A.14) into Eq. (A.12), an extra phase term is introduced:

$$|n_1, n_2\rangle_{\hat{H}''} = e^{iN\phi} \sum_{s=0}^N e^{-is(2\phi)} d_{s-\frac{N}{2}, n-\frac{N}{2}}^{\frac{N}{2}}(2\theta) |s, N-s\rangle_{\hat{H}}. \quad (\text{A.15})$$

Eq. (A.15) presents the eigenstates of the coupled harmonic oscillator, where one can replace 2ϕ by α and 2θ by β to correspond to Eq. (2.1.11).

Appendix B

Derivation of the General Expression for a High-order Hermite-Gaussian Mode Transforming through an ABCD System with the Huygens Integral

The general form for the Huygens integral in one transverse dimension in terms of the ABCD matrix can be given by

$$u(x_2, z_2) = \sqrt{\frac{j}{B\lambda_0}} \exp(-jkL) \times \int_{-\infty}^{\infty} u(x_1, z_1) \exp\left[-j \frac{\pi(Ax_1^2 - 2x_1x_2 + Dx_2^2)}{B\lambda_0}\right] dx_1. \quad (\text{B.1})$$

where λ_0 is the optical wavelength in free space and L is the length for the ABCD system.

B.1 Input a Hermite-Gaussian Mode

Consider an input beam of a high-order Hermite-Gaussian (HG) mode in the form

$$u_n(x_1, z_1) = \sqrt{\frac{\sqrt{2}}{2^n n! \omega_1 \sqrt{\pi}}} H_n\left(\frac{\sqrt{2} x_1}{\omega_1}\right) \exp\left(-j \frac{\pi x_1^2}{\lambda_1 q_1}\right). \quad (\text{B.2})$$

where λ_1 is the wavelength in the medium where the beam is currently located. The field distribution of the HG mode propagates through a distance L hence can be written as

$$u_n(x_2, z_2) = \sqrt{\frac{j}{B\lambda_0}} \left\{ \int_{-\infty}^{\infty} \left[\sqrt{\frac{\sqrt{2}}{2^n n! \omega_1 \sqrt{\pi}}} H_n\left(\frac{\sqrt{2} x_1}{\omega_0}\right) e^{-j \frac{\pi x_1^2}{\lambda_1 q_1}} \right] \right.$$

$$\left. \times e^{-j \frac{\pi(Ax_1^2 - 2x_1x_2 + Dx_2^2)}{B\lambda_0}} dx_1 \right\}, \quad (\text{B.3})$$

where the phase term $\exp(-jkL)$ has been neglected since it does not affect the intensity distribution $|u_n(x_2, z_2)|^2$. Employing the generating function of the Hermite polynomials, $e^{2\xi t - t^2} = \sum_{n=0}^{\infty} H_n(\xi) t^n / n!$, we can further obtain

$$\begin{aligned} & \sum_{n=0}^{\infty} \frac{t^n}{\sqrt{n!}} u_n(x_2, z_2) \\ &= \sqrt{\frac{j}{B\lambda_0}} \sqrt{\frac{2}{\pi}} \int_{-\infty}^{\infty} \sum_{n=0}^{\infty} \frac{t^n}{\sqrt{n!}} \sqrt{\frac{1}{2^n n! \omega_1}} H_n\left(\frac{\sqrt{2} x_1}{\omega_1}\right) e^{-j \frac{\pi x_1^2}{\lambda_1 q_1}} e^{-j \frac{\pi(Ax_1^2 - 2x_1x_2 + Dx_2^2)}{B\lambda_0}} dx_1 \\ &= \sqrt{\frac{j}{B\lambda_0 \omega_1}} \sqrt{\frac{2}{\pi}} \int_{-\infty}^{\infty} \left[\sum_{n=0}^{\infty} \frac{(t/\sqrt{2})^n}{n!} H_n\left(\frac{\sqrt{2} x_1}{\omega_1}\right) \right] e^{-j \frac{\pi x_1^2}{\lambda_1 q_1}} e^{-j \frac{\pi(Ax_1^2 - 2x_1x_2 + Dx_2^2)}{B\lambda_0}} dx_1 \\ &= \sqrt{\frac{j}{B\lambda_0 \omega_1}} \sqrt{\frac{2}{\pi}} \int_{-\infty}^{\infty} e^{\frac{2x_1 t}{\omega_1} - \frac{t^2}{2}} e^{-j \frac{\pi x_1^2}{\lambda_1 q_1}} e^{-j \frac{\pi(Ax_1^2 - 2x_1x_2 + Dx_2^2)}{B\lambda_0}} dx_1. \end{aligned} \quad (\text{B.4})$$

Calculate the exponent with allocation method and simplify the equation with $\lambda_0 = \lambda_1$, the exponent can be derived to be

$$\begin{aligned} & 2 \frac{t}{\omega_1} x_1 - \frac{t^2}{2} - j \frac{\pi x_1^2}{\lambda_1 q_1} - j \frac{\pi(Ax_1^2 - 2x_1x_2 + Dx_2^2)}{B\lambda_0} \\ &= -j \frac{\pi}{\lambda_0} \left(\frac{1}{q_1} + \frac{A}{B} \right) x_1^2 + \left(\frac{2t}{\omega_1} + j \frac{2\pi}{\lambda_0} x_2 \right) x_1 - \left(\frac{t^2}{2} + j \frac{\pi D}{\lambda_0 B} x_2^2 \right) \\ &= -j \frac{\pi}{\lambda_0} \left(\frac{1}{q_1} + \frac{A}{B} \right) \left\{ x_1^2 - 2 \left[\left(\frac{t}{\omega_1} + j \frac{\pi}{\lambda_0 B} x_2 \right) / j \frac{\pi}{\lambda_0} \left(\frac{1}{q_1} + \frac{A}{B} \right) \right] x_1 \right\} \\ &+ \left[\left(\frac{t}{\omega_1} + j \frac{\pi}{\lambda_0 B} x_2 \right) / j \frac{\pi}{\lambda_0} \left(\frac{1}{q_1} + \frac{A}{B} \right) \right]^2 \left\{ + \left[\left(\frac{t}{\omega_1} + j \frac{\pi}{\lambda_0 B} x_2 \right) / j \frac{\pi}{\lambda_0} \left(\frac{1}{q_1} + \frac{A}{B} \right) \right] \right. \\ &\left. - \left(\frac{t^2}{2} + j \frac{\pi D}{\lambda_0 B} x_2^2 \right) \right\}. \end{aligned} \quad (\text{B.5})$$

Applying the integral identity $\int_{-\infty}^{\infty} \exp(-ax^2) dx = \sqrt{\pi/a}$ to Eq. (B.5) and substituting

the obtained exponent into Eq. (B.4), we can rewrite Eq. (B.4) as

$$\sum_{n=0}^{\infty} \frac{t^n}{\sqrt{n!}} u_n(x_2, z_2) = \sqrt{\frac{\sqrt{2}}{\omega_1 \sqrt{\pi}}} \sqrt{\frac{1}{A+B/q_1}} e^{\left[\left(\frac{t}{\omega_1} + j \frac{\pi}{\lambda_0 B} x_2 \right)^2 / j \frac{\pi}{\lambda_0} \left(\frac{1}{q_1} + \frac{A}{B} \right) \right] - \frac{t^2}{2} - j \frac{\pi D}{\lambda_0 B} x_2^2}. \quad (\text{B.6})$$

To eliminate the series in the left hand side (LHS) of Eq. (B.6) and find the expression for the amplitude distribution $u_n(x_2, z_2)$, we should apply again the generating function of the Hermite polynomials to the right hand side (RHS). See the exponent first,

$$\begin{aligned} & \left[\left(\frac{t}{\omega_1} + j \frac{\pi}{\lambda_0 B} x_2 \right)^2 / j \frac{\pi}{\lambda_0} \left(\frac{1}{q_1} + \frac{A}{B} \right) \right] - \frac{t^2}{2} - j \frac{\pi D}{\lambda_0 B} x_2^2 \\ &= - \underbrace{\left(\frac{1}{2} + \frac{1}{\pi \omega_1^2 (1/q_1 + A/B) / \lambda_0} j \right) t^2}_{(1)} + 2 \underbrace{\frac{1}{B \omega_1 (1/q_1 + A/B)}}_{(2)} x_2 t - j \left(\frac{\pi}{\lambda_0 q_2} \right) x_2^2, \quad (\text{B.7}) \end{aligned}$$

where $1/q_2 = (C + D/q_1)/(A + B/q_1)$. Define a new parameter t' for the term (1) in

Eq. (B.7), where

$$t'^2 = \frac{1}{2} \left(1 + \frac{2}{\pi \omega_1^2 (1/q_1 + A/B) / \lambda_0} j \right) t^2, \quad (\text{B.8})$$

$$\Rightarrow t' = \frac{t}{\sqrt{2}} \sqrt{1 + \frac{2}{\pi \omega_1^2 (1/q_1 + A/B) / \lambda_0} j}. \quad (\text{B.9})$$

Furthermore, employ the parameter t' derived in Eq. (B.9) and define a new parameter ξ' for term (2) in Eq. (B.7):

$$2\xi' t' = 2\xi' \frac{t}{\sqrt{2}} \sqrt{1 + \frac{2}{\pi \omega_1^2 (1/q_1 + A/B) / \lambda_0} j} = 2 \frac{1}{B \omega_1 (1/q_1 + A/B)} x_2 t, \quad (\text{B.10})$$

$$\Rightarrow \xi' = \frac{\sqrt{2}}{B \omega_1 (1/q_1 + A/B)} \frac{1}{\sqrt{1 + 2j / [\pi \omega_1^2 (1/q_1 + A/B) / \lambda_0]}} x_2$$

$$= \frac{\sqrt{2}}{\sqrt{A+B/q_1} \sqrt{(A+B/q_1)\omega_1^2 + 2\lambda_0 j/\pi B}} x_2. \quad (\text{B.11})$$

Substitute Eq. (B.9) and Eq. (B.11) into Eq. (B.7), Eq. (B.7) can be rewritten as

$$\begin{aligned} & \sum_{n=0}^{\infty} \frac{t^n}{\sqrt{n!}} u_n(x_2, z_2) \\ &= \sqrt{\frac{\sqrt{2}}{\omega_1 \sqrt{\pi}}} \sqrt{\frac{1}{A+B/q_1}} \underbrace{e^{-t^2 + 2\xi t - j\frac{\pi D}{\lambda_0 B} x_2^2}}_{\text{generating func}} \\ &= \sqrt{\sqrt{\frac{2}{\pi}}} \left(\frac{1}{A+B/q_1}\right)^{n+(1/2)} \sum_{n=0}^{\infty} \frac{t^n}{\sqrt{n!}} \sqrt{\frac{1}{2^n n! \omega_1}} \left(\frac{\omega_2}{\omega_1}\right)^n H_n\left(\frac{\sqrt{2}x_1}{\omega_2}\right) e^{-j\frac{\pi x_2^2}{\lambda_0 q_2}}, \end{aligned} \quad (\text{B.12})$$

where $\omega_2 = \omega_1 \sqrt{(A+B/q_1)^2 + j[2B\lambda_0(A+B/q_1)/\pi\omega_1^2]}$.

Compare the RHS and LHS term-by-term, the field distribution can be given by

$$\begin{aligned} u_n(x_2, z_2) &= \sqrt{\frac{\sqrt{2}}{2^n n! \omega_1 \sqrt{\pi}}} \left(\frac{1}{A+B/q_1}\right)^{n+(1/2)} \\ &\quad \times \left(\frac{\omega_2}{\omega_1}\right)^n H_n\left(\frac{\sqrt{2}x_2}{\omega_2}\right) \exp\left(-j\frac{\pi x_2^2}{\lambda_0 q_2}\right) \end{aligned} \quad (\text{B.13})$$

For a high-order HG mode in the two transverse dimension (x,y), Eq. (B.13) can be modified as

$$\begin{aligned} u_{n,m}(x_2, y_2, z_2) &= u_n(x_2, z_2) u_m(y_2, z_2) \\ &= \left(\frac{\omega_{2x}}{\omega_{1x}}\right)^n \left(\frac{\omega_{2y}}{\omega_{1y}}\right)^m \sqrt{\frac{1}{2^{n+m-1} (n+m)! \pi \omega_{1x} \omega_{1y}}} \\ &\quad \times \left(\frac{1}{A_x + B_x/q_{1x}}\right)^{n+1/2} \left(\frac{1}{A_y + B_y/q_{1y}}\right)^{m+1/2} H_n\left(\frac{\sqrt{2}x_2}{\omega_{2x}}\right) H_m\left(\frac{\sqrt{2}y_2}{\omega_{2y}}\right) \\ &\quad \times \exp\left(-j\frac{\pi x_2^2}{\lambda_0 q_{2x}}\right) \exp\left(-j\frac{\pi y_2^2}{\lambda_0 q_{2y}}\right), \end{aligned} \quad (\text{B.14})$$

B.2 Input a Rotated Hermite-Gaussian Mode

We first expand the rotated high-order HG modes into a set of HG basis without rotation and find the weighting coefficients:

$$u_{n,m}(\xi_1, \eta_1, z_1) = u_n(\xi_1, z_1) u_m(\eta_1, z_1) \quad (\text{B.15})$$

$$= \sum_{s=0}^N D_s(\theta) u_{n,m}(x_1, y_1, z_1), \quad (\text{B.16})$$

where $N=n+m$, and the coordinates (ξ, η) for the optical beam follow the relation:

$$\begin{cases} \xi_1 = x_1 \cos \theta + y_1 \sin \theta \\ \eta_1 = x_1 (-\sin \theta) + y_1 \cos \theta \end{cases} \quad (\text{B.17})$$

From the generating function in the two transverse dimensions, we have

$$e^{-r^2+2\bar{\xi}r} e^{-t^2+2\bar{\eta}t} = \sum_{m=0}^{\infty} \frac{H_m(\bar{\xi}) r^m}{m!} \sum_{n=0}^{\infty} \frac{H_n(\bar{\eta}) t^n}{n!}, \quad (\text{B.18})$$

where $\bar{\xi} = \sqrt{2}\xi/\omega_1$, $\bar{\eta} = \sqrt{2}\eta/\omega_1$, $\bar{x} = \sqrt{2}x/\omega_1$, and $\bar{y} = \sqrt{2}y/\omega_1$. Here we have assumed that the input mode is an isotropic, i.e. the beam radius in x and y directions are the same. Substitute Eq. (B.17) into the LHS of Eq. (B.18):

$$\begin{aligned} & e^{-r^2+2\bar{\xi}_1 r} e^{-t^2+2\bar{\eta}_1 t} \\ &= e^{-r^2+2\bar{\xi}_1 r} e^{-t^2+2\bar{\eta}_1 t} \\ &= e^{-r^2+2(\bar{x}_1 \cos \theta + \bar{y}_1 \sin \theta) r} e^{-t^2+2[\bar{x}_1 (-\sin \theta) + \bar{y}_1 \cos \theta] t} \\ &= e^{-(r \cos \theta - t \sin \theta)^2 + 2(r \cos \theta - t \sin \theta) \bar{x}_1} e^{-(r \sin \theta + t \cos \theta)^2 + 2(r \sin \theta + t \cos \theta) \bar{y}_1}. \end{aligned} \quad (\text{B.19})$$

Apply the generating function to Eq. (B.19):

$$\begin{aligned} & e^{-(r \cos \theta - t \sin \theta)^2 + 2(r \cos \theta - t \sin \theta) \bar{x}_1} e^{-(r \sin \theta + t \cos \theta)^2 + 2(r \sin \theta + t \cos \theta) \bar{y}_1} \\ &= \sqrt{\frac{\pi}{2}} \omega_1 e^{j \frac{\pi \omega_1^2 (\bar{x}_1^2 + \bar{y}_1^2)}{2\lambda_0 q_1}} \sum_{N=0}^{\infty} 2^{N/2} \end{aligned}$$

$$\begin{aligned}
 & \times \sum_{s=0}^N \frac{(r \cos \theta - t \sin \theta)^s}{\sqrt{s!}} \frac{(r \sin \theta + t \cos \theta)^{N-s}}{\sqrt{(N-s)!}} u_{s,N-s}(x_1, y_1, z_1) \\
 & = \sqrt{\frac{\pi}{2}} \omega_1 e^{j \frac{\pi \omega_1^2 (\bar{x}_1^2 + \bar{y}_1^2)}{2\lambda_0 q_1}} \sum_{N=0}^{\infty} 2^{N/2} \\
 & \times \left[\sum_{s=0}^N \sum_{v_1=0}^s \sum_{v_2=0}^{N-s} \frac{C_{v_1}^s (r \cos \theta)^{v_1} (-t \sin \theta)^{s-v_1}}{\sqrt{s!}} \right. \\
 & \left. \frac{C_{v_2}^{N-s} (r \sin \theta)^{v_2} (t \cos \theta)^{N-s-v_2}}{\sqrt{(N-s)!}} u_{s,N-s}(x_1, y_1, z_1) \right]. \tag{B.20}
 \end{aligned}$$

Similarly, the RHS in Eq. (B.18) can be modified as

$$\begin{aligned}
 & \sum_{m=0}^{\infty} \frac{H_m(\bar{\xi}_1) r^m}{m!} \sum_{n=0}^{\infty} \frac{H_n(\bar{\eta}_1) t^n}{n!} \\
 & = \sqrt{\frac{\pi}{2}} \omega_1 e^{j \frac{\pi \omega_1^2 (\bar{\xi}_1^2 + \bar{\eta}_1^2)}{2\lambda_0 q_1}} \times \left[\sum_{m=0}^{\infty} \sqrt{\frac{2}{\pi}} \sqrt{\frac{1}{2^m m! \omega_1}} \frac{(\sqrt{2}r)^m}{\sqrt{m!}} H_m(\bar{\xi}_1) e^{-j \frac{\pi \omega_1^2 \bar{\xi}_1^2}{2\lambda_0 q_1}} \right. \\
 & \left. \times \sum_{n=0}^{\infty} \sqrt{\frac{2}{\pi}} \sqrt{\frac{1}{2^n n! \omega_0}} \frac{(\sqrt{2}t)^n}{\sqrt{n!}} H_n(\bar{\eta}_1) e^{j \frac{\pi \omega_1^2 \bar{\eta}_1^2}{2\lambda_0 q_1}} \right] \\
 & = \sqrt{\frac{\pi}{2}} \omega_1 e^{j \frac{\pi \omega_1^2 (\bar{\xi}_1^2 + \bar{\eta}_1^2)}{2\lambda_0 q_1}} \sum_{N=0}^{\infty} 2^{N/2} \sum_{m=0}^N \frac{r^m}{\sqrt{m!}} \frac{t^{N-m}}{\sqrt{(N-m)!}} u_{m,N-m}(\xi_1, \eta_1, z_1). \tag{B.21}
 \end{aligned}$$

Comparing Eq. (B.20) and Eq. (B.21) term-by-term, we can obtain the relation:

$$\begin{cases} (LHS) & r^{v_1+v_2} = r^m & (RHS) \\ (LHS) & t^{s-v_1+N-s-v_2} = t^{N-m} & (RHS) \end{cases} \Rightarrow v_1 + v_2 = m. \tag{B.22}$$

Moreover, let $v_1 = m - v$, and $v_2 = v$, there follows the relations that

$$\begin{cases} v_1 = 0 \sim s \\ v_2 = 0 \sim N - s \\ m = 0 \sim N \end{cases} \tag{B.23}$$

Therefore, Eq. (B.20) can be rewritten as

$$\begin{aligned}
 & \sqrt{\frac{\pi}{2}} \omega_1 e^{j \frac{\pi \omega_1^2 (\bar{x}_1^2 + \bar{y}_1^2)}{2\lambda_0 q_1}} \sum_{N=0}^{\infty} 2^{N/2} \sum_{m=0}^N \frac{r^m}{\sqrt{m!}} \frac{t^{N-m}}{\sqrt{(N-m)!}} u_{m,N-m}(x_1, y_1, z_1) \\
 &= \sqrt{\frac{\pi}{2}} \omega_1 e^{j \frac{\pi \omega_1^2 (\bar{x}_1^2 + \bar{y}_1^2)}{2\lambda_0 q_1}} \sum_{N=0}^{\infty} 2^{N/2} \left[\sum_{s=0}^N \sum_{m=0}^N \sum_v \frac{C_{m-v}^s (r \cos \theta)^{m-v} (-t \sin \theta)^{s-m+v}}{\sqrt{s!}} \right. \\
 & \quad \left. \times \frac{C_v^{N-s} (r \sin \theta)^v (t \cos \theta)^{N-s-v}}{\sqrt{(N-s)!}} u_{m,N-m}(x_1, y_1, z_1) \right] \\
 &= \sqrt{\frac{\pi}{2}} \omega_1 e^{j \frac{\pi \omega_1^2 (\bar{x}_1^2 + \bar{y}_1^2)}{2\lambda_0 q_1}} \sum_{N=0}^{\infty} 2^{N/2} \left[\sum_{s=0}^N \sum_{m=0}^N \right. \\
 & \quad \left. \sum_v \frac{s!(N-s)! r^m t^{N-m} (\cos \theta)^{N-s+m-2v} (-\sin \theta)^{s-m+2v} (-1)^v}{\sqrt{s!} \sqrt{(N-s)!} (m-v)! (s-m+v)! v! (N-s-v)!} u_{m,N-m}(x_1, y_1, z_1) \right].
 \end{aligned} \tag{B.24}$$

Since Eq. (B.21) is equivalent to Eq. (B.24) and the length is conserved under rotation, we can compare Eq. (B.21) and Eq. (B.24) term-by-term to obtain the field distribution as follows

$$u_{n,m}(\xi_1, \eta_1, z_1) = \sum_{s=0}^N d_{s-\frac{N}{2}, m-\frac{N}{2}}^2(\theta) u_{s,N-s}(x_1, y_1, z_1), \tag{B.25}$$

where

$$\begin{aligned}
 d_{s-\frac{N}{2}, m-\frac{N}{2}}^2(\theta) &= \sqrt{s!} \sqrt{(N-s)!} \sqrt{m!} \sqrt{(N-m)!} \\
 & \quad \times \sum_{v=\max[0, m_1-n_1]}^{\min[N-n_1, m_1]} \frac{(-1)^v \left[\cos\left(\frac{\beta}{2}\right) \right]^{n_1+m_1-2v} \left[\sin\left(\frac{\beta}{2}\right) \right]^{n_2-m_1+2v}}{v! (N-n_1-v)! (m_1-v)! (n_1-m_1+v)!}.
 \end{aligned} \tag{B.26}$$

Consider the case for the input beam traveling through an ABCD system, it is evident that the output beam can be directly obtained to be

$$u_{n,m}(\xi_2, \eta_2, z_2) = \sum_{s=0}^N d_{s-\frac{N}{2}, m-\frac{N}{2}}^2(\theta) u_{s,N-s}(x_2, y_2, z_2). \tag{B.27}$$

Curriculum Vitae

Personal Data

Name: Yu-Chieh Lin

Sex: Female

Birthday: Dec. 17, 1985

Nationality: Taiwan

E-mail: prudencejade.ep98g@nctu.edu.tw

prudencejade@gmail.com

Mobile Phone: 886-912-712415

Education

2003-2005 Kaohsiung Municipal Kaohsiung Girls' Senior High School, Kaohsiung, Taiwan.

2006-2009 B.S. in Department of Electrophysics, National Chiao Tung University, Hsinchu, Taiwan.

2009-2013 Ph.D. in Department of Electrophysics, National Chiao Tung University, Hsinchu, Taiwan.

Work History

2010 T. A. of Quantum Mechanics

2010-2011 T. A. of General Physics (I) & (II)

2011-2013 Pre-PhD T. A. of General Physics (I) & (II)

Research Interest

Laser Physics

Quantum Physics

Publication List

(1) Journal papers:

1. **Y. C. Lin**, P. H. Tuan, Y. T. Yu, H. C. Liang, K. W. Su, K. F. Huang, and Y. F. Chen, "Observation of Disordered Wave Functions with Conical Second Harmonic Generation and Verification of Transition from Extended to Pre-localized states in Weak Localization," Phys. Rev. B, **87**, 045117 (2013).
2. **Y. C. Lin**, T. H. Lu, K. F. Huang, and Y. F. Chen, "Model of commensurate harmonic oscillators with SU(2) coupling interactions: Analogous observation in laser transverse modes," Phys. Rev. E, **85**, 046217 (2012).
3. H. C. Liang, J. C. Tung, T. W. Wu, C. H. Tsou, **Y. C. Lin** and Y. F. Chen "Formation and recurrence of quasicrystalline patterns from quantum dynamics of suddenly released matter waves: Analogous manifestation of optical waves," Europhys. Lett., **99**, 10005 (2012)
4. Y. F. Chen, **Y. C. Lin**, W. Z. Zhuang, H. C. Liang, K. W. Su, and K. F. Huang, "Generation of large orbital angular momentum from superposed Bessel beams corresponding to resonant geometric modes," Phys. Rev. A, **85**, 043833 (2012).
5. **Y. C. Lin**, T. H. Lu, K. F. Huang, and Y. F. Chen, "Generation of optical vortex array with transformation of standing-wave Laguerre-Gaussian mode," Opt. Express, **19**, 10293 (2011).
6. Y. F. Chen, H. C. Liang, **Y. C. Lin**, Y. S. Tzeng, K. W. Su, and K. F. Huang, "Generation of optical crystals and quasicrystal beams Kaleidoscopic patterns and phase singularity," Phys. Rev. A, **83**, 053813 (2011).
7. H. C. Liang, P. Y. Chiang, Y. J. Huang, **Y. C. Lin**, and Y. F. Chen, "Simultaneous self-mode-locking of TEM_{0,0} and TEM_{1,0} modes in a

- Nd:YVO4 laser: Application for measuring the thermal focal length,” *Laser Phys.* **21**, 480 (2011).
8. Y. T. Yu, Y. J. Huang, P. Y. Chiang, **Y. C. Lin**, K. F. Huang, and Y. F. Chen, “Non-paraxial contributions to the far-field pattern of surface-emitting lasers: a manifestation of the momentum-space wavefunctions of quantum billiards,” *J. Opt.* **13**, 075705 (2011).
 9. Y. F. Chen, **Y. C. Lin**, K. F. Huang, and T. H. Lu, “Spatial transformation of coherent optical waves with orbital morphologies,” *Phys. Rev. A*, **82**, 043801 (2010).
 10. T. H. Lu, **Y. C. Lin**, Y. F. Chen, and K. F. Huang, “Generation of multi-axis Laguerre-Gaussian beams geometric modes of a hemiconfocal cavity,” *Appl. Phys. B* **27** (2010).
 11. Y. F. Chen, Y. J. Huang, P. Y. Chiang, **Y. C. Lin**, and H. C. Liang, “Controlling number of lasing modes for designing short-cavity self-mode-locked Nd-doped vanadate lasers,” *Appl. Phys. B* **23** (2010).
 12. T. H. Lu, **Y. C. Lin**, H. C. Liang, Y. J. Huang, Y. F. Chen, and K. F. Huang, “Observation of lasing modes with exotic localized wave patterns from astigmatic large-Fresnel-number cavities,” *Opt. Lett.* **35**, 345 (2010).
 13. H. C. Liang, Y. J. Huang, **Y. C. Lin**, T. H. Lu, Y. F. Chen, and K. F. Huang, “Picosecond optical vortex converted from multigigahertz self-mode-locked high-order Hermite-Gaussian Nd:GdVO4 lasers,” *Opt. Lett.* **34**, 3842 (2009).
 14. T. H. Lu, **Y. C. Lin**, Y. F. Chen, and K. F. Huang, “Observation and analysis of coherent optical waves emitted from large-Fresnel number degenerate cavities,” *Opt. Express* **17**, 3007 (2009).
 15. T. H. Lu, **Y. C. Lin**, Y. F. Chen, and K. F. Huang, “Three-Dimensional coherent optical waves localized on trochoidal parametric surfaces,” *Phys. Rev.*

Lett. **101**, 233901 (2008).

(2)Conference papers:

1. T. H. Lu, and **Y. C. Lin** “Generation of High-order Coaxial and Multi-axial Laguerre-Gaussian Beams from Degenerate Laser Cavities” Conference on Lasers and Electro-Optics/Pacific Rim Sydney, Australia, August 28, (2011).
2. **Y.C. Lin**, K. W. Su, and Y. F. Chen, “ Various patterns transformed by a $\pi/2$ cylindrical lens mode converter,” The fifth Workshop of the Stimulated Brillouin Scattering and Phase Conjugation supported by the Japan Laser Society and Light-wave synthesis research group in Optical Society of Japan, oral presentation (2010).
3. **Y. C. Lin**, T. H. Lu, H. C. Liang, Y. J. Huang, Y. F. Chen, and K. F. Huang, “Exotic localized wave patterns observed from astigmatic large-Fresnel-number cavities,” Annual Meeting of the Physical Society of Republic of China, poster presentation (2010).
4. **Y. C. Lin**, T. H. Lu, Y. F. Chen, and K. F. Huang, “The formation of three-dimensional coherent waves localized on trochoidal parametric surfaces by longitudinal-transverse coupling,” Annual Meeting of the Physical Society of Republic of China, poster presentation (2009).

(3) Award and Honor:

1. **林毓捷**, “從幾何光學-波動光學的對應性研究具有大角動量之雷射模態”國科會大專生參與專題研究計畫, 研究創作獎 (2008)
2. 龍騰微笑競賽 <<**Team-laser**>>, 佳作 (2011)

3. 優良助教獎 (2011)
4. 100 年度交通大學學生優良期刊論文獎
5. 101 年度交通大學學生優良期刊論文獎

